Advanced Space Concepts Laboratory

Department of Mechanical and Aerospace Engineering

Faculty of Engineering

University of Strathclyde

Polynomial motion planning in spacecraft attitude and docking to tumbling debris

Albert Caubet-Domingo

Submitted in fulfilment of the requirements for the degree of

Doctor of Philosophy

2016

This thesis is the result of the author's original research. It has been composed by the author and has not been previously submitted for examination which has led to the award of a degree.

Albert Caubet
Glasgow, Scotland, 04/04/2016

"Why did you want to climb Mount Everest?"
"Because it's there"

—George Mallory, teacher and mountaineer

Acknowledgements

Why did I want to do a PhD? Because it was there, as Mallory said. Like a mountain climb, it is challenge, a journey of learning, waiting to be explored. And like a mountain climb, once on top of it one is left to discover that another mountain awaits in the horizon. In the climb of my PhD, quite a lot of people was there holding the rope—securing, guiding, climbing along. Hence, I would like to express my gratitude to them all.

To Josep Boada and Elisabet Canalias back in Toulouse, who helped me make the decision of starting this PhD, and to Hubert Fraysse, who relieved me from my duties in his office to start a new adventure.

To Daniel "Dan" Garcia Yarnoz, who offered me his unconditional support in so many situations, professionally and personally. And to Chris Lowe, who inspired great adventures.

To the folks of the Advanced Space Concepts Laboratory—the core of my experience at the University of Strathclyde, the brave companions at conferences overseas, the heroes of coffee breaks. Briefly, friends: Jeannette, Dan, Pau (big researcher role models, those three), Andreas, Chris, Steve, Marcel, Juanma, David, Ross, Annalisa, Lorenzo, Jonathan, Chiara, Ciara, Patricia, Giuliano, Jose, Edu, et al.

To Prof. Colin McInnes, head of the ASCL, who pioneered in polynomial planning applied to attitude manoeuvres back in the '98. Finding his paper brought a healthy dose of humility.

To the folks of the Astronet-II network: Luca, Zubin, Fabrizio, Alex, Mattia, Eli, Andrea, Marta, Rocio, Claudiu, Steve, Willem, Mohammad, Lili, Pawel, and Pedro. With a special mention to its coordinators Gerard Gomez and Josep Masdemont, and to my supervisor during the Deimos Space placement, Miguel Hagenfeldt.

To the European Commission, who made possible the Marie Curie fellowship PITN-GA-2011-289240 AstroNet-II, within the FP7 framework.

Finally, to Dr. James D. Biggs, my supervisor, who guided me and helped me at all times, but who at the same time gave me the freedom needed to spark creativity, and who made everything look clearer after nothing made sense at all.

To Mum, Dad, Brother, and Sister.

To Scotland and its people.

Abstract

Motion or trajectory planning is a key aspect of the advances in the performance and autonomy of spacecraft operations. However, the computational resources of spacecraft are still limited. In this sense, using polynomials to shape trajectories, and computing accelerations and other parameters via inverse dynamics, is an efficient approach to obtain suboptimal solutions. In this thesis the area of attitude manoeuvres is covered, as well as translational motions in the frame of docking to a tumbling satellite for Active Debris Removal missions (in which the detumbling case is also studied). In the case of attitude slew manoeuvres, quaternions are shaped with polynomials and normalised. Issues such as numerical stability of high-order polynomials and the special case of spin-to-spin manoeuvres have been addressed. Regarding trajectory optimisation, efficient algorithms for time minimisation are proposed, along with obstacle avoidance methods. The performance of the polynomial trajectories compared to optimal control is analysed. The polynomial motion planning method is applied to manoeuvres of flexible spacecraft, assessing how the smoothness of motions can limit induced vibrations. In the scenario of docking to a tumbling target (based on Envisat), trajectories are generated with polynomials and fuel is optimised. An axisymmetric approximation of the target is used to analytically evaluate its dynamics. A cylindrical surface enclosing the target is defined for obstacle avoidance purposes. The docking strategy is divided in three segments (first approach, hovering, docking axis approach), to enhance safety

and robustness. While in the attitude case the trajectory is tracked with a simple controller or performed in open-loop, in the docking scenario the feedback loop is closed by re-computing the trajectory planning algorithm with a certain frequency. Finally, the problem of detumbling the satellite is addressed. A concept is proposed based on an external module equipped with magnetorquers and carried by the chaser, which performs an autonomous docking to the target, and proceeds to stabilise its rotation. A preliminary design and sizing of the system is realised, and simulations are performed to assess its feasibility.

Contents

List of Symbols and Acronyms

Constants and Variables

$\mathbf{a}$	Acceleration vector
$\mathbf{B}$	Magnetic field vector
$\mathbf{e}$	Basis vector or eigenaxis
$\mathbf{F}$	Force
$\mathbf{H}$	Magnetic intensity vector
$\mathbf{h}$	Angular momentum
$\mathbf{M}$	Magnetising field
$\mathbf{m}$	Magnetic moment
$\mathbf{q}$	Quaternion vector
$\mathbf{q}^*$	Un-normalised quaternion vector
$\mathbf{r}$	Position vector
$\mathbf{T}$	Torque
$\mathbf{u}$	Torque
$\mathbf{v}$	Velocity vector
$\mathbf{w}$	Generic vector
A	Direction cosine matrix (transposed of R)
a_{ij}	ij-th polynomial coefficient
C	Differentiability class
f_c	Fuel consumed
I	Inertia (matrix) or current (variable)
$I_{1,2,3}$	Principal moments of inertia
J	Optimisation performance index

K_d	Derivative gain
K_p	Proportional gain
m	Mass (variable) or number of boundary conditions (index)
N	Number of coil turns
n	Polynomial degree
N_d	Demagnetising factor
P	Power
q_i	i-th quaternion element
R	Rotation matrix (transposed of A)
$s_{1,2,3}$	Axis-azimuth coordinates
t	Time
T_s	Sampling time
t_s	Stabilisation time
V	Voltage
x	X coordinate
y	Y coordinate
z	Z coordinate

α	Alpha
α	Generic angle
$\boldsymbol{\omega}$	Angular velocity
ϵ	Relative error
η	Error ratio
γ	Obstacle avoidance angle
λ	Slenderness ratio
μ_0	Free air magnetic permeability
μ_r	Relative magnetic permeability
ρ	Density
τ	Scaled time
θ	Eigenangle

Superscripts

^{B}	Relative to body frame
^{I}	Relative to inertial frame
^{T}	Transposed (matrix)

Subscripts

$_{0}$	Initial
$_{d}$	Difference
$_{e}$	Error
$_{f}$	Final
$_{i}$	i-th coordinate
$_{t}$	Total
$_{B}$	Resolved in body frame
$_{cmd}$	Commanded
$_{dp}$	Docking point
$_{ins}$	Insertion
$_{I}$	Resolved in inertial frame
$_{max}$	Maximum value
$_{min}$	Minimum value
$_{MT}$	Magnetorquer
$_{OA}$	Obstacle Avoidance
$_{pln}$	Planned
$_{r}$	Reaction wheel
$_{sc}$	Spacecraft
$_{total}$	Total
$_{wet}$	Wet (mass)
$_{wp}$	Waypoint

Acronyms

ED	Energy Density
SE	Specific Energy
A(D)CS	Attitude (Determination) and Control System

CM	Centre of Mass
CMG	Control Moment Gyro
DLR	Deutsches Zentrum fr Luft- und Raumfahrt
DOF	Degrees of Freedom
EO	Earth Observation
ESA	European Space Agency
GEO	Geostationary Earth Orbit
GNC	Guidance, Navigation, and Control
ISS	International Space Station
JAXA	Japan Aerospace eXploration Agency
LEO	Low Earth Orbit
LIDAR	Light Detection And Ranging
LQR	Linear Quadratic Regulator
MOI	Moment of Inertia
MPC	Model Predictive Control
MRP	Modified Rodrigues Parameters
NASA	National Aeronautics and Space Administration
RCS	Reaction Control System
TRL	Technology Readiness Level

List of Figures

List of Tables

Chapter 1

Introduction

1.1 Preface

The work in this thesis covers three major topics or applications: (a) attitude slew manoeuvres, (b) docking to an uncooperative satellite, and (c) debris detumbling. While they are apparently independent areas of study, the same polynomial motion planning method is applied to both the attitude and docking problems. However, how the method is applied and where the focus is put is different, since each problem has its own peculiarities. In the debris detumbling case, a system is proposed where docking with a tumbling satellite is required, connecting those two topics—In the developments in the docking problem are used to help in the sizing of the detumbling system.

For each topic studied, new literature had to be reviewed, new problems had to be defined, new models had to be coded, and new solutions had to be obtained. While this diversification prevented me from testing even more cases or addressing more aspects of a particular area, it expanded my body of knowledge, kept me out of the comfort zone, and satisfied my curiosity. The result is a thesis where the chapters have all different flavours, and yet they are linked together by a common thread. At the end of the day, I hope that the ideas proposed here are found useful to researchers and engineers, and may inspire future work.

1.2 On the motion planning problem

Motion planning refers to the problem of defining a feasible trajectory subject to constraints [3]. Additionally, the trajectory can be optimised according to a specified cost function.

There is a variety of techniques to generate a trajectory. Optimal control theory is capable of achieving global optimality, but at high computational cost, and convergence is not guaranteed. Pseudospectral methods for optimal control [4] or a range of other methods [5] have a numerical approach, where global optimality is not guaranteed but good solutions can be obtained. The computational cost is still relatively high (amongst trajectory planning methods), but real-time applications in aerospace have been proposed [6]. Then there are methods focused on generating a geometric path, such as the Rapidly-exploring Random Tree (RRT) or A-star algorithms [3]. Those methods can rapidly find paths in highly constrained spaces, but the dynamics of the system along the path are not taken into account. Polynomial-based motion planning is a popular method due to its low computational cost and ease of manipulation, yet good trajectories can be obtained, hence is widely used e.g. in robotic manipulators [7] and computer graphics [8].

An internal model is used to evaluate the forces and torques of the system from the kinematics (the generated trajectory), an approach known as inverse dynamics. Also, the internal model can account for path constraints (obstacles) and other parameters, either for optimisation or constraint enforcement. If the internal model used to plan the trajectory were perfect, open-loop commands would make the system follow the motion without deviations. However, the internal model is a simplification of the real world which do not account for a number of effects (which may be stochastic). Therefore, closed-loop feedback control should track the trajectory to avoid divergence from the planned path. Alternatively, the feedback loop can be closed by re-computing the trajectory with a certain frequency, where the acceleration profile commanded in open loop is periodically updated.

Cubic splines, a form of polynomial planning, is a popular method for connecting path points, as in Guan [9]. Planning a motion with a single polynomial has some differences with respect to using splines or other piece-wise interpolating methods. A single polynomial ensures the smoothness (C^∞ differentiable) along the trajectory. In spline-based motion planning, a number of control points

are needed, which are iterated in the optimisation. The degrees of freedom in the trajectory are given by the number of control points, whereas with a single polynomial the degrees of freedom are obtained through the coefficients of additional terms (giving polynomials of higher degrees). The whole trajectory is being searched at once via iteration of the polynomial's coefficients, while taking into account any performance index and constraints. Overall, feasible trajectories can be obtained with less variables, reducing computational power and increasing the robustness of the optimisation, while being smooth from beginning to end. The numerical stability issues of dealing with high degree polynomials can be overcome via scaling.

There are some works that apply polynomials to other fields, but have a similar approach and conclusions to those found in this thesis. For instance, polynomial trajectory planning has been used in quadcopters by Richter [10]. It focuses on computational speed by using few variables in the polynomial, finding suboptimal solutions with unconstrained optimisation techniques. Also, Williams [11] uses a single polynomial in the joint-space trajectory generation problem of robotics with a via point. He highlights the use of one polynomial passing through this point (instead of two) as a strategy to avoid the problem of infinite spikes in jerk caused by non-smoothness.

Trajectory generation is an important aspect of the broader field of autonomy. In space exploration and exploitation, autonomy is a key technology [12]. In some cases, it allows to optimise tasks and cut costs in spacecraft operations, while in others, such as planetary space probes, autonomy is a hard requirement. Implementing more autonomy in spacecraft drives the need for more computational power. Traditionally, processing power in space has advanced at a slower pace than on Earth, mainly due to robustness requirements. However, there is a trend of increasing processing power—the Curiosity rover has a 200 MHz CPU, while Spirit and Opportunity sported 25 MHz. This trend opens new opportunities in the field of on-board autonomy and trajectory planning, but knowing that the computational resources are relatively limited, the efficiency of the algorithms has to be kept in mind.

In this work, the terminology *motion* or *trajectory* is used to define the time evolution of the position or attitude coordinates, whereas *path* refers to the geometric representation of coordinates in a time-independent space. Also, in the frame of GNC (Guidance, Navigation, and Control) the term *guidance* is understood

here as trajectory generation, providing a moving desired state that brings the subject to the final position and velocity. *Control* refers to the actuators' effort driving the system as a function of the error (weighted by a gain factor) between the current state and a certain desired state. The controller of a system may perform tracking of a trajectory (a time-varying profile of desired states given by guidance, with small error signals involved) or directly bring the system to a prescribed final state (initially, there is a large error signal). In this thesis, the main focus is on the trajectory generation or guidance part—the control aspect is used but no contributions are made, and ideal navigation is considered.

1.3 Spacecraft attitude control

Spacecraft attitude determination and control [13, 14, 15, 16] covers the range of systems and techniques necessary to measure and control the orientation of spacecraft in space, involving attitude dynamics and kinematics. Euler is considered the father of attitude dynamics in the 18th century, which came later than the giants of orbital dynamics, Newton and Kepler. As a matter of fact, Euler's laws of motion are an extension of Newton's laws to the case of rigid-body motion, identifying linear momentum (translational motion) and angular momentum (rotational motion). The Euler's equations of rigid-body dynamics are derived from those, which describe the rotational or attitude motion of a rigid body.

The attitude of a body is described as the rotation of a body-fixed frame with respect to an inertial reference frame [17]. In spacecraft, the body frame is usually centred in the centre of mass and aligned with certain instruments, actuators, or navigation systems. The inertial (or quasi-inertial) reference frame depends on the state of the mission, and have a fixed orientation relative to the star background. Non-inertial frames include the Earth-Centred/Earth-Fixed or the Local-Vertical/Local-Horizontal frames, which induce "virtual accelerations" as seen from the reference frame. The attitude can be represented globally (no singularities) and uniquely (an attitude can only be represented by a single set of coordinates) with so-called rotation matrices R. They transform a vector $\mathbf{v}_B$ resolved in (or as seen from) the body frame B to another resolved in the inertial frame I, as

$$\mathbf{v}_I = R\mathbf{v}_B \tag{1.1}$$

and can rotate the basis vectors of the inertial frame to form the rotated body frame. In R, the columns of the matrix are the basis vectors of the body frame resolved in the inertial frame. There exist other attitude representations which require less parameters, such as the triad of Euler angles, which are intuitive to use but they are not global nor unique. For spacecraft applications, where robustness and computational efficiency are prioritised, four quaternions are used, which are global but not unique (the same attitude can be represented by $+\mathbf{q}$ and $-\mathbf{q}$).

The attitude of a spacecraft can be controlled using a range of actuators. The highest versatility is given by three-axis stabilised spacecraft, which can orient and stabilise themselves in any direction by controlling the three axes. This is achieved using a set of thrusters forming the Reaction Control System (RCS) and/or internal momentum exchange devices such as reaction wheels and Control Momentum Gyroscopes (CMG; also known as control moment gyros). Reaction wheels and CMGs provide a continuous torque profile and high precision, whereas thrusters deliver high torques, and work with discrete pulses. Nonetheless, small thrusters with pulse-width modulation could generate rather precise continuous torque profiles. There are cost-effective actuators such as magnetic torquers, which interact with the Earth magnetic field (mainly used for detumbling and reaction wheels unloading), or solar vanes, but they lack 3-DOF control. Spin or dual-spin stabilisation is a simple and effective way of counteracting environmental torques, but it is not trivial to re-orient a spinning spacecraft and may limit the performance of the instruments. Thanks to the advent of performing on-board computers, sensors, and actuators, the popularity of spin stabilisation is decreasing in favour of three-axis stabilisation.

Spacecraft missions have specific pointing requirements classified in attitude or pointing modes, such as Earth pointing, Sun pointing, inertial pointing, safe mode (usually Sun pointing), etc. These modes drive requirements such as stabilisation and error budgets, met by an appropriate selection of sensors, actuators, and controls. The work in this thesis, however, focuses on slew manoeuvring, i.e. reorienting the spacecraft between pointing states. These manoeuvres occur with more or less frequency depending on the mission. An Earth-pointing telecommunications GEO satellite does not perform many slew manoeuvres throughout its mission. But an astronomical science spacecraft (space telescopes of various spectra) may be constantly re-pointing from object to object. During its short fly-by of Pluto, the New Horizons spacecraft frantically mapped the surface of the dwarf planet and its moons with several instruments. The new generation

of Earth Observation (EO) satellites, such as France's Pleiades, are highly manoeuvrable thanks to powerful CMGs, unlike older similar EO systems such as SPOT.

In spacecraft slew manoeuvres, motion planning can be used to optimise a certain performance parameter and/or satisfy differential and path constraints, before the trajectory is executed. Path or pointing constraints are exclusion areas over the unit sphere where a certain body-fixed axis shall not enter, for instance the boresight of some sensitive instruments must be kept at a minimum angle from the Sun direction. Differential constraints include dynamic and kinematic constraints. They generally require an internal model to calculate torque and other variables, in what is known as an inverse dynamics approach. For instance, it must be ensured that torque is not larger than the actuators' limit at any point in the trajectory. Apart from torque, reaction wheels experience saturation given by the wheels speed limit, which can also be evaluated. Sensors such as star trackers can have a maximum operational angular speed, and flexible structures may require limits on acceleration and jerk to avoid excessive deflection and vibration.

In agile EO missions, a number of ground patches must be sequentially scanned, where scheduling algorithms plan the sequence by estimating if the slew manoeuvre between the end of one patch and the beginning of another is feasible in terms of the actuators' capabilities [18]. Since the feasibility of a manoeuvre can be checked before it is executed, motion planning algorithms can be embedded the layer of scheduling algorithms for Earth Observation satellites.

In previous work on spacecraft attitude motion planning, McInnes [19] first shows the potential of applying inverse dynamics to attitude manoeuvres using polynomials and Euler angles, while Biggs [20] finds reference motions for reorienting a spinning satellite by solving analytically an optimal control problem, and Zhang [21] uses a 5^{th} degree polynomial to obtain a smooth eigenaxis rotation on a flexible spacecraft. In the field of computer graphics, Kim [8] proposes the use of exponential coordinates to satisfy the unit norm constraint of quaternions, with Tanygin [22] and Boyarko [23] applying this approach to spacecraft manoeuvres using inverse dynamics to minimize time and/or energy amongst this class of curves. Following from the work by Boyarko [23], Ventura [24] compares the performance (computational time and optimisation cost) of different attitude representations using splines for motion planning, and shows that the

exponential functions in the quaternion representation require a larger computational expense. Regarding optimisation, Bilimoria and Wie [25] demonstrate that the global time-optimal manoeuvre is performed with a bang-bang torque profile. Interestingly, Junkins [26] proves that for a single-axis rotational manoeuvre, the energy-optimal trajectory is a polynomial, which suggests that this function family may naturally provide energy-efficient manoeuvres.

Obstacle avoidance usually requires the computation of path points, which has been applied to spacecraft maneuvers in [27, 28, 29] with various degrees of computational expense. In some works such as Frazzoli [30] and Tanygin [31], pointing constraints are satisfied using randomised path planning algorithms, and then the time-independent geometric path is tracked with a controller. In contrast, trajectory or motion planning (shaping the attitude parameters with functions of time) addresses both path constraints and dynamic constraints. Randomised path planning performs better at finding a feasible geometric path in highly constrained spaces, but a priori it does not consider the dynamic and kinematic aspects of the motion as time-dependent motion planning does.

Discontinuities in the torque profile such as in bang-bang manoeuvres, or the initial step input given by feedback controllers, result in infinite jerk leading to the excitation of flexible modes (including spillover i.e. post-manoeuvre vibrations) [32, 33]. Several studies [34, 35, 36] propose solutions to this problem by smoothing the discontinuous torque switches of bang-bang manoeuvres, using a variety of functions.

1.4 Active Debris Removal

The number of debris objects in orbit is steadily increasing [37]. At present there are over 20000 catalogued objects greater than 10 cm. Each of these items could severely damage or destroy space assets. A significant proportion of orbital debris was caused by the 2007 Fengyun-1C anti-satellite test and the 2009 Iridium-Cosmos collision. For new spacecraft, space debris remediation activities involve post-mission disposal alongside manoeuvres through-life to avoid potential collisions. Given the number of objects, the number of collision warnings for operators is increasing and collision events can become inevitable (specially if both satellites are out of control). As the number of collisions increases, the debris population will steadily rise until a tipping point is reached where we will

see an uncontrollable, exponential growth of debris items, which will potentially limit the future utilisation of space (known as the Kessler effect).

Therefore, in order to limit the debris generation caused by satellite collisions, certain orbits need be de-populated (in particular the LEO region). Liou [1, 38] suggests that, if every year five to ten objects are removed from LEO, the debris population can be kept under control (Fig. 1.1).

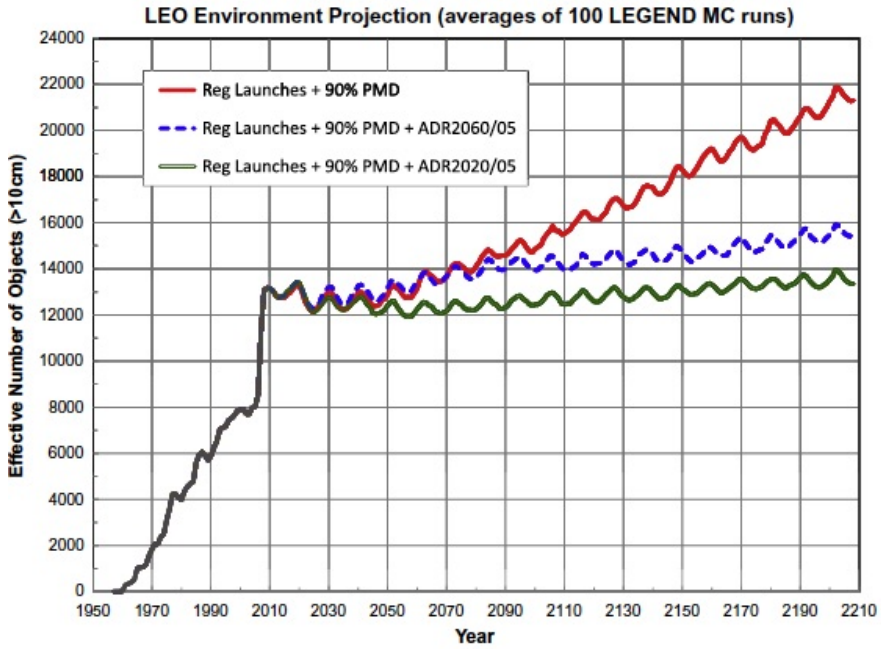

Figure 1.1: Post-Mission Disposal (PMD) of future spacecraft will not control the growth of the space debris population without the addition of Active Debris Removal of existing debris [1]

In particular, ESA is concerned about Envisat, a satellite for environmental studies placed in a LEO orbit. With a mass of 8 tons, bus dimensions of 2.5 x 2.5 x 10 m, and and a solar array 15 m long, it is one of the largest civilian Earth observation satellites. Control of the spacecraft was lost in 2012 after a 10-year mission, preventing its operators from performing the planned de-orbit operation. In its current orbit, it would take approximately 150 years to decay naturally. The LEO region in general is highly populated and the satellite is very large, thus the potential for massive generation of small pieces of debris out of a collision is significant. One of the most important challenges in ADR is interacting with a tumbling and uncooperative target. However, the tumbling state can be difficult to assess: an ESA study [39] found, using radar data, that Envisat is currently rotating at 3 deg/s, when 0.2 deg/s was predicted in simulations. Measurements

show that the anticipated gravity-gradient stabilisation does not occur. Although the reasons are unknown, this discrepancy could be explained by factors such as collisions with small debris, residual speed in reaction wheels, or outgassing.

A number of techniques for ADR missions are being assessed [40], and deorbiting strategies have been proposed [41, 42]. In the frame of ADR, debris objects to rendezvous with, generally out-of-service satellites or upper stages of launchers, are known as *targets*. The active servicing spacecraft is known as the *chaser*. In a typical mission, the chaser must rendezvous and dock or capture with a target satellite, with the goal of modifying its orbit either for re-entry or placement into a disposal orbit. In LEO, usually the most desirable deorbiting scenario is a controlled re-entry, where an accurate impulsive delta-v applied on the target brings the debris down over the South Pacific. In GEO, requirements stipulate that debris shall be transferred out of the protected region, as defined by the IADC (Inter-Agency Debris Coordination Committee).

In order to capture the target, robotic arms can be used, but they require to approach a tumbling target with the subsequent collision risk. A net or a harpoon can be thrown at the target when in close proximity, linking it to the chaser spacecraft by a tether. ESA and Airbus DS, among others, have investigated such concepts for deorbiting: if the target is pulled, as opposed to pushed, the requirement of centre of mass alignment is relaxed. Harpoons for ADR use have been designed and lab tested by Airbus DS [43]. A contactless solution for deorbiting a target, based on the exhaust plume of an electric thruster pushing the debris object, has been proposed by Bombardelli [44]. This method avoids the need for grasping and detumbling, but they cannot ensure a controlled re-entry and could potentially create debris in the form of small fragments.

In this work, the docking and detumbling issues are addressed, and the selected baseline scenarios assume a tumbling motion of the target. Note that environmental torques such as gravity gradient, or internal energy dissipation processes (e.g. fuel sloshing), can bring the target to a flat spin state [45]. However, there are effects difficult to model, such as collisions with small debris (man-made or natural), outgassing, etc., which can cause a tumbling rotation in the target. Tumbling is understood as the situation where the direction of the angular velocity vector is not constant in an inertial reference frame, due to the torque-free dynamics of an asymmetric body. This causes a seemingly chaotic motion of

the body axes, consequently matching the rotation along an axis or grappling a hard-point are difficult and risky operations [46].

1.4.1 Docking

In a traditional docking operation between two active spacecraft [47], when they are in close proximity (having nearly the same orbital position and velocity vectors), they must have a particular attitude relative to each other.

During the rendezvous and docking process, there are space/space communications between vehicles, docking mechanism interfaces, and rendezvous sensor interfaces. The on-board control system of the chaser (GNC) uses data from a variety of sensors (GPS, radar, optical sensors) and actuates the reaction control system, while the target provides data about its state and performs attitude actuations. Simultaneously, both the chaser and the target communicate with ground stations.

In the case where the chaser spacecraft services an active satellite (e.g. to provide station-keeping, refuelling, orbital transfers, etc.) usually there are no dedicated docking sensors or interfaces. However, the target can still provide the required attitude for docking or capture, and can communicate with the ground.

A target being uncooperative means that, on top of the lack of docking interfaces, it cannot control its attitude (it is potentially tumbling) and there is no data coming from it. Thus, docking to an uncooperative and tumbling target presents significant challenges:

- collision risk with the satellite body or appendages;
- fuel-consuming manoeuvres;
- no proper docking port, requiring unconventional capture and structural connection techniques;
- no communication with the target.

The lack of communication between vehicles implies that the chaser must acquire information about the target's state on its own (also known as pose estimation). This can be achieved with LIDARs (Light Detection And Ranging) and cameras. A LIDAR is generally used for long-range measurements, but recent advances make use of them for pose estimation of the target as well [48]. Cameras operate in

the visible and infrared spectrum, and are paired with computer vision algorithms in order to estimate the attitude of the target in real time [49, 50, 51, 52].

The first case of uncooperative docking was the Soyuz T-13 mission in 1985 [53], where docking had to be performed with an unmanned and out-of-service Salyut 7 space station. The Salyut 7 was not tumbling, but spinning about its roll axis. The angular rate was 0.3 deg/s, which was easily matched by the 2-man crew of the Soyuz T-13. They managed to conduct a manual docking while maintaining visual contact with the target, and the only help of a hand-held laser range-finder.

Since autonomous rendezvous and docking is identified by space agencies as a key technology (for satellite servicing and debris removal), there have been a number of technology demonstration missions, such as the Japanese ETS-VII [54], and NASA's Experimental Satellite System (XSS) and Orbital Express missions.

The Orbital Express was the latest mission, launched in 2007 [55, 56], aiming to demonstrate technologies related to automated rendezvous, proximity operations (including guidance based on video data [57]), docking, capture, and refuelling. The ASTRO servicing spacecraft of the Orbital Express mission features a robotic arm, three visible-spectrum cameras, one infrared camera, and a long-range LIDAR. The processing is powered by a 110-200 MHz radiation-hardened processor (giving a 2 Hz update rate during capture).

Also, the German DLR proposed its own technology demonstrator (DEOS [58]). These missions contributed to the development and fly-testing of automated rendezvous and docking technologies, which were used in the cargo spacecrafts HTV (JAXA) and ATV (ESA), but also assessed the feasibility of more advanced robotic aspects that could be used in uncooperative missions. Therefore, in this thesis, it is assumed that most of the GNC technologies involved (specially pose estimation) are available or have a high TRL. In this work, the scenario involves a large body and relatively high tumbling rates, a challenge that could be faced in future missions such as deorbiting Envisat.

A wide variety of techniques have been proposed and applied to simulated docking scenarios, both in the trajectory planning area and in the—mostly nonlinear—control area. For instance, McInnes [59] used an artificial potential field (APF) as a control method for docking and close proximity at the ISS, taking into account thrust and obstacle constraints. Model predictive control (MPC) was applied by Park [60], where a spacecraft approaches a target rotating in flat spin, with emphasis on obstacle avoidance. Lu [61] uses a robust sliding mode

control in a tumbling scenario, and also considers the problem of the spacecraft always pointing to the docking port of the target, integrating the translation and attitude controllers. Also in the field of nonlinear control, Di Mauro [62] argues that solving the SDRE is computationally expensive and proposes an efficient approach to solving it using differential algebra. In an interesting study, [63] an LQR controller and the APF method were combined into an algorithm that was tested on the SPHERES docking testbed inside the ISS.

In [64] the trajectory planning problem for docking has been studied, considering stable and rotating targets, and using optimal control (based on calculus of variations, not direct transcription methods) and splines for trajectory planning. It was found that the spline-based algorithm was much more computationally efficient than the optimal control method, with only a limited loss in optimality. The trajectory generated is then tracked with a linear controller. Michael [65] applies a direct transcription optimal control method (computationally intensive), considering an inertially symmetric rotating target. Ciarcia [66], uses polynomials to shape trajectories in an obstacle avoidance scenario of close proximity flight, and also shows the potential of this type of approach to obtain close-to-optimal trajectories with minimum computational expense (comparing results with an optimal control solver).

1.4.2 Detumbling

An excessive tumbling motion of the target introduces risk of collision, drives strong GNC requirements and produces large loads in mechanical chaser-target interfaces. An advantage of contactless solutions for deorbiting is that they tolerate a certain amount of tumbling rate. However, the delta-v is applied over a long time, thus re-entry is not controlled. Nonetheless, usually the same contactless techniques originally conceived for deorbiting can be used also for detumbling. The operation denoted as detumbling is therefore a strong requirement for many ADR strategies, and may have huge impact on the design of the ADR system itself. Over the years, the academic and industrial community have proposed a variety of strategies and techniques to detumble an uncooperative target. Some of them are mere concepts, while others have a relatively high TRL and have been lab-tested.

Detumbling by contact requires a performing GNC system as the chaser needs to phase its 6-DOF motion with the target and capture it. Once the physical capture has occurred, the chaser, mechanically linked to the target, can reduce the tumbling rate of the composite system, through proper actuation and control.

Robotic arms technology ([67, 68]) is very mature and much research has been done. For ADR missions, the end-effector of the arm must grab firmly to some hard-point on the target, for instance the launch vehicle interfaces that most satellites have. After capture, the robot arm is progressively stiffened using joint force/torque control, transferring momentum from the target to the chaser. Apart from collision risk, a high angular momentum can cause the torques to go beyond the structural resistance of the arm or the hard-point. Robotic arms equipped with a brush at their end-effector could reduce the targets angular momentum through friction, prior to grab the target [69]. The grasping operation can be autonomous or remotely operated.

Other contact systems proposed grapple the target using mechanical tentacles or clamps. Examples are the Gripper-DEMES [70] (dielectrically-actuated tentacles, applicable to microsatellites), the GRASP (by Tethers Unlimited, a technology based on inflatable booms), and the TAKO-Gripper [71] (articulated arms). The latter is part of the TAKO-Flyer system, an external module separated from the chaser that detumbles the target, a concept sharing numerous requirements with the one developed in this thesis.

Nets or harpoons could be used for detumbling by pulling from the tether, provided that the net or harpoon is firmly attached to the target. The challenges involved are the presence of complex elastic modes, difficulty in stabilising a fast tumbling motion, and risk of creating more debris by breaking appendages or parts of the structure when tension is applied. Nets appear to be a more robust solution than harpoons, provided that the net successfully wraps the target satellite. Unlike a net, a harpoon is attached to a single point, offering reduced authority to dampen the rotation, and the forces involved could cause the detachment of the honeycomb structure it is anchored to. Moreover, if the harpoon is used to de-orbit the target by pulling from it, ideally it should be placed in the centre of mass, but for detumbling it should be attached off-centre. There are many uncertainties with these methods, but there is research being conducted on the subject [72].

There is a range of contactless solutions to detumbling. Based on the thruster plume impingement idea used in deorbiting, a similar contactless method can be employed to detumble a satellite using conventional thrusters [73]. ESA has shown interest in this idea regarding the Envisat case, however, difficulties are encountered when the target is tumbling, i.e. their angular rates are not constant along their principal axis of inertia. Thus, the chaser could be required to manoeuvre constantly to direct the plume on the appropriate surface in the appropriate direction. detumbling cylindrical targets with plume impingement can be difficult, if they rotate about their axis of symmetry. Alternatively, there are methods based on induced electrostatic forces [74] or Eddy currents [75].

1.5 Contribution of the thesis

1.5.1 In attitude slew manoeuvring

In motion planning, there is a trade-off between the pursuit of optimality and computational efficiency. The focus of this work is on the development and applications of a motion planning method to optimise attitude trajectories, while satisfying a number of constraints, in a computationally efficient and robust way.

The motion planning method proposed shapes quaternions using polynomials. In this work, quaternions are used as the baseline attitude representation since it is widely used in spacecraft applications, thanks to its computational efficiency (no trigonometric functions are involved) and lack of singularities, despite the fact that they need to be normalised. Additionally, an axis-azimuth representation is applied to the case of spin-to-spin manoeuvres for its suitability to this specific problem, in which the spinning axis is re-pointed without having to de-spin. The polynomial family of functions is convenient due to its efficiency and versatility, and can easily shape trajectories resembling those obtained by an optimal control solver.

In the motion planning method presented, optimisation occurs amongst the set of polynomial trajectories of a certain degree. Hence, the solutions are in fact suboptimal, unlike solutions obtained with optimal control theory, where global optimality can theoretically be achieved. In particular, time minimization is discussed. Other performance metrics are possible, such as energy (based on the accumulated square root of torque) or fuel consumption. However, the resulting

torque profiles given by polynomials are smooth and continuous, being more suited to reaction wheels or control moment gyros (CMG) than to a reaction control system (RCS). With reaction wheels fuel optimisation is not relevant, and the figure of merit is the manoeuvre time. Regarding reaction wheels, an interesting parameter to minimise is the remaining wheel speed at the end of the manoeuvre, since it drives the need for unloading these actuators. Using inverse dynamics, this issue is also addressed with polynomial motion planning.

A time optimisation strategy is proposed, which employs a combination of root-finding and unconstrained optimisation (although constraints are taking into account with penalty functions), aiming to minimize computational cost and ensure convergence, as opposed to using nonlinear programming (NLP) solvers [23, 24]. The problem of optimising a trajectory in the presence of path or pointing constraints is also addressed, using both a deterministic and a heuristic approach.

The smoothness of the resulting trajectories, along with the ability to monitor acceleration and jerk, make this method particularly suited to spacecraft with flexible appendages. The method presented aims to reduce vibrations using a guidance approach rather than a feedback control method, by providing continuously smooth torque along the trajectory—specially at the endpoints. The combination of fast manoeuvres and smooth control can be particularly suited to agile Earth observation satellites, where traditionally a certain cool-down time must be allocated between pictures to settle spillover vibrations.

Applications of the method proposed include:

- micro- and nano-satellites with limited attitude control resources, where relatively fast yet feasible manoeuvres can be performed;
- agile satellites needing to re-point quickly, and where the feasibility of a series of patch scans must be verified in the scheduling algorithm;
- spacecraft with pointing constraints;
- spacecraft with flexible structures;
- spin-stabilised spacecraft needing to re-orient its spin axis;
- a combination the above.

1.5.2 In uncooperative docking

As outlined before, uncooperative docking to a tumbling target presents one of the most challenging scenarios in the current state of spaceflight technology. The

technology roadmap covers many areas, from GNC to capture mechanisms. A chapter of this thesis contributes to the guidance and control area.

A guidance method is proposed for the "final approach to contact" phase [47], which occurs within tenths of meters of the uncooperative target, and implies the approach of the chaser to the capture point or the achievement of capture conditions. The scenario involves a tumbling Envisat. A docking strategy is proposed, in which the approach trajectory is divided in segments. A keep-out closed surface is defined which fits the body and its appendages, where the chaser shall not enter unless it is in the final docking approach.

The focus of this work is on efficient trajectory planning in the Euclidean three-dimensional space, which generates reference time-varying position, velocity, and acceleration vectors. The spacecraft coordinates are shaped with polynomials of a certain degree considering certain boundary conditions, efficiently defining a reference trajectory. Thrust, fuel consumption, and other parameters are evaluated via inverse dynamics. Path constraints are also enforced, preventing collisions with the tumbling target and its appendages. Closed-form solutions of the target attitude motion are obtained to avoid on-board integration. This allows to rapidly obtain an approximation of the final desired state. Also, the closed-loop control is performed by periodically re-computing the trajectory.

In the docking scenario, a chaser with 6-DOF motion provided by a reaction control system (RCS) is considered. The 6-DOF requirement stems from the camera and LIDAR of the chaser, which need to continuously point towards the target in order to estimate its attitude state (pose estimation) and distance. Nevertheless, the case of a chaser equipped with a single thruster is also addressed. The chaser can follow the reference trajectory by steering the thruster direction with the attitude control system (ACS). Hence, the trajectory planning algorithm must evaluate the rate of change of the reference acceleration direction so that it can be performed within the ACS torque limits.

While polynomial motion planning methods (splines) have been used before in docking and close proximity flight (showing its potential in terms of efficiency and optimality), this work studies a realistic scenario of a tumbling target with appendages, and proposes innovative strategies tailored to this problem. This results in a unique approach to the trajectory optimisation and target state prediction (achieving fast computation speeds). Also, fuel consumption, instead of energy, is directly evaluated and minimised.

Ultimately, in this thesis an effort has been made to provide insight on the challenges presented by the uncooperative docking problem, and how to address part of them with polynomial motion planning and particular docking strategies.

1.5.3 In debris detumbling

In this thesis, a novel system for detumbling passive targets in the context of ADR is proposed, the Attitude Stabilization Electromagnetic Module (ASEM). As previously discussed, a spacecraft approaching a tumbling satellite has a higher collision risk and the capture operation is more complex. Moreover, if the angular momentum involved is large, the peak loads on a robotic arm capturing it can be significant.

The purpose of this work is to outline the design of a system that stabilises the attitude motion of a debris body prior to capture by the spacecraft, reducing the risk of the operation. A small module with magnetorquers and a power source, piggyback carried by the chaser spacecraft, uses its own RCS to perform an autonomous docking to the tumbling target, attaching itself to the structure. The module then acts as an external magnetic actuator that damps the targets angular momentum by interacting with the Earths magnetic field. A special control law is implemented for magnetic stabilisation, which minimises both the energy spent and the detumbling time. Once the target is stabilised, the chaser spacecraft can approach it slowly to perform a safe capture or docking.

Note that this ADR concept does not eliminate the need to perform an uncooperative docking, hence it is not purely contactless, but it delegates the task to a smaller, more rugged, and more agile vehicle than the chaser spacecraft. Once the target is stabilised, the chaser can approach it slowly, with no risk of a moving appendage colliding with it. This work focuses on the detumbling problem of the mission. The deorbit strategy itself is beyond the scope of this study, however, other authors have addressed the problem [41, 42].

The most similar concept that was found in the literature is the TAKO-Flyer, proposed by Yoshida and Nakanishi [71]. In this thesis, however, the design is much more detailed. Although developed independently, the ASEM concept also uses magnetorquers, but they are powered by a compact battery instead of solar panels. Also, the proposed attachment system is based on drills and the newly-developed space adhesive, instead of the Gripper system, which might not scale

well with large targets such as Envisat. Nevertheless, the existence of a similar concept demonstrates the interest in the idea of an external module—TAKO stands for "Target Collaborativize".

1.6 Thesis structure

The problem of motion planning in attitude slew manoeuvres is covered in Chapters 2 and 3. In Chapter 2 the baseline method is presented, where quaternions are shaped with polynomials to define attitude manoeuvres. Some issues are discussed and addressed, such as normalisation, winding, and numerical stability regarding high-order polynomials. In the same chapter, the benefits of a smooth trajectory regarding spacecraft with flexible structures is analysed. Simulations of a flexible spacecraft model are realised and the performance of the method regarding vibrations reduction is evaluated.

In Chapter 3, optimisation of the polynomial trajectories is addressed. The issues of time optimisation, obstacle avoidance, and minimisation of post-manoeuvre reaction wheel speed are discussed. Then, the performance of the polynomial planning method is compared with an optimal control solver, to assess how far away low-degree polynomial trajectories are from optimal solutions. Similarly, different attitude representations other than quaternions are tested, in order to study whether a certain type of attitude coordinates provides better results (as is the case of spin-to-spin manoeuvres, discussed in Chapter 2).

In Chapter 4, the problem of docking to a tumbling target (based on Envisat) is addressed, with polynomial motion planning being proposed as a guidance and control method. While the baseline trajectory-generating method is the same as in the previous chapters on attitude manoeuvres, in this case three Cartesian independent coordinates are shaped for translational motions, and the issues addressed in terms of optimisation and performance are different. First, the torque-free attitude dynamics of the target is addressed, followed by the description of the method. The docking strategy that will be used in the study is presented. Different aspects of trajectory optimisation, based on the internal model, are developed, including the case of a single-thruster spacecraft. Finally, the guidance and control approach is presented and tested in simulations.

Finally, in Chapter 5, the same Envisat scenario is used as the case study of the ASEM system (for Attitude Stabilisation Electromagnetic Module), an external

module for detumbling of debris. Initially, a trade-off discussion of different architectures of the system is discussed, and a decision is made. Before the design of the selected architecture, the control problem of magnetic detumbling is discussed, since it drives some elements of the system. Then a preliminary design is conducted, with a description and initial sizing of its elements (including the uncooperative docking manoeuvre), and a parametric optimisation of the system as a whole where mass is minimised. The selected system is tested in several detumbling simulations.

1.7 Published work

- *An inverse dynamics approach to the guidance of spacecraft in close proximity of tumbling debris*, Caubet, A., Biggs, J., 66th International Astronautical Congress, Jerusalem 2015
- *A Motion Planning Method for Spacecraft Attitude Maneuvers Using Single Polynomials*, Caubet, A., Biggs, J., AAS/AIAA Astrodynamics Specialist Conference, Vail 2015
- *Design of an Attitude Stabilization Electromagnetic Module for Detumbling Uncooperative Targets*, Caubet, A., Biggs, J., IEEE Aerospace Conference, Big Sky 2014
- *Optimal Attitude Motion Planner for Large Slew Maneuvers Using a Shape-Based Method*, Caubet, A., Biggs, J., AIAA Guidance Navigation and Control Conference, Boston 2013

Chapter 2

Shaping attitude trajectories with single polynomials

In this chapter, the polynomial motion planning method applied to attitude control is presented, but the specifics of trajectory optimisation are discussed in a different chapter. Issues such as winding and numerical stability are addressed. The spin-to-spin special case is studies, where a different attitude parameterisation is used. The evaluation of torque and other parameters via inverse dynamics is presented, and the open-loop torque profile of the trajectory is obtained. This polynomial planning method can be applied to the problem of attitude manoeuvres with flexible appendages, due to the smoothness of the generated trajectories. The method is applied to a multi-body model of a flexible spacecraft, where its capacity of avoiding vibrations is assessed. The effects of varying the polynomial order and using feedback control for tracking are compared.

2.1 Polynomial motion planning using quaternions

The proposed method represents the attitude of a rigid body with a prescribed analytically defined function of time. Polynomial functions are chosen since they are smooth, and easy to manipulate. Polynomials are parameterised to match prescribed boundary conditions on attitude, velocity, and higher order derivatives. Once the desired attitude trajectory has been shaped, the torque profile can be obtained with inverse dynamics. Quaternions are used as the baseline attitude

representation since they are non-singular, computationally efficient, and widely used in the ADCS of spacecraft.

2.1.1 Method description

The trajectory of each quaternion in the S^3 unit sphere is shaped by the rational polynomial function

$$q_i(t) = \frac{q_i^*(t)}{\|\mathbf{q}^*(t)\|} \tag{2.1}$$

for $i = 1, ..., 4$, where $q_i^*(t)$ is a polynomial:

$$q_i^*(t) = a_{i0} + a_{i1}t + a_{i2}t^2 + ... + a_{in}t^n = \sum_{j=0}^{n} a_{ij}t^j \tag{2.2}$$

Since the quaternions depicted by the * supercript are individually shaped, they form a vector in $\mathbb{R}^4$ whose norm is not constant, thus each component i is normalized in Eq. (2.1) using the quaternion unit norm

$$\|\mathbf{q}^*(t)\| = \sqrt{q_1^*(t)^2 + q_2^*(t)^2 + q_3^*(t)^2 + q_4^*(t)^2} \tag{2.3}$$

In order to shape a trajectory with these polynomials, certain boundary conditions must be considered for any manoeuvre time t_f. By selecting the prescribed boundary values $q_i(0)$ and $q_i(f)$ and their derivatives, it results in a system of linear equations that can be solved to find the value of the polynomials' coefficients. The m boundary conditions of the manoeuvre determine the minimum required degree $n = m - 1$ of the polynomial, resulting in a system of m linear equations from which the coefficients a_{ij} can be obtained, given a final manoeuvre time. The minimum number of boundary conditions that define a slew manoeuvre are the initial and final attitude and velocity (requiring at least a 3^{rd} degree polynomial to define the quaternions' trajectories):

$$\begin{bmatrix} 1 & 0 & 0 & 0 & 0 \\ 0 & 1 & 0 & 0 & 0 \\ 1 & t_f & t_f^2 & t_f^3 & t_f^4 \\ 0 & 1 & 2t_f & 3t_f^2 & 4t_f^3 \end{bmatrix} \begin{bmatrix} a_{i0} \\ a_{i1} \\ a_{i2} \\ a_{i3} \end{bmatrix} = \begin{bmatrix} q_i(0) \\ \dot{q}_i(0) \\ q_i(t_f) \\ \dot{q}_i(t_f) \end{bmatrix} \tag{2.4}$$

Note that Eq. 2.4 is a linear system formed by the polynomial of Eq. 2.2 and its derivatives, not by the rational function representing the normalised quaternions

(Eq. 2.1), since the boundary conditions are normalized (i.e. $q_i(0) = q_i^*(0)$ and $q_i(t_f) = q_i^*(t_f)$).

Boundary conditions on acceleration can be introduced, either for arbitrary manoeuvres (not necessarily rest-to-rest) or for enforcing zero torque at the trajectory endpoints. Enforcing zero torque may be required for flexible spacecraft, to avoid vibration-inducing discontinuities in angular acceleration. For the same reason, the instantaneous jerk (time derivative of acceleration) at the boundaries can be forced to zero so that torque is smooth at the endpoints.

The degree of the polynomial can be increased beyond $n = m - 1$ (i.e. the minimum polynomial degree needed for matching boundary conditions), which introduces degrees of freedom to the system in the form of the additional coefficients. The extended polynomial of degree $n = m - 1 + k$, for m boundary conditions and k additional terms, becomes

$$q_i^*(t) = a_{i0} + a_{i1}t + a_{i2}t^2 + ... + a_{i,m-1}t^{m-1} + ... + a_{i,m-1+k}t^{m-1+k} \tag{2.5}$$

If a scenario with $m = 8$ boundary conditions is considered (for certain values of attitude, velocity, acceleration, and jerk at the trajectory endpoints), the 8 coefficients can be solved by a polynomial of degree 7. However, the degree of the polynomial can be increased to 8 by including an additional term ($k = 1$ in Eq. (2.5)). Assuming that the additional free coefficient a_{i8} is guessed or known, the rest of the coefficients that make the trajectory match the boundary conditions are determined by the following linear system of equations:

$$\begin{bmatrix} 1 & 0 & 0 & 0 & 0 & 0 & 0 & 0 \\ 0 & 1 & 0 & 0 & 0 & 0 & 0 & 0 \\ 0 & 0 & 2 & 0 & 0 & 0 & 0 & 0 \\ 0 & 0 & 0 & 6 & 0 & 0 & 0 & 0 \\ 1 & t_f & t_f^2 & t_f^3 & t_f^4 & t_f^5 & t_f^6 & t_f^7 \\ 0 & 1 & 2t_f & 3t_f^2 & 4t_f^3 & 5t_f^4 & 6t_f^5 & 7t_f^6 \\ 0 & 0 & 2 & 6t_f & 12t_f^2 & 20t_f^3 & 30t_f^4 & 42t_f^5 \\ 0 & 0 & 0 & 6 & 24t_f & 60t_f^2 & 120t_f^3 & 210t_f^4 \end{bmatrix} \begin{bmatrix} a_{i0} \\ a_{i1} \\ a_{i2} \\ a_{i3} \\ a_{i4} \\ a_{i5} \\ a_{i6} \\ a_{i7} \end{bmatrix} = \begin{bmatrix} q_i(0) \\ \dot{q}_i(0) \\ \ddot{q}_i(0) \\ \dddot{q}_i(0) \\ q_i(t_f) - a_{i8}t_f^8 \\ \dot{q}_i(t_f) - 8a_{i8}t_f^7 \\ \ddot{q}_i(t_f) - 56a_{i8}t_f^6 \\ \dddot{q}_i(t_f) - 336a_{i8}t_f^5 \end{bmatrix} \tag{2.6}$$

where the vector on the right-hand side contains the selected boundary conditions and the a_{i8} coefficient. The coefficients a_{ij} of the i-th quaternion are then a function of the manoeuvre final time t_f and the corresponding boundary conditions. Therefore, for given boundary conditions, in Eq. (2.6) the variables of the trajectory are t_f and a_{i8}. If no extra degrees of freedom are needed, $a_{i8} = 0$ and the polynomial becomes of degree 7—the minimum required.

The values of the additional coefficients can be iterated in an optimization process while solving Eq. (2.6). In other words, the optimizer re-shapes the trajectory by adjusting the additional coefficients, while maintaining the trajectory endpoints at the specified boundary conditions. Alternatively, a more deterministic approach—no optimisation required—can be considered, where k trajectory waypoints (represented by quaternions) are selected, thus k equations are included in the system, which as a unique solution. In this case, besides matching the boundary conditions, the trajectory will pass through the specified attitudes *at the specified times*. At the waypoints, given the use of a single polynomial between endpoints, the curve is smooth (i.e. of differentiability class C^∞).

While Eq. (2.6) can be solved with linear algebra methods, it is more efficient to calculate the coefficients using closed-form expressions (which can be rapidly obtained with a symbolic mathematics software). Note that each polynomial degree has a different set of expressions.

The initial and final values of the quaternions' time derivatives in Eq. (2.6) can be obtained, given the boundary angular velocities, via the kinematics equation:

$$\begin{bmatrix} \dot{q}_1 \\ \dot{q}_2 \\ \dot{q}_3 \\ \dot{q}_4 \end{bmatrix} = \frac{1}{2} \begin{bmatrix} 0 & \omega_3 & -\omega_2 & \omega_1 \\ -\omega_3 & 0 & \omega_1 & \omega_2 \\ \omega_2 & -\omega_1 & 0 & \omega_3 \\ -\omega_1 & -\omega_2 & -\omega_3 & 0 \end{bmatrix} \begin{bmatrix} q_1 \\ q_2 \\ q_3 \\ q_4 \end{bmatrix} \tag{2.7}$$

The boundary values of $\ddot{q}_i$ and $\dddot{q}_i$ are obtained by differentiating Eq. (2.7) with respect to time:

In an analogous way, this polynomial motion planning method can be used with other attitude representations, simply by replacing the quaternions by the corresponding coordinates in Eqs. (2.5) and (2.6) if normalisation is required. The kinematics equation of every particular attitude representation applies instead of (2.7). Euler angles or MRP are potential alternatives to quaternions which do not require normalisation, although they have singularities (MRP are "safer" to use than Euler angles since they are singular at 2π instead of $\pi/2$). Rotation matrices could be used by planning the trajectory of five of their nine elements with polynomials and finding the rest using orthogonal relations, but normalisation is needed and there may be singularities when solving the rest of the elements.

2.1.2 Quaternion unwinding

When selecting the endpoint attitudes, note that quaternions are not unique in the sense that the same attitude in the $SO(3)$ space can be represented both by $\mathbf{q}$ and $-\mathbf{q}$. However, a trajectory shaped between $q_i(0)$ and $q_i(t_f)$ is different than one connecting $q_i(0)$ with $-q_i(t_f)$. This may result in a winding trajectory, where the desired attitude is reached through a long path. Figure 2.1 illustrates an example of winding using the motion planning method. Subfigures 2.1a and 2.1b show the evolution of the quaternion components, while subfigures 2.1c and 2.1d depict the path of the body axes on the unit sphere. Manoeuvres A and B, generated by shaping quaternions with minimum-order polynomials, have the same duration and initial quaternion $\mathbf{q}_0$. The final attitude is the same, but manoeuvre A was shaped using the positive quaternion $\mathbf{q}_f$ whereas in B the manoeuvre was generated with its negative counterpart $-\mathbf{q}_f$. The specific pair of initial and final attitudes was chosen since the length difference between the paths to reach the same point is very obvious. Results show a larger displacement in manoeuvre A, implying higher torques for the same duration (or more time required to perform the manoeuvre).

To avoid this issue, the sign of the quaternions should be selected according to a metric based on the difference between $\mathbf{q}(0)$ and $\pm\mathbf{q}(t_f)$. Specifically, if $\mathbf{q}_d$ is the difference between the endpoint attitudes, expressed in quaternion algebra as

$$\mathbf{q}_d = \mathbf{q}_f \cdot \mathbf{q}_0^{-1} \tag{2.8}$$

the corresponding rotation angle $\theta_d = 2\cos^{-1}(q_{d4})$ should be less than π in order to avoid a winding trajectory.

2.2 Numerical stability of high degree polynomials

High degree polynomials may have sensitivity issues, where small errors in the inputs cause relatively large errors in the outputs. In the attitude control scenario, the main source of error comes from sensor inaccuracies, namely the current attitude and velocity values that are inputs to the linear system. Mathematically speaking, the matrix of the linear system in Eq. (2.6), expressed in the form $Ax = b$, can be ill-conditioned for too high polynomial orders and t_f values. A

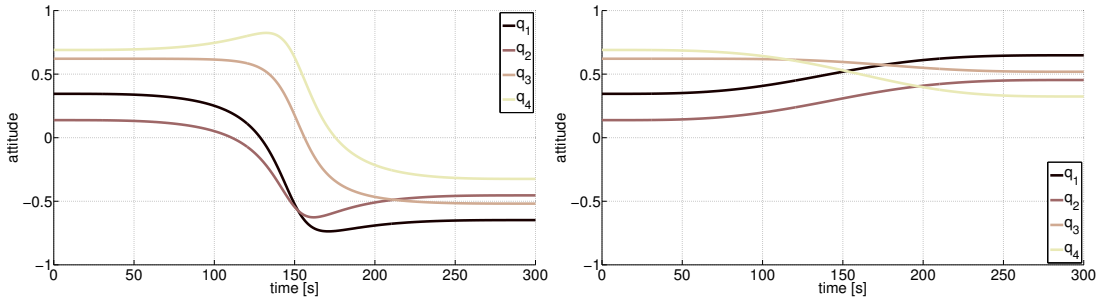

(a) Quaternions (manoeuvre A)

(b) Quaternions (manoeuvre B)

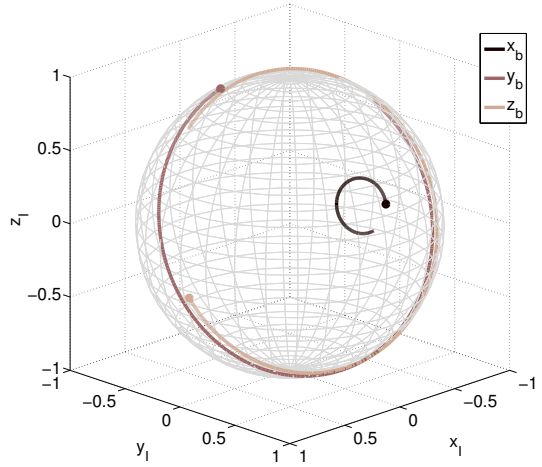

(c) Body axes motions (manoeuvre A)

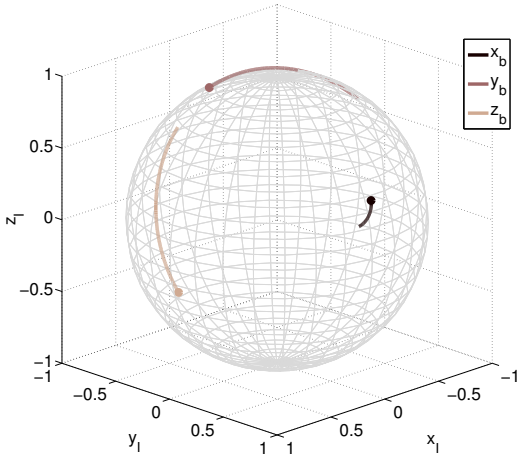

(d) Body axes motions (manoeuvre B)

Figure 2.1: Comparison of two manoeuvres with equal boundary attitudes. Manoeuvre A experiences unwinding.

matrix is ill-conditioned if it is close to being singular, therefore non-invertible. A metric of the conditioning of a matrix is its condition number C, or the ratio of the largest to smallest singular value in the singular value decomposition. The order of magnitude of C gives an estimate of the digits of accuracy lost in solving a linear system with that matrix.

In order to reduce the condition number of the matrix, the time domain can be scaled so that the final time is 1, to prevent some elements in A from being too large. For instance, with the new variable $\tau \in [0, 1]$, where $\tau = t/t_f$, the condition number is reduced from 10^{18} (for $m = 8$ and $t_f = 300$ sec) to 10^4. The scaled coefficients can be calculated by solving the corresponding linear system. Note that the vector of boundary values changes due to the differentiation with respect to a scaled variable. The differential operator with respect to time can

be expressed as

$$\frac{d}{dt} = \frac{d}{dt}(\tau)\frac{d}{d\tau} \tag{2.9}$$

by replacing $\tau = t/t_f$, Eq. (2.9) becomes

$$\frac{d}{dt} = \frac{1}{t_f}\frac{d}{d\tau} \tag{2.10}$$

which can be raised to the k-th derivative. Thus, the corresponding k-th time derivatives of the scaled quaternions are calculated as

$$\frac{d^k q_i(\tau)}{d\tau^k} = t_f^k \cdot \frac{d^k q_i(t)}{dt^k} \tag{2.11}$$

and the boundary values in the right-hand side vector of Eq. (2.6) must be adjusted accordingly (while in the matrix, $t_f = 1$). The scaled coefficients $\overline{a}_{in}$ of the polynomial in τ are related to the original ones by

$$a_{in} = \frac{\overline{a}_{in}}{t_f^n} \tag{2.12}$$

A sensitivity analysis was performed to assess the effect of input errors to the system, considering a polynomial of degree 7. Monte Carlo simulations were run with arbitrary boundary attitudes and velocities (on the order of 10^4 cases). The endpoint velocities are bounded within 1 rpm, and the final time is fixed at 300 seconds. For each random manoeuvre, a uniformly distributed error on the initial attitude and velocity parameters was applied, of ± 0.001 on quaternions (about 1 degree of error) and ± 0.0001 rad/s on angular velocities.

The sensitivity effects can be assessed by the relative error of the polynomial's coefficients (the outputs of the system). In particular, the maximum relative error among a polynomial's coefficients is

$$\epsilon_{a,max} = \max_n \left(\frac{a_n - \hat{a}_n}{a_n} \right) \tag{2.13}$$

where $\hat{a}_{in}$ are the coefficients calculated with input errors.

Figure 2.2 is an histogram of the maximum relative error $\epsilon_{a,max}$ for all the trajectory runs. The great majority of cases have a $\epsilon_{a,max}$ lower than 0.05, and the probability of larger errors decreases exponentially. For visualization purposes, the cases with errors above 1 have been removed from this figure, which correspond to the 0.67% of the total and where the largest value is 8.

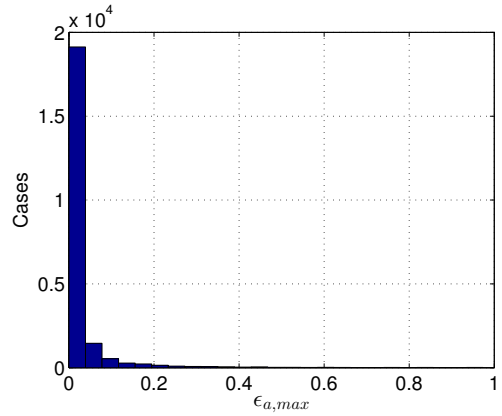

Figure 2.2: Histogram of coefficients' maximum relative error

For every random manoeuvre, the error eigenangle θ_e between the nominal trajectory and the one with input errors is calculated along the time domain. In Fig. 2.3 the maximum relative errors are plotted against the corresponding maximum value of θ_e along the trajectory or $\theta_{e,max}$, each point in the figure representing a single trajectory run. Interestingly, the results show that $\epsilon_{a,max}$ and the maximum trajectory divergence are uncorrelated.

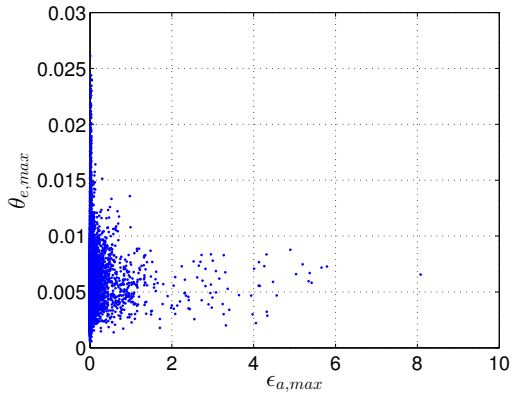

Figure 2.3: The trajectory divergence with respect to the coefficients' maximum relative error

This effect has two causes. First, the largest relative errors correspond to very small coefficient values, thus the polynomial term they are associated with does not contribute in a significant way to the trajectory shaping. This is shown in Fig. 2.4 where the coefficients, scaled with the final time as $a_n t_f$, are plotted against their corresponding maximum relative error $\epsilon_{a,max}$. In this figure, the largest errors correspond to the smallest scaled coefficients' values.

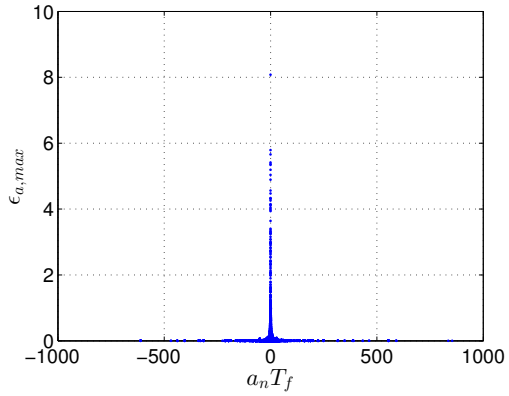

Figure 2.4: Relationship between the coefficients' scaled values and their corresponding maximum relative errors

Second, the occurrence of significantly large errors is rare, and two or more coefficients with a large error are unlikely to coexist in the same polynomial. To assess this effect, a special ratio between a polynomial's coefficients mean error and the maximum error is analyzed, as shown in Eq. (2.14).

$$\eta_a = \left(\frac{\epsilon_{a,0}}{\epsilon_{a,max}} + \frac{\epsilon_{a,1}}{\epsilon_{a,max}} + ... + \frac{\epsilon_{a,n}}{\epsilon_{a,max}} \right) \tag{2.14}$$

Where $\epsilon_{a,n}$ is the relative error of a_n. The ratio η_a is a measure of how large the maximum error of a coefficient is with respect to the rest of the coefficients' errors in the polynomial. Thus, the more similar the coefficients' errors are, the larger η_a will be. Similarly, if one coefficient's error is far larger than the rest, η_a will be close to one; if two errors are large, η_a will be two, and so on. Figure 2.5 shows η_a against $\epsilon_{a,max}$, where it can be seen that very large errors are single occurrences within a polynomial's set of coefficients.

Figure 2.6 shows an histogram of $\theta_{e,max}$ for every run. The distribution of maximum error is centered at 0.005 rad (about 0.3 deg), exponentially decreasing to a maximum value of 0.02 rad (1.43 deg). Figure 2.7 shows the distribution of the error at the final point of the trajectory ($\theta_{e,end}$), where all the cases are of the order $\mathcal{O}(10^-8)$ most of them fall below $0.5 \cdot 10^{-8}$. Thus, no major adjustment would be required to stabilize the spacecraft along the final attitude after the guided manoeuvre.

Results show that the maximum divergence occurs at mid-trajectory points. Note that every planned trajectory, independently of the divergence from the nominal manoeuvre (with no input errors), satisfies all the constraints and will be followed

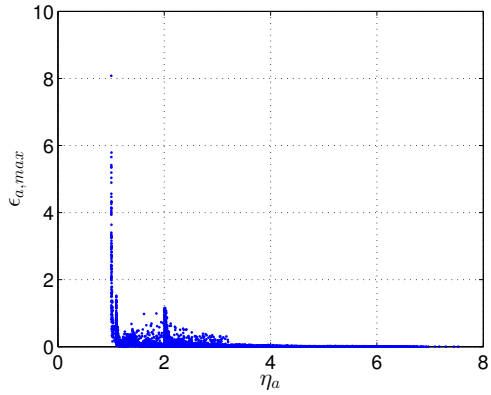

Figure 2.5: The error ratio with respect to the maximum error is an indicator of the frequency of large errors within the set of a polynomial's coefficients

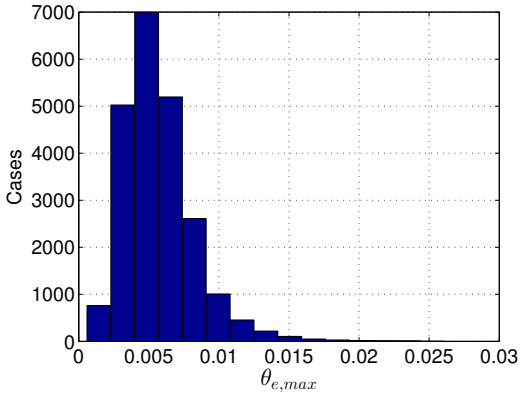

Figure 2.6: Histogram of the maximum values of θ_e per trajectory

by the spacecraft at the performance of the attitude tracking controller. In other words, even if input errors caused a large divergence of the trajectory, it would still be feasible.

The following results are an analysis of the precision loss introduced by the normalization of the quaternions and their derivatives (Eqs. (2.1-2.21b)). To assess its magnitude, the relative error of the normalized final quaternions with respect to the final q^* are calculated over thousands of random manoeuvres. The results are shown in form of histograms in Fig. 2.8. The precision loss remains very low at relative error values of order -12 and -13. Also, the probability of encountering relatively high errors decreases exponentially. As expected, the average error is larger in the normalization of higher quaternion derivatives, due to the larger number of required computations.

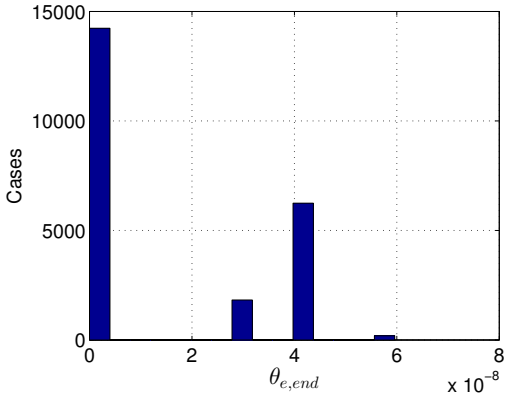

Figure 2.7: Histogram of the final endpoint values of θ_e per trajectory

2.3 Spin-to-spin manoeuvres using an axis-azimuth representation

Quaternions define the full attitude (i.e. the three body axes). However, in the special case of spin-to-spin manoeuvres, only the direction of the spinning body axis is relevant. In other words, the phase angle of the other two axes about the spinning axis at the end of the manoeuvre is not relevant. Therefore, if quaternions or another full attitude representation was used, this final phase angle must be chosen which adds a degree of freedom to the trajectory planning.

In order to avoid this, the direction of the pointing axis can be parameterised with two spherical coordinates such as azimuth and declination angles (s_1 and s_2), which can be expressed independently as time polynomials. These two coordinates form a reduced attitude representation [76]. A third parameter (s_3), describing the rotation angle about the pointing or spinning axis, completes the full attitude in what is known as axis-azimuth representation [17] (Fig. 2.9). The s_3 angle is also expressed as a polynomial, however, its final value s_{f3} is not included in the boundary conditions set. This approach is convenient for spin-to-spin manoeuvres, i.e. transferring the spacecraft from the current pointing direction and spinning state ($\mathbf{s}_0 = [s_{01}\, s_{02}\, s_{03}]^T$ and $\dot{\mathbf{s}}_0 = [0\, 0\, \dot{s}_{03}]^T$) to another one ($\mathbf{s}_f = [s_{f1}\, s_{f2}]^T$ and $\dot{\mathbf{s}}_f = [0\, 0\, \dot{s}_{f3}]^T$). Note that s_{f3} is not included in the set of boundary conditions.

In fact, the resulting attitude representation formed by the parameters s_1, s_2, and s_3 is a particular combination of intrinsic Euler angles. For instance, assume a spacecraft with an instrument aligned with the body axis y, which is

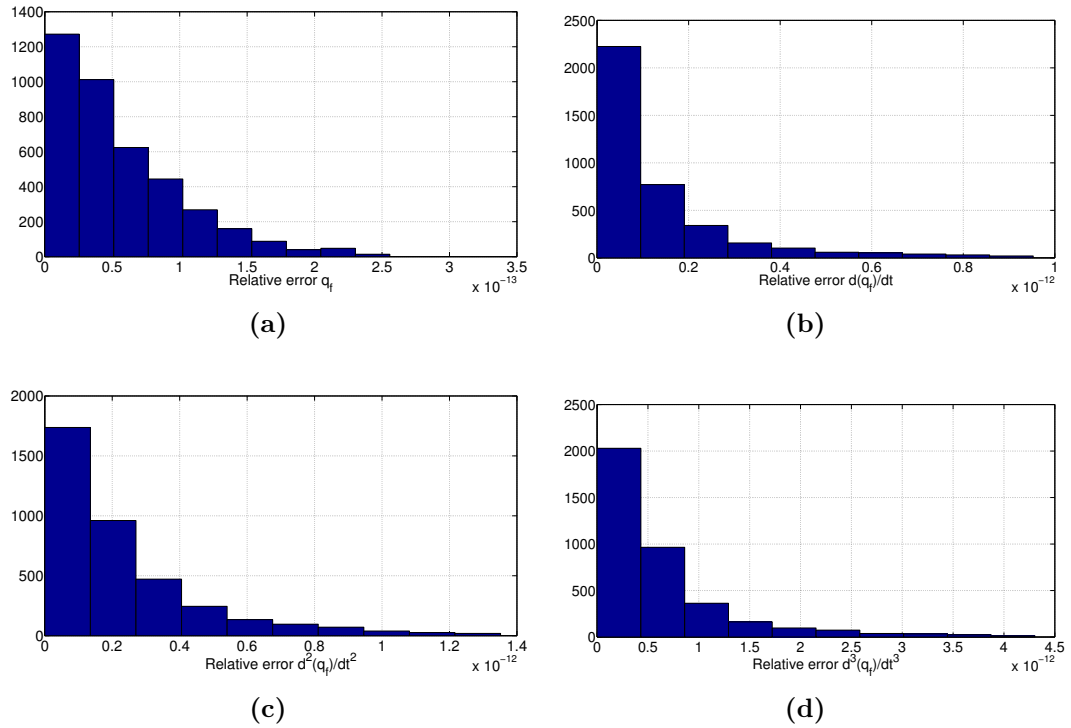

Figure 2.8: Histograms of the distribution of relative error of final quaternion values over random manoeuvres

required to point in different directions. In this case, the attitude can be described as a z-x'-y" Euler rotation, where the corresponding rotation matrix is $R = R_z(s_1)R_x(s_2)R_y(s_3)$. The order of the x and z rotations is not relevant, but the third rotation must be around the pointing axis (y in this case). With $m = 8$ boundary conditions for s_1 and s_2 their polynomials are at least of degree $n = 7$:

$$s_i(t) = a_{i0} + a_{i1}t + a_{i2}t^2 + ... + a_{i7}t^7 \tag{2.15}$$

For $i = 1,\ 2$. Their coefficients are:

$$\begin{aligned}
a_{i0} &= s_{i0} \\
a_{i1} &= \dot{s}_{i0} \\
a_{i2} &= a_{i3} = 0 \\
a_{i4} &= -\tfrac{5}{t_f^4}(7s_{i0} - 7s_{if} + 4\dot{s}_{i0}t_f + 3\dot{s}_{if}t_f) \\
a_{i5} &= \tfrac{3}{t_f^5}(28s_{i0} - 28s_{if} + 15\dot{s}_{i0}t_f + 13\dot{s}_{if}t_f) \\
a_{i6} &= -\tfrac{2}{t_f^6}(35s_{i0} - 35s_{if} + 18\dot{s}_{i0}t_f + 17\dot{s}_{if}t_f) \\
a_{i7} &= \tfrac{10}{t_f^7}(2s_{i0} - 2s_{if} + \dot{s}_{i0}t_f + \dot{s}_{if}t_f)
\end{aligned} \tag{2.16}$$

However, for $i = 3$, there are only 7 boundary conditions, thus $a_{37} = 0$. The

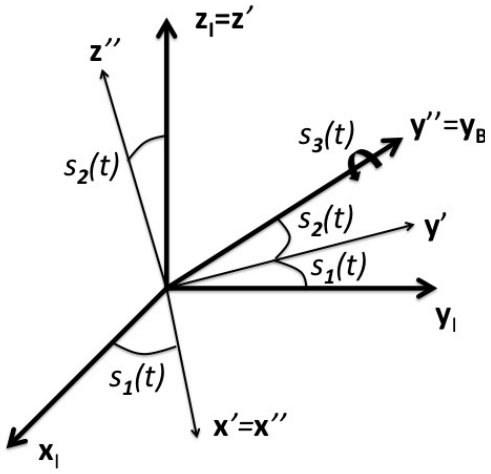

Figure 2.9: Axis-azimuth attitude representation ($\mathbf{y}_B$ being the pointing/spinning body axis)

coefficients of the 6^{th} degree polynomial of s_3 are:

$$\begin{aligned} a_{30} &= s_{30} \\ a_{31} &= \dot{s}_{30} \\ a_{32} &= a_{33} = 0 \\ a_{34} &= -\tfrac{5}{2t_f^3}(\dot{s}_{30}t_f - \dot{s}_{3f}t_f) \\ a_{35} &= \tfrac{3}{t_f^4}(\dot{s}_{30}t_f - \dot{s}_{3f}t_f) \\ a_{36} &= -\tfrac{1}{t_f^5}(\dot{s}_{30}t_f - \dot{s}_{3f}t_f) \end{aligned} \tag{2.17}$$

Figure 2.10 shows the body axes paths of a spin-to-spin manoeuvre in an inertial frame, where the pointing axis y_b precesses towards the target direction (depicted by a point at the end of the path line) while the other two orthogonal axes keep rotating about it. In Figure 2.11, the two coordinates defining the direction of the pointing axis (s_1 and s_2) are driven to their final desired values, while s_3 follows a constant rate trajectory (since the prescribed initial and final spin rates are the same) where the final value of the angle was not specified.

The singularity associated with Euler angles occurs when calculating their time derivatives with the kinematics equation from angular velocity data with an angle. However, in this case the kinematic equation is not needed to calculate the time derivative of the angles: firstly, at the endpoints, the angles' derivatives are simply the prescribed spinning rates ($\dot{s}_{03} = \dot{\omega}_0$ and $\dot{s}_{f3} = \dot{\omega}_f$); secondly, the angles' derivatives of the trajectory are obtained by differentiating the polynomial.

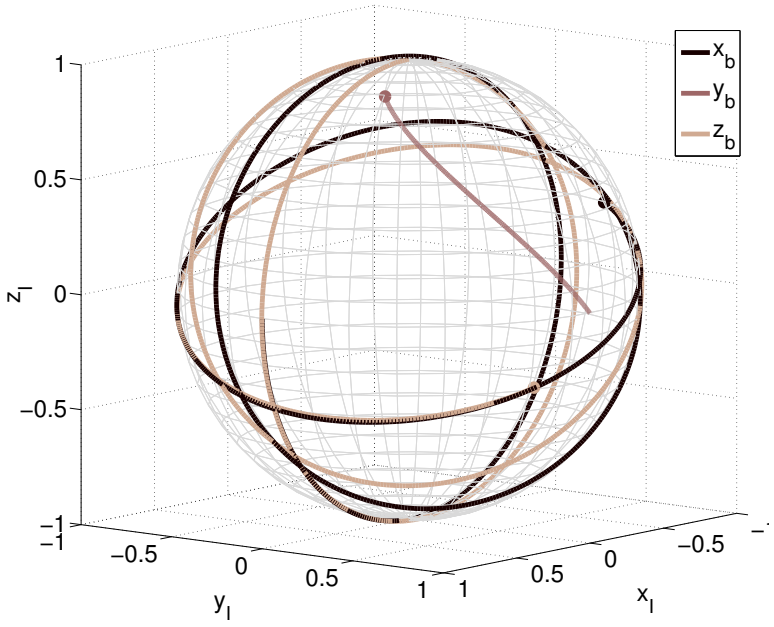

Figure 2.10: Path of the body axes on the unit sphere, in a spin-to-spin manoeuvre

Inversely, no singularities arise when evaluating the angular velocities and accelerations from the angles' derivatives. Finally, the trajectory can be converted to quaternions if required by the attitude control system of the spacecraft, at the cost of having to use trigonometric functions.

2.4 Inverse dynamics

A simple model of a fully actuated rigid body has been used to obtain the torque profile. The Euler's equation of rigid-body dynamics relates the torque u_i (along the body i-th axis) to the angular velocity ω_i and acceleration $\dot{\omega}_i$ and principal moments of inertia I_i, as

$$\begin{aligned} u_1 &= I_1\dot{\omega}_1 - (I_2 - I_3)\omega_2\omega_3 \\ u_2 &= I_2\dot{\omega}_2 - (I_3 - I_1)\omega_1\omega_3 \\ u_3 &= I_3\dot{\omega}_3 - (I_1 - I_2)\omega_1\omega_2 \end{aligned} \tag{2.18}$$

The angular velocities and accelerations are related to quaternions and their time derivatives through the rotational kinematics [15], as

$$\begin{aligned} \omega_1 &= 2(\dot{q}_1 q_4 + \dot{q}_2 q_3 - \dot{q}_3 q_2 - \dot{q}_4 q_1) \\ \omega_2 &= 2(\dot{q}_2 q_4 + \dot{q}_3 q_1 - \dot{q}_1 q_3 - \dot{q}_4 q_2) \\ \omega_3 &= 2(\dot{q}_3 q_4 + \dot{q}_1 q_2 - \dot{q}_2 q_1 - \dot{q}_4 q_3) \end{aligned} \tag{2.19}$$

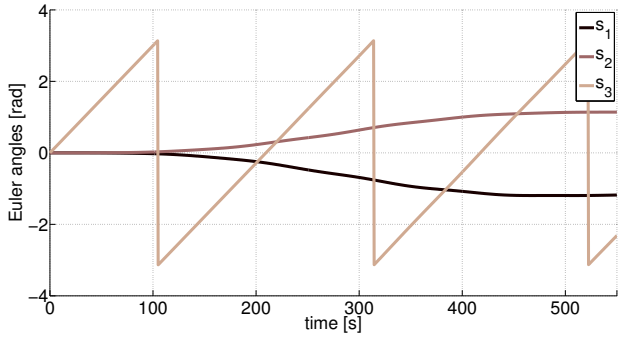

Figure 2.11: Trajectory of the attitude coordinates, in a spin-to-spin manoeuvre

$$\begin{aligned}\dot{\omega}_1 &= 2(\ddot{q}_1 q_4 + \ddot{q}_2 q_3 - \ddot{q}_3 q_2 - \ddot{q}_4 q_1)\\ \dot{\omega}_2 &= 2(\ddot{q}_2 q_4 + \ddot{q}_3 q_1 - \ddot{q}_1 q_3 - \ddot{q}_4 q_2)\\ \dot{\omega}_3 &= 2(\ddot{q}_3 q_4 + \ddot{q}_1 q_2 - \ddot{q}_2 q_1 - \ddot{q}_4 q_3)\end{aligned} \tag{2.20}$$

Analytical expressions for the quaternion derivatives are obtained by differentiating Eq.(2.1) with respect to time:

$$\dot{q}_i(t) = \frac{\dot{q}_i^*(t)}{\|\mathbf{q}^*(t)\|} - \frac{q_i^*(t)}{\|\mathbf{q}^*(t)\|^3}\left(\sum_{i=1}^{4} q_i^*(t)\dot{q}_i^*(t)\right) \tag{2.21a}$$

$$\ddot{q}_i(t) = \frac{\ddot{q}_i^*(t)}{\|\mathbf{q}^*(t)\|} - \frac{\dot{q}_i^*(t)}{\|\mathbf{q}^*(t)\|^3}\left(\sum_{i=1}^{4} q_i^*(t)\dot{q}_i^*(t)\right) + q_i^*(t)\left[\frac{3}{\|\mathbf{q}^*(t)\|^5}\left(\sum_{i=1}^{4} q_i^*(t)\dot{q}_i^*(t)\right)^2 - \frac{1}{\|\mathbf{q}^*(t)\|^3}\left(\sum_{i=1}^{4}(\dot{q}_i^*(t)^2 + q_i^*(t)\ddot{q}_i^*(t))\right)\right] \tag{2.21b}$$

Since the quaternions in Eqs. (2.19) and (2.20) can be replaced by their corresponding time-dependent polynomials (Eq. (2.1) and their derivatives), whose coefficients are a function of the manoeuvre time t_f, ultimately the torque is a function of t and t_f (given a set of boundary conditions for a particular manoeuvre). Evaluating the torque along the trajectory during the planning is essential to ensure that the actuators always remain within their operational limits when executing the manoeuvre. Similarly, an additional time differentiation of Eq. (2.20) allows for the evaluation of jerk along the manoeuvre if required.

If the actuators are reaction wheels, it can be useful to assess the speed build-up during the manoeuvre, to ensure that they will not become saturated. Assuming that the wheels are aligned with the body axes, the planned torque can be related to the derivative of their angular momentum. The body angular velocity is considered negligible compared to the magnitude of typical wheels' speeds.

Therefore the wheel's acceleration and moment of inertia can be related to the torque provided along its axis by

$$\mathbf{u} \approx -\mathbf{I}_r \dot{\boldsymbol{\omega}}_r \tag{2.22}$$

Where the vector $\dot{\boldsymbol{\omega}}_r$ contains the wheels' angular acceleration and $\mathbf{I}_r = \text{diag}(I_{r1},\, I_{r2},\, I_{r3})$ contains their moments of inertia. The wheels' speeds are obtained by replacing Eq. (2.18) into Eq. (2.22) and integrating:

$$\boldsymbol{\omega}_r(t) \approx -\frac{1}{\mathbf{I}_r}\left(\mathbf{I}(\boldsymbol{\omega}(t) - \boldsymbol{\omega}(0)) + \int_0^t \boldsymbol{\omega} \times (\mathbf{I}\boldsymbol{\omega})dt\right) + \boldsymbol{\omega}_r(0) \tag{2.23}$$

where the angular velocity of the body $\boldsymbol{\omega}$ can be replaced by Eq. (2.19). While the integral in Eq. (2.23) has a closed-form solution as a function of time and the polynomial coefficients, it is so complex that it is computationally more efficient to evaluate it numerically.

2.5 Trajectory smoothness analysis

A trajectory (i.e. a function of time $f(t)$) is said to be *smooth* if derivatives $f^{(n)}$ exist for all positive integers n, also known to be of class C^∞. If the trajectory is shaped by a polynomial, it is infinitely differentiable in the domain $t = (0, t_f)$, regardless of its degree. However, the motion of the spacecraft before and after said trajectory can be at rest, at a constant speed, or generally at a different state than during the slew manoeuvre. Therefore, looking at the trajectory in the whole $t = (-\infty, \infty)$ domain, it seems clear that it is not C^∞ differentiable at $t = 0$ and $t = t_f$.

Consider a rotation along a single axis, where the θ angle is shaped by a third-degree polynomial, and with a final time of $t_f = 300$ s. The angle, angular velocity, acceleration, and jerk are shown in Fig. 2.12 (where the time domain spans before and after the manoeuvre).

Clearly, the velocity (Fig. 2.12b) is a second-order function and thus the acceleration (Fig. 2.12c), which is proportional to the torque in the singe-axis case, is linear. The acceleration is continuous and smooth during the manoeuvre, but it is not continuous at the endpoints—therefore, jerk tends to infinite (Fig. 2.12d). To achieve acceleration continuity at the endpoints their values must be specified accordingly in the boundary conditions, requiring a 5^{th}-degree polynomial.

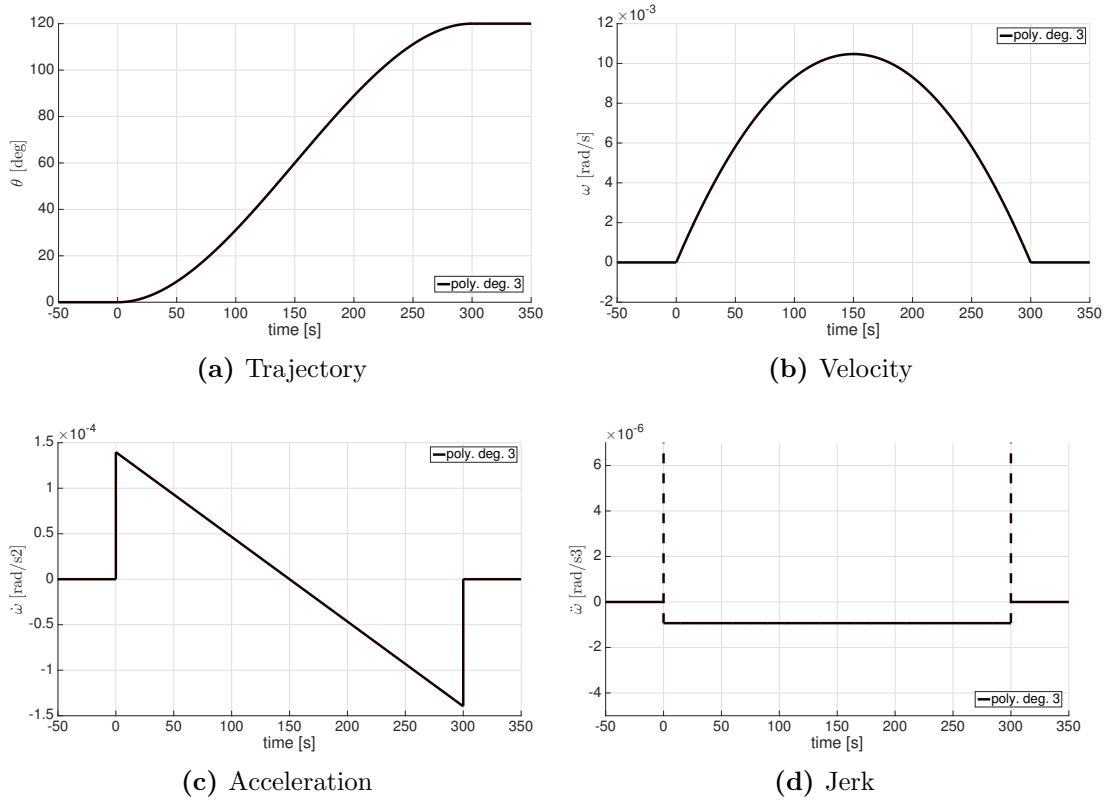

(a) Trajectory **(b)** Velocity

(c) Acceleration **(d)** Jerk

Figure 2.12: Single-axis rotational manoeuvre generated with a 3^{rd}-degree polynomial, analogous to a minimum-energy manoeuvre.

However, the acceleration at the endpoints would still not be smooth, or non-differentiable. Continuity and C^1 differentiability at the endpoints can only be achieved by a 7^{th}-degree polynomial which enforces zero jerk boundary values. For comparison, the motions shaped by the different polynomials and a bang-bang manoeuvre are shown in Fig. 2.13.

These considerations are relevant because, in spacecraft with flexible appendages, short-period vibrations are induced due to non-smooth torque or discontinuous jerk. If torque is, not only non-smooth but also discontinuous, such as with a 3^{th}-degree polynomial trajectory or a bang-bang torque profile, the induced vibrations are even larger. Note that suddenly switching off the torque cause vibrations as much as switching it on. High acceleration or jerk do not cause vibrations *per se* if their time profiles are smooth, affecting only the tip displacement magnitude of the appendages during the manoeuvre.

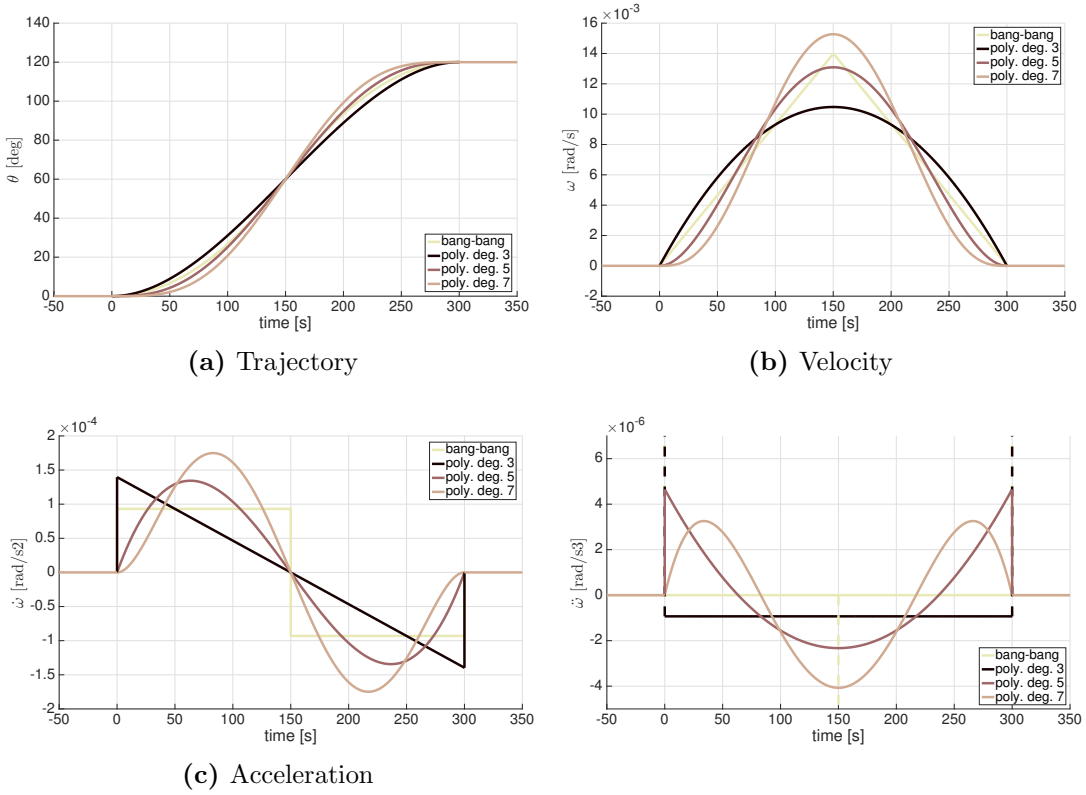

(a) Trajectory

(b) Velocity

(c) Acceleration

Figure 2.13: Single-axis rotational manoeuvre with polynomials of different degrees and a bang-bang manoeuvre.

2.6 Applications to spacecraft with flexible structures

Flexible spacecraft or spacecraft with flexible appendages introduce additional challenges due to vibration modes and a varying inertia matrix. To study how the proposed method performs in this scenario, simulations with a flexible spacecraft model have been realized. Environmental effects such as solar radiation pressure are not considered since they are long-term effects.

2.6.1 Multi-body flexible spacecraft model

The spacecraft has been modeled as a multi-body object, formed by a central cuboid with two solar panels, joint together by hinges (torsional spring and damper), as in Fig. 2.14. As opposed to modeling a spacecraft with Bernoulli beams [26], a multi-body does not need assumed vibration modes and it is shown

to be more representative of the three-dimensional case when compared to a numerical model [77].

Kane's method [78] is used to derive the dynamic equations (Eqs. (2.24) and (2.26)). In Eqs. (2.24-2.27c) θ_p is the deflection angle of the solar panel at the hinge, k and c are the stiffness and damping rate, $E_p = [\mathbf{e}_l\, \mathbf{e}_n\, \mathbf{e}_r]^T$ defines the panel-fixed frame (with its basis vectors resolved in the spacecraft's body frame) centered at the mid-point of the hinge C, $\mathbf{I}_b$ and $\mathbf{I}_p = \text{diag}(I_l,\, I_n,\, I_r)$ are respectively the inertia matrices of the central body and a panel, m_p is the mass of a panel, $\mathbf{r}_p$ is the distance (in body frame) from the body's center of mass to the panel's center of mass, $\mathbf{r}_C = [r_{Cl}\, r_{Cn}\, r_{Cr}]^T$ is the distance (in panel frame) from the body's center of mass to the hinge, d is the distance between C and the spacecraft's center of mass and $\mathbf{u}_{cmd}$ is the applied or commanded torque. The superscript $^\times$ indicates a skew-symmetric matrix.

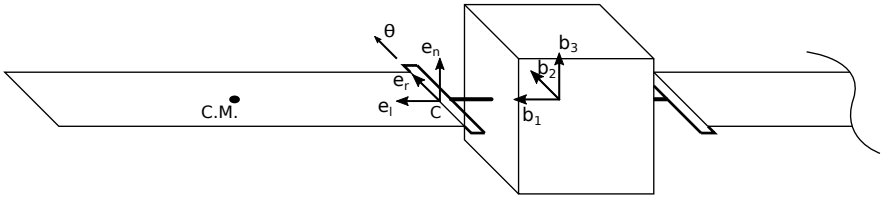

Figure 2.14: Spacecraft with hinged symmetric panels

The equations of motion of each panel are

$$\mathbf{A}_1\dot{\boldsymbol{\omega}} + B_1\ddot{\theta}_p = C_1 - k\theta - c\dot{\theta}_p \tag{2.24}$$

where

$$\mathbf{A}_1 = I_r\mathbf{e}_r^T + m_p d(r_{pl}\mathbf{e}_r^T - r_{Cr}\mathbf{e}_l^T) \tag{2.25a}$$

$$B_1 = I_r + m_p d^2 \tag{2.25b}$$

$$C_1 = m_p d[r_{Cn}(\omega_r^2 + \omega_l^2) - \omega_n(\omega_r r_{Cr} + \omega_l r_{pl})] - \omega_l\omega_n(I_n - I_l) \tag{2.25c}$$

and the equations of motion of the body are

$$\mathbf{A}_2\dot{\boldsymbol{\omega}} + \mathbf{B}_2\ddot{\theta}_p = \mathbf{C}_2 \tag{2.26}$$

where

$$\mathbf{A}_2 = \mathbf{I}_b + 2\mathbf{E}_p\mathbf{I}_p\mathbf{E}_p^T - 2m_p\mathbf{r}_p^\times\mathbf{r}_p^\times \tag{2.27a}$$

$$\mathbf{B}_2 = 2m_p d\mathbf{r}_p^\times\mathbf{e}_n + 2I_r\mathbf{e}_r \tag{2.27b}$$

$$\mathbf{C}_2 = \mathbf{u}_{cmd} - 2\dot{\theta}[(I_l - I_n)(\omega_l\mathbf{e}_n + \omega_n\mathbf{e}_l) + 2m_p d\mathbf{r}_p^\times\boldsymbol{\omega}^\times\mathbf{e}_n] + 2m_p\mathbf{r}_p^\times(d\dot{\theta}^2\mathbf{e}_l - \boldsymbol{\omega}^\times\boldsymbol{\omega}^\times\mathbf{r}_p) - \boldsymbol{\omega}^\times[(\mathbf{I}_b + 2\mathbf{I}_p)\boldsymbol{\omega} + 2\mathbf{I}_r\dot{\theta}\mathbf{e}_r] \tag{2.27c}$$

The motion of the spacecraft can be integrated by combining Eqs. (2.24) and (2.26) to eliminate dependence from $\ddot{\theta}$. The simulations have been realised considering a spacecraft with a body inertia matrix $\mathbf{I}_b = \text{diag}(310, 310, 310)$ kgm^2 and 3×1 m solar panels with a mass of 40 kg, resulting in a total inertia of $\mathbf{I}_t = \text{diag}(316, 894, 887)$ kgm^2. The hinges linking the panels with the body have a stiffness of 12 N m rad^{-1} and a damping of 0.01 kg m^2 s^{-1} rad^{-1}. The actuators are reaction wheels limited to 0.15 Nm.

2.6.2 Manoeuvres with open-loop torque profile

Via inverse dynamics, the required torque can be computed at every time t. Therefore, this torque profile can be commanded to the actuators in *open loop* to perform the manoeuvre. The torque has been predicted using a simplified internal model of the system using a rigid-body. Therefore there will be a divergence from the nominal attitude since unmodelled flexible structures (and environmental disturbances) are involved. However, simulations in open-loop are conducted to evaluate the effect of different polynomials on the vibrations of appendages. Minimum-time manoeuvres are computed using polynomials with no free coefficients, thus polynomials of lower degree will generate faster trajectories for a given maximum torque.

Figure 2.15 shows a rest-to-rest manoeuvre planned with a 7^{th}-degree polynomial, where it is clear that with torque commanded in open-loop the spacecraft is unable to meet the final attitude with precision. The error, measured as the angle between the actual final direction of each axis and the desired one, is $\mathbf{e}_{axes,n7} = [7.5, 11.4, 8.9]$ deg, for the three body axes. The error found in the manoeuvres using fifth- and third-degree polynomials are, respectively, $\mathbf{e}_{axes,n5} = [7.5, 11.6, 9.2]$ and $\mathbf{e}_{axes,n3} = [7.7, 11.7, 9.6]$. While polynomials of lower degree have a larger error, the relative difference with other polynomials is small.

Figures 2.16a and 2.16b show the evolution of the deflection angle of the solar panels at the hinges θ_p, which is proportional to the panels' tip displacement, and its derivative $\dot{\theta}_p$. Results using polynomials of different degrees are compared. Zero jerk at the endpoints of the trajectory can be achieved by a trajectory shaped with a polynomial of degree 7, zero acceleration can be achieved by a polynomial of degree 5 (continuous but not smooth at the endpoints), and a

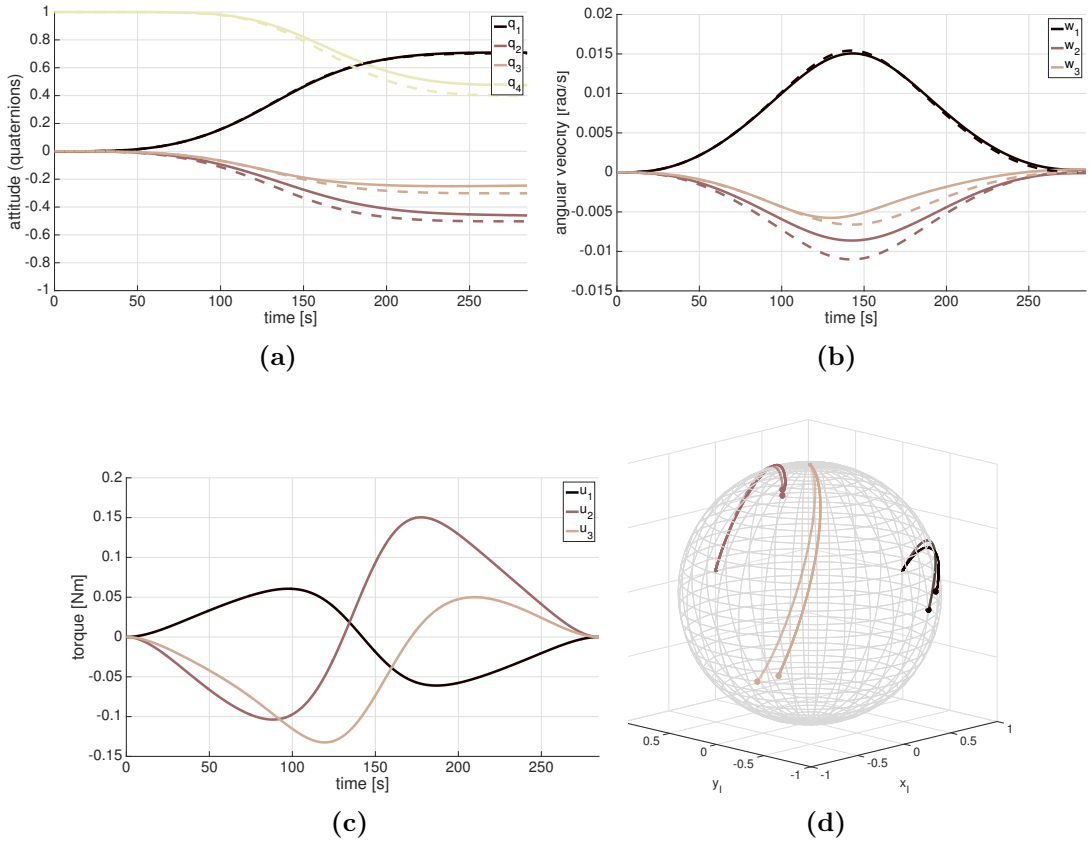

Figure 2.15: 7^{th}-degree polynomial trajectory with torque commanded in open-loop. (Solid lines are simulated values; dashed lines are planned values.)

polynomial of degree 3 suffices to enforce zero velocity only. The torques planned with a 3^{rd} degree polynomial are not continuous at the endpoints, causing large short-period vibrations (which are better appreciated in $\dot{\theta}_p$). When the torque is cut off the spacecraft is left with residual vibrations, known as *spillover*. This situation is significantly improved with a 5^{th}-degree polynomial. The torque at the endpoints, while not smooth, is continuous, significantly reducing the initial vibration and the spillover. With a 7^{th}-degree polynomial, short-period vibrations are unnoticeable. However, enforcing smoothness at the endpoints requires a slower manoeuvre: given the same spacecraft parameters, the minimum final time is $t_f = 284$ s with a 7^{th}-degree polynomial, $t_f = 242$ s with a 5^{th}-degree one, and $t_f = 191$ s with a 3^{th}-degree one.

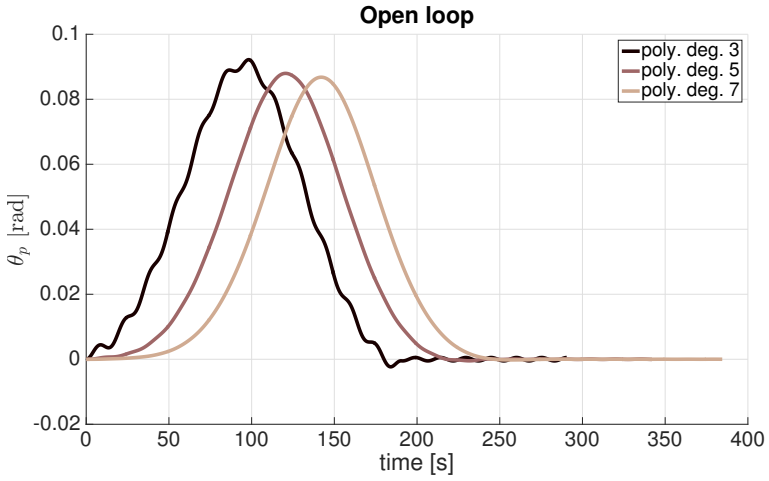

(a) Solar panel angle

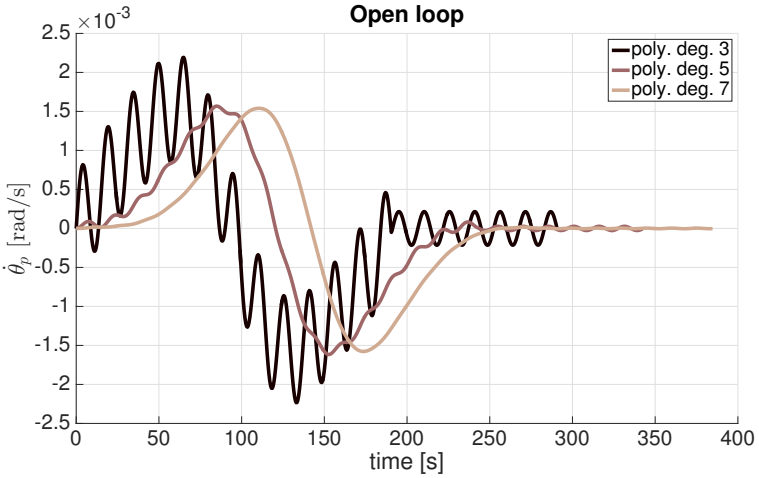

(b) Time derivative of the panel angle

Figure 2.16: Solar panel deflection angle, for a manoeuvre planned with different polynomials. Torque commanded in open-loop.

2.6.3 Trajectory tracking with a feedback controller

In order to reject the disturbances caused by unmodelled dynamics and environmental effects, a closed loop implementation is required. In these simulations, a proportional-derivative (PD) quaternion feedback controller [15] tracks the desired attitude and angular velocity (Eq. (2.28)). Since a prediction of the torque is available, the controller can be augmented by including it as a feed-forward command.

$$\mathbf{u}_{cmd} = -K_p \mathbf{q}_e - K_d \boldsymbol{\omega}_e + \mathbf{u}_{pln} \tag{2.28}$$

In Eq. 2.28, K_p and K_d are the proportional and derivative coefficients, q_e is

the error quaternion, $\boldsymbol{\omega}_e$ is the error angular velocity, and $\mathbf{u}_{pln}$ is the estimated torque as obtained by the planning. Since this PD controller is used for tracking, it involves very small errors. Also, it is aided by a feed-forward torque, hence the controller only has to reject the unmodelled effects and environmental disturbances. For these reasons, stability is not an issue here, as opposed to the cases where a linear controller has to drive a spacecraft directly between two distant attitude states, involving large errors with nonlinear dynamics.

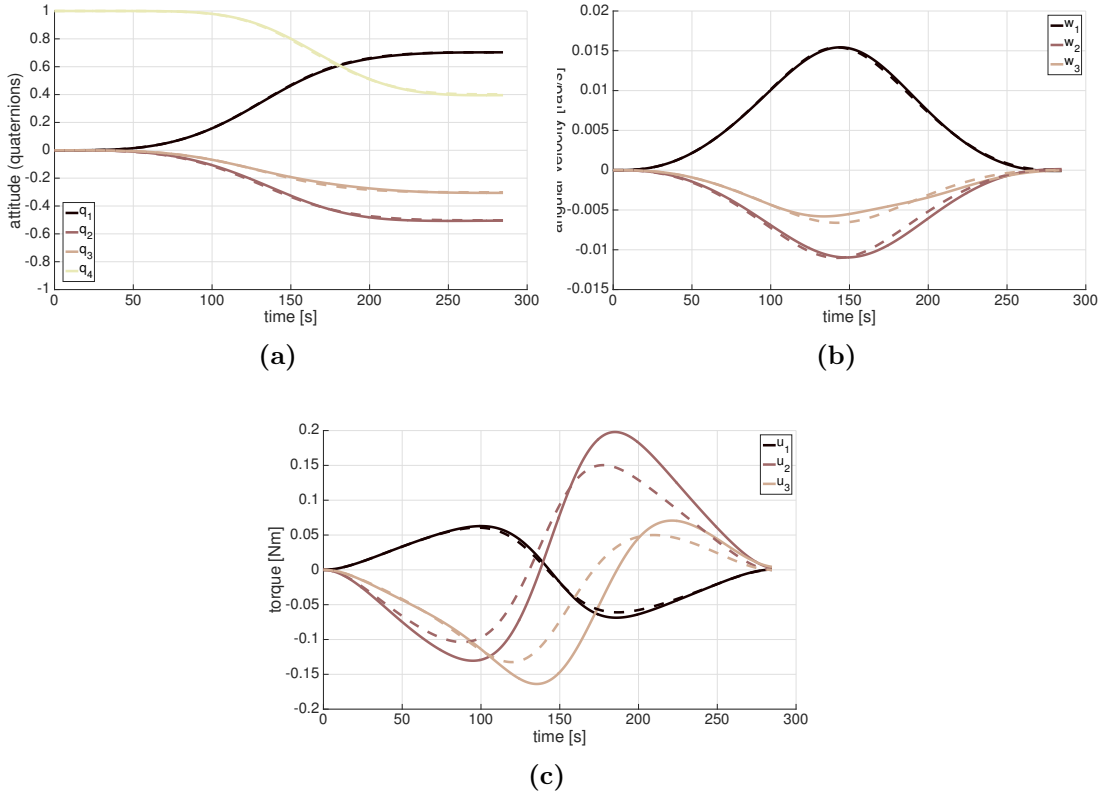

Figure 2.17: 7^{th}-degree polynomial trajectory with closed-loop tracking of the planned trajectory. (Solid lines are simulated values; dashed lines are planned values.)

Figure 2.17 shows the trajectory planned with a 7^{th}-degree polynomial and tracked using feedback control. Note that the actual torque (as given by the control law) is higher than the planned torque due to the disturbance rejection caused by large flexibility (low stiffness). Trajectories planned with other polynomials show a similar behaviour. This result stresses the need of applying an appropriate safety margin in the selected t_f or the maximum torque constraint during the planning phase. In contrast to Fig. 2.15, using feedback tracking greatly im-

proves the error. After the spacecraft reaches the final attitude, the controller is still actuating to stabilise the spacecraft into this attitude.

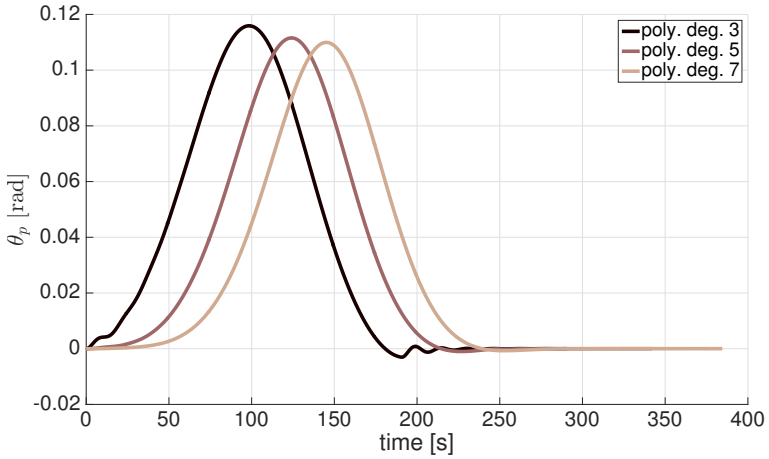

(a) Solar panel angle

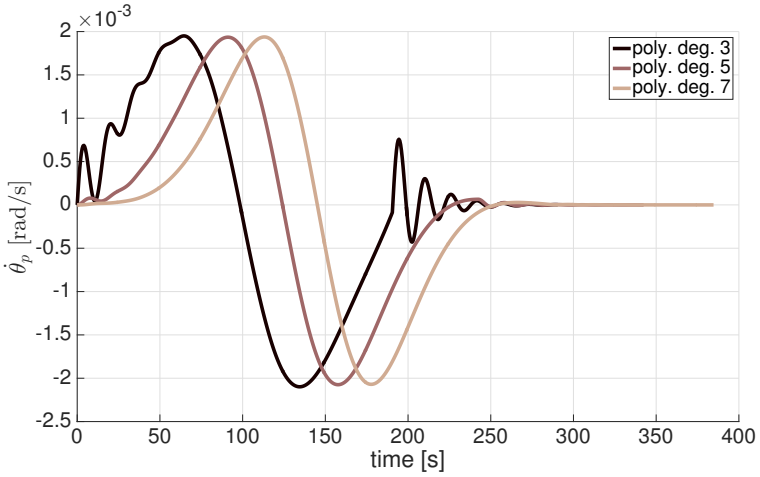

(b) Time derivative of the panel angle

Figure 2.18: Solar panel deflection angle, for a manoeuvre planned with different polynomials. Closed-loop tracking.

Figure 2.18 shows the deflection of the solar panel and its time derivative. A longer time is shown after the end of the manoeuvre to depict the post-manoeuvre stabilisation time. The 3^{th}-degree polynomial excites vibrations at the start of the manoeuvre (Fig. 2.18a), however, the feedback control tracking the trajectory acts as a damper of the oscillations that would remain if open-loop control was implemented. At the end of the manoeuvre the torque is cut off and more vibrations are induced, but the controller slowly stabilises the attitude. With a 5^{th}-degree polynomial the induced vibrations are much smaller and the tracker

stabilises them faster, while with a 7^{th}-degree polynomial there are virtually no initial or spillover vibrations.

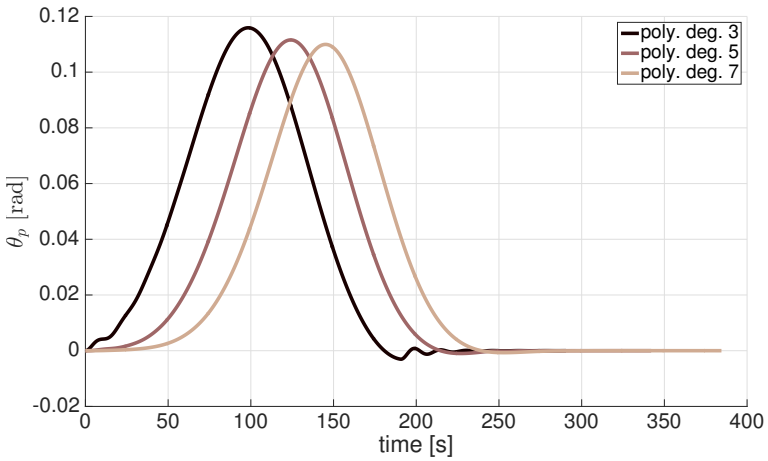

Figure 2.19: Detail of time derivative of the panel angle, after the manouevres. Closed-loop tracking.

The results of these simulations, highlighted in the post-manoeuvre detail (Fig. 2.19), show that the very short stabilisation time required by a longer manoeuvre (with a 7^{th}-degree polynomial, which does not induce spillover) is compensated by a faster one which causes spillover and requires a larger stabilisation time. It can be argued that an advanced controller specifically designed for damping spillover vibrations can reduce the stabilisation time. However, hardware has its limitations, and the frequency and amplitude of spillover can be reduced only to a certain extent via feedback control. For instance, missions with high precision requirements rely on star trackers with relatively large sampling times, rendering the implementation of such controllers difficult. Therefore, it might be appropriate to choose a 7^{th}-degree polynomial which does not excite the spacecraft's appendages. A compromise solution might be using a 6^{th}-degree polynomial, which generates quicker trajectories by having a non-smooth start. Given that the initial vibrations are be reduced to a certain extent by the tracking controller or by natural damping during the manoeuvre, and the fact that the trajectory is smooth (C^3 differentiable) at the end, spillover vibrations are virtually eliminated. This would allow any sensitive instrument to be readily available after the manoeuvre, which is the main goal of reducing spillover vibrations. Additionally, the simulations show that this manoeuvre is 16 s faster than the 7^{th}-degree polynomial (on the same baseline manoeuvre).

Taking the aforementioned into consideration, choosing the right polynomial for shaping the trajectory will depend mainly on the specific mission requirements and constraints. For a fixed manoeuvre time, lower degree polynomials generate trajectories with lower acceleration and torque peaks, leading to smaller maximum tip displacement, but the endpoints might not be as smooth as those provided with higher order polynomials. It is advised to use a very smooth ending torque to prevent spillover. For instance, the post-manoeuvre stabilisation time can be costly for agile observation satellites, since they are inactive between repointing and taking an image. The sloshing of fuel is another effect that forces a spacecraft to stabilise after a slew manoeuvre. However, since sloshing dynamics can be modelled using a mass-spring model [14]—analogous to the multi-body model for solar panels used in this section—the benefits of the smooth polynomial planning also apply. Implementing trajectory tracking is recommended over open-loop control, to both minimize the attitude error and damping vibrations, although larger torques must be accounted for. If there is a constraint on some appendage's maximum tip displacement, a limit on maximum acceleration can be considered so that a higher t_f may be chosen, even if the torque is well below the actuators' limit. Finally, with this method, the design of the spacecraft structure can be allowed to be less stiff (reducing cost and weight), and still prevent large oscillations.

2.7 Chapter summary

In this chapter, a method for shaping the trajectory of attitude slew manoeuvres using single polynomials has been presented. Quaternions have been used as the baseline attitude representation. The coefficients of the polynomials are found by matching the boundary conditions of the manoeuvre, although additional degrees of freedom can be included by increasing the degree of the polynomials. Concerns regarding numerical issues commonly arise when working with high order polynomials, therefore an analysis has been conducted. Scaling time has been proposed as a method to prevent numerical stability problems. While quaternions can be used for planning arbitrary manoeuvres, an axis-angle attitude representation has been proposed for the special case of spin-to-spin manoeuvres. More efficient trajectories are obtained, since this representation naturally provides a precessing motion of the spinning axis.

Smoothness in the trajectory profile prevents short-period oscillations—such as spillover—from arising in flexible spacecraft. Even spacecraft with very rigid structures can experience vibrational problems due to fuel slosh. A feature of polynomials is that they are smooth along its domain, however, smoothness at the trajectory endpoints (down to a certain differentiability class) has to be enforced by the boundary conditions. It has been shown how vibrations can be prevented with this guidance approach, rather than using a dedicated controller working at high frequency to stabilise the spacecraft, which most spacecraft do not implement (leaving vibrations to dampen naturally).

This polynomial planning method is an inverse dynamics method, i.e. torques are derived from a given trajectory. Not only torque but a slew of data can be obtained from the planned trajectory such as reaction wheel speed, fuel consumption, or path of pointing vectors, *before* the manoeuvre is executed. This offers the possibility of re-planning the trajectory if some performance index is to be optimised or if a certain constraint is not satisfied. To this end, the different degrees of freedom of the polynomial trajectories (the final time and any additional coefficients) can be used to reshape the trajectory. The next chapter focuses on this constrained trajectory optimisation problem, presenting the efficiency and effectiveness of this polynomial method.

Chapter 3

Attitude trajectory optimisation in the presence of constraints

The manoeuvre time t_f and any free coefficients of the polynomial must be selected in order to calculate the rest of the coefficients, defining a trajectory which satisfies the boundary conditions. Those variables can be selected in an optimization process, so that a certain performance index (single- or multi-objective) is optimised, amongst the class of polynomial motions, while constraints are satisfied. In this chapter, dynamic constraints such as maximum torque and reaction wheel speed are explored, which are evaluated from the quaternions and their derivatives with an internal model (i.e. inverse dynamics). Also, path constraints or pointing keep-out areas are introduced. While this is a nonlinear constrained optimization problem, the use of computationally intensive algorithms (such as sequential quadratic programming (SQP)) has been avoided. A more efficient approach as a tailored combination of root-finding and unconstrained optimization has been used, as well as pre-computed analytical functions. The main performance index considered is manoeuvre time. A multi-objective fuel-time cost function could be implemented if a RCS was used. However, this work focuses on the use of reaction wheels, since they are more suited to the continuous and smooth control provided by the trajectories planned with polynomials. Thus, alongside time a performance index related to reaction wheels is considered, consisting on the angular momentum stored in the wheels at the end of the manoeuvre. The performance of the polynomial planning method is compared with an optimal control solver, and also amongst different attitude representations.

3.1 Time optimisation

Once the boundary conditions of a particular manoeuvre have been selected, the remaining variable necessary to determine the polynomial coefficients (Eq. 2.6) is the manoeuvre final time t_f (provided that there are no free coefficients or they have been given). In this section the goal of finding the minimum t_f is addressed, requiring the evaluation of the torque to check the feasibility of the trajectory. While a generic optimiser can be used, tailored methods are proposed aiming to maximise computational efficiency and robustness.

3.1.1 Optimising time via root-finding

The manoeuvre duration t_f affects the torque profile, with shorter final times resulting in higher torques. A criterion for choosing t_f is to find its minimum value such that the calculated maximum torque in the manoeuvre (of any axis, in absolute value) is equal to the actuator's torque limit u_{lim}. In an analogous way, other differential constraints can be considered, such as a limit on velocity, acceleration, jerk, or the reaction wheels rate.

It is possible to obtain an expression of the planned torque as a function of time and t_f by combining the equations of rigid-body dynamics and the polynomials representing the attitude parameters. However, due to the high non-linearity of this expression, finding the minimum t_f with a purely analytical approach is not practical. A more efficient strategy consists in discretising the trajectory and evaluating the torques at each node ($u_i(t_k)$ for the i-th axis and k-th node). The difference with the torque limit u_{lim} is calculated at each node and the maximum value of the set is obtained:

$$J_i = \max_k(|u_i(t_k)| - u_{lim}) \tag{3.1}$$

where J_i is the largest difference amongst all nodes of the i-th axis' torque profile. The three axes can be combined in $J = \max\{J_1,\, J_2,\, J_3\}$.

As shown in Figure 3.1, the optimum point corresponds to $J = 0$. If $J > 0$, the final time is lower but the maximum torque is above the limit, whereas if $J < 0$ the trajectory is feasible but the final time can be arbitrarily large. The evolution of J with t_f is monotonically decreasing, as shown in the example of Figure 3.2. Finding the root of this curve, corresponding to the minimum t_f of a particular

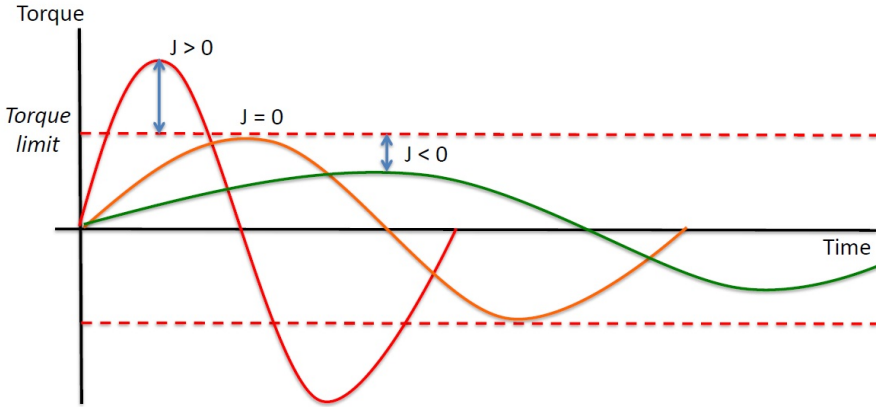

Figure 3.1: Illustration of torque profiles with different final times, with J being a metric of the peak height

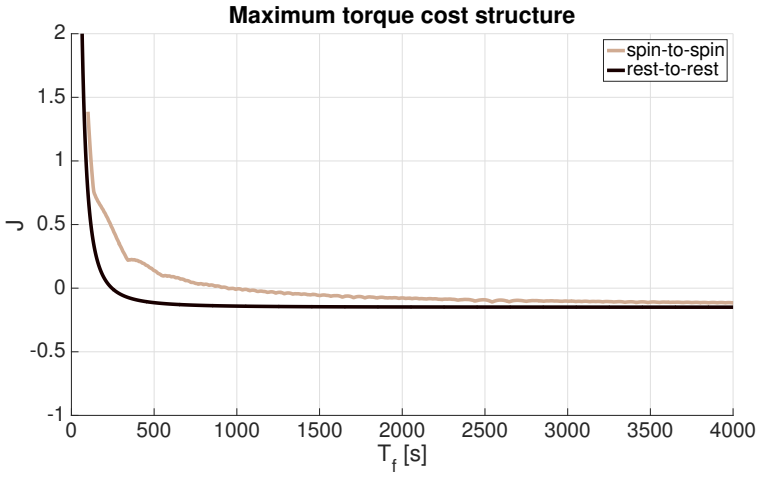

Figure 3.2: Evolution of J (maximum torque over the limit) with manoeuvre time

path, is performed with very few iterations. While gradient-based optimization algorithms would use J^2 to find the optimum, the J performance index allows to (a) know if a trajectory is feasible (in terms of torque) simply by checking the sign of J, and (b) use a root-finding algorithm, such as the bisection method, which are more efficient than numerical gradient-based ones.

For this simulation, a large satellite with small reaction wheels has been modelled. The rest-to-rest manoeuvre (planned with quaternions) is of 90 deg and the slew of the spin-to-spin case (planned with axis-azimuth) is 115 deg long, with endpoint spin rates of 1.8 deg/s. Note that the planned torque profile is a prediction based on an internal model, and its accuracy will determine how large the difference is between the planned and the real torque (when the trajectory is tracked with

feedback control). Considering an additional safety margin on the torque limit or on t_f is advised to account for model inaccuracies and other disturbances (such as solar radiation pressure, atmospheric drag, etc).

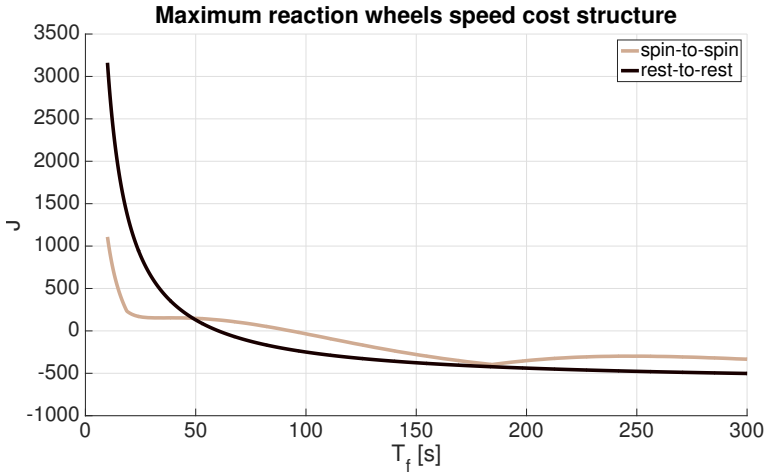

Figure 3.3: Evolution of J (maximum reaction wheels speed over the limit) with manoeuvre time

In an analogous way to the torque profile, the reaction wheels peaks can be found and checked against the speed limit. The performance index (or cost) structure shown in Fig. 3.3 features a similar behaviour to that of torque. The spin-to-spin case is not monotonically decreasing, thus, if there was more than one zero the first one would be chosen as corresponding to the minimum manoeuvre time.

Arbitrary move-to-move manoeuvres (such as the ones used by EO satellites) have a similar behaviour to rest-to-rest ones, as shown in Figs. 3.4 and 3.5. For comparison, the same manoeuvre planned with Euler angles has been included. Note that unlike the spin-to-spin case, where a particular axis-azimuth representation is used, in this case the full final attitude is specified with Euler angles. The move-to-move manoeuvre is 130 deg long with endpoint velocities of 4.5 deg/s, using more capable actuators than in the rest-to-rest case.

In Fig. 3.4, the cost index (related to the torque peak) decreases monotonically and asymptotically with the manoeuvre time, both with quaternions and Euler angles. However, for the same manoeuvre Euler angles provide a noticeable longer minimum time (the zero of the function) than quaternions. When looking at the wheels' momentum peak (Fig. 3.5), quaternions provide a monotonically decreasing behaviour but Euler angles do not, which could imply the existence of

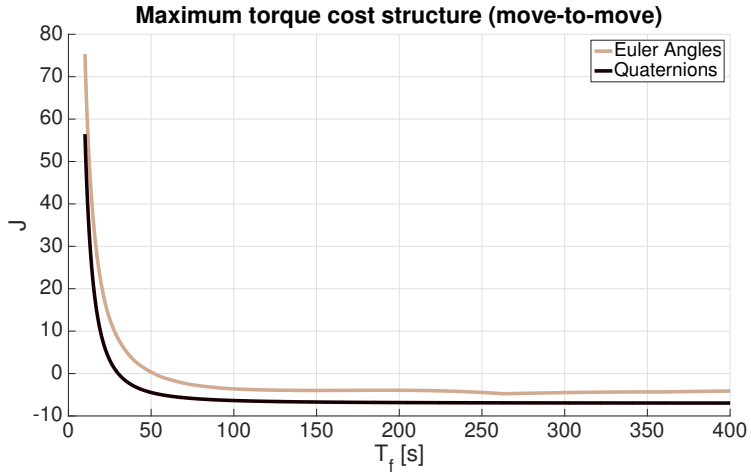

Figure 3.4: Evolution of J (maximum torque over the limit) with manoeuvre time, for an arbitrary move-to-move manoeuvre

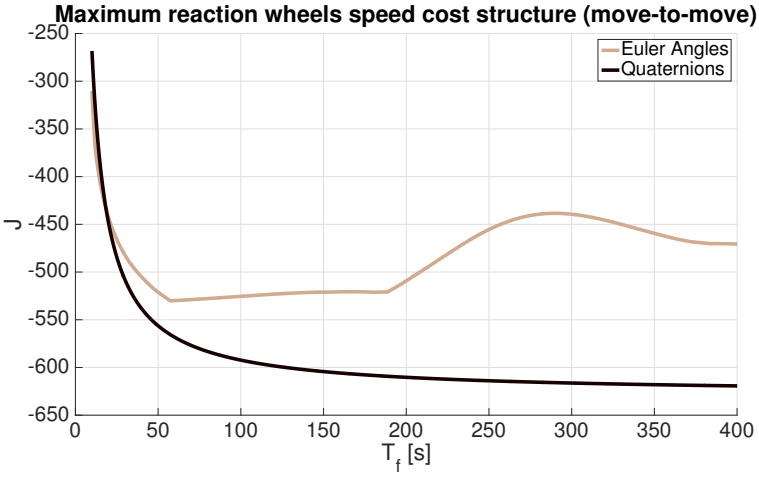

Figure 3.5: Evolution of J (maximum reaction wheels speed over the limit) with manoeuvre time

multiple zeros under certain conditions. However, in this simulation the wheel's momentum capacity is large enough to not being a bottleneck.

It is insightful to look at a degenerated move-to-move manoeuvre with an exceedingly long final time, regarding the fundamental differences between planning with quaternions and Euler angles. For an arbitrarily large final time, in the manoeuvre planned with quaternions (Fig. 3.6) the trajectory makes the spacecraft brake down, loiter for most of the allocated manoeuvre time, and spin up again when the final time approaches. In contrast, in the Euler angles manoeuvre (Fig. 3.7) the spacecraft is kept rotating, until it reaches the final state at the specified

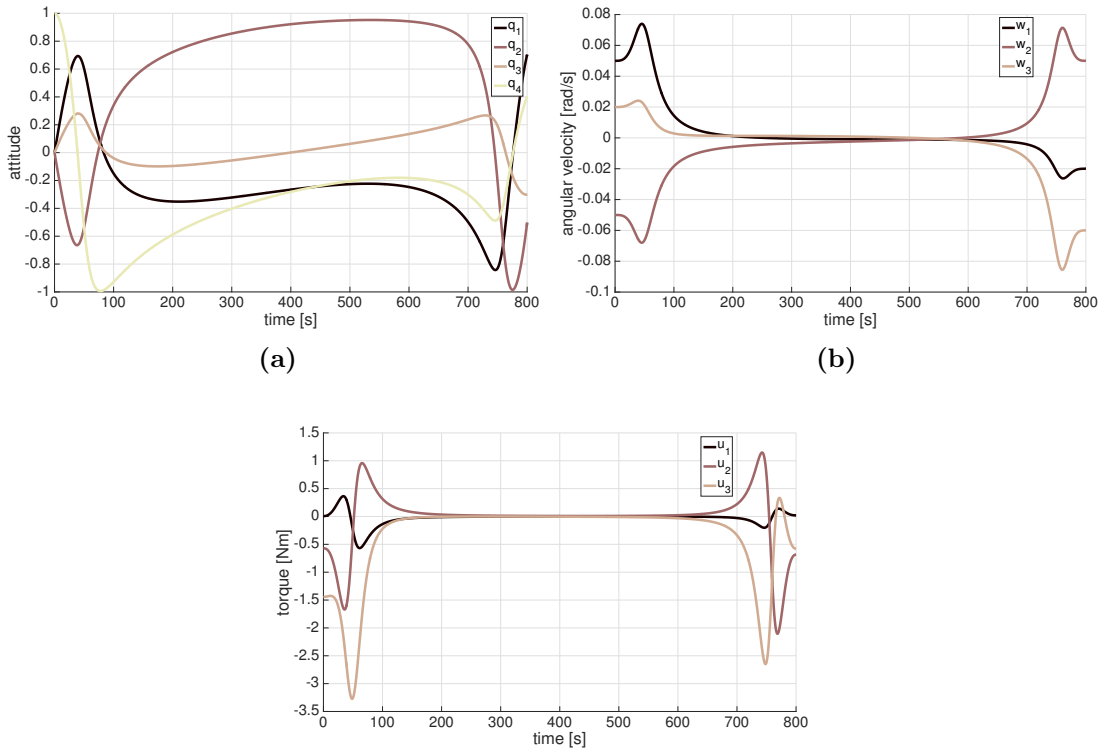

Figure 3.6: $7^{th}t$-degree polynomial move-to-move manoeuvre planned with quaternions, with an arbitrarily long final time

time. This is caused by the planned profiles of the Euler angles, which reach values multiple times over $2{\cdot}\pi$ on the course of the manoeuvre. Instead, quaternions are bounded between -1 and 1. Essentially, the spacecraft motion is obtained by inverse dynamics from the attitude profile, therefore different attitude representations will show different behaviours.

Notice that the torque at the endpoints is not zero. This is due to the prescribed boundary conditions, which force a constant angular velocity vector on the spacecraft. However, the body is asymmetric, and a torque equal to the gyroscopic precession will be required at the endpoints to maintain the prescribed state. Since the manoeuvre is planned with a $7^{th}t$-degree polynomial, the torque at the endpoints will be continuous and smooth even if non-zero.

Finally, other paths (still matching the prescribed boundary values) may have a lower final time, which can be explored by polynomials with additional terms. In this case, free variables are added to the system, whose value can be selected by an optimizer. Best results are obtained with a two-layer optimization approach

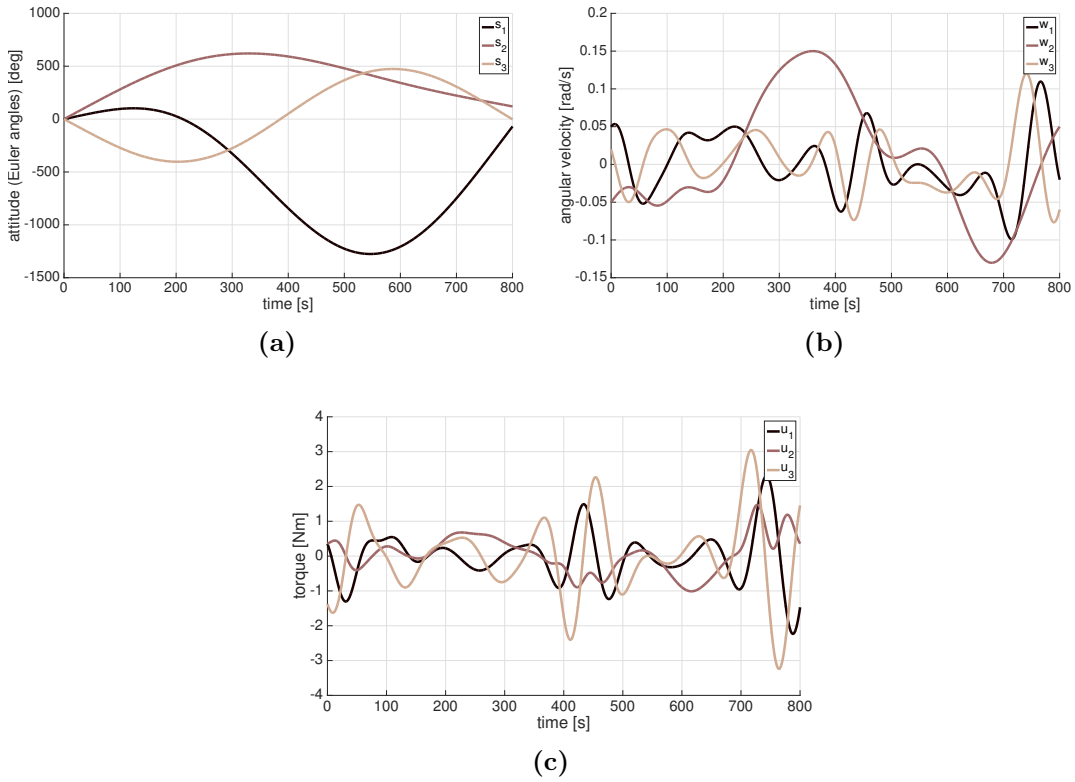

Figure 3.7: $7^{th}t$-degree polynomial move-to-move manoeuvre planned with Euler angles, with an arbitrarily long final time

(Fig. 3.8). The outer layer explores the space of $4\times k$ free coefficients (considering 4 quaternions, shaped with polynomials of degree $m+k$), using an unconstrained optimization method with manoeuvre time as the performance index. At every iteration of the optimizer, the root-finding algorithm runs as the inner loop, giving the minimum feasible time for that specific trajectory. This approach is robust in the sense that, even if the optimizer converges to a local optimum, the trajectory will satisfy torque constraints. While there exists a global minimum time amongst the set of trajectories given by polynomials of a certain degree, it can be reduced if higher degrees are used. The absolute global optimum of the problem could be that given by polynomials of infinite degree (although it would be impossible to solve), or a computational optimal control method (although global optimality is not guaranteed).

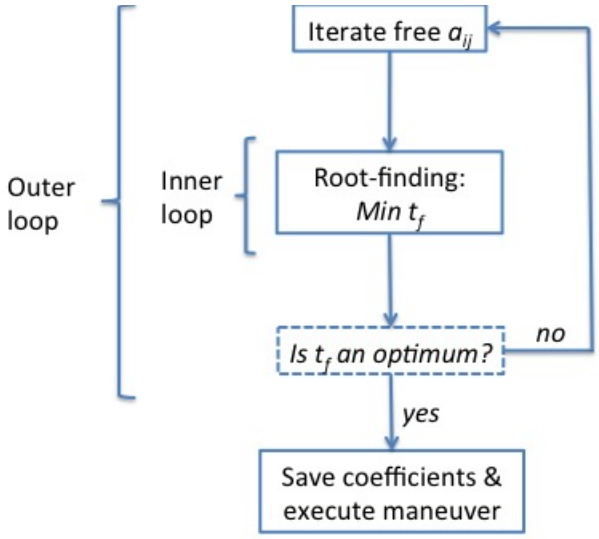

Figure 3.8: Two-layer time optimization algorithm

3.1.2 Optimising time via pre-computed analytical functions

In an effort to keep the computational overhead as low as possible, an analytic function for calculating the minimum final time has been developed—the so-called t_f-*function*. This strategy is based on the assumption that the minimum time of a manoeuvre mainly depends on a number of selected parameters, such as the travelled distance.

3.1.2.1 Rest-to-rest t_f-*function*

In the rest-to-rest case using quaternions, the rotation angle θ_f, representing the length of the slew, is one of the drivers of the manoeuvre duration. In an asymmetric spacecraft, the actuators require more power if the manoeuvre is performed along high inertia axes. Therefore, another main driver of t_f is the moment of inertia along the rotation axis (I_e), calculated using

$$I_e = \hat{\mathbf{e}}_B^T \mathrm{I} \hat{\mathbf{e}}_B \tag{3.2}$$

where I is the matrix of of principal moments of inertia and $\hat{\mathbf{e}}_B$ the rotation axis as previously defined.

When a large enough Monte-Carlo simulation is performed with random manoeuvres, a cloud of points is obtained by plotting t_f with θ_f and I_e, which has

a surface pattern (Fig. 3.9). With a data-fitting tool a parametric cubic surface can be well approximated.

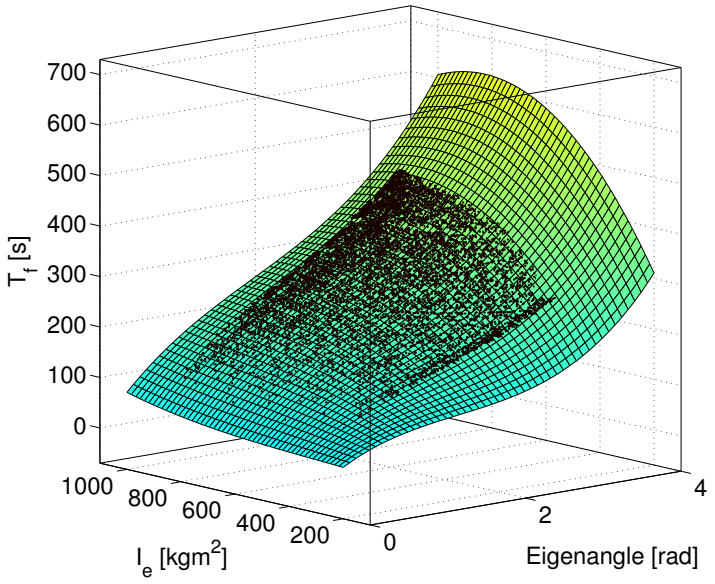

Figure 3.9: Cubic surface fitting a cloud of points corresponding to random manoeuvres

However, the surface $t_f = f(\theta_f, I_e)$, as obtained by data-fitting, is essentially an average, thus a margin on the estimated t_f must be added so that the torque limit is respected in all possible manoeuvres. Despite the advantage of quickly estimating t_f, some performance is lost since the calculated manoeuvre duration will not be the minimum possible. As an example, with the model studied in this work, with the rest-to-rest t_f-*function* most of the predicted times are under 30% larger than the actual minimum final time (Fig. 3.10). The larger errors correspond to small displacements, which have short associated manoeuvre times. The R-squared value for this example is 0.986.

3.1.2.2 Spin-to-spin t_f-*function*

The manoeuvre final time can also be analytically estimated in the spin-to-spin scenario. However, in this case the moment of inertia metric is no longer valid. The angle between the initial and final pointing vectors (α), analogue to θ_f, can still be used as a parameter in the t_f-*function*. A second parameter can

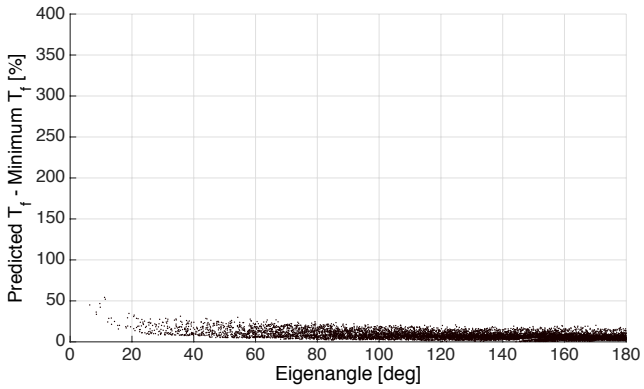

Figure 3.10: Difference between the predicted and minimum final times, in % (rest-to-rest)

be selected to form a surface pattern in the Monte-Carlo analysis based on the difference between the endpoints of the angles s_1 and s_2 (Eq. (3.3)).

$$L_s = \sqrt{|s_{10} - s_{1f}|^2 + |s_{20} - s_{2f}|^2} \tag{3.3}$$

A parametric surface is obtained as $t_f = f(\alpha, L_s)$ via data-fitting. A 4^{th} degree surface can be fitted, resulting in an R-squared value of 0.995. The difference between the t_f predicted by the funciton and the and optimum value can be as high as 400%. However, Fig. 3.11 shows that, as in the previous case, high differences correspond to short duration manoeuvres, thus the error in absolute terms is not large.

A *t_f-function* in the spin-to-spin case is, again, model-specific, and every set of surface coefficients is valid only for specific endpoint spin rates. For a spinning spacecraft featuring a limited amount of spin rate values, it is feasible to store the function coefficients for every mode. Note that it is not possible to consider path constraints with the *t_f-function* approach.

3.2 Obstacle avoidance

The path of the body axes on the unit sphere can be diverted in order to avoid pointing constraints. This is usually required by sensitive optical instruments

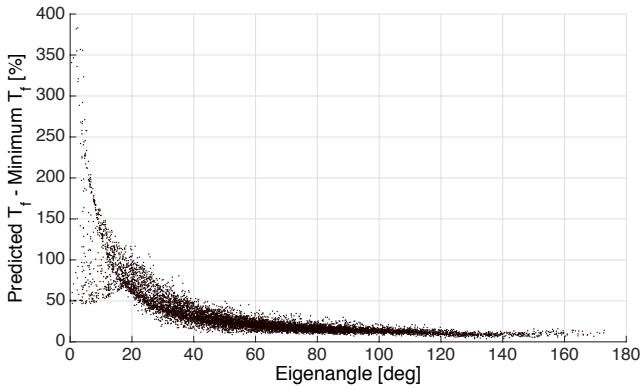

Figure 3.11: Difference between the predicted and minimum final times, in % (spin-to-spin)

that shall avoid having the Sun in its field of view to avoid damage, or by star trackers that shall not be blinded. The static path constraints [27] or keep-out areas are represented by cones intersecting the unit sphere. The intersecting circle should not be trespassed by the path of the constrained body axis $\mathbf{v}_i^I(t)$, in other words, the angle between $\mathbf{v}_i^I(t)$ (resolved in the inertial frame) and the cone axis $\mathbf{w}_c$ should not be smaller than the cone angle γ_c:

$$\mathbf{v}_i^I(t) \cdot \mathbf{w}_c \leq \cos(\gamma_c) \tag{3.4}$$

The pointing body axis can be evaluated from quaternions with

$$\mathbf{v}_i^I = (q_4^2 - \|\vec{q}\|^2)\mathbf{v}_i^B + 2(\vec{q}^T\mathbf{v}_i^B)\vec{q} + 2q_4(\vec{q} \times \mathbf{v}_i^B) \tag{3.5}$$

where $\vec{q} = [q_1,\, q_2,\, q_3]^T$ and $\mathbf{v}_i^B$ is the pointing axis resolved in the body frame.

3.2.1 Using waypoints

Obstacle avoidance can be achieved in a deterministic way using a suitable path point, which implies adding an additional equation to the linear system of boundary conditions. For instance, if a 4^{th}-degree polynomial was used with 4 boundary conditions and one waypoint, the system to calculate the polynomial coefficients would be:

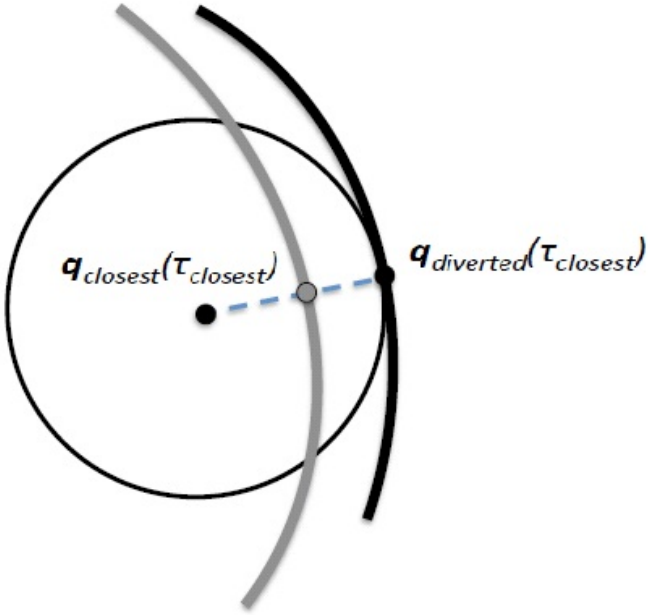

Figure 3.12: A path crossing the keep-out area is diverted by forcing it to pass through a determined waypoint

$$\begin{bmatrix} 1 & 0 & 0 & 0 & 0 \\ 0 & 1 & 0 & 0 & 0 \\ 1 & t_f & t_f^2 & t_f^3 & t_f^4 \\ 0 & 1 & 2t_f & 3t_f^2 & 4t_f^3 \\ 1 & t_{wp} & t_{wp}^2 & t_{wp}^3 & t_{wp}^4 \end{bmatrix} \begin{bmatrix} a_{i0} \\ a_{i1} \\ a_{i2} \\ a_{i3} \\ a_{i4} \end{bmatrix} = \begin{bmatrix} q_i(0) \\ \dot{q}_i(0) \\ q_i(t_f) \\ \dot{q}_i(t_f) \\ q_i(t_{wp}) \end{bmatrix} \tag{3.6}$$

Where $q_i(t_{wp})$ is the prescribed waypoint to be reached at time t_{wp}.

A single waypoint is enough to divert the path away from the obstacle. The point is selected by calculating the nearest point of the nominal path to the cone center and moving it to the closest point on the circle (Fig. 3.12). This implies rotating the attitude about the axis $\mathbf{w}_c \times \mathbf{v}_i^I(t_{wp})$ by an angle $\gamma_c - \gamma$. When time is adimensional, the $\tau_{wp} = t_{wp}/t_f$ of the diverted point is the same as the original one, as shown in Fig. 3.12 with $\tau_{closest} = \tau_{wp}$. The resulting path of the pointing axis is tangent to the keep-out cone, and a new minimum t_f is evaluated for the diverted trajectory. This approach is suboptimal, but as it is deterministic it avoids the optimisation process and a feasible motion is obtained.

The limitation of this approach is on manoeuvres with arbitrary endpoint velocities. In this case the variable t_f affects the path, thus the time-minimisation and the obstacle avoidance problems are coupled. However, in the case of spin-to-spin

using the previously described parametrisation, the path of the pointing axis is not dependent on t_f, and an analogous approach to the rest-to-rest scenario can be applied.

3.2.2 Using unconstrained optimisation

Obstacle avoidance can be carried out using unconstrained optimization of the free parameters. Constraints can be taken into account in unconstrained optimization with a penalty function acting as a performance index. The penalty function, which shall be minimised down to zero for the trajectory to be feasible, considers the keep-out area as

$$J_{OA} = \begin{cases} \max_k(\mathbf{v}_i^I(t_k) \cdot \mathbf{w}_c - \cos(\gamma_c)) & \text{if } \mathbf{v}_i^I(t) \cdot \mathbf{w}_c > \cos(\gamma_c); \\ 0 & \text{otherwise.} \end{cases} \tag{3.7}$$

where the trajectory is discretised and $\mathbf{v}_i^I(t_k)$ depicts the pointing at the k-th node. Essentially, the magnitude of J_{OA} in Eq. (3.7) is directly proportional to the closest distance to the center of the cone when the trajectory path crosses it. Therefore, during the optimization, the path "slides down" and out of the keep-out area. When the path of the axis is tangent or anywhere outside the keep-out area, the penalty is constant at zero—deactivating the obstacle avoidance optimisation process.

The obstacle avoidance penalty function can be included in the two-layer optimization for finding the minimum time described in Section 3.1.1. As soon as the path crosses a keep-out area, the obstacle avoidance algorithm is activated and time minimization is not considered, until the penalty index J_{OA} becomes zero. The flow chart of the algorithm of time optimization with pointing constraints is shown in Figure 3.13. The torque constraints are embedded in the inner loop (the root-finding process described in the previous section), which are used to find the minimum t_f for every iterated combination of free coefficients. This t_f becomes the performance index when obstacle avoidance is not activated ($J_{OA} = 0$). An interesting property of rest-to-rest manoeuvres, for some given values of free coefficients, is that the axes' paths remain unchanged when varying the manoeuvre time t_f. Therefore, in the obstacle avoidance part of the algorithm, the final time can be adimensionalised.

Figure 3.14 shows the path of the pointing axis (black line), using an additional term on the polynomials ($k = 1$ in Eq. (2.5))—thus, four free variables are in-

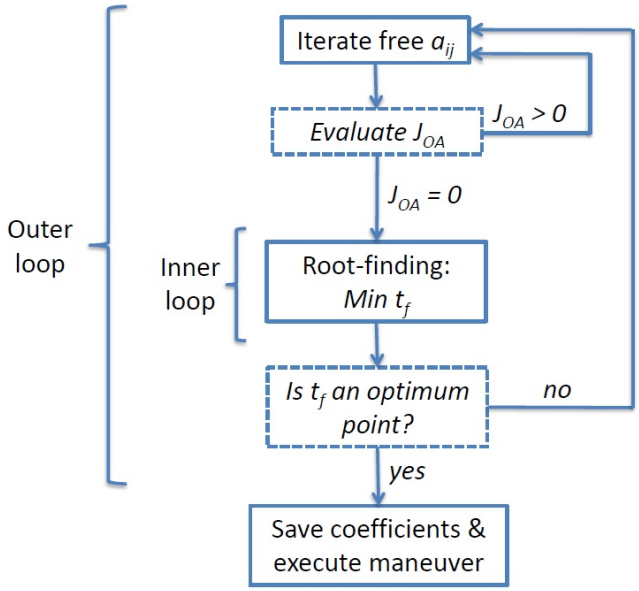

Figure 3.13: Two-layer time optimization algorithm with obstacle avoidance

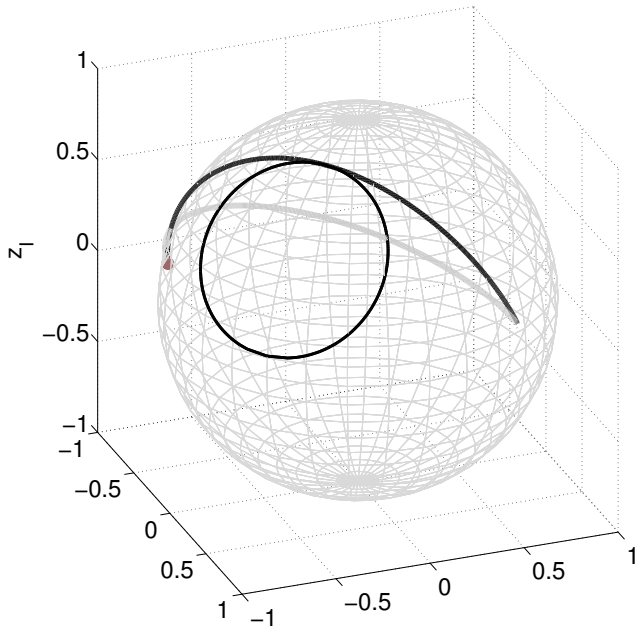

Figure 3.14: Paths of the pointing body axis on the unit sphere and keep-out circle, for the nominal trajectory (grey line) and the diverted one (black line)

cluded. The grey line shows an initial-guess trajectory (minimum polynomial degree for matching boundary conditions) which does not satisfy the path constraint. While the obstacle avoidance algorithm forces the path out of the cone,

in this case the one featuring the minimum time happens to cross the keep-out area, making the optimizer converge to a path tangent to the circle (i.e. the minimum-time trajectory satisfying the pointing constraint).

Again, manoeuvres with arbitrary endpoint velocities, the variable t_f affects the path, thus the time-minimisation and the obstacle avoidance problems are coupled. The two-layer approach can still be used, but in this case the actual t_f must be considered in the outer layer (where path constraints are checked).

3.3 Minimisation of reaction wheels momentum storage

Via inverse dynamics it is possible to obtain, apart from the torque profile of the manoeuvre, the evolution of the reaction wheels' speed. This could be necessary in spacecraft with limited resources, where reaction wheels can become easily saturated if they are small (relative to the spacecraft's moments of inertia). Most spacecraft equip reaction wheels since they are the most precise type of actuators, and are simpler and lighter than control moment gyros (CMG). Unlike CMGs, however, they build up speed which needs to be unloaded or desaturated. Usually, they are unloaded with magnetorquers (when in LEO) or with a Reaction Control System (RCS), in which case manoeuvring with reaction wheels is not exactly propellant-less.

However, since the momentum stored in the reaction wheels can be predicted via inverse dynamics, it is possible to optimise the trajectory so that the wheels speed at the end of the manoeuvre is minimum or, ideally, zero. The momentum stored in the wheels can be estimated with

$$\mathbf{h}_r(t_f) = \int_0^{t_f} \mathbf{u}\, dt + \mathbf{h}_r(0) \tag{3.8}$$

where $\mathbf{u}$ is the predicted torque and $\mathbf{h}_r(0)$ is the initial angular momentum of the wheels. The torque is computed numerically, thus it is straightforward to numerically integrate Eq. 3.8.

The goal is to minimise $\mathbf{h}_r(t_f)$. To this end, the degree of the polynomials shaping the quaternions is increased by one in order to use the free coefficients to re-shape the path. In rest-to-rest trajectories, the path and the final time are decoupled.

Thus, as happens with torque, the wheels' momentum tends to zero as time tends to infinite. In order to avoid arbitrarily large manoeuvre durations, a multi-objective optimisation is necessary where the performance index is a weighted sum of the momentum and the final time, as:

$$J_r = k_r \mathbf{h}_r(t_f)^T \mathbf{h}_r(t_f) + t_f \tag{3.9}$$

where k_r is a weighting factor.

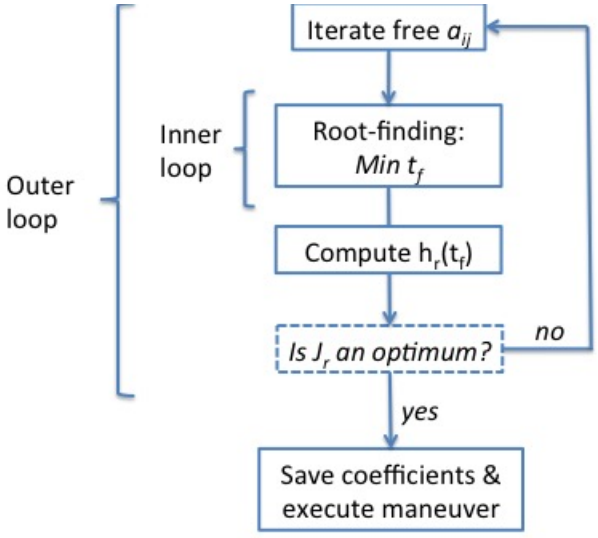

Figure 3.15: Two-layer time optimization algorithm with reaction wheels momentum

A two-layer optimisation algorithm is implemented (Fig. 3.15), where the inner loop finds the minimum-time trajectory (via root-finding) and the outer loop searches the free coefficients to minimise the final momentum. In other words, the minimum momentum trajectory will also have the minimum time possible for that path (t_f in Eq. 3.9). This approach is robust since the search of the free coefficients space is based on pure unconstrained optimisation. Since feasibility is controlled by selecting an appropriate t_f in the inner loop, every iteration of the free coefficients results in a feasible trajectory. If pointing constraints are present, this algorithm can be merged with obstacle avoidance (Fig. 3.13). A heuristic simplex-based optimisation methods has been used, yielding better results than gradient-based methods at the expense of higher computation times (although they are below one second, in a desktop computer using *Matlab*).

Figure 3.16 shows a minimum-time baseline manoeuvre planned with polynomials of degree 7, the minimum required to match boundary conditions. The spacecraft

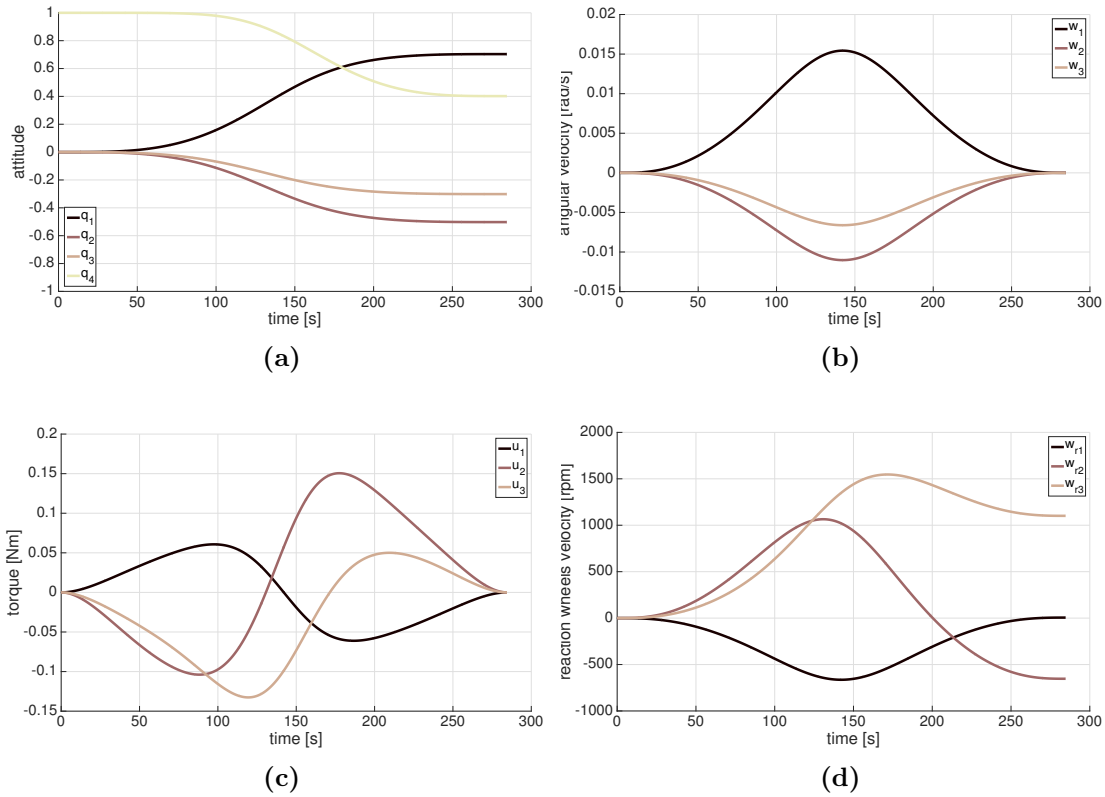

Figure 3.16: $7^{th}t$-degree polynomial baseline manoeuvre

model is based on a 2000-kg body with solar panels, equipped with reaction wheels limited to 0.15 Nm, 6000 rpm, and a moment of inertia of 0.07 kgm^2. In Fig. 3.16d, the maximum final speed of the wheels is over 1000 rpm. In contrast, Fig. 3.17 shows a maneouvre planned with $8^{th}t$-degree polynomials, whose degrees of freedom are used to minimise the reaction wheels final momentum or speed. In this case, more weight is placed on the wheels momentum term in Eq. 3.9. Note that the final speed of the reaction wheels in the optimised case is almost zero. However, the manoeuvre time ($t_f = 434$ s) is significantly larger than the baseline manoeuvre ($t_f = 284$ s). While the wheels momentum is minimised and the constraints are satisfied, the spacecraft undertakes a seemingly chaotic path (Fig. 3.18).

A compromise between final wheels speed and final time can be achieved by balancing the weight in the performance index (Eq. 3.9). Results in Fig. 3.19 show a significant decrease in the manoeuvre time ($t_f = 326$ s) while keeping the wheels final momentum to relatively small values. Finally, Fig. 3.20 shows a minimum-time trajectory amongst the set of $8^{th}t$-degree polynomial trajectories,

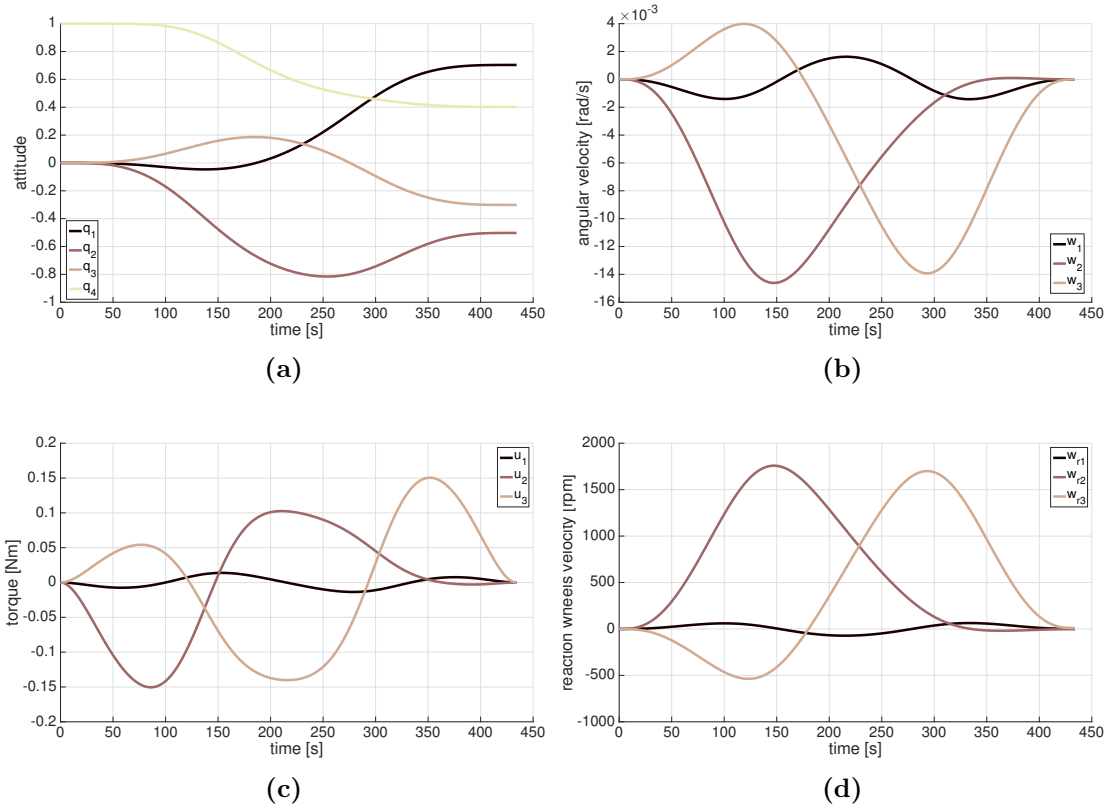

Figure 3.17: Minimum final wheels momentum trajectory planned with $8^{th}t$-degree polynomials

i.e. setting $k = 0$ in Eq. 3.9. The manoeuvre duration is $t_f = 220$ s, but the final wheels speed is much larger, of the same order of magnitude than the baseline manoeuvre.

In conclusion, using motion planning enables feasible and optimal manoeuvring with reaction wheels, providing a range of benefits to spacecraft and driving new designs. Firstly, ensuring that the manoeuvre will not saturate the wheels, gives confidence that the spacecraft will not lose control capacity even if those wheels are small (which is not guaranteed if classical feedback control is used). This enables a smaller margin in the reaction wheels capability, saving cost and mass budget that can be allocated to payload. Secondly, minimising the final momentum storage (i.e. the final wheels speed) could make using reaction wheels almost propellant-less in slew manoeuvring, since there is no need for substantial desaturation. For those reasons, using this motion planning approach reaction wheels can effectively replace CMGs or the RCS in its usual job of performing the slew manoeuvres, saving fuel or augmenting the capabilities of nanospacecraft (e.g.

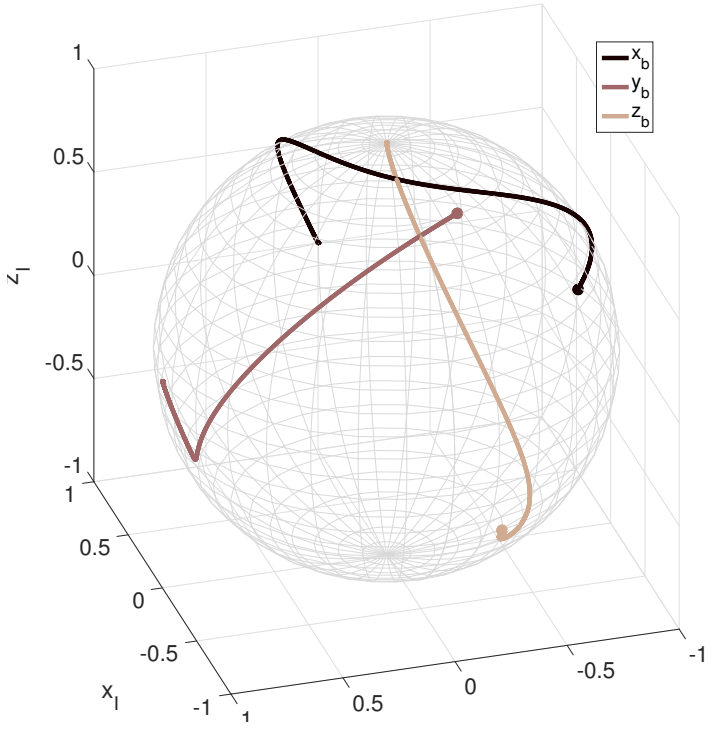

Figure 3.18: Axes path of minimum final wheels momentum trajectory

cubesats) which cannot accommodate an RCS. Additionally, unlike thrusters of a certain size, reaction wheels are capable of precise and very smooth torque profiles. Finally, a zero-propellant manoeuvre (ZPM) was realised as an experiment in the ISS, using pseudospectral optimal control and CMGs as the actuators [79] and taking into account a high fidelity dynamic model. In contrast, the motion planning approach presented is computationally more efficient, thus this type of ZPM manoeuvres can be computed on-board in a regular basis.

3.4 Performance comparison with an optimal control solver

Using polynomials to shape the trajectories yields suboptimal results, in terms of torque and time. Thus, it is worth comparing the results of this method with those of a pseudospectral optimal control solver (PSOPT). Using a direct transcription method for optimal control, close-to-optimal solutions can be obtained.

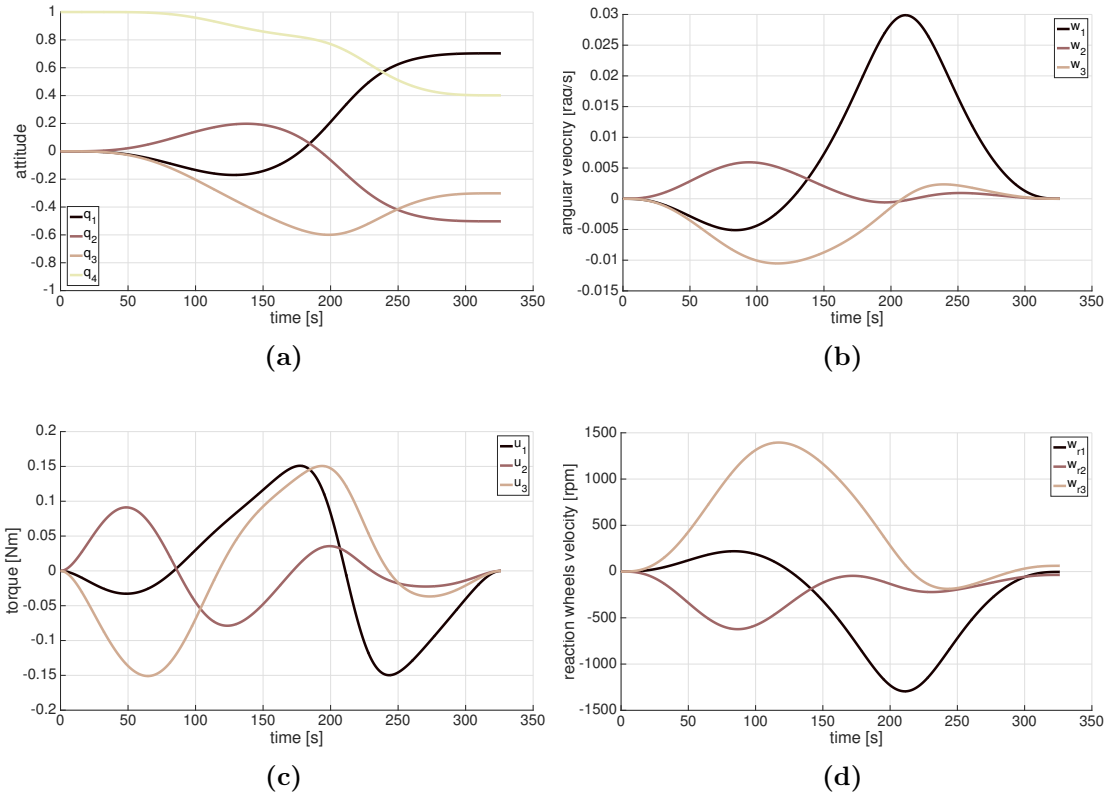

Figure 3.19: Balanced final wheels momentum - time trajectory planned with $8^{th}t$-degree polynomials

3.4.1 Rest-to-Rest manoeuvres

The trajectory of a baseline rest-to-rest manoeuvre has been planned with a fixed final time. In PSOPT, the same final time has been given and the following cost function has been considered:

$$J = \int_0^{t_f} \mathbf{u}^T \mathbf{u} \, dt \tag{3.10}$$

which is a measure of the energy spent on the manoeuvre.

Figure 3.21 shows a fixed manoeuvre time comparing both methods. The axes path is similar in both cases. The angular velocity obtained with the polynomial method is symmetric, accelerating the first half of the trajectory (almost linearly) and decelerating the second half. The optimal control solution, however, has a less symmetric profile since it accounts for the moments of inertia of the spacecraft.

While the time of the trajectory is fixed, the cost as in Eq. 3.10 is 60% higher with the polynomial method than with PSOPT. The cost of other random manoeuvres

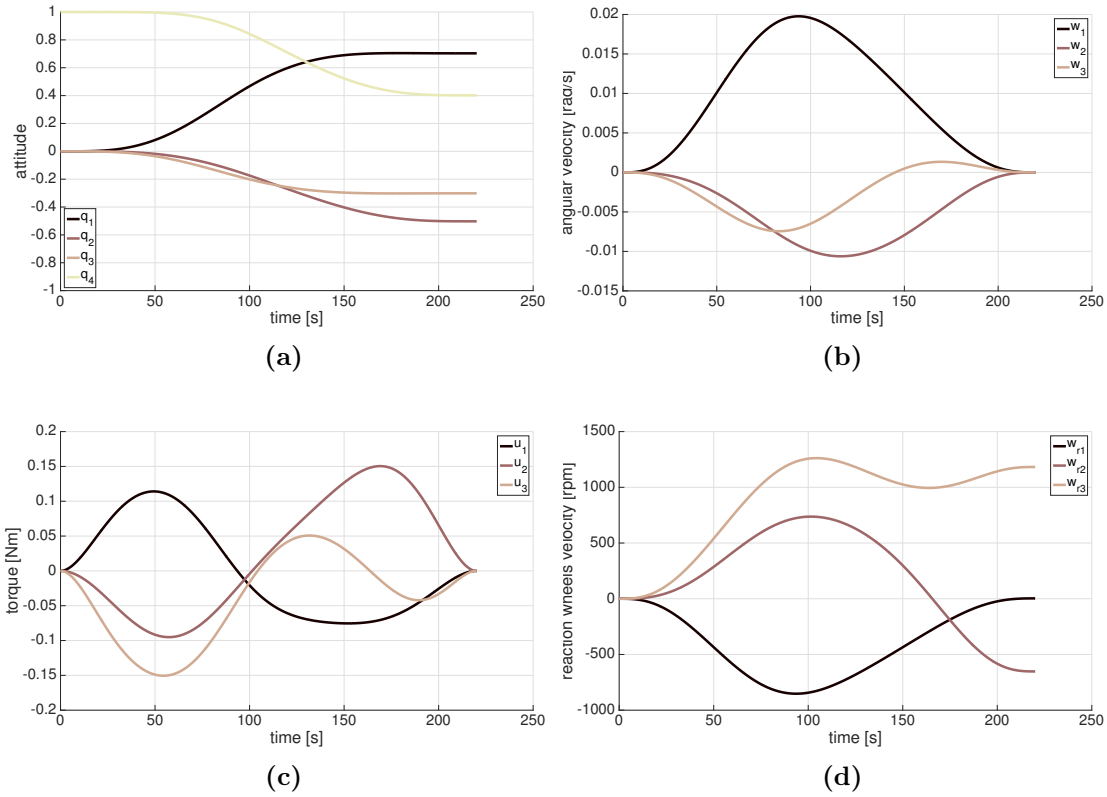

Figure 3.20: Minimum final time trajectory planned with $8^{th}t$-degree polynomials

fall within this order of magnitude.

3.4.2 Single axis rotation

An interesting result arises when simulating a rotational manoeuvre about one of the spacecraft's axes. In this case, as shown in Fig. 3.22, the trajectory is very similar, and the cost of the polynomial trajectory in terms of energy is higher only by 13%.

These results suggest that, in a single-axis basis, the class of polynomial trajectories naturally provide solutions with a relatively low energy cost, considering that no optimisation of this cost function has been undertaken.

3.4.3 Time-optimal manoeuvres

Figure 3.23 depicts a manoeuvre where time is minimised. As expected, the optimal control solution is of bang-bang type. The shape of the polynomial

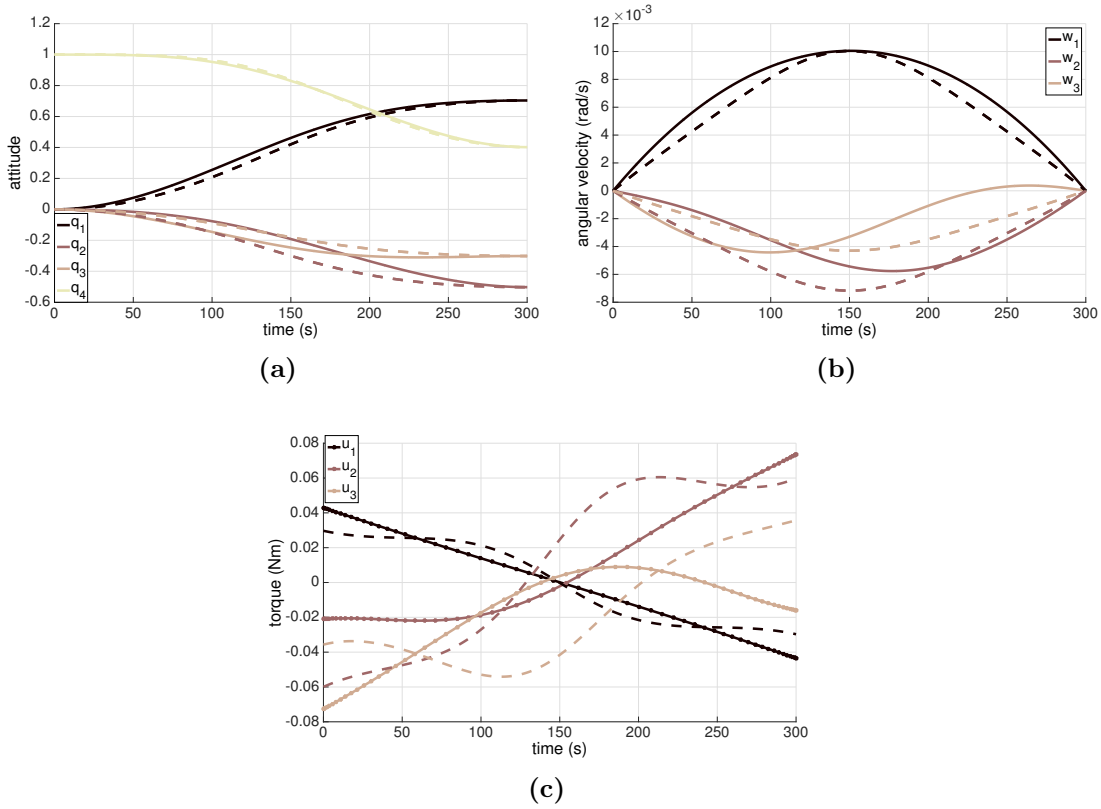

Figure 3.21: Fixed-time, minimum energy trajectory. Solid/marked lines: PSOPT, dashed lines: 3^{th}-degree polynomial

trajectory is essentially the same as in the fixed-time case, but the maximum torque is allowed to be equal to the actuators' limit (Section 3.1), in this case of 0.15 Nm. PSOPT is shown to improve the manoeuvre time by 19%, but the energy cost is increased by a factor of two with respect to the polynomial solution. Therefore, the polynomial method yields trajectories with a final time relatively close to the optimal solution, while maintaining the energy efficiency.

There exist paths that have a lower final time, which can be explored by polynomials with additional terms, using the two-layer algorithm described in Section 3.1.1.

Figure 3.24 shows a minimum-time trajectory planned with a 4^{th}-degree polynomial. The last term of each polynomial is not required to match the boundary conditions, instead it gives a degree of freedom to the optimisation (resulting in four free coefficients, one per quaternion). The final time obtained is 179.8 s, lower than the manoeuvre planned with a 3^{rd}-degree polynomial (190.5 s), but higher than the optimal value of 160 s given by PSOPT, although the latter

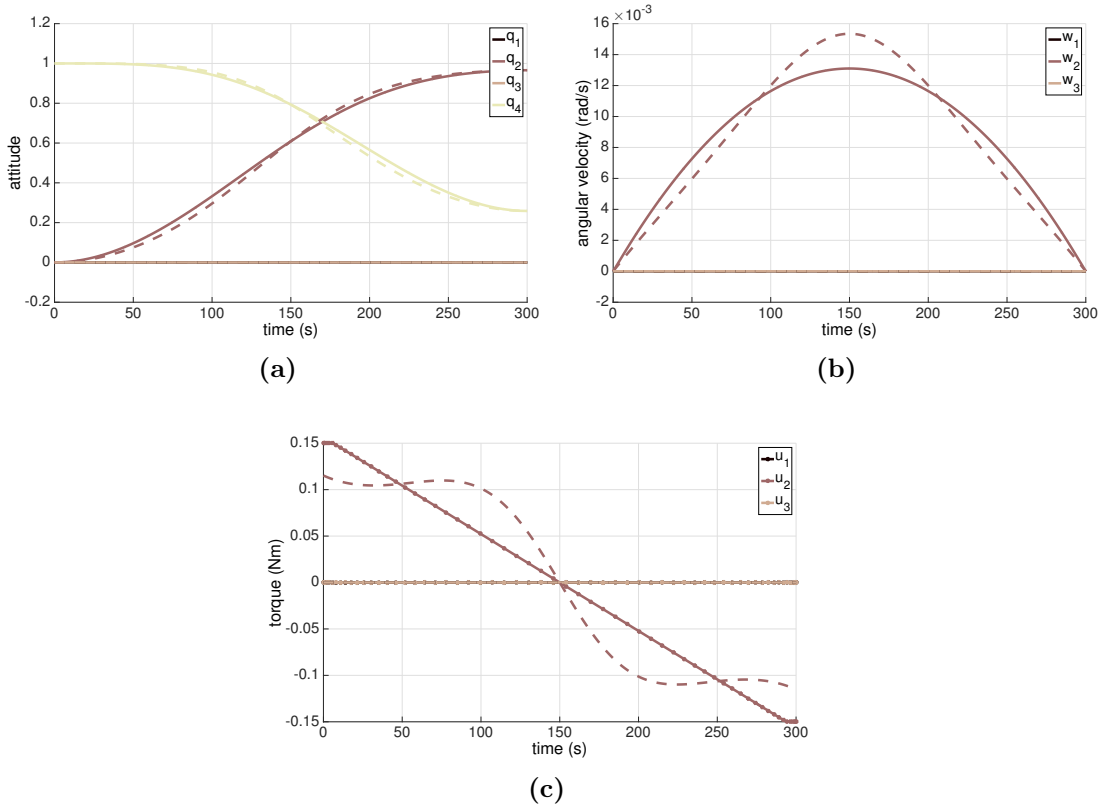

Figure 3.22: Fixed-time, minimum energy trajectory about the y-axis. Solid/marked lines: PSOPT, dashed lines: 3^{th}-degree polynomial

method can take tens to hundreds of seconds to compute. A further increase in the polynomial degree would improve the final time in an asymptotic way—a polynomial of infinite degree would match the result of the optimal control solver. However, an increasing amount of degrees of freedom makes the problem more difficult to converge, therefore, a trade-off must be considered. This is shown in Fig. 3.25, where the same arbitrary manoeuvre was computed with polynomials of 4^{th}, 5^{th}, 6^{th}, and 7^{th} degree, each adding four extra free coefficients as optimisation variables. The optimisation was run in a laptop with Matlab® and a heuristic algorithm. Results were averaged over five runs for each polynomial degree.

3.5 Comparison of attitude representations

A polynomial of infinite degree—hence with infinite DOF—can shape any trajectory using any type of attitude representation. However, using a minimum

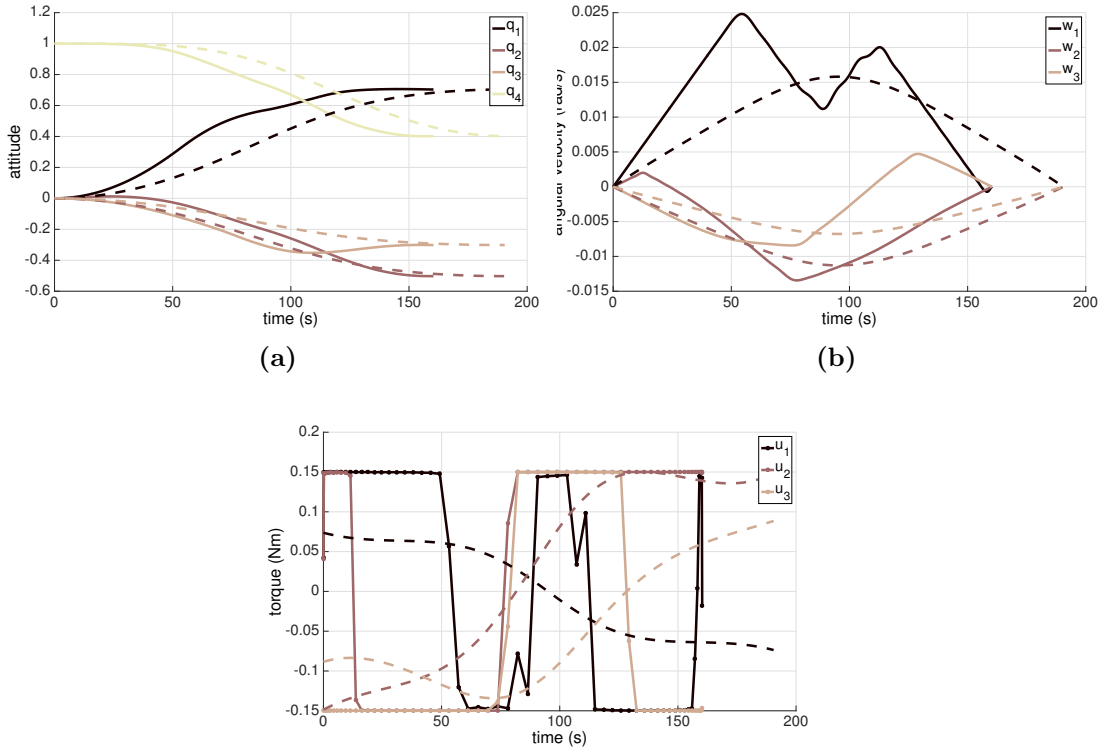

Figure 3.23: Minimum-time trajectory. Solid/marked lines: PSOPT, dashed lines: 3^{th}-degree polynomial

order polynomial (matching boundary conditions only) or one with few degrees of freedom, the choice of attitude representation matters in the shaping of the trajectory. This section focuses on how quaternions, Euler angles, and Modified Rodrigues Parameters (MRP) compare when planning the same arbitrary rest-to-rest and move-to-move manoeuvres with 3^{rd}-degree polynomials, the performance index being the final time.

Quaternions are the preferred choice of attitude parameters in spacecraft for their globality (lack of singularities) and computational efficiency (the attitude matrix has no trigonometric functions; although this benefit might be reminiscent of the time when spacecraft processors were seriously limited). Euler angles have 90-degree singularities, hence although visually intuitive they are unfit for spacecraft manoeuvres. Modified Rodrigues Parameters are attractive for control because although it has a singularity, at 360 degrees it is far away from the origin.

Different spacecraft have been considered for the rest-to-rest and the move-to-move manoeuvres. A summary of the resulting manoeuvre times for all cases can

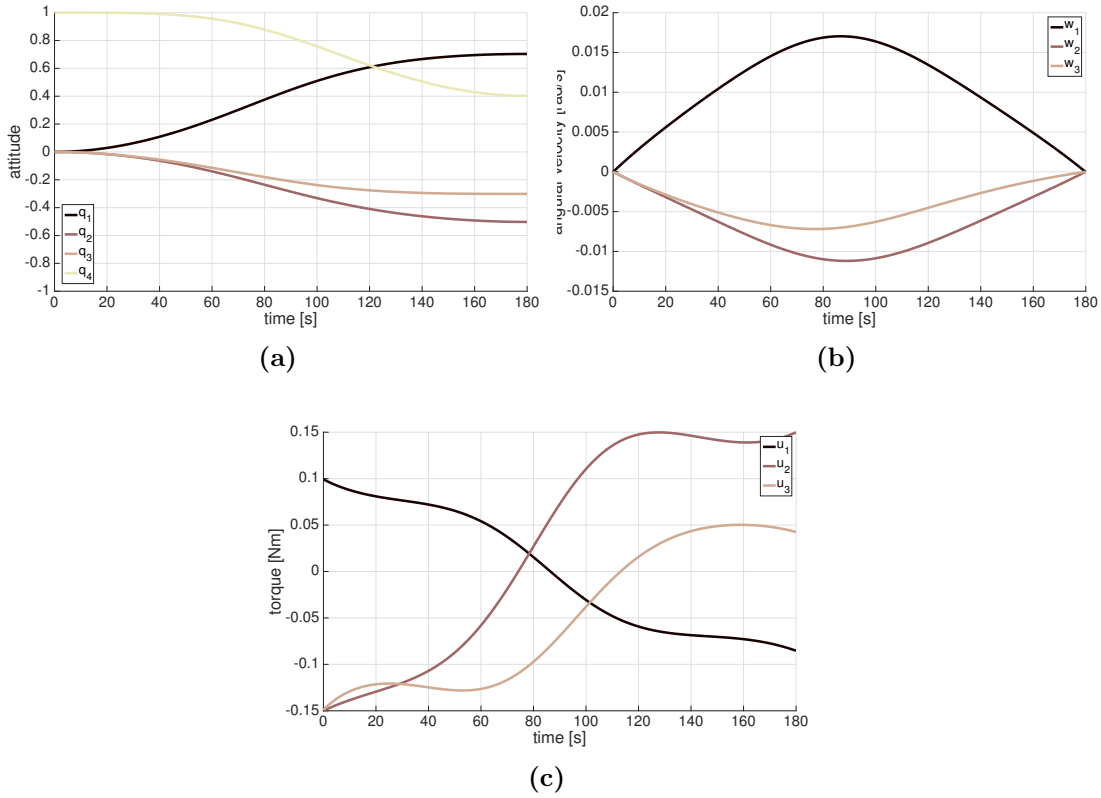

Figure 3.24: Minimum-time trajectory, planned with one degree of freedom in a 4^{th}-degree polynomial (per quaternion)

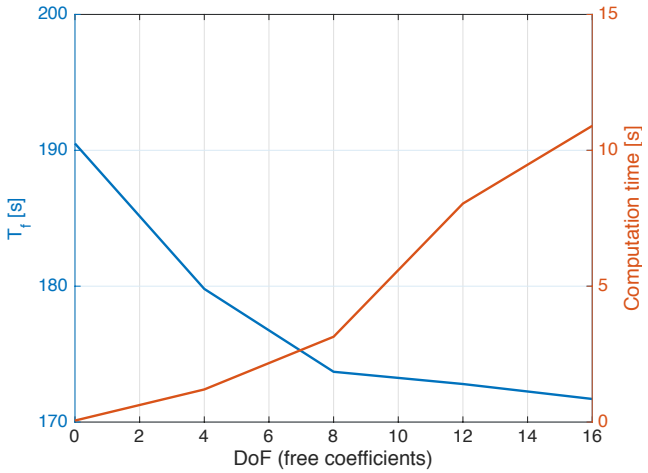

Figure 3.25: Evolution of the optimisation solution (final time) and computational time as a function of the trajectory's degrees of freedom (base polynomial is of degree 3)

	Rest-to-rest	Move-to-move
Quaternions	203.6	24.5
MRP	205.2	25.3
Euler angles (z-x-y)	226.5	25.9
Euler angles (z-y-x)	326.5	unfeasible
Euler angles (shifted frame)	199.2	28.4

Table 3.1: Minimum manoeuvre times (seconds) for different representations

be found in Table 3.1.

3.5.1 Rest-to-rest case

In the rest-to-rest case a torque limit of 0.15 Nm and an inertia matrix $\mathbf{I} = \text{diag}(316, 894, 887)$ kgm^2 have been considered.

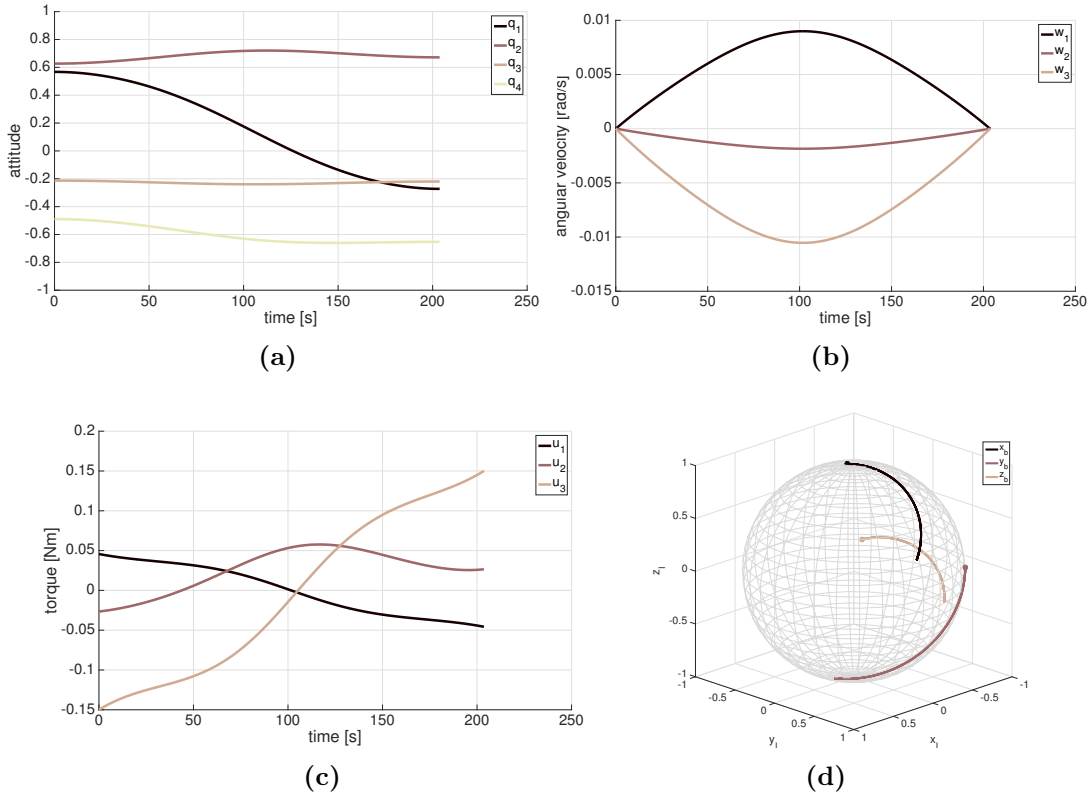

Figure 3.26: Minimum-time rest-to-rest manoeuvre planned with quaternions

Figures 3.26 and 3.27 show trajectories planned with quaternions and MRP. The body axes paths are very similar, although the velocity and torque profiles are

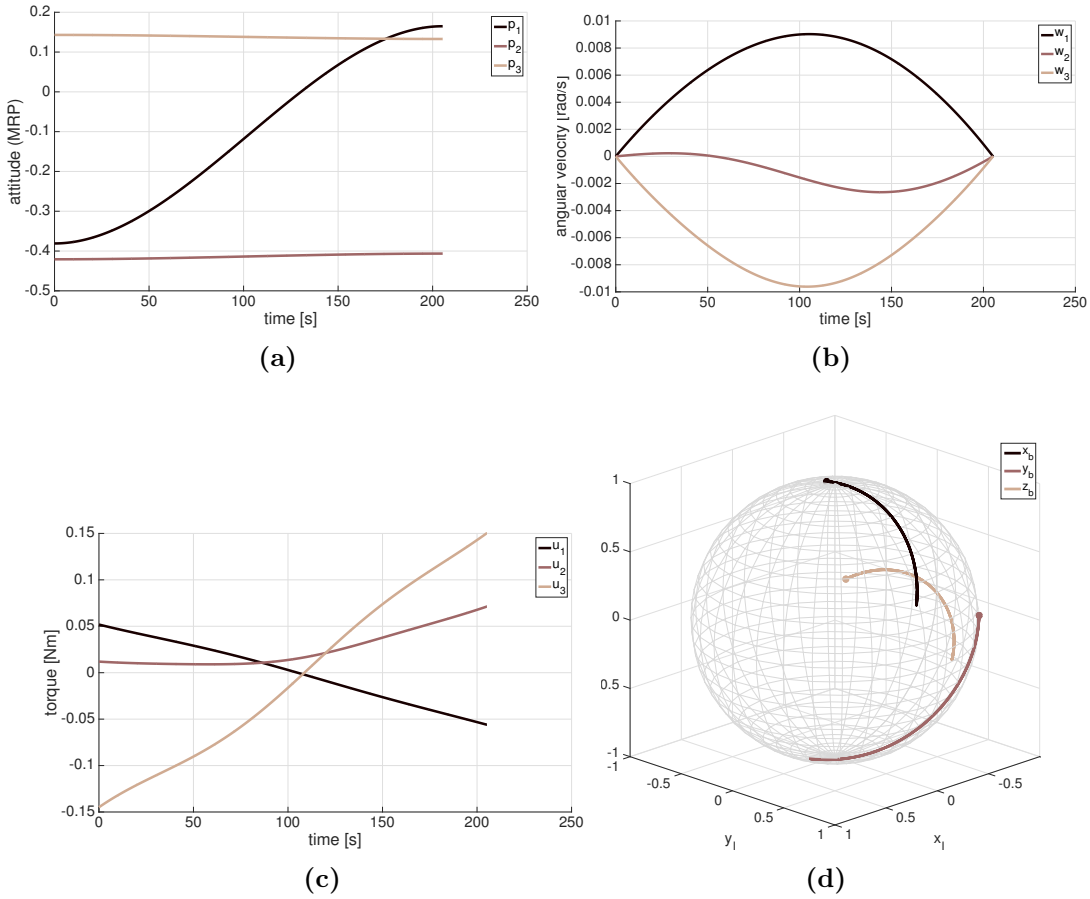

Figure 3.27: Minimum-time rest-to-rest manoeuvre planned with MRP

slightly different, leading to different minimum times of 203.6 s and 205.2 s respectively. The similarity in the manoeuvre is not surprising since MRP and quaternions are both derived from the Euler axis-angle representation. However, the initial and final MRP values must be adjusted to prevent large winding:

$$\mathbf{p}_{0,f} = \frac{\mathbf{p}_{0,f}}{\|\mathbf{p}_{0,f}\|^2} \quad \text{if } \|\mathbf{p}_{0,f}\| > 1 \tag{3.11}$$

For the special case of rest-to-rest manoeuvres planned with quaternions and shaped by polynomials with no degrees of freedom, the resulting trajectory is an eigenaxis rotation. However, a trajectory shaped with MRP is not.

Figure 3.28 shows a trajectory shaped with Euler angles. With a minimum time of 226.5 s, the trajectory is slower than its quaternions and MRP counterparts. Euler angles are not unique, being able to represent the same attitude with twelve different sequences of rotations. Figure 3.29 shows the manoeuvre shaped with

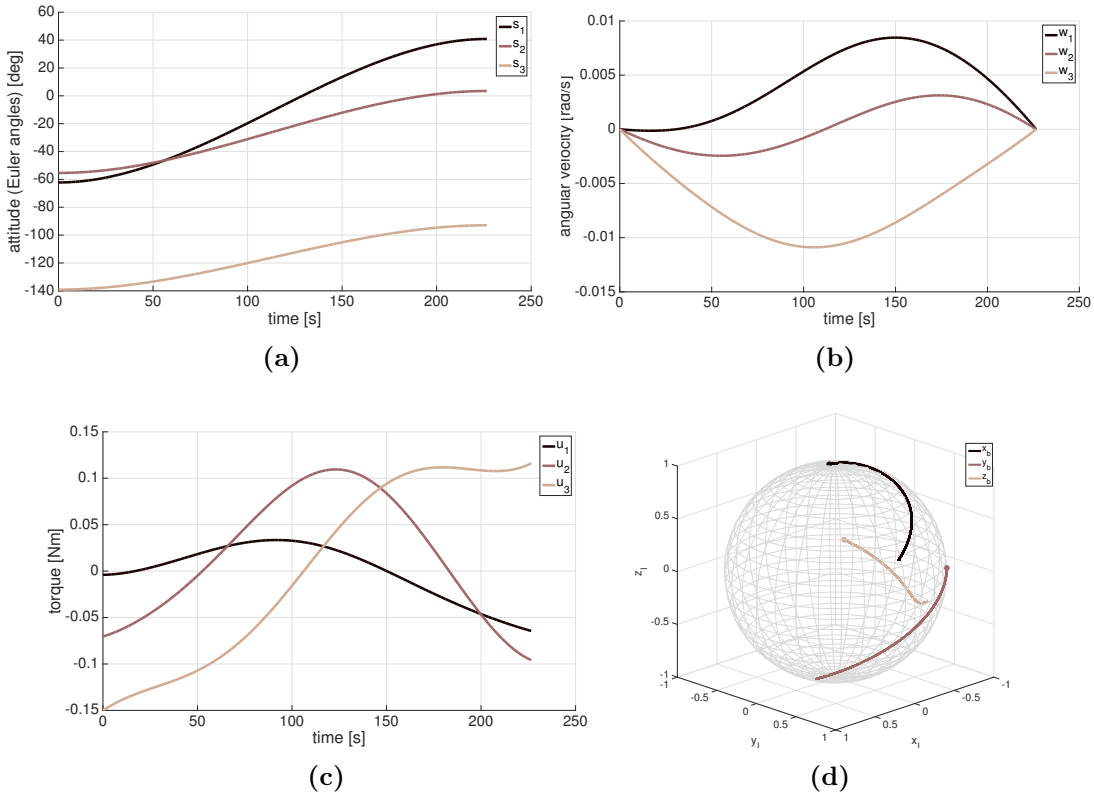

Figure 3.28: Minimum-time rest-to-rest manoeuvre planned with Euler angles (z-x-y)

another combination of Euler angles, resulting in a different trajectory with a minimum time of 326.5 s, longer than the previous case due to a larger path. Also, unwinding can be prevented by measuring the difference between the initial and final angles and adjusting them accordingly, which can be done with a simple algorithm.

An axis-azimuth type of representation (as the one used in the spin-to-spin case) can improve the rest-to-rest trajectories of asymmetric body. The torque resources of a spacecraft can be used most efficiently if the path of the minor axis of inertia is minimum (i.e. a great-circle on the sphere), since reorienting this axis implies applying torques about the other axes which have larger moments of inertia. In this scenario, the minor axis would slew following a great-circle while the other two would rotate about it until the final attitude is reached. To achieve this behaviour, Euler angles can be used with an appropriate reference frame.

Figure 3.30 shows a reference frame or inertial frame where the $\hat{\mathbf{z}}_I$ vector defines a plane where both body axes $\hat{\mathbf{x}}_0$ and $\hat{\mathbf{x}}_f$ lie in, and $\hat{\mathbf{x}}$ depicts the minor axis of

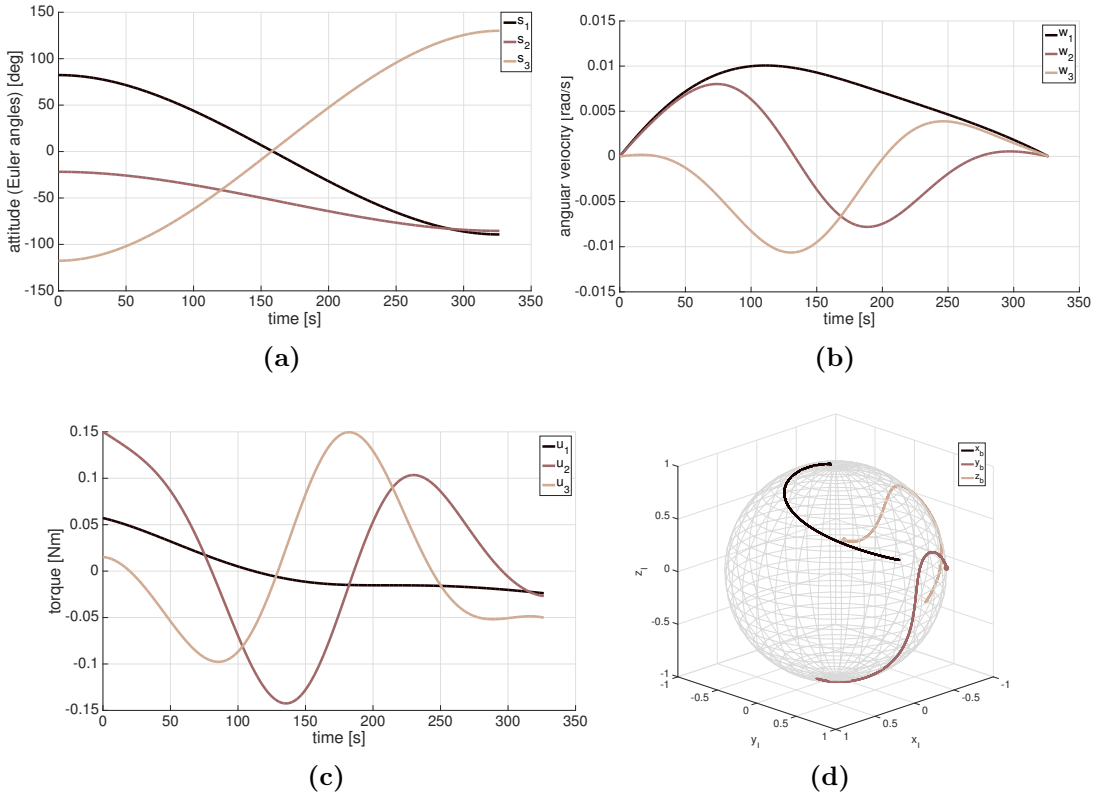

Figure 3.29: Minimum-time rest-to-rest manoeuvre planned with Euler angles (z-y-x)

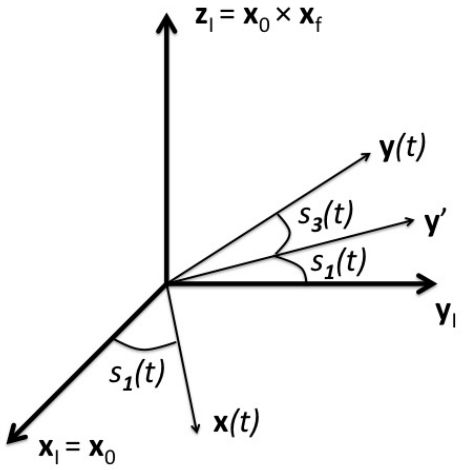

Figure 3.30: Schematics of Euler angles (z-y-x) with shifted reference frame

inertia of the spacecraft. Overall, the new frame is defined by

$$R_I = [\hat{\mathbf{x}}_0 \;\; (\hat{\mathbf{z}}_I \times \hat{\mathbf{x}}_0) \;\; (\hat{\mathbf{x}}_0 \times \hat{\mathbf{x}}_f)] \tag{3.12}$$

The endpoint attitudes (defined as rotation matrices) resolved in the new frame are

$$\begin{aligned} R_0^* &= R_I^T R_0 \\ R_f^* &= R_I^T R_f \end{aligned} \tag{3.13}$$

which can be converted back to Euler angles. If the Euler angles sequence is z-y-x and the angles about them are s_1-s_2-s_3, the new endpoint angles about y are $s_{02} = 0$ and $s_{f2} = 0$. When shaping $s_2(t)$ with a polynomial and those boundaries, the result is constant at zero, meaning that $\hat{\mathbf{x}}(t)$ goes along a great-circle whose position on it is defined by $s_1(t)$. Figure 3.31 shows the resulting trajectory, which obtains the shortest time of 199.2 s.

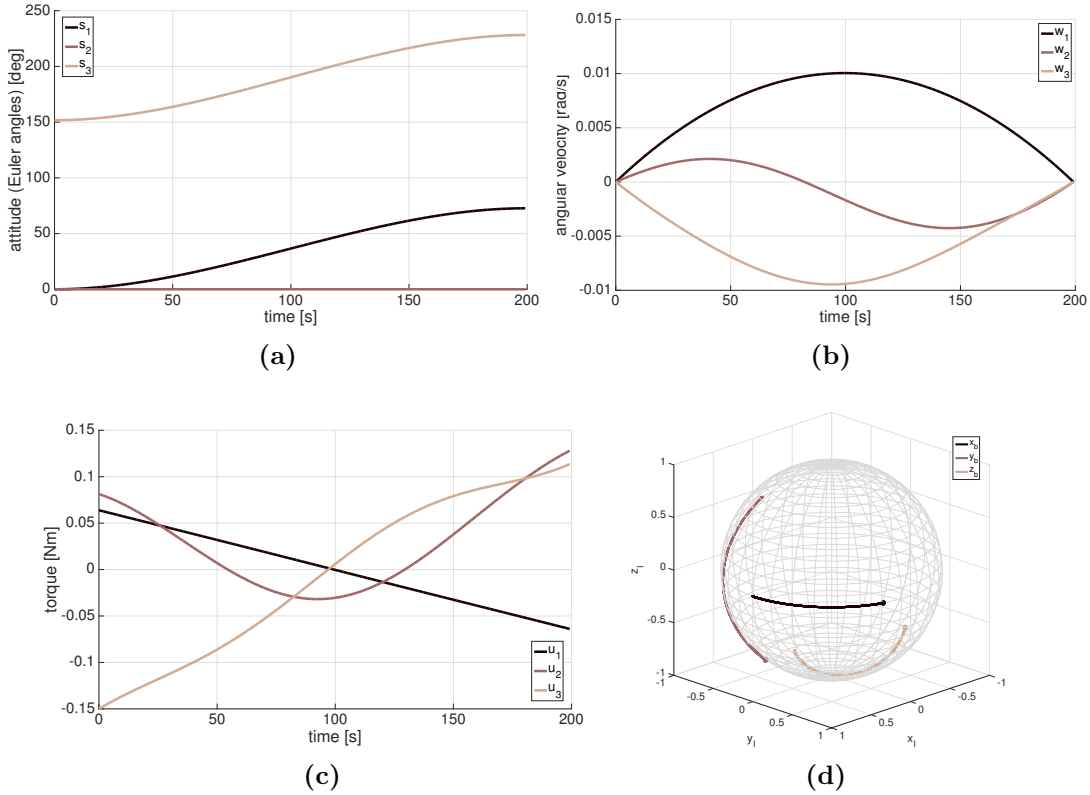

Figure 3.31: Minimum-time rest-to-rest manoeuvre planned with Euler angles and change of reference frame

3.5.2 Move-to-move case

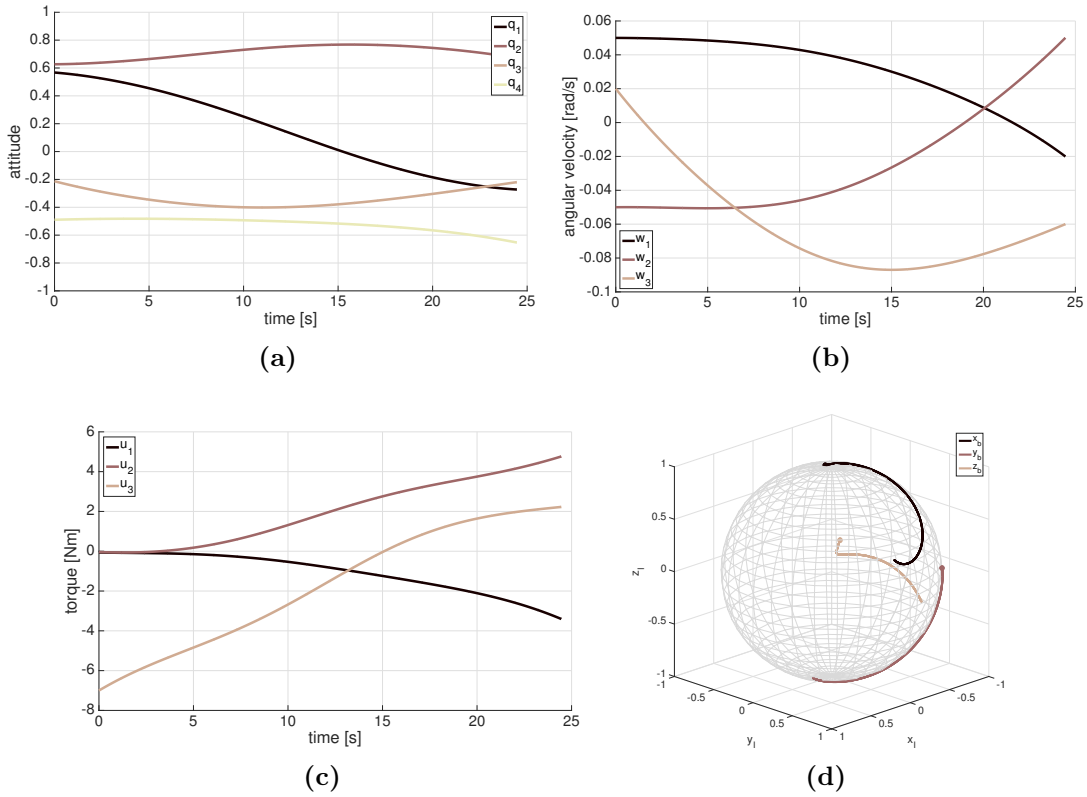

Figure 3.32: Minimum-time move-to-move manoeuvre planned with quaternions

Figures 3.32, 3.33, and 3.34 show the manoeuvre with arbitrary boundary velocities. In these simulations an agile satellite has been considered with a torque limit of 7 Nm and moments of inertia $\mathbf{I} = \text{diag}(400, 450, 500)$ kgm^2. There are no significant differences between the three types of representations, with the notable exception of the z-y-x rotation sequence of Euler angles. In this case, the final angles are close to cause a singularity when applying the kinematic equations, resulting in large values of the angles' time derivatives at the endpoint. This results in an empty set of feasible trajectories, which can be visualised by the torque peak-based cost structure (Fig. 3.35).

The strategy of defining a new reference frame described in the previous section is not useful for move-to-move manoeuvres, since the minor axis does not follow a great-circle in an arbitrary case ($t_f = 28.4$ s). Note that a feasible trajectory was found in this case even if a z-y-x combination was used, thus changing the reference frame can be considered to avoid singularities in Euler angles as well as changing the rotation sequence.

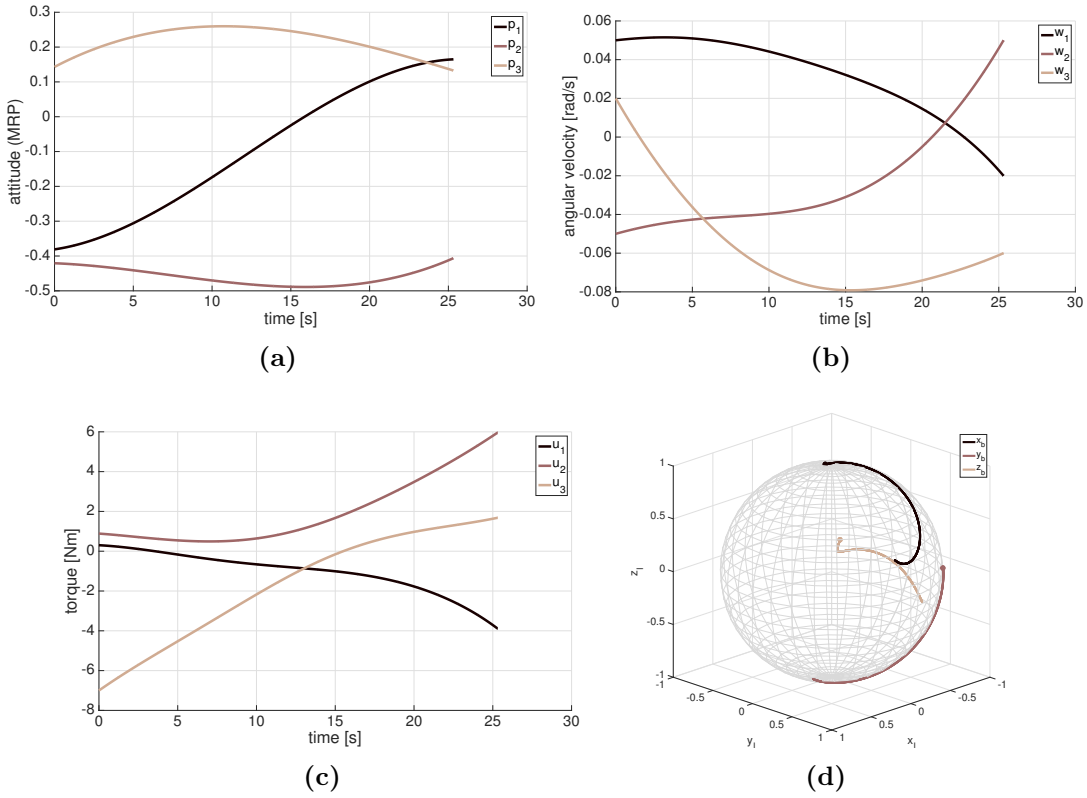

Figure 3.33: Minimum-time move-to-move manoeuvre planned with MRP

3.6 Chapter summary

Trajectory optimisation with polynomial motion planning has been addressed. In regards of time minimisation, the torque peak, which is related to the selected manoeuvre time, drives the minimum time that can be chosen. With this information, the minimum time is used with a very efficient root-finding method instead of a constrained optimisation algorithm. It has been found that trajectories generated shaping quaternions yield better results than shaping Euler angles. An optimisation algorithm that combines the root-finding method with the search of free coefficients of higher order polynomials is presented. Additionally, an analytical method for estimating the minimum time, using pre-computed analysis, is presented for the rest-to-rest and spin-to-spin cases.

Obstacle avoidance is addressed, which can be achieved with two alternative methods: a more efficient waypoint-based approach, or a more versatile unconstrained optimisation approach (with penalty functions). Yet, unconstrained optimisation algorithms tend to be more efficient than constrained methods.

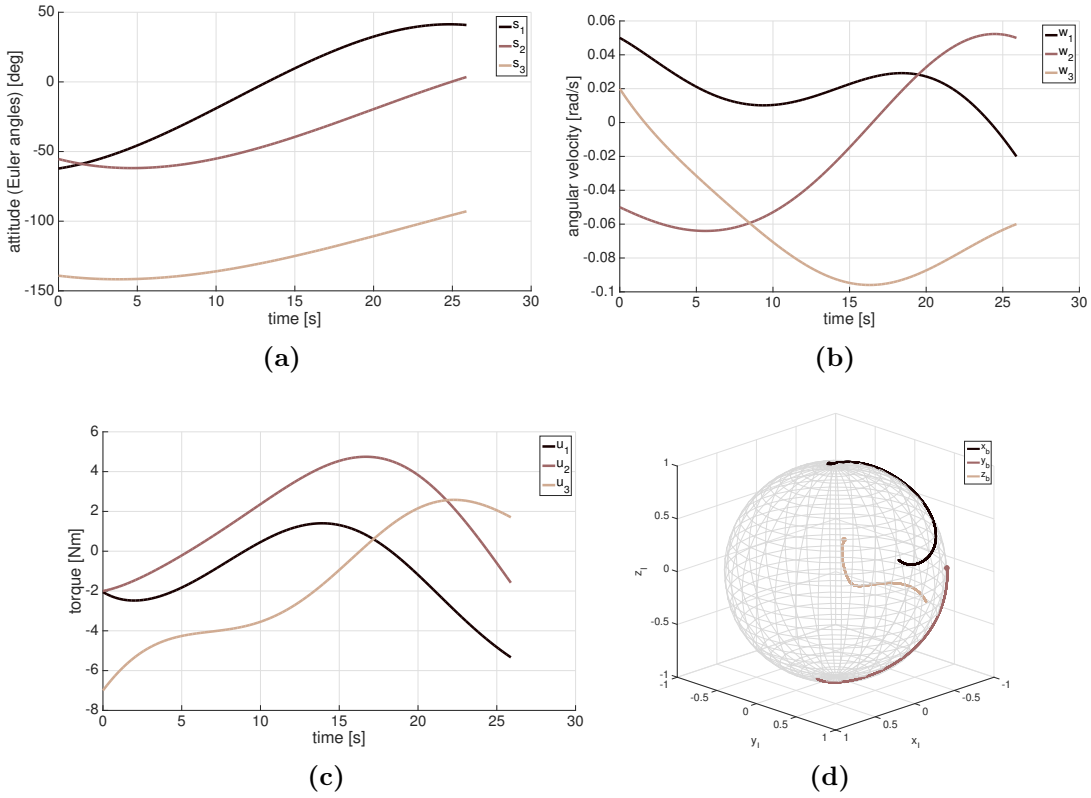

Figure 3.34: Minimum-time move-to-move manoeuvre planned with Euler angles (z-x-y)

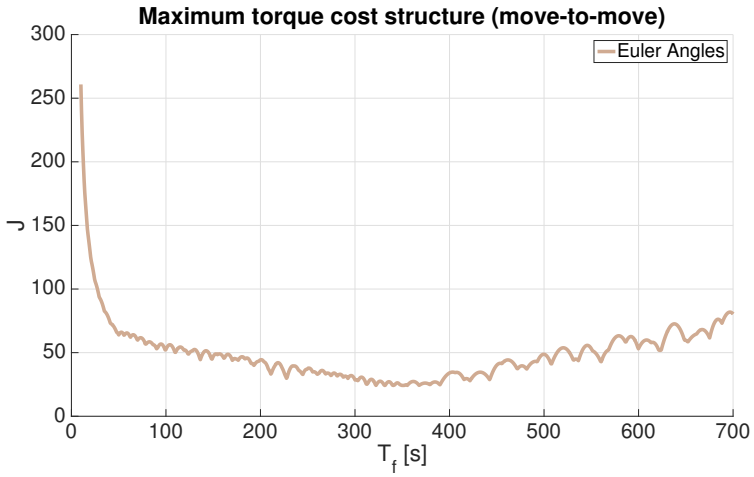

Figure 3.35: Evolution of J (maximum torque over the limit) with manoeuvre time, for an arbitrary move-to-move manoeuvre shaped with Euler angles (z-y-x)

While time optimisation and obstacle avoidance are commonly studied problems, the minimisation of the reaction wheels speed after the manoeuvre is discussed

here. It can be achieved with the motion planning method and inverse dynamics (requiring a numerical integration), and it can reduce the need of unloading the wheels if they are used for slew manoeuvres, saving time and/or fuel.

The optimality of the trajectories generated by the polynomial planning method, particularly with low-degree polynomials, is assessed by comparing it with an optimal control solver. If an energy-based performance index is used in the optimal control solver, the trajectories are rather similar, considering that the lowest-degree polynomial trajectory is obtained analytically. In time-optimal manoeuvres, the optimal control solver has the advantage of producing bang-bang trajectories, but with only an extra term in the polynomial, the final time is only worse by less than 15% (and the torque profile is smooth).

Finally, how different attitude representations behave in generating minimum-time trajectories is studied. Quaternions are shown to fare better than MRPs and Euler angles (besides their lack of singularities), but shifting the reference frame can make Euler angles perform similarly.

In conclusion, planning trajectories using single polynomials to shape quaternions is computationally very efficient with the optimisation strategies presented, while retaining features such as time minimisation and obstacle avoidance. When the polynomial method is compared to optimal control, the latter still produces better solutions. However, the performance index of both is within the same order of magnitude, while the computational expense of optimal control can be orders of magnitude higher.

In the next chapter, the polynomial motion planning method is used with Cartesian coordinates to generate translational trajectories.

Chapter 4

Uncooperative docking of a tumbling target using polynomial motion planning

In this chapter, the polynomial motion planning method is applied to the problem of docking onto a tumbling target. Most aspects referring the method itself (such as limiting numerical stability via scaling, additional DOF with higher-degree polynomials, etc.) have been addressed in the previous chapters on attitude manoeuvres, thus are not overly re-explained here.

The scenario is based on a tumbling Envisat, rotating at a baseline rate of 1 rpm (6 deg/s). Firstly, the kinematics and dynamics of an axisymmetric body (an approximation of the Envisat body) in torque-free motion is presented. The goal is to obtain closed-form solutions that can be used in the trajectory planning algorithm. Secondly, the polynomial motion planning method in the Euclidean space is introduced. The baseline approach and docking strategy is presented, where the trajectory is divided in different segments with their own particularities. In the trajectory optimisation section, different studies are conducted relative to the docking strategy, the effect of higher order polynomials, and the case of a single-thruster chaser. Finally, the trajectory planning and feedback control algorithm is discussed and simulation results are presented.

Regarding the terminology, *docking* is understood as the act of attaching the chaser to the target by any means, without necessarily implying the existence of an actual docking port. Thus, *docking point* is used to depict a generic point of

contact on the structure of the target.

4.1 Free motion of an axisymmetric target

The target spacecraft is considered to be a body in torque-free motion. Small environmental torques due to solar radiation pressure, drag, or gravity gradient, are neglected since the duration of the docking scenario is too short for those perturbations to have a significant effect. The rigid body equations of motion with zero torque are

$$\dot{\boldsymbol{\omega}} = -J^{-1}(\boldsymbol{\omega} \times (J\boldsymbol{\omega})) \tag{4.1}$$

where $\boldsymbol{\omega}$ is the angular velocity of the body resolved in the body-fixed frame B and J is the inertia matrix. If the inertia matrix does not have products of inertia (i.e. it is diagonal), Eq. (4.1) becomes

$$\begin{aligned} \dot{\omega}_1 &= [(J_2 - J_3)/J_1]\omega_2\omega_3 \\ \dot{\omega}_2 &= [(J_3 - J_1)/J_2]\omega_1\omega_3 \\ \dot{\omega}_3 &= [(J_1 - J_2)/J_3]\omega_1\omega_2 \end{aligned} \tag{4.2}$$

Where the J_i are the principal moments of inertia. If the body is asymmetric, Eq. (4.1) needs to be numerically integrated (closed-form solutions exist for triaxial inertia matrices, but involve Jacobi elliptic functions [13]). However, analytical solutions of the torque-free motion can be found if the body presents axial symmetry (axisymmetric body), as shown in Markley and Crassidis [13]. A variety of satellites present a certain degree of axial symmetry, such as ESA's Envisat, despite the equipment and solar panel (Fig. 4.1). Therefore, the analytical solution arising from the axisymmetric approximation can be used in the internal model of a guidance algorithm.

Essentially, in the axisymmetric case the angular momentum $\mathbf{H}$, the angular velocity $\boldsymbol{\omega}$, and the body axis of symmetry $\hat{\mathbf{e}}_1$ are coplanar and the angles between them remains constant (Fig. 4.2). The $\hat{\mathbf{e}}_1$ body axis rotates around the angular momentum $\mathbf{h}$ following a circular path, whereas the other two body axes spin about $\hat{\mathbf{e}}_1$.

When the axisymmetric body is prolate (as shown in Fig. 4.2), it has principal moments of inertia $J_1 < J_2 = J_3$. Thus, from Eq. 4.2 is clear that the component ω_1 (resolved in the body-fixed frame) is constant, and from the analysis of rigid body motion it follows that

$$\omega_1 = \frac{h_{1,B}}{J_1} \tag{4.3}$$

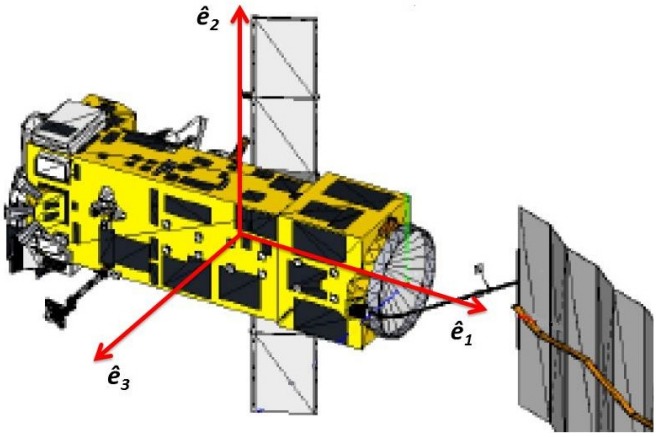

Figure 4.1: Envisat satellite (ESA)

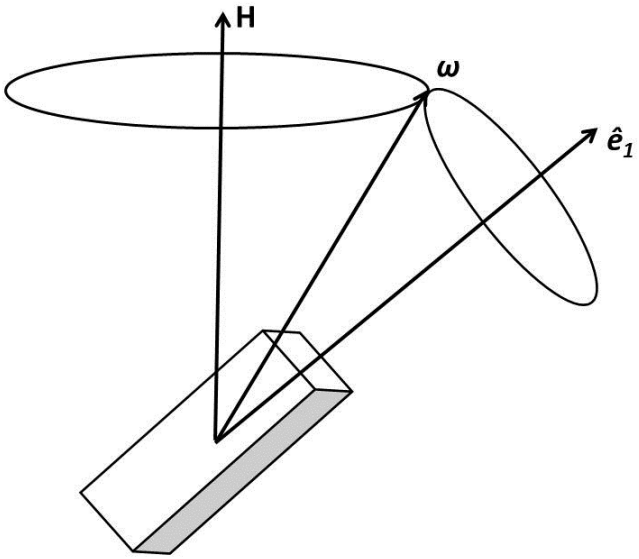

Figure 4.2: Torque-free motion of an rigid body with axial symmetry $J_1 < J_2 = J_3$

where $h_{1,B}$ is the first component (resolved in the body-fixed frame B) of the angular momentum vector, which is constant in the inertial frame. Solving the differential equations of Eq. (4.2), we find the solutions

$$\begin{aligned} \omega_2(t) &= \omega_t \sin(\lambda_0 + \omega_p t) \\ \omega_3(t) &= \omega_t \cos(\lambda_0 + \omega_p t) \end{aligned} \tag{4.4}$$

where

$$\omega_t = \frac{h_{t,B}}{J_t} \tag{4.5}$$

with $J_t = J_2 = J_3$ and $h_{t,B} = h_{2,B} = h_{3,B}$. The factor ω_p is known as the *body nutation rate*, i.e. the spin rate of the body about $\hat{\mathbf{e}}_1$ or the projection of $\boldsymbol{\omega}$ on

the $\hat{\mathbf{e}}_1$ vector in Fig. 4.2, and its value is

$$\omega_p = (1 - \frac{J_1}{J_t}) \tag{4.6}$$

When solving the kinematic equations, it is assumed that the x axis of the body-centred inertial frame I is aligned with the angular momentum vector h. The direction cosine matrix $A_{131}(\phi, \theta, \psi)$ represents a 1-3-1 sequence of extrinsic Euler rotations of the body with respect to the I frame. The corresponding angles are

$$\begin{aligned} \theta &= \cos^{-1}\left(\tfrac{J_1\omega_1}{\|\mathbf{h}\|}\right) \\ \phi &= \phi_0 + \omega_p t \\ \psi &= \psi_0 + \omega_l t \end{aligned} \tag{4.7}$$

where

$$\omega_l = \frac{\|\mathbf{h}\|}{J_t} \tag{4.8}$$

The factor ω_l is the *inertial nutation rate*, at which $\hat{\mathbf{e}}_1$ and $\boldsymbol{\omega}$ rotate about the angular momentum vector, or the projection of $\boldsymbol{\omega}$ on the $\mathbf{h}$ vector. Finally, the values ϕ_0, ψ_0, and λ_0 can be found from the initial conditions. Alternatively, closed-form solutions in quaternions for the axisymmetric case are developed in Maclean et al [80].

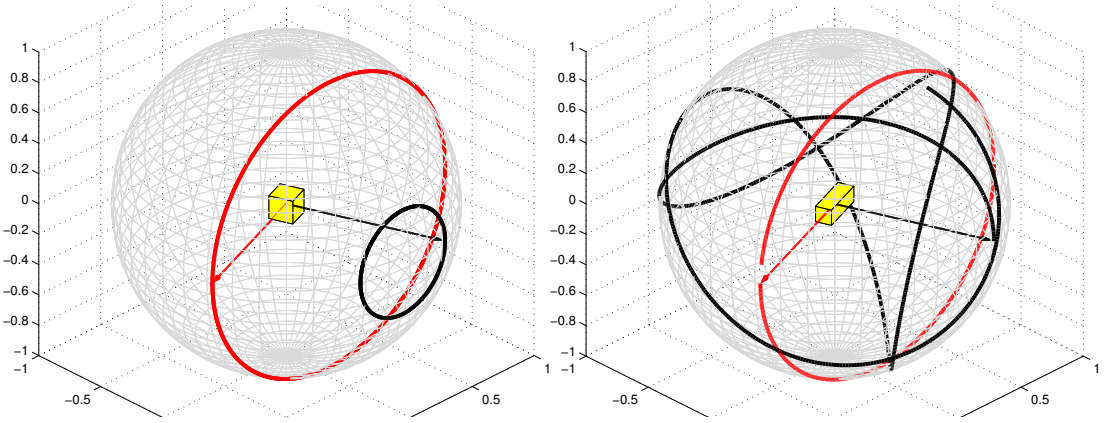

(a) Symmetric body **(b)** Axisymmetric body

Figure 4.3: Path of the axes $\hat{\mathbf{e}}_1$ (red) and $\hat{\mathbf{e}}_2$ (black)

Figure 4.3 shows the paths of the axes $\hat{\mathbf{e}}_1$ and $\hat{\mathbf{e}}_2$ on the unit sphere. The figure on the left shows the natural motion of a perfectly symmetric body. The moments of inertia are all equal, thus the equation of motion is greatly simplified yielding a constant angular velocity vector. In this case, the paths of the axes are easily

predictable. In contrast, in Fig. 4.3b we can appreciate how, with an axysimmetric body, the path of the first axis is circular whereas the second axis follows a seemingly chaotic path. However, for a purely axisymmetric spacecraft the motion of the axes can also be predicted analytically, which is useful for guidance and control purposes in the docking scenario.

Usually, a chaser spacecraft equipped with a grappling arm will dock into the launcher ring adapter, which would be located along the minor axis of inertia in prolate axisymmetric spacecraft such as Envisat. The docking point is on the side along the $\hat{\mathbf{e}}_2$ or $\hat{\mathbf{e}}_3$ axis, since the launcher ring adapter in the model considered is obstructed by the solar panel (Fig. 4.1). Also, these axes undergo a non-trivial motion (unlike the $\hat{\mathbf{e}}_1$ axis) resulting a worst-case scenario for the study.

4.2 Polynomial motion planning method

This method represents each position coordinate of the chaser spacecraft as a time-dependent polynomial:

$$r_i(t) = a_{i0} + a_{i1}t + a_{i2}t^2 + ... + a_{in}t^n = \sum_{j=0}^{n} a_{ij}t^j \tag{4.9}$$

for $i = 1, 2, 3$, where $\mathbf{r}_R(t) = [r_1(t),\, r_2(t),\, r_3(t)]_R^T$ is the position of the spacecraft resolved or projected on a certain reference frame depicted by the subscript R. The velocity $\dot{\mathbf{r}}_R(t)$ can be obtained by differentiating the polynomial in Eq. (4.9) with respect to time, as

$$\dot{r}_i(t) = a_{i1} + 2a_{i2}t + ... + na_{in}t^{n-1} = \sum_{j=1}^{n} ja_{ij}t^{j-1} \tag{4.10}$$

while the acceleration $\ddot{\mathbf{r}}_R(t)$ is found by differentiating twice. Note that the velocity and acceleration obtained by differentiating Eq. (4.9) are relative to the R frame, which might or might not be inertial.

The coefficients a_{ij} in Eq. (4.9) can be obtained by matching the prescribed $m = n + 1$ boundary conditions of the manoeuvre. This results in a system of m linear equations that can be easily solved, given the final time t_F. The minimum number of boundary conditions defining a manoeuvre are the initial and final position and velocity (requiring a 3^{rd} degree polynomial to represent the coordinates' trajectories). A prescribed final acceleration can be enforced

in order to smooth the trajectory at the arrival point, to which a 4^{th} degree polynomial is required. In this case, the system of linear equations is

$$\begin{bmatrix} 1 & 0 & 0 & 0 & 0 \\ 0 & 1 & 0 & 0 & 0 \\ 1 & t_f & t_f^2 & t_f^3 & t_f^4 \\ 0 & 1 & 2t_f & 3t_f^2 & 4t_f^3 \\ 0 & 0 & 2 & 6t_f & 12t_f^2 \end{bmatrix} \begin{bmatrix} a_{i0} \\ a_{i1} \\ a_{i2} \\ a_{i3} \\ a_{i4} \end{bmatrix} = \begin{bmatrix} r_i(0) \\ \dot{r}_i(0) \\ r_i(t_f) \\ \dot{r}_i(t_f) \\ \ddot{r}_i(t_f) \end{bmatrix} \tag{4.11}$$

where the vector on the right-hand side contains the selected boundary conditions. The Eq. (4.11) can be solved with linear algebra solvers or finding the closed-form expressions for the unknown coefficients.

In this docking scenario, an inertial frame I is set with its origin in the centre of mass (CM) of the body, and a body-fixed frame B is rotating with the target. For instance, if the planned trajectory $\mathbf{r}_B(t)$ is chosen to be resolved in the body-fixed frame (as depicted by the subscript B), the velocity of the chaser will be $\mathbf{v}_B^B(t) = \dot{\mathbf{r}}_B(t)$, the superscript indicating that it is seen from or relative to the B frame. Using the equations of kinematics in a rotating reference frame, the velocity relative to the I frame can be calculated as

$$\mathbf{v}_B^I = \mathbf{v}_B^B + \boldsymbol{\omega}_B \times \mathbf{r}_B \tag{4.12}$$

where ω_B is the angular velocity of the target resolved in the B frame. Similarly, the relative acceleration is $\mathbf{a}_B^B(t) = \ddot{\mathbf{r}}_B(t)$, and the acceleration relative to the inertial frame I is

$$\mathbf{a}_B^I = \mathbf{a}_B^B + 2\boldsymbol{\omega}_B \times \mathbf{v}_B^B + \boldsymbol{\omega}_B \times (\boldsymbol{\omega}_B \times \mathbf{r}_B) + \frac{\mathrm{d}\boldsymbol{\omega}_B}{\mathrm{d}t} \times \mathbf{r}_B \tag{4.13}$$

where the last term must be accounted for since the angular velocity vector does not have a constant direction (although it has a constant norm). The time derivative of the angular velocity in B frame can be found by differentiating Eq. (4.4). Finally, any generic vector $\mathbf{w}_B$ can be resolved in the I frame as

$$\mathbf{w}_I = R(t)\mathbf{u}_B \tag{4.14}$$

where $R(t)$ is the rotation matrix of the frame B with respect to I, i.e. the target's attitude. It can be evaluated with Eq. 4.7 and $R(t) = A_{131}^T(\phi, \theta, \psi)$.

In the inverse dynamics approach the thrust is evaluated with the acceleration profile, which is a polynomial. Therefore, since the thrust along the trajectory can be predicted, it is possible to enforce the maximum thrust constraint. If a

trajectory was planned such that at some point in the trajectory the commanded acceleration could not be achieved by the Reaction Control System (RCS), the chaser would drift off-course—the planned trajectory would be unfeasible. Note that in

$$\mathbf{F}(t) = m(t)\mathbf{a}^I(t) \tag{4.15}$$

the mass is time-dependent, accounting for fuel consumption. With the rocket equation it is possible to numerically evaluate the mass at every point t_k of the trajectory, as

$$m(t_{k+1}) = m(t_k)e^{(\Delta v(t_k)/(g_e I_{sp}))} \tag{4.16}$$

where $\Delta v(t_k) = \|\mathbf{v}(t_{k+1}) - \mathbf{v}(t_k)\|$, $g_e = 9.81$ m/s^2, and I_{sp} is the specific impulse of the RCS.If the time step is small, the exponential function can be approximated (first-order Taylor series), resulting in

$$m(t_{k+1}) = m(t_k)\left(1 - \frac{\Delta v(t_k)}{g_e I_{sp}}\right) \tag{4.17}$$

Alternatively, if the fuel consumption is much smaller than the initial wet mass, or $m(t_f) \approx m_{wet}$, in Eq. (4.15) we can consider a constant mass and the thrust becomes a time-dependent polynomial. The mass flow can be related to the thrust with

$$F(t) = \dot{m} g_e I_{sp} \tag{4.18}$$

where $F(t) = \|\mathbf{F}(t)\|$. Combining 4.18 and 4.15 the following is obtained:

$$\dot{m} = \frac{m_{wet}}{g_e I_{sp}}\|\mathbf{a}^I(t)\| \tag{4.19}$$

where $\dot{m} = \frac{dm}{dt}$, thus Eq. 4.19 can be numerically integrated to evaluate the approximated total fuel consumed f_c:

$$f_c = \int_0^{f_c} dm = \frac{m_{wet}}{g_e I_{sp}} \int_0^{t_f} \|\mathbf{a}^I(t)\| dt \tag{4.20}$$

where t_f is the duration or final time of the trajectory.

Compared to Eq. 4.16, this approximation is computed 50% faster. Note that a the fuel consumption and thrust profile predicted with m_{wet} will always be larger than one calculated with the more accurate $m(t)$, thus there is no risk of reaching the thrust limit due to this approximation.

4.3 Approach and Docking strategy

In the considered scenario, the chaser starts from a standing position 50 m away from the target. We consider a keep-out sphere enclosing the target and all its appendages (antennas, solar panels), and centred at its CM. The trajectory of the chaser, from the standing position to the docking point, is designed as a sequence of three segments:

Segment 1. The first segment brings the chaser from the initial position to a point aligned with the docking axis, at a distance equal to the radius of the keep-out sphere. This position is fixed in the body frame.

Segment 2. Secondly, the chaser follows this point, essentially performing body-fixed hovering over the target for a certain duration. This segment allows for a safe go/no-go decision time before the final segment.

Segment 3. Finally, the chaser moves within the keep-out sphere towards the docking point following an obstacle-free linear path.

This strategy focuses on safety and ensures obstacle avoidance in a robust way. Every segment has its own particularities, thus the polynomial motion planning method is implemented in different ways.

4.3.1 Segment 1 - First approach

In order to obtain a polynomial trajectory we need to define the boundary conditions and the manoeuvre time. In the first segment, the trajectory is planned in the inertial frame I. The initial state of the chaser is the current standing position $\mathbf{r}_I(0)$, 50 m away from the target's CM, and the current velocity $\dot{\mathbf{r}}_I(0)$, which should be close to zero. The initial time t_0 and the final manoeuvre time t_f of segment 1 are provided by an optimiser (detailed in the following section) so that fuel consumption is minimised and the thrust limit is satisfied.

The final position is given by the motion of the hovering point at the final time, as

$$\mathbf{r}_I(t_f) = \mathrm{R}(t_f)\mathbf{r}_{hp,B} \tag{4.21}$$

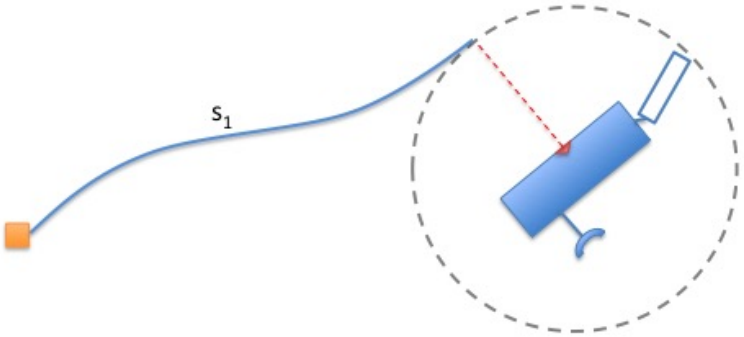

Figure 4.4: First approach segment schematics. The chaser spacecraft goes from a standing position to intersecting a moving point over the target

where $\mathbf{r}_{hp,B}$ is the prescribed hovering position resolved in the body frame (a constant vector) and the target's attitude at the final time $\mathrm{R}(t_f)$ is predicted with Eq. (4.7). The final velocity is

$$\dot{\mathbf{r}}_I(t_f) = \boldsymbol{\omega}_I(t_f) \times \mathbf{r}_I(t_f) \tag{4.22}$$

where the angular velocity is evaluated with Eq. (4.4). Finally, a desired final acceleration is enforced corresponding to the acceleration at the hovering point:

$$\ddot{\mathbf{r}}_I(t_f) = \boldsymbol{\omega}_I(t_f) \times \dot{\mathbf{r}}_I(t_f) + \frac{\mathrm{d}\boldsymbol{\omega}_I}{\mathrm{d}t}(t_f) \times \mathbf{r}_I(t_f) \tag{4.23}$$

Those boundary conditions, along with the manoeuvre time t_f, are used in Eq. (4.11) to obtain the polynomial coefficients shaping the trajectory.

4.3.2 Segment 2 - Hovering

In the hovering segment, the chaser tracks a point over the target fixed in the B frame, for a certain duration $t_f = t_{s2}$. For this purpose, the polynomial planner in closed loop is used with a receding horizon, i.e. at each sample step the trajectory is re-computed with the same final time t_{s2}. Best results are obtained by planning the trajectory in the B frame, since the commanded acceleration accounts for the fictitious accelerations arising in a rotating frame, which are predicted with the internal model of the target's motion. Using trajectory planning for tracking yields a better performance than classic closed-loop regulators, if the loop frequency is low.

The initial conditions correspond to the current state resolved in B. Specifically, the velocity must be relative to B. The final position vector is $\mathbf{r}_{hp,B}$ and the

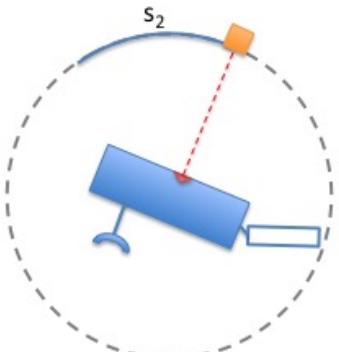

Figure 4.5: Hovering segment schematics. The chaser spacecraft follows a fixed point over the target

final velocity (as seen from B) is zero. No final acceleration is specified in this segment. The commanded acceleration profile (relative to the I frame) must be obtained with Eq. (4.13). The approximate attitude and angular velocity of the body-fixed frame can be evaluated in near-real time with the analytical equations described in Section 4.1.

As seen from the body frame point of view, if the current position of the spacecraft is offset from the hovering point, it will come back to the desired (predicted) position in a finite time t_{s2} and following a linear path. However, if the sample time T_s at which the trajectory is recomputed is smaller than t_{s2}, the new trajectory will be shorter in distance but the prescribed final time will still be t_{s2}, therefore the spacecraft will converge to the desired hovering position asymptotically. Besides, when the spacecraft and target current states are updated and the final target state is predicted, there will be errors that might make convergence difficult. Hence, the sample time T_s and the final time (receding horizon) t_{s2} must be tuned taking these considerations into account.

4.3.3 Segment 3 - Docking approach

When the *go* decision has been made, the chaser spacecraft stops hovering to initiate the "descent" towards the docking point along the docking axis, a linear approach relative to the body-fixed frame B. In this segment, the chaser is inside the keep-out sphere, thus the path defined must be obstacle-free and must be followed accurately to prevent collision risk. As in the hovering segment, the trajectory is planned in the B frame. The spacecraft must follow a linear path to avoid obstacles, therefore the motion is planned in a single coordinate (aligned

with the docking axis), while the other two coordinates—perpendicular to the docking axis—are set to zero. However, as in the first segment, the manoeuvre must be executed in a fixed time t_{s3}. At each time step, the trajectory is re-computed with the current spacecraft state as the initial conditions and the remaining manoeuvre time $t_f = t_{s3} - t$. The final conditions, in B frame, are the docking point position $\mathbf{r}_{dp,B}$ (parallel to $\mathbf{r}_{hp,B}$), zero relative velocity (although a residual "touchdown" velocity can be enforced depending on the docking system), and zero relative acceleration. The final relative acceleration is set to zero, so that the inertial acceleration points towards the target at the moment of contact, since the spacecraft is only applying the centripetal acceleration to maintain itself on the docking point. The rationale behind this requirement is to prevent the plume of the thrusters from interacting with the target's surface. As in segment 2, the commanded acceleration profile, which includes the fictitious accelerations due to the rotating frame, is obtained with Eq. (4.13) and the equations of motion of the axisymmetric body.

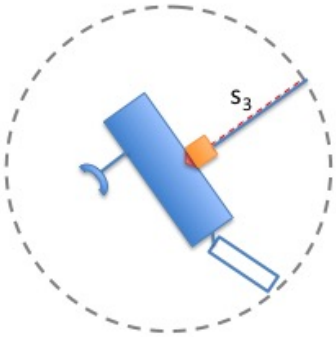

Figure 4.6: Docking segment schematics. The chaser follows an obstacle-free path towards the docking or attachment point

4.4 Trajectory optimisation

This section presents two strategies for designing the trajectory that brings the chaser from its initial standpoint to the docking point. Essentially, the manoeuvre is divided into segments with different characteristics, and a polynomial is used to shape the motion of each segment. The optimisation of the trajectory in terms of fuel is discussed.

4.4.1 3-segment strategy

This section focuses on the minimisation of the fuel consumed mainly in the first segment, amongst the class of trajectories defined by 4^{th} degree polynomials (matching 5 boundary conditions—including final acceleration), considering a 3-segment strategy. The duration of the hovering segment is chosen arbitrarily, while the duration of segment 3 can be selected such that the fuel consumption is minimal. In segment 1, one of the optimisation variables is the manoeuvre time t_f (an input in Eq. (2.6)). (Here it is considered that $t_f = t_{s1}$, which are used interchangeably.)

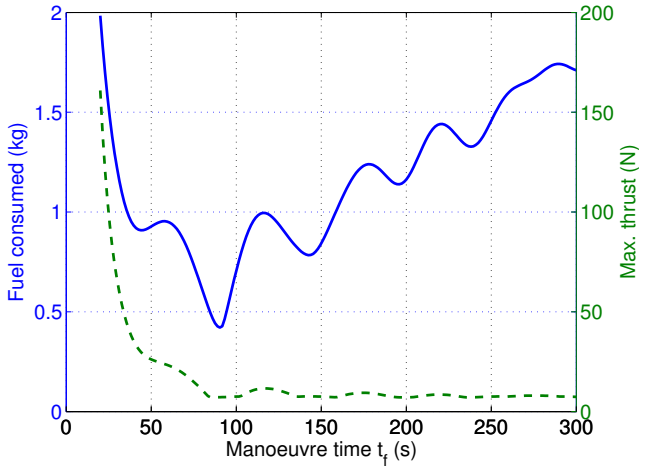

Figure 4.7: Fuel consumption (blue-solid) and max. thrust (green-dashed) along every manoeuvre as a function of manoeuvre time t_f.

The case study considers a 100-kg spacecraft with an RCS of I_{sp} =50 s. Figure 4.7 shows the evolution of fuel consumption for different manoeuvre times t_f from an initial position 50 m away from the centre of mass of the target. This plot represents the structure of the optimisation cost function, featuring multiple local minima, where a gradient-based optimiser might get stuck in. However, since the computational overhead is low due to the analytical prediction of the target's motion, it is feasible to implement an exhaustive search (brute force) of the optimisation search space, at least as a way of finding a good initial guess for a gradient-based or heuristic optimisation.

The other optimisation variable considered is the initial time t_0, or the waiting time before starting the approach. This waiting time allows the target's docking

axis to rotate to a more favourable position with respect to the standing position of the chaser.

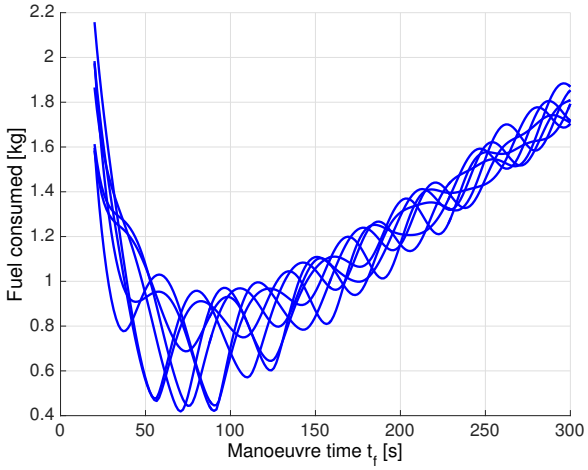

Figure 4.8: Fuel consumption as a function of t_f, for different t_0 cases (ranging from 0 to 200 s)

Figure 4.8 shows the cost function structure (as in Fig. 4.7) for several t_0 values ranging from 0 to 200 s (for clarity, only 7 cases are shown). There is, thus, a global minimum for certain values of t_f and t_0. Figure 4.9 shows the evolution of the minimum fuel consumed as a function of t_0. In this case, the minimum fuel values found in 4.8 (in the t_f domain) for every t_0 case are plotted, with a denser mesh. We can observe a repeating pattern, with a fuel consumption improvement of 43% in the best case with respect to the worst case.

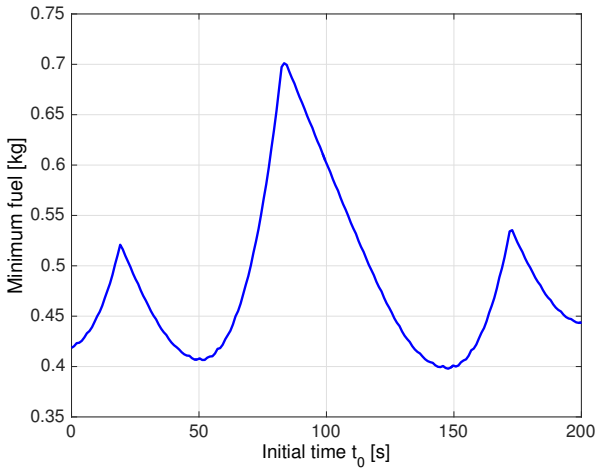

Figure 4.9: Minimum fuel consumed (over the range of t_f) as a function of t_0

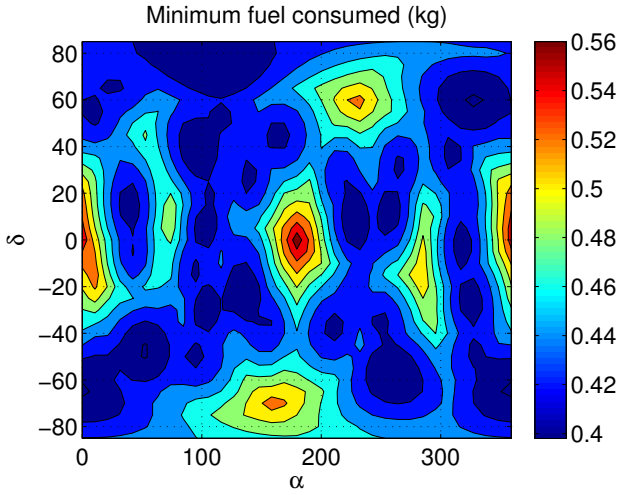

Figure 4.10: Fuel consumption as a function of the initial standing position (in polar coordinates, constant distance at 50 m)

Figure 4.10 shows that the initial standing position is also relevant to the fuel consumption. Specifically, it shows that the most unfavourable starting positions are along the angular momentum vector **h**, either in front of it or at the back (as seen in the consumption peaks at $\alpha = 0$ and $\alpha = 180$). The **h** vector is visualised in Fig. 4.11, where the body axes revolve around it.

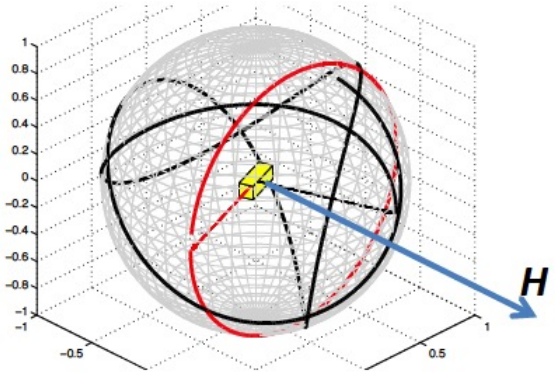

Figure 4.11: Direction of angular momentum vector **h** of a rotating asymmetric body (**h** is aligned with inertial x-axis)

Note that the optimisation variables of initial position and initial time are somewhat redundant, e.g. apart from waiting for the target to rotate to a favourable position the spacecraft can reposition itself with respect to the target. However, repositioning takes time and fuel, and the spacecraft must be able to move into the optimal position within the waiting time, which complicates the optimisation

process and the operations. Therefore, stemming from the results shown in Fig. 4.10, in an operational scenario it would be desirable to choose an arbitrary initial position as long as it lies on a favourable region, e.g. close to the plane perpendicular to **h** containing the target. Then, from this position, the fuel consumption would be optimised by searching only the t_0 and t_f variables. Said optimisation can be computed on-board or on the ground.

The feasibility of the trajectory in terms of maximum thrust must be ensured, requiring constrained optimisation algorithms. If computational resources are limited, unconstrained optimisation with penalty functions could be used (although they do not specifically enforce constraints). In Fig. 4.7 the t_f value corresponding to the lowest maximum thrust is close to that of the optimum fuel. Nonetheless, the maximum thrust should be checked at every iteration, and a higher t_f than the fuel-optimum might be chosen as a result of the constrained optimisation. Also, it must be ensured that the path does not intersect the keep-out sphere enclosing the target. Varying t_0 and t_f can modify the path enough to avoid the simple spherical obstacle, and the final acceleration condition helps generating collision-free paths by avoiding sharp turns close to the endpoint.

During the hovering segment, the fuel consumption rate is constant and its duration is pre-determined by mission requirements. As to the optimisation of the third segment, only the $t_{s3} = t_f$ variable is considered. Since the trajectory is planned relative to the body frame, the fuel consumption does not depend significantly on the target's attitude. Therefore, the t_{s3} can be a pre-determined value regardless of the trajectory parameters of segment 1—i.e. the optimisation processes of the first and third segments are decoupled.

Figure 4.12 shows the fuel consumption for a range of segment durations, with a minimum at $t_{s3} = 25$ s. However, the larger the final time is, the lower the thrust peak will be. Hence, a compromise solution should be selected by the optimiser if the actuators' capabilities are limited. Finally, in this work a requirement on final acceleration is considered, to avoid the plume of the thrusters from interacting with the target's surface. If this requirement was relaxed, faster trajectories with less fuel expenditure and maximum thrust could be designed.

In this case study, the initial position has been fixed. The trajectory parameters for a minimum fuel consumption are an initial time of $t_0 = 0$ s, $t_{s1} = 70.91$ s, and $t_{s3} = 25$ s. The hovering time is arbitrarily set at $t_{s2} = 10$ s.

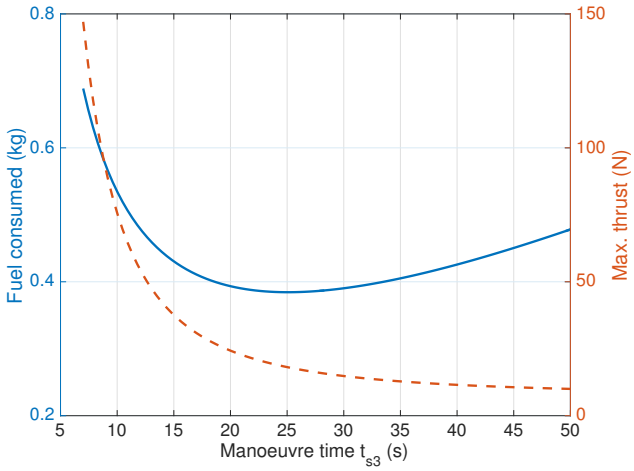

Figure 4.12: Segment 3 (with zero final relative acceleration and zero initial relative velocity): Fuel consumed (left axis) and maximum thrust (right axis), for a range of segment durations

Figure 4.13 shows the planned position, velocity, and acceleration of the chaser, in the inertial frame and relative to the target's body frame. During the first segment, the chaser undergoes a high-low-high acceleration profile, during which the chaser acquires a certain speed, then turns the trajectory to match the motion of the hovering point. The relative velocity to the body is zero during hovering and the total acceleration is almost constant (since it only compensates for the centrifugal acceleration). At the very end of the third segment the position and velocity profiles approach their final values more smoothly, due to the requirement of zero final relative acceleration (which corresponds to the centripetal inertial acceleration at the docking point). At the start of the third segment, there is an acceleration peak, the maximum of the overall manoeuvre, which can be reduced by increasing the duration of the third segment at the cost of a larger fuel expenditure. In this case, if the acceleration peak was halved, the maximum thrust requirement of the RCS would be reduced by 50%, lowering the size and weight of the thrusters. This would imply doubling the segment duration which would increase the fuel consumption by 25%.

The fuel consumed is shown in Fig. 4.14. The final seconds of the first segment, the hovering segment, and the first half of the third segment experience the highest consumption rate. Different strategies or requirements could lower the overall fuel consumed, such as not matching the accelerations between segments or removing the hovering segment.

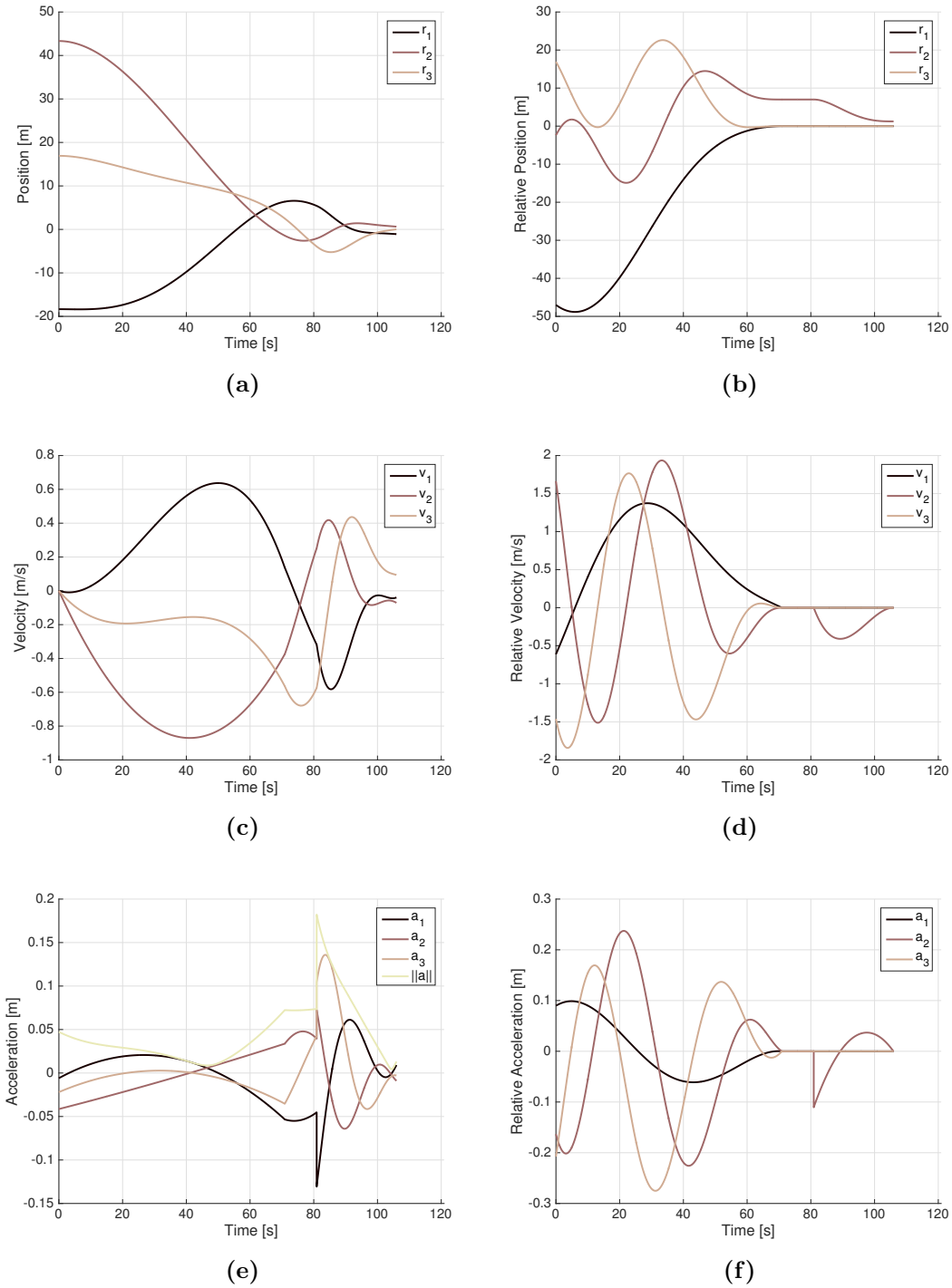

Figure 4.13: Trajectory of 3-segment strategy. The relative trajectory is from the body frame B.

Figure 4.15 shows the trajectory in the inertial frame, with the chaser arriving to the keep-out sphere tangentially to the hovering point, following the hovering

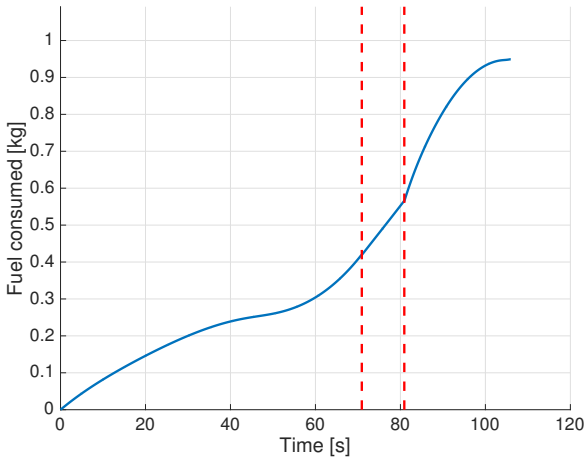

Figure 4.14: Fuel consumption of the 3-segment trajectory

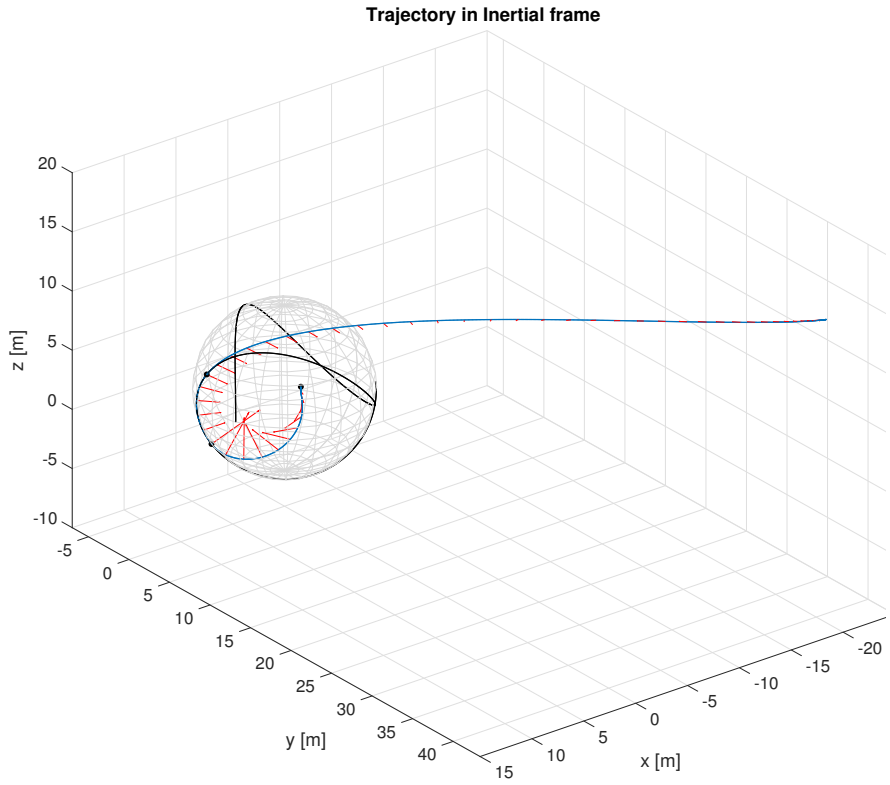

Figure 4.15: 3-segment trajectory in the inertial frame I. Arrows depict the acceleration vector. The path of the docking axis is shown on the keep-out sphere.

position, and moving into the sphere (a spiralling path as seen from I). The trajectory seen from the body-fixed frame shown in Fig. 4.16 gives a better insight to the three-segment strategy, where the chaser follows a linear path inside the keep-out sphere from a fixed location over the docking point. Note how the

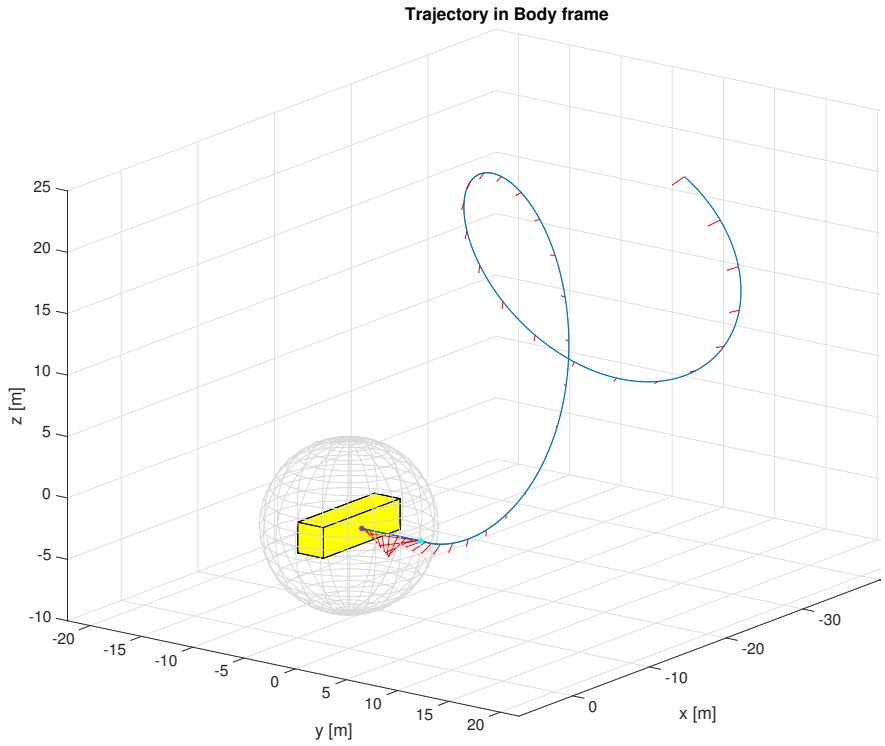

Figure 4.16: 3-segment trajectory in the body frame B. Arrows depict the acceleration vector.

docking path is linear and much more thrust-intensive.

It is interesting to look at a trajectory with an arbitrarily long t_{s1} time, to gain some insight on how the final times parameters affect the trajectory (Fig. 4.17). If a long final time is imposed the trajectory experiences winding, moving away only to come back towards the target, so that the chaser is in motion yet arrives at the specified (long) time. Twice the necessary fuel is spent. Since the only degree of freedom of the trajectory shaped by those polynomials is the final time, the optimisation is computationally efficient, but it is not possible to adjust the trajectory to a more efficient approach, such as just moving slower or coasting. However, a requirement for an arbitrary final time is not necessary, and the results presented show that by carefully selecting (via optimisation) the final times and boundary conditions it is possible to obtain feasible manoeuvres with low fuel consumption.

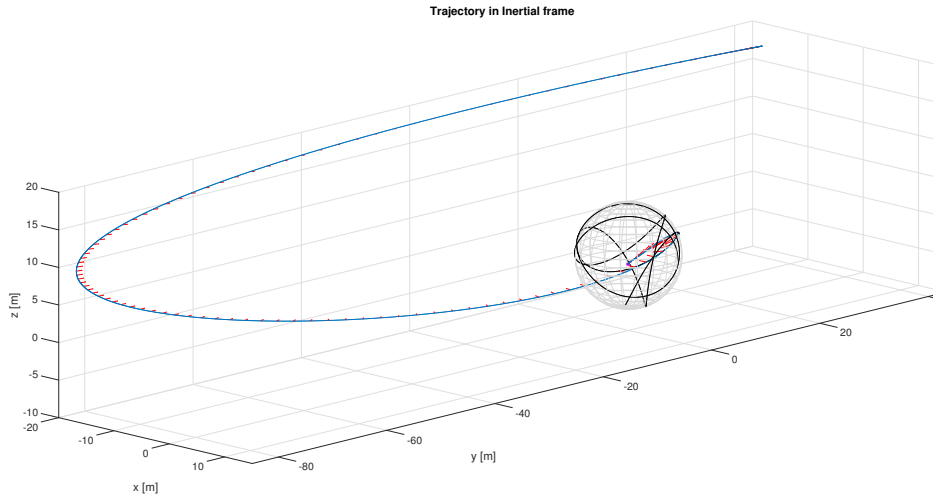

Figure 4.17: 3-segment trajectory in the inertial frame I. Arrows depict the acceleration vector. The path of the docking axis is shown on the keep-out sphere.

4.4.2 2-segment strategy

The hovering segment, on the surface of the keep-out sphere, allocates time for ensuring a correct alignment before the final approach and for a safe abort manoeuvre. Alternatively, fuel can be saved by removing the hovering segment from the trajectory, and entering the sphere with a certain velocity. This insertion velocity, or $\mathbf{v}^B_{B,ins}$, is parallel to the docking axis and specified relative to and resolved in the body frame. Thus, $\mathbf{v}^B_{B,ins}$ becomes the initial velocity of segment 3, and the final velocity of segment 1 (when converted to the inertial frame). Although there is no hovering segment (segment 2), the docking approach will be still called segment 3 for consistency with the nomenclature.

Regarding the docking approach segment (segment 3), there are two free variables—the initial velocity ($\mathbf{v}^B_{B,ins}$) and the final time or segment duration (t_{s3}). If the performance index of the optimisation is the fuel consumption, the cost structure is shown in Fig. 4.18, which features a global optimum.

Figure 4.19 shows the minimum fuel consumption vs. the initial velocity, for all the final times. In other words, for any initial velocity, the minimum fuel is found across the range of t_{s3}. In this case, in segment 3 the optimal point is found at an initial or insertion velocity of 0.7 m/s and a trajectory duration of 23 s. However, the insertion velocity $\mathbf{v}^B_{B,ins}$ is also the final velocity of segment 1, and as a boundary condition it affects its trajectory. The minimum fuel consumption (for a range of waiting times t_0 and final times t_{s1}) is (roughly) linearly decreasing with

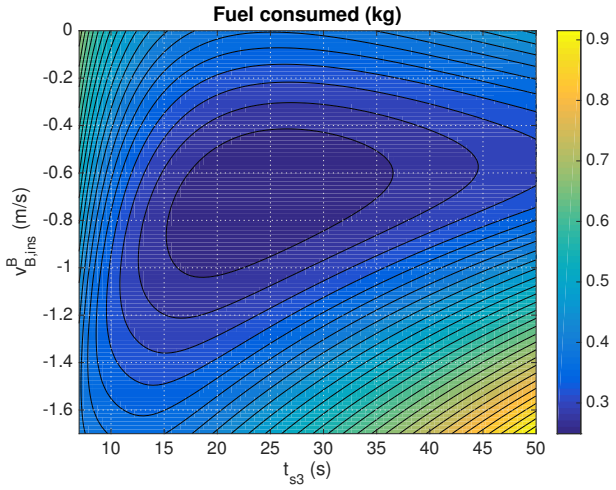

Figure 4.18: Segment 3: Fuel consumption as a function of the initial (or insertion) velocity and the segment duration

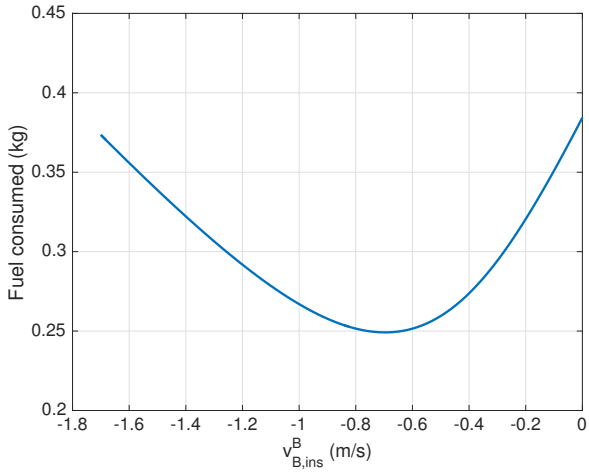

Figure 4.19: Segment 3: Minimum fuel consumption for the range of final times, as a function of the initial (or insertion) velocity

the insertion velocity, with the minimum at $\|\mathbf{v}^B_{B,ins}\| = 0$ m/s (Fig. 4.20). The case portrayed considers a fixed initial position (in a favourable area as depicted by Fig. 4.10), and a free final acceleration (unlike the 3-segment scenario, thus the polynomial is of 3^{rd} degree).

Hence, the fuel optimisation must combine both segments. The sum of combined consumptions is shown in Fig. 4.21, where the global optimum corresponds to an insertion velocity between each segment's optimum value. In the case shown here, the optimum trajectory parameters are $\|\mathbf{v}^B_{B,ins}\| = 0.39$ m/s, $t_0 = 32.7$ s, $t_{s1} = 180$ s, and $t_{s3} = 26.8$ s. Note that the aforementioned figures depict the

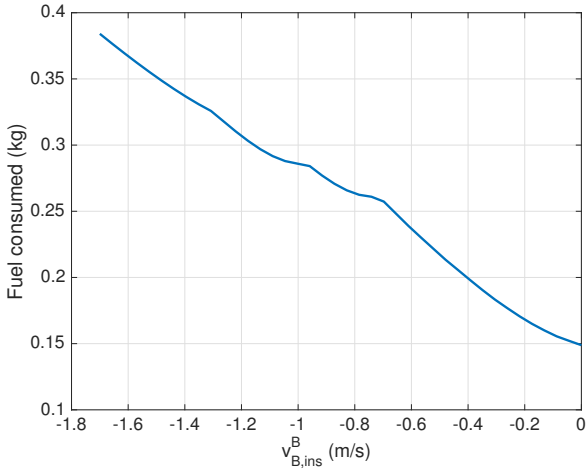

Figure 4.20: Segment 1 (no final acceleration is enforced): Minimum fuel consumption for the range of initial and final times, as a function of the final (or insertion) velocity

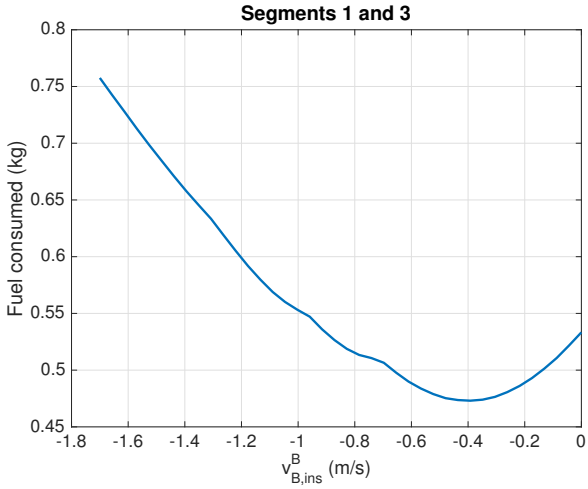

Figure 4.21: Segments 1 and 3: Total minimum fuel consumption as a function of the final (or insertion) velocity

structure of the performance index which has been obtained with a brute force computation. Before the manoeuvre is executed, these four parameters must be found with an optimisation algorithm that should find a solution as close to the global optimum as possible in a relatively short amount of time.

Figure 4.22 shows the planned position, velocity, and acceleration of the chaser, in the inertial frame and relative to the target's body frame. The last 27 seconds correspond to the docking segment. Notice how the relative acceleration of the final segment has a parabolic shape, which slows down the chaser (as seen from the

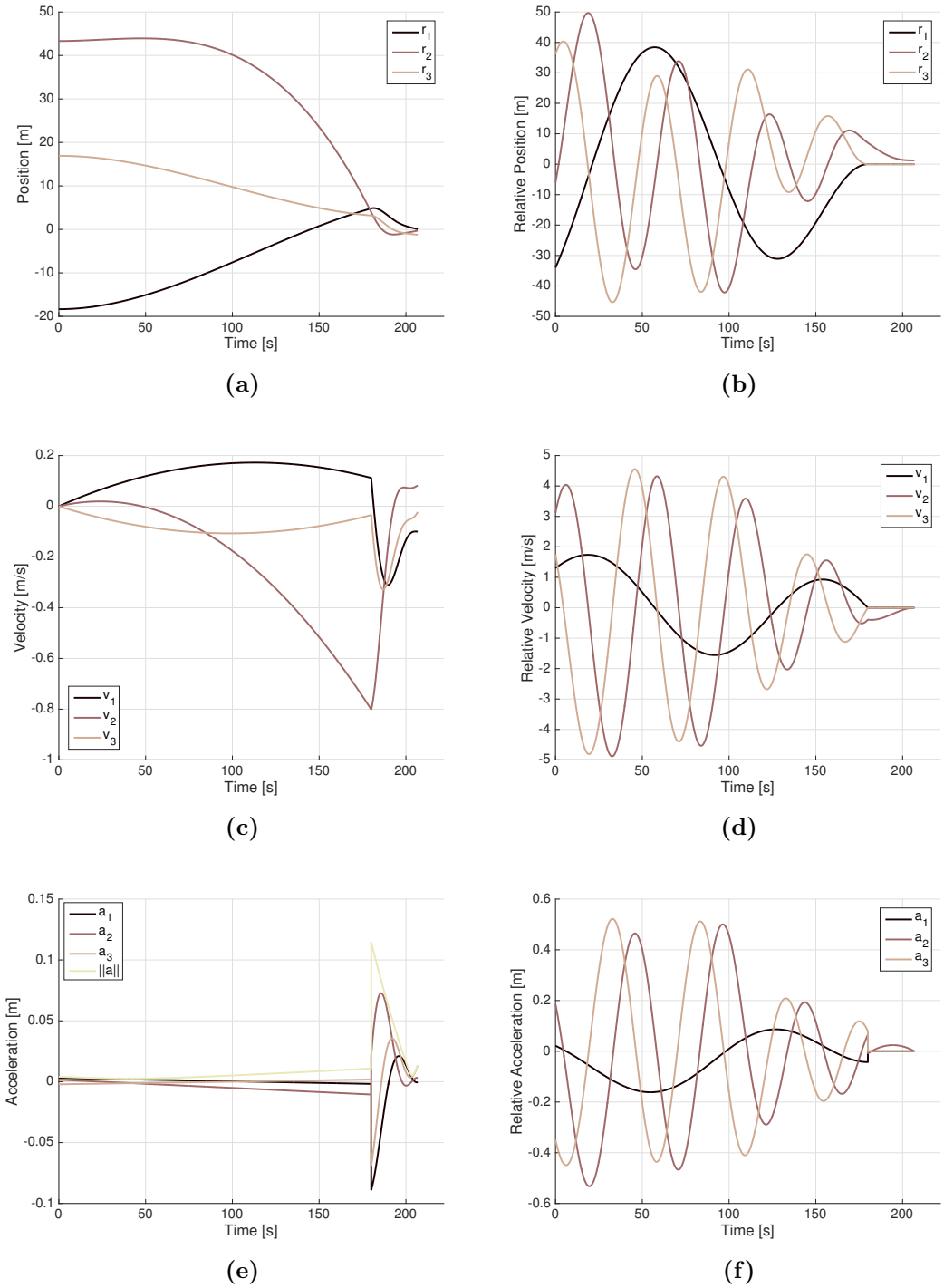

Figure 4.22: Trajectory of 2-segment strategy. The relative trajectory is from the body frame B.

target) until the final velocity is zero on the surface (as depicted by the final offset in the relative position figure). However, the inertial acceleration, i.e. the actual

acceleration commanded to the chaser, experiences a peak at the intersection point which counteracts the centripetal and coriolis accelerations (in this case the initial relative acceleration is close to zero). In comparison to the docking segment, the acceleration applied during the approach segment is relatively low. This is due to the long time allocated for segment 1, in which the chaser is slowly accelerated to the desired intersection position and velocity—in this case a final acceleration is not specified as a boundary condition.

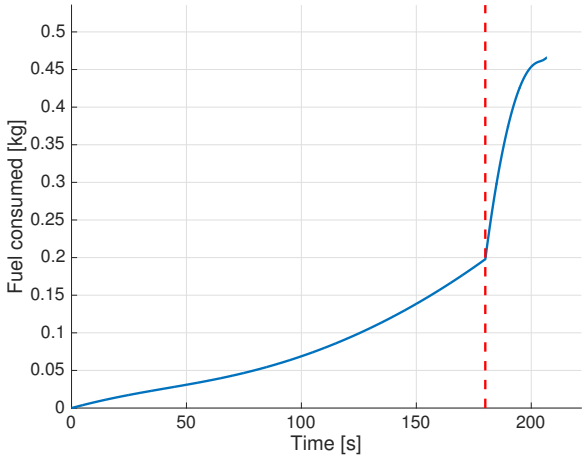

Figure 4.23: Fuel consumption of the 2-segment trajectory

The fuel consumed is shown in Fig. 4.23. The fuel consumed in the last segment is almost the same as the much longer first segment, due to the higher acceleration (thrust) involved. The thrust jump at the intersection can be avoided by prescribing the final acceleration of segment 1 to be equal to the initial acceleration planned in segment 3. Although the fuel expenditure will be higher, it might avoid some precision loss in a real system by smoothing the trajectory.

Figure 4.24 shows the path of the chaser in the inertial frame. The trajectory penetrates the keep-out sphere, in contrast with the hovering scenario in which the caser approaches the keep-out sphere tangentially (Fig. 4.15). This is due to the radial component of the terminal velocity of segment 1. It can be visualised how the acceleration is small during segment 1, until the thrusters kick in when the chaser enters the keep-out sphere in order to follow the docking axis. When the path is represented in the body frame (Fig. 4.25), large winding appears due to the long duration of segment 1, during which the target keep revolving.

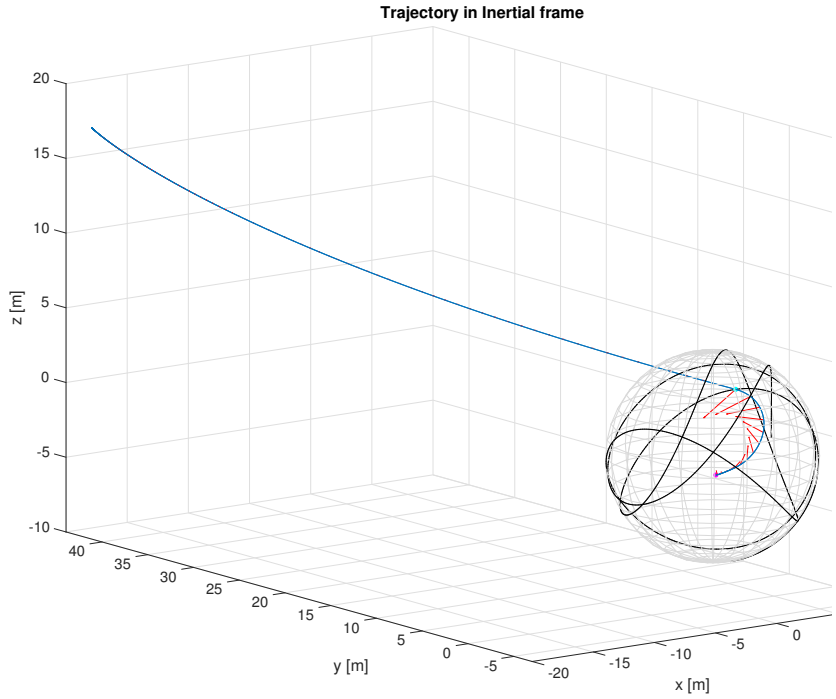

Figure 4.24: 2-segment trajectory in the inertial frame I. Arrows depict the acceleration vector. The path of the docking axis is shown on the keep-out sphere.

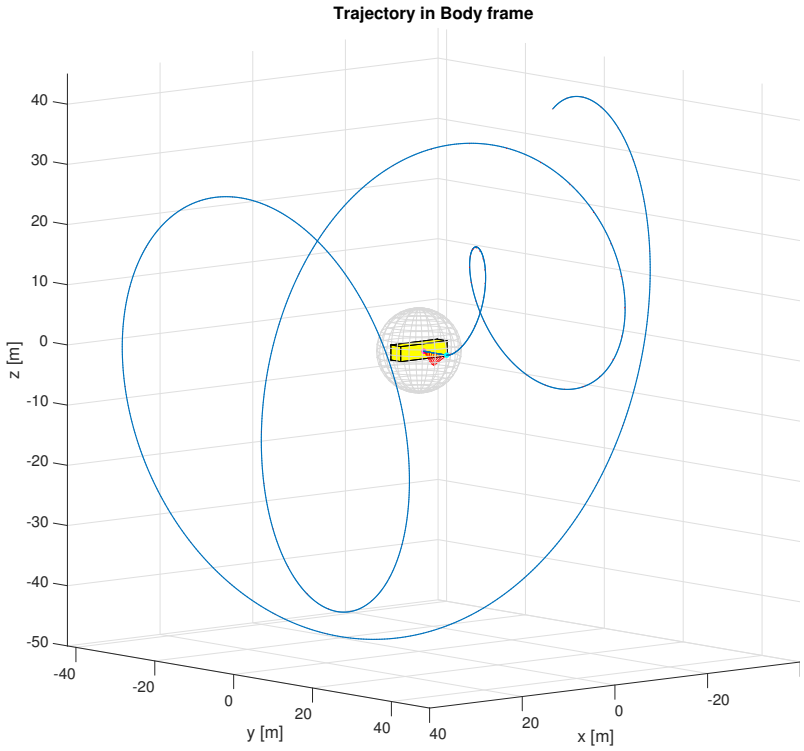

Figure 4.25: 2-segment trajectory in the body frame B.

4.4.3 Higher order polynomials

So far, the polynomials have had the necessary degree so that all their coefficients can be calculated from the boundary conditions. In this case, the free variables were the initial and final time. However, more free variables can be included by increasing the order of the polynomial. The system of equations given by the boundary conditions (Eq. (4.11)) would be underdetermined, but the additional coefficients can be guessed. Thus, if there are 5 boundary conditions and the polynomial of each coordinate i is of degree 5 (i.e. with 6 coefficients), the system becomes

$$\begin{bmatrix} 1 & 0 & 0 & 0 & 0 \\ 0 & 1 & 0 & 0 & 0 \\ 1 & t_f & t_f^2 & t_f^3 & t_f^4 \\ 0 & 1 & 2t_f & 3t_f^2 & 4t_f^3 \\ 0 & 0 & 2 & 6t_f & 12t_f^2 \end{bmatrix} \begin{bmatrix} a_{i0} \\ a_{i1} \\ a_{i2} \\ a_{i3} \\ a_{i4} \end{bmatrix} = \begin{bmatrix} r_i(0) \\ \dot{r}_i(0) \\ r_i(t_f) - a_{i5}t_f^5 \\ \dot{r}_i(t_f) - 5a_{i5}t_f^4 \\ \ddot{r}_i(t_f) - 20a_{i5}t_f^3 \end{bmatrix} \tag{4.24}$$

In Eq. (4.24) the additional free coefficients, corresponding to the higher order terms, are included in the known boundary conditions vector. Note that here the final time t_f corresponds to the trajectory duration, since the initial or waiting time is offset to zero. Therefore, they become optimisation variables that can further minimise fuel consumption (the performance index), since essentially more degrees of freedom are included in the trajectory. With this approach, the boundary conditions will always hold for any value of the free coefficients, since the rest of the coefficients are calculated by matching the boundary conditions. The order of the polynomial can be arbitrarily large—there will be more variables to be found in the optimisation process, increasing the computational cost but also improving the optimum value.

Thus, it is possible to test how much the trajectory can be optimised and at which cost. If the first segment is optimised with no additional terms, the fuel consumed is 0.42 kg. From a fixed standing position, only the initial and final time are considered in the computation, which took 0.1 s to obtain the optimum (Matlab® script on a laptop PC). Then, polynomials with increased degree can be used. If a 5^{th}-degree polynomial is used with the same number of boundary conditions, 3 new variables are included (a coefficient for each coordinate). In this case, the consumed fuel is 0.33 kg, computed in 0.67 s. The 6^{th}- and 7^{th}-degree polynomials were also tested.

Results are shown in Table 4.1 and Fig. 4.26. In the figure, the actual waiting times of the trajectories are different, but they are all offset to zero in order to

Case	Fuel consumed (kg)	Computation time (s)
4^{th}-deg. poly.	0.42	0.10
5^{th}-deg. poly.	0.33	0.67
6^{th}-deg. poly.	0.27	1.71
7^{th}-deg. poly.	0.26	2.73

Table 4.1: Optimal fuel values and computational cost using polynomials of different degrees (5 boundary conditions, segment 1)

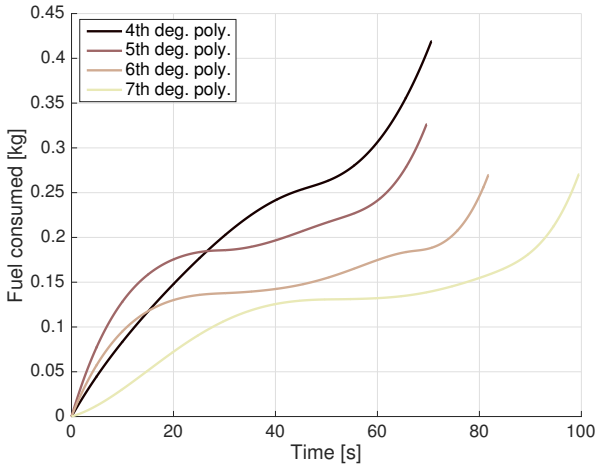

Figure 4.26: Comparison of fuel consumption for trajectories shaped with different polynomials (5 boundary conditions, segment 1)

compare the duration of the manoeuvres. Firstly, it seems clear that after 2 additional terms in the polynomial (6^{th}-degree), there is no significant improvement but the computational time is increased by 60%. Secondly, the lower consumption trajectories shaped by higher degree polynomials tend to have a higher duration. Thirdly, higher degree polynomials feature a near-zero consumption rate in mid-trajectory, meaning that the chaser is essentially coasting. This suggests that a "bang-off-bang" type of manoeuvre is more fuel-efficient.

In this study, unconstrained optimisation has been used with the Nelder-Mead algorithm has been used. However, in an operational scenario the maximum thrust and other possible constraints should be included in the optimisation, either in terms of penalty functions (efficient but not robust) or with an explicitly constrained optimisation algorithm (robust but less efficient). Finally, note that the motion of the target is evaluated at every iteration of the optimisation, thus the fact that it can be computed analytically is fundamental to increase the

computational efficiency.

4.4.4 Obstacle avoidance

In the baseline scenario, the keep-out surface is a sphere of a certain radius, enclosing the rotating target. The final segment takes place within the sphere, but collisions are avoided by keeping the chaser on a prescribed safe linear path (or very close to it, given some margins). Outside the volume of the sphere there are no obstacles to collide with, therefore the path of the first segment must not intersect the sphere. The distance between the chaser and the sphere's surface is

$$d_s(t) = \|\mathbf{r}(t)\| - r_e \tag{4.25}$$

where $d_s(t)$ is the distance between the chaser and the sphere's surface, r_e is the radius of the sphere, and $textbfr(t)$ represents the polynomial trajectory with the origin located at the centre of the sphere. The obstacle avoidance constraint implies that the norm of the chaser's position shall be greater than the keep-out sphere's radius at any time, which can be formally described as

$$\min_t d_s(t) \geq 0 \quad \forall\, t \in [t_0,\, t_0 + t_f] \tag{4.26}$$

The value of $\min_t d_s(t)$ depends on the optimisation variables (t_0, t_f, and any free coefficients), and is one of the an inequality constraints of the optimisation problem. The minimum of $d_s(t)$ should be found with an exhaustive search by discretising the trajectory to ensure global optimality. However, during the optimisation it was very unlikely to find an iteration whose trajectory intersected the keep-out sphere. This can be explained by the simple, smooth trajectories generated by polynomials of relatively low order and the choice of reasonable boundary conditions. However, a spherical shape enclosing a slender cuboid leaves a lot of inside volume obstacle-free, where the chaser could fly safely. Also, the hovering or insertion point to the docking approach is relatively far away from the body, and a significant amount of fuel is spent during this final segment. Hence, a non-spherical keep-out volume better fitting the shape of the body could improve the performance of the manoeuvre. Figure. 4.27 hows a detailed shape of a satellite based on Envisat, including its large solar panel and its SAR. A cylinder with an elliptical cross-section minimises the obstacle-free volume inside the keep-out geometry.

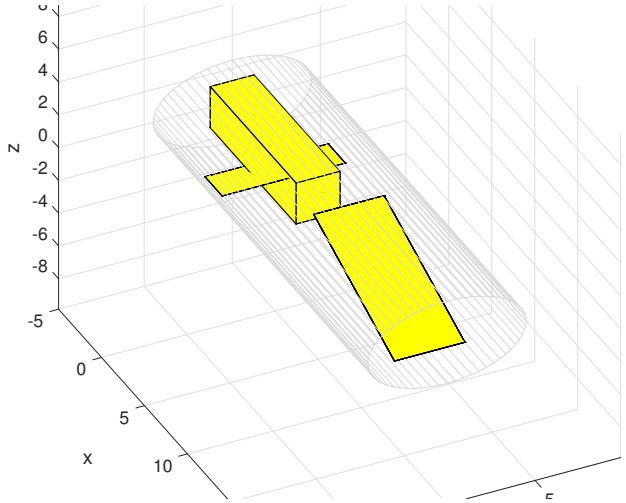

Figure 4.27: Keep-out cylinder of elliptical cross-section enclosing a satellite model based on Envisat

Note that the cylinder rotates about the centre of mass of the system, located at the satellite body. The implicit equation of the cylinder with elliptical section and aligned along the x direction is

$$\frac{y^2}{a^2} + \frac{z^2}{b^2} = 1 \quad \forall\, x \in [-L_1,\, L_2] \tag{4.27}$$

where a and b are the semiaxes of the elliptical base. The chaser's position vector is expressed in the body frame with the target's attitude matrix:

$$\mathbf{r}_B(t) = R^T(t)\mathbf{r}_I(t) \tag{4.28}$$

The cylinder has a finite length, thus the chaser could be inside it if $r_{1B}(t) \in [-L_1,\, L_2]$, and the closest distance to the surface occurs on the plane $x = r_{1B}(t)$, which intersects the cylinder forming an ellipse. Thus, the closest distance of the point $\mathbf{w} = (r_{2B}(t),\, r_{3B}(t))$ to an ellipse must be found, for all the discrete times t_k. However, it is not possible to calculate it analytically—it requires numerical root-finding. An analytical approximation is used, which serves the purpose of obstacle avoidance nonetheless. The line passing by the centre of the ellipse and $\mathbf{w}$ is

$$(x, y) = c\frac{\mathbf{w}}{\|\mathbf{w}\|} \tag{4.29}$$

where c is a parameter that can be found by replacing Eq. 4.29 into Eq. 4.27, in order to obtain the intersection $\mathbf{p}$ of this line with the ellipse. Finally, the distance $d_c(t) = \|\mathbf{w} - \mathbf{p}\|$ can be calculated, and its minimum value over all the (discrete) time domain is the constraint function for the cylinder.

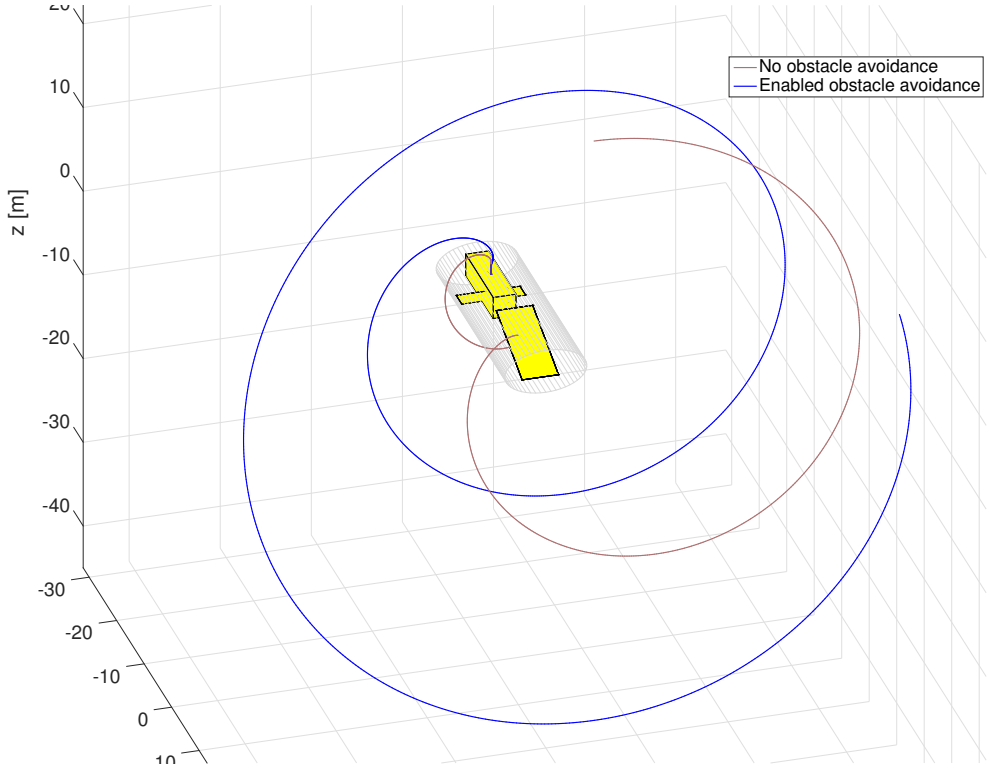

Figure 4.28: Detail: Trajectories (no free coefficients) in the body frame B, with a detailed shape of the satellite and solar panel. With and without obstacle constraints.

Figure 4.28 shows trajectories shaped by 4^{th}-degree polynomials and 5 boundary conditions, i.e. the trajectory is only determined by the initial and final times. In the case shown, if no obstacle avoidance is considered, the trajectory intersects the cylinder impacting the solar panel. When the obstacle is taken into account in the optimisation, the trajectory avoids intersecting the cylinder while minimising fuel. The duration of the first trajectory is 113 s, while the second is 84 s. With the same boundary conditions, as seen in Fig. 4.29 the fuel consumption with a keep-out cylinder is significantly lower than with a sphere.

Finally, in order to improve the efficiency of the obstacle avoidance algorithm, only the points with $r_I(t) < max(L_1, L_2)$ (plus a certain margin) should be considered for a potential collision. Thus, only final part of the trajectory, from where this condition is first satisfied, should be converted to the body frame and checked for possible collisions. While keep-out surfaces with complex geometries that accurately fit the target can be considered, it is advisable to use convex shapes to facilitate the optimisation.

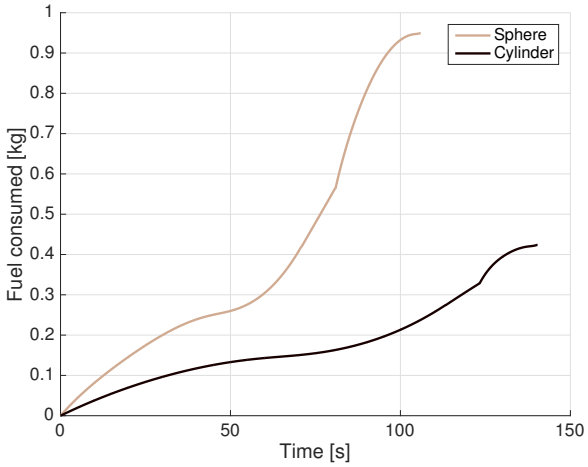

Figure 4.29: Fuel consumptions of two trajectories (no free coefficients) considering a cylindrical keep-out volume and a sphere.

Another aspect of obstacle avoidance is the case where a propulsion system failure occurs. In this scenario, a fail-safe or drift-away trajectory is that in which the velocity vector does never point towards the target. In the hovering segment, the spacecraft would naturally drift away in case of thruster failure, since centripetal force would no longer be applied. Segment 3, however, can be single-point failure. Precisely, this is why the hovering phase is introduced: to give the opportunity of a last health check. In segment 3—a linear path towards the docking point—the relative radial velocity could be limited, so that when it is added with the predicted tangential velocity at every point, the resultant points away from the (spinning) target. Since the constraint of zero final acceleration makes the radial velocity decrease as the spacecraft approaches the docking point, a complete fail-safe segment 3 is achievable. In segment 1, the simplest way to ensure a fail-safe situation is to use a keep-out sphere, instead of a surface closely fitting the target. With a sphere and hovering point, the polynomial trajectories naturally provide a spiral-in approach; hence at any point the spacecraft would drift away in case of propulsion failure. A smallest keep-out surface means a less fuel-expensive hovering and final segments, but trajectories might not be fail-safe. In this case, a penalty function can be introduced in the simulation to avoid the velocity vector from pointing to the target. The resulting fail-safe trajectory, however, reduces the fuel savings made by choosing a non-spherical keep-out surface.

4.4.5 Torque constraints of a single-thruster chaser

The baseline scenario of this work considers a chaser spacecraft with 6-DOF control, i.e. the translational motion is decoupled from the rotational motion. This assumption stems from the requirement that the chaser must constantly point its cameras and range-finders independently of its flight path. This would be allowed by a set of RCS thrusters on the spacecraft. However, in this section it is discussed how a spacecraft with a single thruster can perform the same docking manoeuvre (the target-pointing requirement is not considered). In this scenario, the ADCS system steers the spacecraft according to the direction of the planned acceleration vector. The attitude control system is not specified (e.g. reaction wheels or attitude-only small thrusters) but its torque limit is low enough so that it must be enforced as a constraint in the trajectory optimisation process.

During the optimisation, the torque profile $\mathbf{T}(t)$ is numerically evaluated with the normalised acceleration vector $\hat{\mathbf{a}}(t)$ (whose elements are time polynomials), which is

$$\hat{\mathbf{a}}(t) = \frac{\ddot{\mathbf{r}}^I(t)}{\|\ddot{\mathbf{r}}^I(t)\|} \tag{4.30}$$

If the angle between the acceleration vectors $\hat{\mathbf{a}}(t)$ and $\hat{\mathbf{a}}(t+dt)$ is

$$d\theta = \cos^{-1}(\hat{\mathbf{a}}(t) \cdot \hat{\mathbf{a}}(t+dt)) \tag{4.31}$$

then

$$\dot{\theta}(t) = \frac{d\omega}{dt} = \frac{\cos^{-1}(\hat{\mathbf{a}}(t) \cdot \hat{\mathbf{a}}(t+dt))}{dt} \tag{4.32}$$

which can be approximated with a sufficiently small $dt \leftarrow \Delta t$. Using the second-order Taylor expansion, the inverse cosine function can be avoided:

$$\cos, d\theta \approx 1 - \frac{d\theta^2}{2} \approx \hat{\mathbf{a}}(t) \cdot \hat{\mathbf{a}}(t+dt)) \tag{4.33}$$

thus

$$d\theta = \sqrt{2(1 - \hat{\mathbf{a}}(t) \cdot \hat{\mathbf{a}}(t+dt)))} \tag{4.34}$$

which can replace the term $d\theta$ in Eq. 4.32. The angular acceleration of $\hat{\mathbf{a}}(t)$ can be similarly evaluated with

$$\ddot{\theta}(t) \approx (\dot{\theta}(t+\Delta t) - \dot{\theta}(t))\frac{1}{\Delta t} \tag{4.35}$$

Finally, assuming that the torque vector lies in the plane orthogonal to $\hat{\mathbf{a}}$ (there is no torque applied along the direction of the acceleration vector, which in turn

is fixed to the body and parallel to the thruster direction) and the moment of inertia I_{ch} is the same in any direction in this plane, the torque is

$$\mathbf{T}(t) = I_{ch}\ddot{\theta}(t) \tag{4.36}$$

The assumption of equal moment of inertia in the $\hat{\mathbf{a}}$ plane would be valid in the case of a cylindrical body, which most likely the chaser spacecraft is not. Additionally, if the total torque vector is composed by two or more vectors corresponding to actuators in different directions, the torque limit is not the same in all directions. However, these assumptions can provide a fair enough prediction of the torque profile used to ensure the feasibility of the trajectory in terms of the attitude actuators. Worst-case parameters should be chosen for robustness—the highest I_{ch} and the lowest torque limit T_{lim}.

Figure 4.30 shows the torque profile of the trajectory (segment 1) where the torque limit is not considered. The optimisation variables are the initial and final time (no free polynomial coefficients).

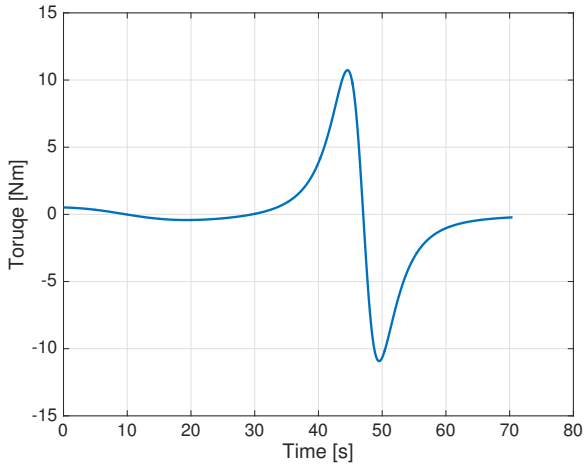

Figure 4.30: Torque profile of a trajectory shaped with 4-th-deg. polynomials. No torque constraint is considered.

Due to the continuous nature of the polynomial functions that shape the trajectory), there are no instantaneous changes in the acceleration direction (except at the intersection points between segments). Therefore, the acceleration vector changes direction smoothly and an attitude system should be able to track it. However, there is a singularity where the acceleration reduces its magnitude along a fixed direction, reaches zero, and increases again in the opposite sense. In this case, the spacecraft should instantaneously slew by 180 deg (unless it

had a *second* thruster pointing in the opposite sense). In Fig. 4.30, situations close to this singularity cause the high torque peaks which rend a single-thruster spacecraft unable to follow this trajectory.

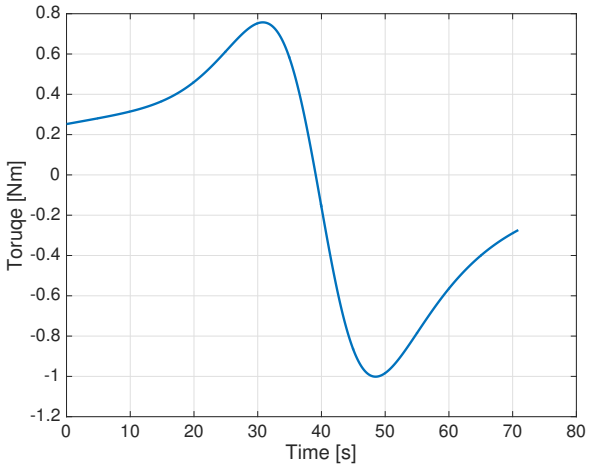

Figure 4.31: Torque profile of a trajectory shaped with 4-th-deg. polynomials. Maximum torque is limited to 1 Nm.

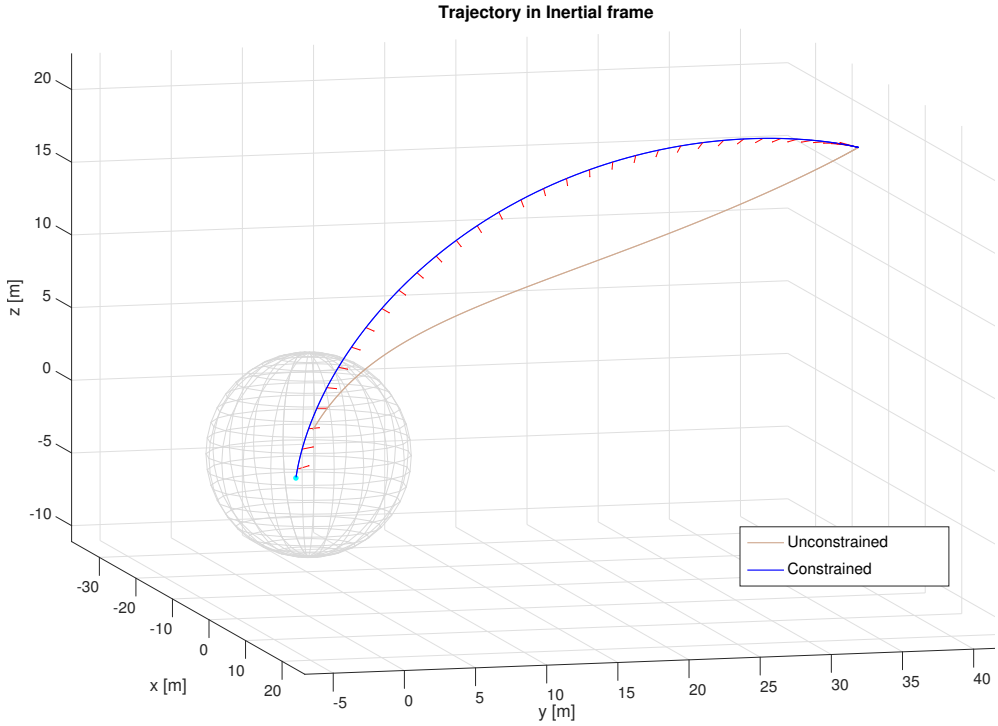

Figure 4.32: Segment 1 of a trajectories shaped with 4-th-deg. polynomials. Both the torque constrained and unconstrained cases are shown.

When the torque constraint is taken into account in the optimisation, with a torque limit of $T_{lim} = 1$ Nm and a moment of inertia of $I_{ch} = 310$ kgm^2, a feasible trajectory is found. The new torque profile is shown in Fig. 4.31, where the maximum torque in the profile is equal to the torque limit. Figure 4.32 shows the trajectories in the inertial frame of the torque-constrained and unconstrained cases. Note how the constrained case the trajectory is less linear, which induces an overall higher acceleration magnitude, which avoids the singularity case previously described. However, the fuel consumed is higher, at 0.52 kg as opposed to the 0.42 kg of the unconstrained case. Note that the feasible (torque-constrained) trajectory has a similar duration to the unconstrained one, but the initial time happens 4 s later—enough to substantially modify the trajectory.

However, the lowest maximum torque that a trajectory with only two optimisation variables (initial and final time) can find is $T_{max} = 0.55$ Nm (0.56 kg consumed). Thus, if a lower torque limit was required, higher order polynomials would be required. With one additional term feasible trajectories are found with a torque limit of 0.41 Nm (Fig. 4.33b), and 0.6 kg of fuel consumed (as opposed to the 0.33 kg of the unconstrained case). As shown in Fig. 4.33a, the torque peak in the unconstrained case is much higher than the one in Fig. 4.30, yet the attainable torque limit is lower due to the additional degrees of freedom.

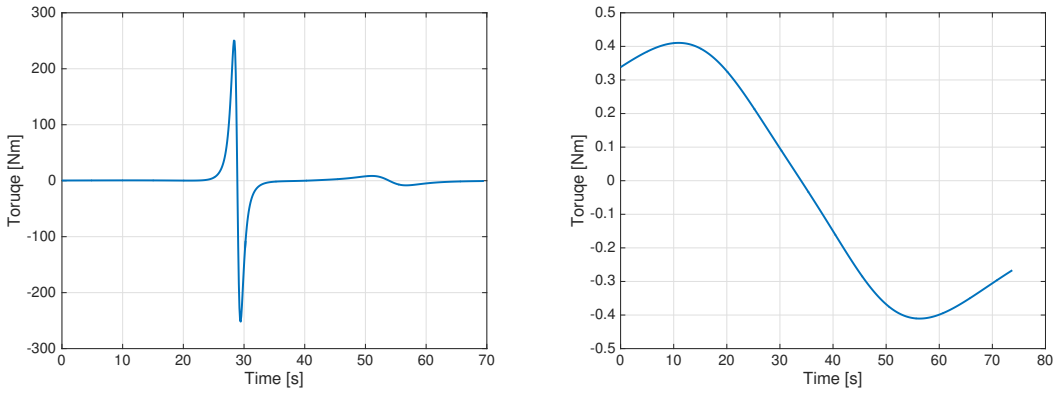

(a) **(b)**

Figure 4.33: Torque profile of a trajectory shaped with 5-th-deg. polynomials. Maximum torque is limited to 0.4 Nm.

In segment 2, an analogous approach is conducted. In conclusion, on the one hand a single-thruster spacecraft is a simpler system than a 6-DOF one; on the other

hand the trajectory planning is more complex and the solutions are more fuel-consuming. Also, the fact that the chaser is not able to observe the target at all times makes feedback guidance and control impossible, unless there is an external observer (e.g. another spacecraft in close proximity or a fractioned navigation system).

4.5 Simulations

4.5.1 Guidance and control approach

The final conditions of the trajectory are obtained using a prediction of the target's attitude at a certain time t_f. An axisymmetric body approximation is used, which allows to evaluate the target's motion analytically. However, there will be a discrepancy between the internal model and the real inertia matrix. This results in an offset between the predicted and actual position. Many spacecraft have some degree of axial symmetry, so the matrix of inertia can be roughly approximated to be purely axisymmetric. The actual target inertia matrix accounted for in the simulation is [39]

$$J_{sc} = \begin{bmatrix} 17023 & 397 & -2171 \\ 397 & 124826 & 344 \\ -2171 & 344 & 129112 \end{bmatrix} \tag{4.37}$$

However, the axisymmetric inertia matrix implemented in the internal model of the trajectory planner is

$$J_{mdl} = \begin{bmatrix} 17000 & 0 & 0 \\ 0 & 127000 & 0 \\ 0 & 0 & 127000 \end{bmatrix} \tag{4.38}$$

causing the actual target's attitude to diverge from the predicted one as time goes. The error between the predicted and actual natural motion of the target can be visualized in Fig. 4.34. Thus, the smallest the sample time at which the current state of the target is updated, the lowest the error will be.

When the spacecraft is idle at the prescribed initial/standing position, the trajectory optimisation of the first segment is run (either on-board or ground-based). The trajectory parameters are obtained, i.e. the initial or waiting time t_0, the final time or trajectory duration t_{s1}, and any free coefficients of polynomials with additional terms (beyond the matching of boundary conditions). The trajectory

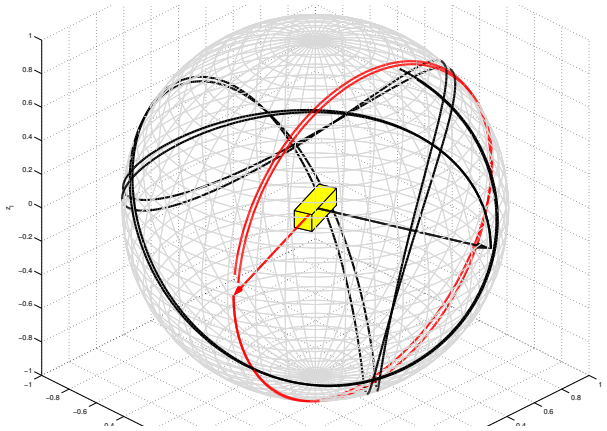

Figure 4.34: Path of the axes $\hat{\mathbf{e}}_1$ (red-dashed) and $\hat{\mathbf{e}}_2$ (black-solid) for the actual and the approximated bodies

parameter of the third segment (duration) is predetermined since it does not depend on the current state of the target, being planned in the body frame.

During the manoeuvre, the optimised trajectory parameters remain fixed. However, the predicted and actual attitude of the target diverge. To overcome this divergence, the set of polynomial coefficients (which are determined by the boundary conditions) are re-computed at the sample rate of the navigation system, which determines the current rotational state of the target and the chaser's relative position. The acceleration profile is commanded to the RCS until the next refreshment of the trajectory.

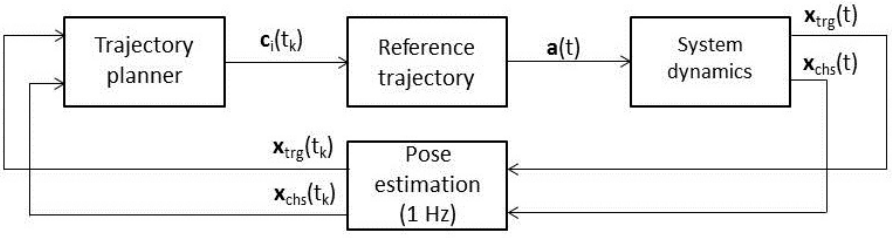

Figure 4.35: Guidance system block schematics

As shown in Fig. 4.35, this approach creates a feedback loop, which makes the system robust to the aforementioned model inaccuracy and other disturbances. The vector $\mathbf{c}_i(t_k)$ contains the polynomial coefficients of the coordinate $i = \{1, 2, 3\}$, which is updated at every sample time t_k by the *trajectory planner* block (except for any free coefficients, which are fixed). In the *trajectory planner* block, the final state of the target is analytically evaluated at the remaining time-to-go from the time at the sample ($t_{go} = t_{s1} - t_k$), and equating the initial boundary

conditions to the state at the sample (i.e. $\mathbf{r}(0) = \mathbf{r}_k$ and $\dot{\mathbf{r}}(0) = \dot{\mathbf{r}}_k$), the trajectory coefficients can be updated with

$$\begin{bmatrix} 1 & 0 & 0 & 0 & 0 \\ 0 & 1 & 0 & 0 & 0 \\ 1 & t_{go} & t_{go}^2 & t_{go}^3 & t_{go}^4 \\ 0 & 1 & 2t_{go} & 3t_{go}^2 & 4t_{go}^3 \\ 0 & 0 & 2 & 6t_{go} & 12t_{go}^2 \end{bmatrix} \begin{bmatrix} a_{i0} \\ a_{i1} \\ a_{i2} \\ a_{i3} \\ a_{i4} \end{bmatrix} = \begin{bmatrix} r_i(0) \\ \dot{r}_i(0) \\ r_i(t_{go}) - a_{i5}t_{go}^5 \\ \dot{r}_i(t_{go}) - 5a_{i5}t_{go}^4 \\ \ddot{r}_i(t_{go}) - 20a_{i5}t_{go}^3 \end{bmatrix} \tag{4.39}$$

Note that after updating the coefficients with $t_f = t_{go}$ (Eq. 4.39), the clock time is reset to zero, although it is also possible to plan the polynomial with a non-zero initial time equal to the clock time at the sample. Since only minor adjustments are made to the trajectory, it is not necessary to re-check the constraints that were already satisfied in the trajectory optimisation. When the coefficients are updated at every sample time (T_s =1 s in the example of Fig. 4.35), they are passed into the *reference trajectory* block. In this block, the instantaneous acceleration is calculated with the polynomial using the corresponding coefficients and the clock time t. The output acceleration is commanded to the RCS system (unmodelled, but assumed to output the required thrust to match the acceleration profile). A schematic diagram applicable to segments 1 and 3 is shown in Fig. 4.36. The chaser follows the planned (or predicted) trajectory until the states of the chaser and target are updated at every sample time t_k, forcing a re-direction of the trajectory given the new predicted final state of the target.

The different segments follow this guidance scheme each with a particular flavour. The hovering and final approach trajectories (segments 2 and 3) are planned in the *trajectory planner* block relative to the body frame, thus, unlike segment 1, the target's final attitude is not calculated there. Instead, the current attitude of the target is calculated in the *reference trajectory* block using the last known state and the time from it ($t - t_k$). This predicted attitude is used to convert the planned trajectory from the body frame to the inertial frame, to obtain the actual commanded acceleration. (In other words, it evaluates the fictitious forces the chaser has to counteract in order to follow the body-frame trajectory as planned). Since the *reference trajectory* block works in real time (or at the highest possible frequency), using an analytical approach to predict the target's motion (such as the one presented in Sec. 4.1) is critical for obtaining an acceleration profile as smooth as possible. In contrast, while the maximum frequency of the *trajectory planner* block can also be very high, it is limited by the update rate of the navigation system.

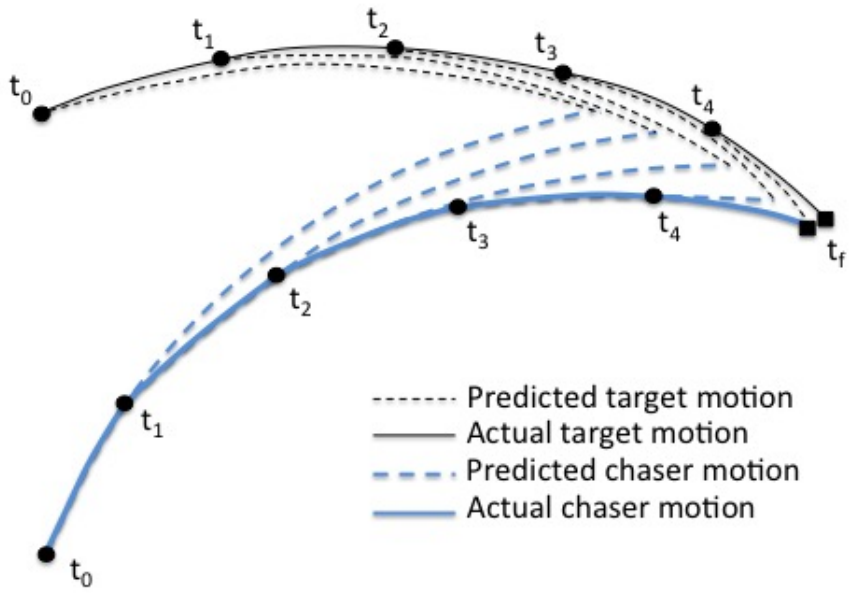

Figure 4.36: Schematics of the guidance approach (segments 1 and 3)

Finally, during the hovering segment, a receding horizon approach has been used with the same polynomial method in order to regulate the position of the chaser. The chaser reaches the desired final position (i.e. the hovering point) from the last known state at the specified receding horizon time. Or more accurately, it reaches the *predicted* final position, using the polynomial acceleration profile calculated in the last sample time. If the sample time T_s is equal to the receding horizon time T_{rh}, a new sample will be obtained at the end of the calculated trajectory. In a perfect world, the chaser would be right at the hovering point, but there will be an error proportional to the internal model inaccuracy (and other perturbations if present). Hence, a new trajectory will be computed in order to bring the chaser to the new predicted final position in T_{rh} seconds. As shown in the schematics of Fig. 4.37, there will always be an offset given by the time between samples and the internal model accuracy.

4.5.2 Results

In the simulation initial conditions, the chaser's standing position distance is 50 m. The chaser spacecraft has a wet mass of 100 kg, its RCS has a maximum thrust magnitude set to 15 N in any direction (which is a simplification of the cube defined by the total thrust vector), and an I_{sp} of 50 s (cold gas). The target

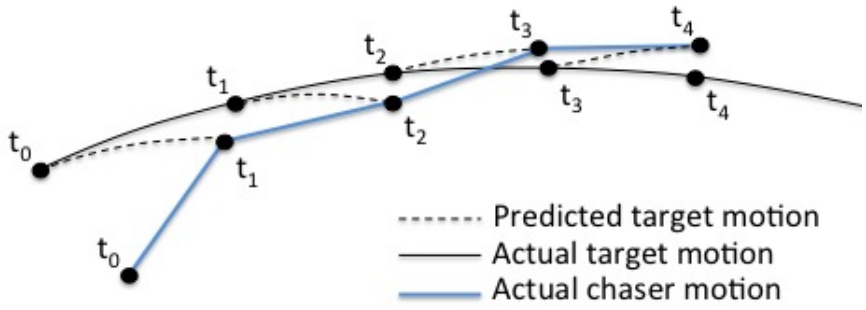

Figure 4.37: Schematics of the guidance approach (segment 2 with receding horizon)

is based on Envisat, with a keep-out surface of cylindrical shape with elliptic base. Its body has dimensions 10×2×2 m, and the solar panel 10×4 m. The 3-segment strategy is implemented with the same parameters as in Sec. 4.4.1. At the start of the manoeuvre, the target $\hat{\mathbf{e}}_1$ body axis has an angle with $\mathbf{h}$ of 70 deg, and the magnitude of the angular velocity is 6 deg/s (1 rpm). The simulation propagates the orbits of the two bodies to account for the virtual acceleration of orbital relative motion. The target is in a 800 km circular orbit inclined 98 deg.

The guidance scheme is implemented as shown in Fig. 4.35. The baseline sample time is 1 s [81], although recent advances using LIDAR-based pose estimation techniques [48] improve the 1-second sampling rate for pose estimation of the target.

The purpose of this section is to demonstrate the feasibility of the polynomial planning method using the guidance strategy previously described. Simulations have been performed shaping the trajectory using a) polynomials with additional terms (or two free coefficients per polynomial), and b) polynomials with the minimum degree. In the first case, the trajectory has a duration of 112.3 s, while in the second case it has a longer duration of 113.3 s. The initial time has been set to zero. Although both durations are similar, the free coefficients in the first case modify the trajectory (in the first segment) so that the fuel consumption is lower. Both cases have the same prescribed hovering time (10 s) and third segment duration (17 s). The body-fixed hovering occurs 1.5 m above the docking point.

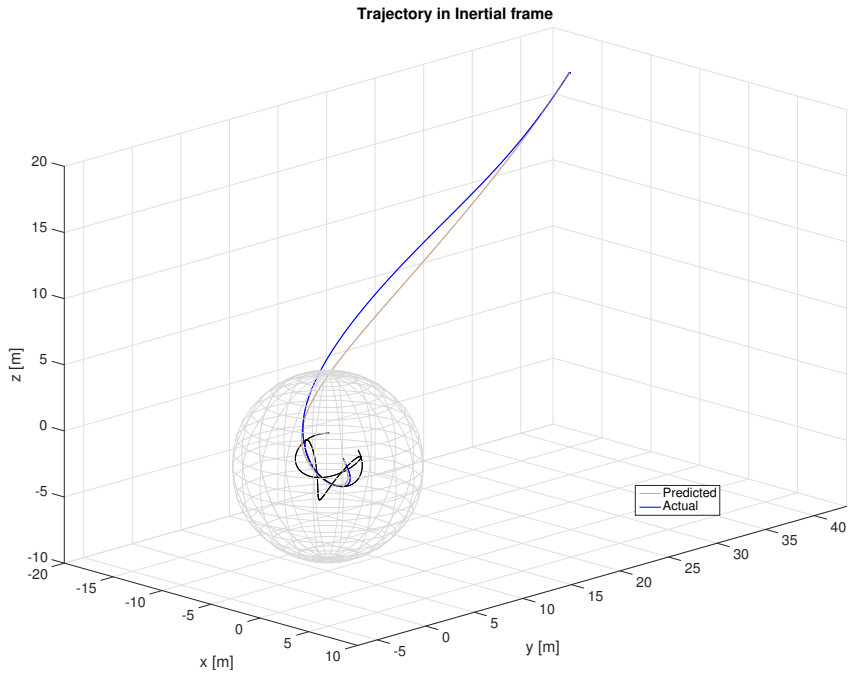

Figure 4.38: Trajectory of the simulation in the inertial frame (minimum-order polynomial). A 7-meter radius sphere is shown for scale.

4.5.2.1 Minimum-order polynomials

Figures 4.38 and 4.39 show the trajectories in the inertial and body frame, respectively. The actual or simulated trajectory is compared with the one used for calculating the chaser motion during the optimisation process. The actual trajectory diverges from the predicted one mostly due to the axisymmetric approximation of the target used in the internal model to evaluate its motion. The hovering and the docking segments—which are critical due to the proximity to the target—match the prescribed paths with precision, as seen in the trajectory expressed in the body frame.

In Fig. 4.40 the thrust profile is represented, with the two dashed vertical lines separating the segments of the trajectory. Close to the end of the first segment the thrust experiences jittering, since as the time-to-go tends to zero, any error would induce infinite acceleration. This effect is mitigated by starting the tracking of the hovering point (with receding horizon) a few seconds before the actual t_{s1} time. Similarly, the thrusters are cut-off one second before reaching the final time of segment 3. As shown in Fig. 4.41, the difference between the predicted fuel consumption, which has been optimised, and the actual one is not large—however, a safety margin should be considered if the fuel budget is tight.

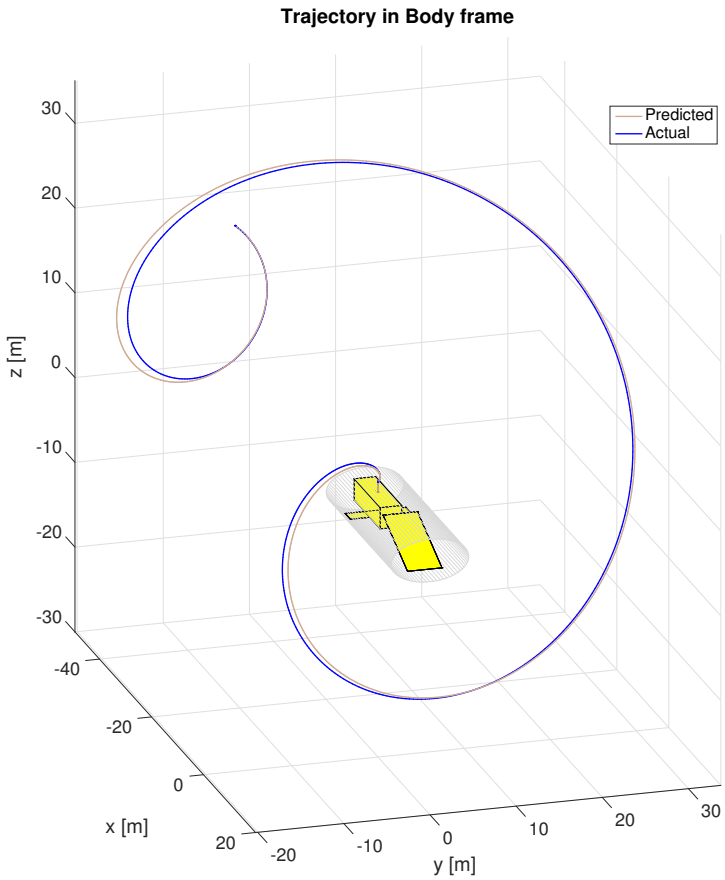

Figure 4.39: Trajectory of the simulation relative to the body frame (minimum-order polynomial).

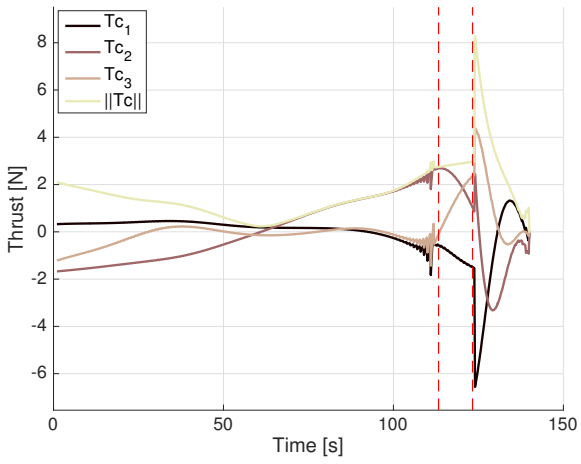

Figure 4.40: Commanded thrust (minimum-order poly.). Vertical lines separate trajectory segments.

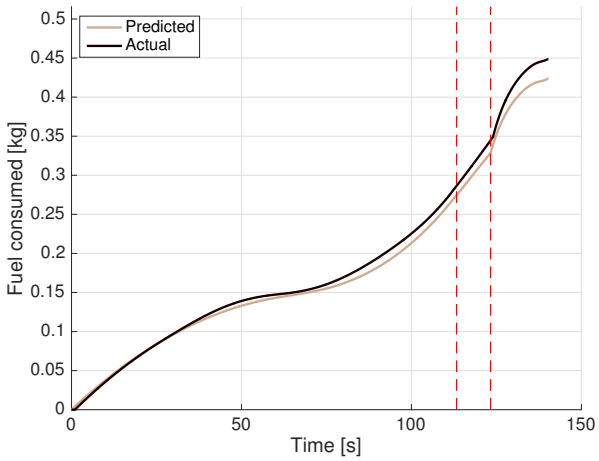

Figure 4.41: Predicted and actual (simulated) fuel consumption (minimum-order poly.). Vertical lines separate trajectory segments.

Figure 4.42 show the position, velocity and acceleration relative to the target's body frame. The chaser is shown maintaining its fixed position at the hovering point (relatively close to the target but still at the edge of the obstacle free area), before accelerating to make contact smoothly with the docking point below.

4.5.2.2 Polynomials with two additional terms

Figures 4.43 and 4.44 show the trajectory shaped using polynomials with two additional terms and the fuel consumption. The fuel consumption is lower than the one obtained using minimum-order polynomials, but the difference between the predicted and the actual consumption is higher. Large values of the free coefficients may cause larger divergences of the actual trajectory with respect to the predicted one, due to the increased sensitivity of the polynomial functions to changes in the boundary conditions. The sensitivity could be limited if the magnitude of the free coefficients was limited in the optimisation, making the actual trajectory diverge less from the predicted one, despite the internal model inaccuracies.

Another simulation is performed where the free coefficients have one order of magnitude less than the previous case. As seen in Fig. 4.46, the predicted fuel consumption at the end of the first segment is higher than the one in Fig. 4.44, since some optimisation variables have been limited. However, the difference between the predicted and the actual values is smaller, as seen in Fig. 4.45, and

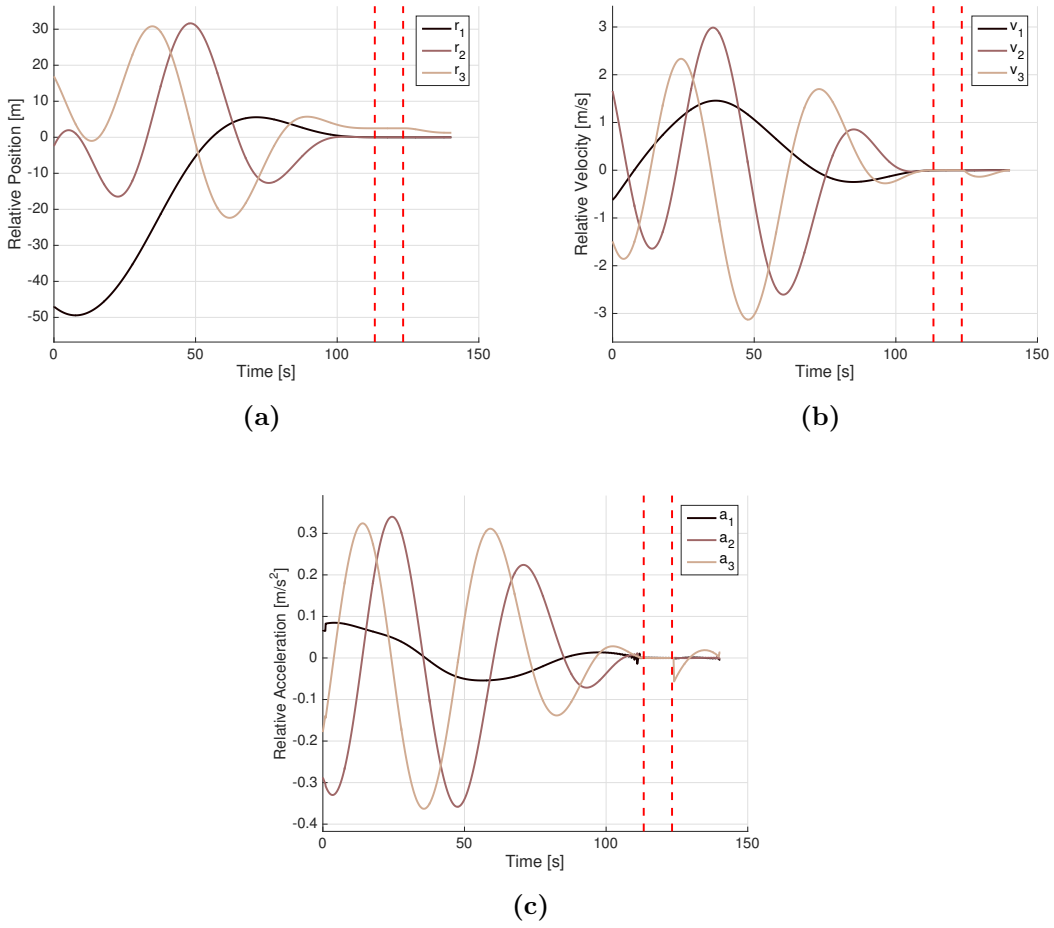

Figure 4.42: Position, velocity and acceleration components relative to the body frame (minimum-order poly.).

is of the same order as the minimum-order case (Fig. 4.41). Nonetheless, the better optimisation of the first case compensates the reduced divergence of the second, and the actual fuel consumption is the same in both cases. It could be good practice, however, to choose the limiting of the free coefficients since it is a controllable factor—rather than hoping that the difference with the predicted optimal consumption will not be too high.

Also, note that the distance between the actual and predicted paths is rather similar in both cases (Figures 4.43 and 4.45), and also in the minimum-order polynomial case (Fig. 4.38). The divergence of the actual path with the predicted one poses a risk of collision if this constraint is not taken into account at every re-computation of the trajectory (which it isn't, in order to simplify the on-board algorithm during the manoeuvre). However, as seen in the body frame (Fig. Fig.

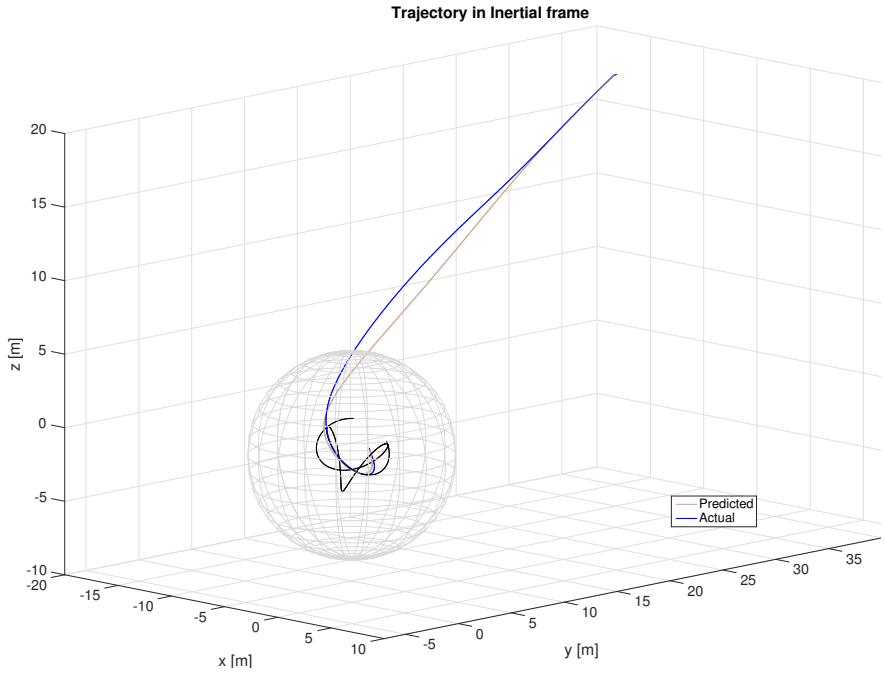

Figure 4.43: Trajectory of the simulation in the inertial frame (two free coefficients). A 7-meter radius sphere is shown for scale.

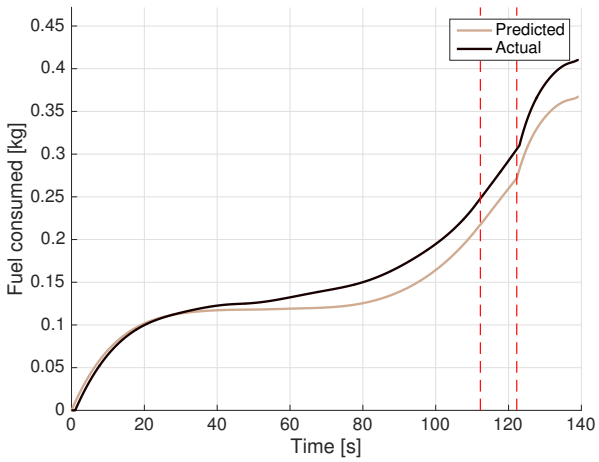

Figure 4.44: Predicted and actual (simulated) fuel consumption (two free coefficients). Vertical lines separate trajectory segments.

4.39), the divergence is small enough so that an intersection of the actual path with the keep-out surface is unlikely.

Alternatively, depending on the computational resources available, the free coefficients could be re-optimised at every sample time during the manoeuvre. However, this makes the software design much more critical, since convergence of the

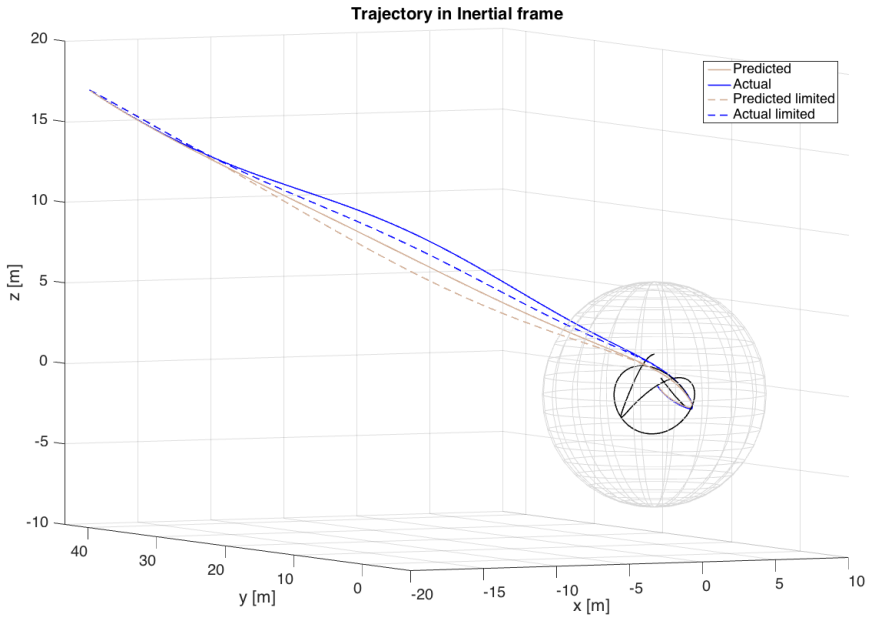

Figure 4.45: Trajectory of the simulation in the inertial frame (two free coefficients). Dotted lines: coefficients with limited magnitude; solid: unconstrained magnitude. A 7-meter radius sphere is shown for scale.

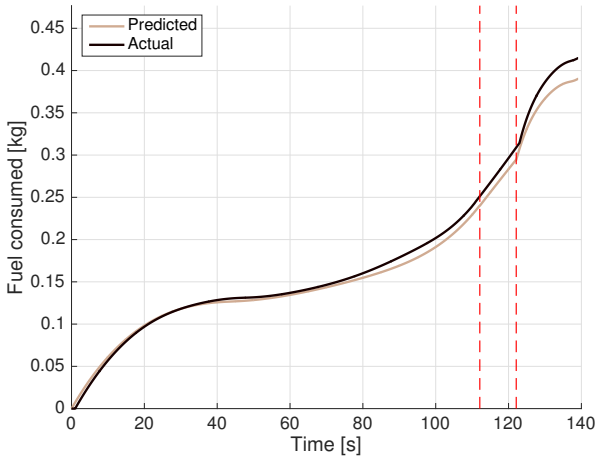

Figure 4.46: Predicted and actual (simulated) fuel consumption (two free coefficients with limited magnitude). Vertical lines separate trajectory segments.

optimisation to a feasible solution should be ensured (otherwise, the manoeuvre should be aborted if a feasible solution was not obtained within the allocated sample time).

4.5.2.3 Re-optimisation after waiting time

It has been shown that the initial time of the trajectory, which allows for the target to rotate to a favourable attitude before starting the manoeuvre, has an influence on the fuel expenditure (Fig. 4.9). However, if the waiting time is long, the chaser will initiate the manoeuvre with the target at a different initial attitude that the one it was used to optimise the trajectory's first segment, leading to a trajectory with a higher divergence (from the predicted one) than one with $t_0 = 0$. This divergence is exacerbated in the case of polynomials with additional terms, which leads to a higher fuel consumption. However, this effect is significantly minimised if the free coefficients are updated with the target's attitude moments before the predicted initial time, so that the predicted and initial attitudes of the target are the same. In this case, the optimisation is simplified by the fact that the initial time and final time are fixed, and the previously found coefficients can be used as an initial guess.

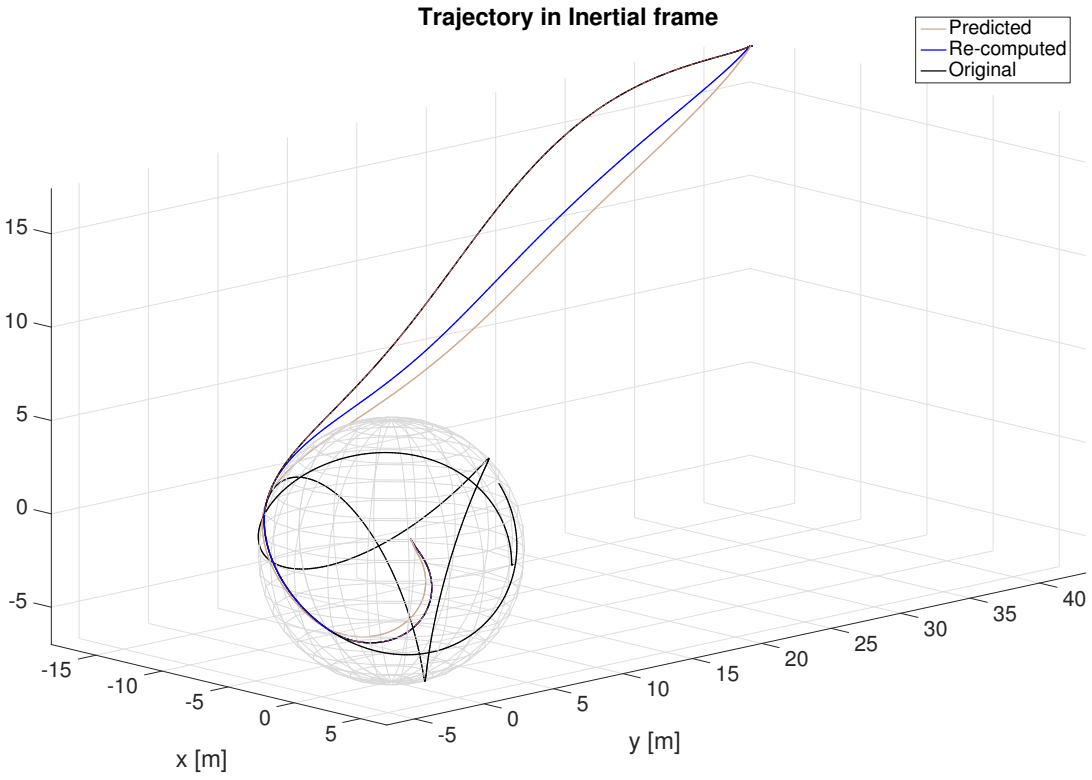

Figure 4.47: Predicted, original, and re-computed (1st segment) trajectories (polynomials with two additional terms) shown in the inertial frame

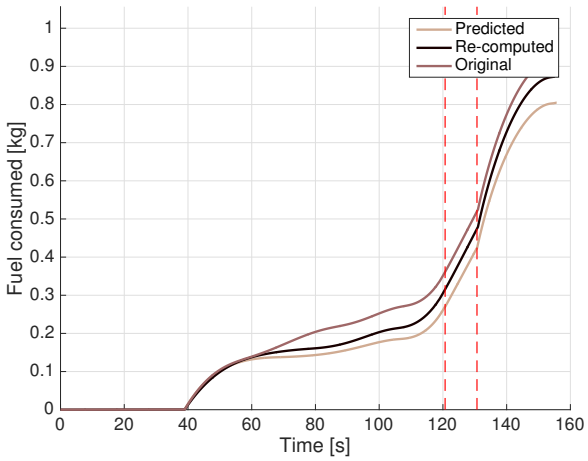

Figure 4.48: Fuel consumption of the predicted, original, and re-computed (1st segment) trajectories (polynomials with two additional terms)

Figure 4.47 shows a manoeuvre with a waiting time of 38 s and a duration of 81 s, where the trajectory is shaped with 6^{th}-degree polynomials (two extra coefficients per coordinate). The original trajectory that the chaser would follow with the trajectory parameters obtained before the initial time diverges from the predicted trajectory. The trajectory which uses the re-computed free coefficients follows more closely the predicted one and spends less fuel (Fig. 4.48).

4.5.2.4 Robustness to long sample times

One of the characteristics of the guidance method presented is its ability to endure a low sample rate thanks to the internal model. In the uncooperative docking scenario, longer-than-usual sample times are likely due to complex vision-based navigation systems. In this subsection, the guidance method is stressed by testing a range of sample times. The test sample times are $T_s = 1$, 5, 10, 30 seconds, and the metric chosen for performance comparison is the relative position error during the critical segments—hovering and final approach. The cylindrical keep-out surface and the docking axis aligned with the 3^{rd} body axis are considered.

Figure 4.49 shows the error in relative position, during hovering and final approaches (marked by the vertical lines), for different sample times. The range of the y-axis in the figures is the same for all cases ($\pm$ 20 cm). Expectedly, a very low error is obtained with a 1 s sample time. A maximum of 5 cm error is obtained with 5 s (Fig. 4.51b) but the error at the end of the third segment is below

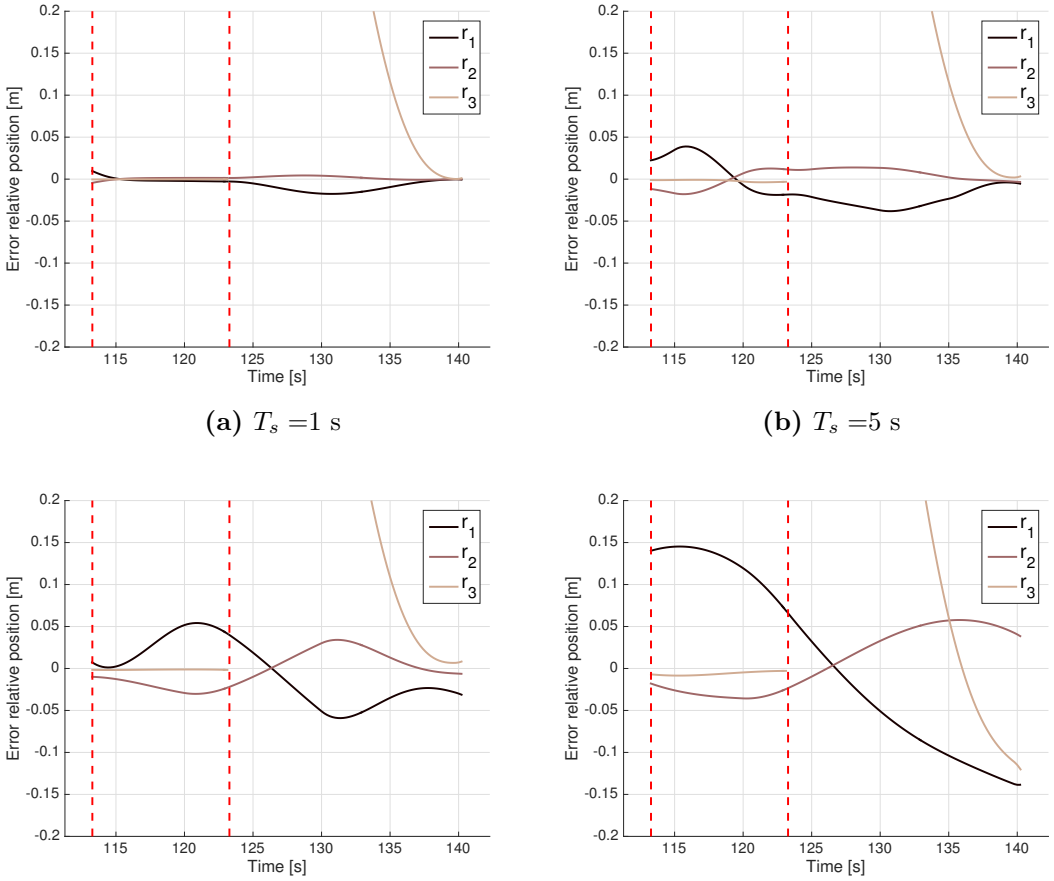

(a) T_s =1 s **(b)** T_s =5 s

(c) T_s =10 s **(d)** T_s =30 s

Figure 4.49: Relative position error of the hovering and final segments, for different sample times.

1 cm. Higher errors are obtained with T_s =10 s, but still within the 5 cm range. The error is much larger with a sample time of 30 s, where for the most part of the 2^{nd} and 3^{rd} segments the manoeuvre is performed in open-loop. Whether or not a 15-cm error is acceptable depends on the requirements of the mission (the trajectory is visualised in Fig. 4.50). Additionally, note that the altitude component (r_3) has a better accuracy than the other components, implying that the chaser oscillates about the hovering point at roughly the same distance from the target and close to the keep-out surface.

Regarding the receding horizon time approach used in the hovering segment, its ratio over the sample time defines how rapidly the chaser corrects its position (the smaller it is, the more aggressively the chaser will react). However, the receding horizon time should not be larger than the designated hovering time, or

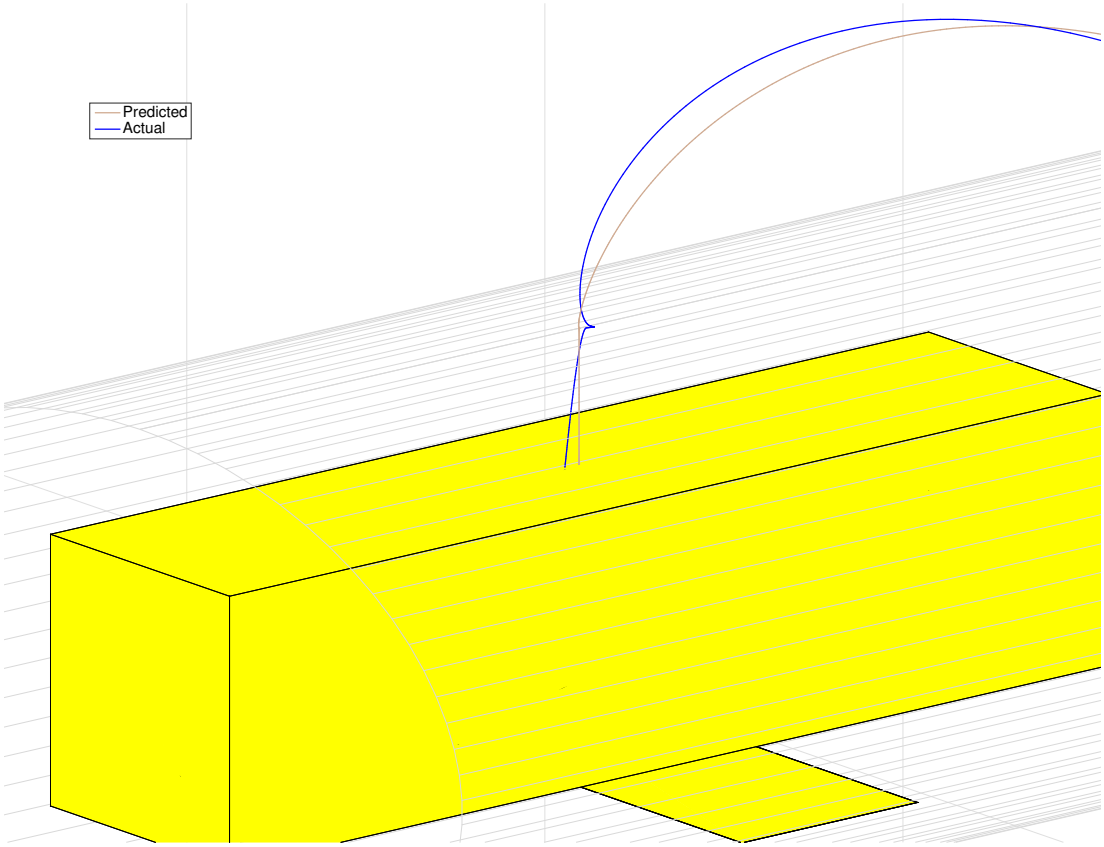

Figure 4.50: Close-up detail of the spacecraft: Final segments of a trajectory simulated with T_s =30 s. The light brown trajectory represents the trajectory obtained in the first optimisation, while the blue one is the simulation result.

the error at the beginning of the final segment would be larger than the minimum possible. Some tuning of those parameters is required, and during this study it was found that receding horizon times somewhat larger than the sample time (1 to 3 times) was a fair trade-off—with the exception of sample times larger than the duration of the hovering segment. Figure 4.51 illustrates these points by comparing different receding horizon times (1 s and 6 s, for a simulation with a fixed sample time of 1 s).

4.6 Chapter summary

A trajectory planner based on polynomial shaping of the chaser spacecraft coordinates has been presented. A three-segment trajectory approach has been proposed for docking safely with an uncooperative target. A keep-out sphere has been used as a means for simple and safe obstacle avoidance, as well as a more

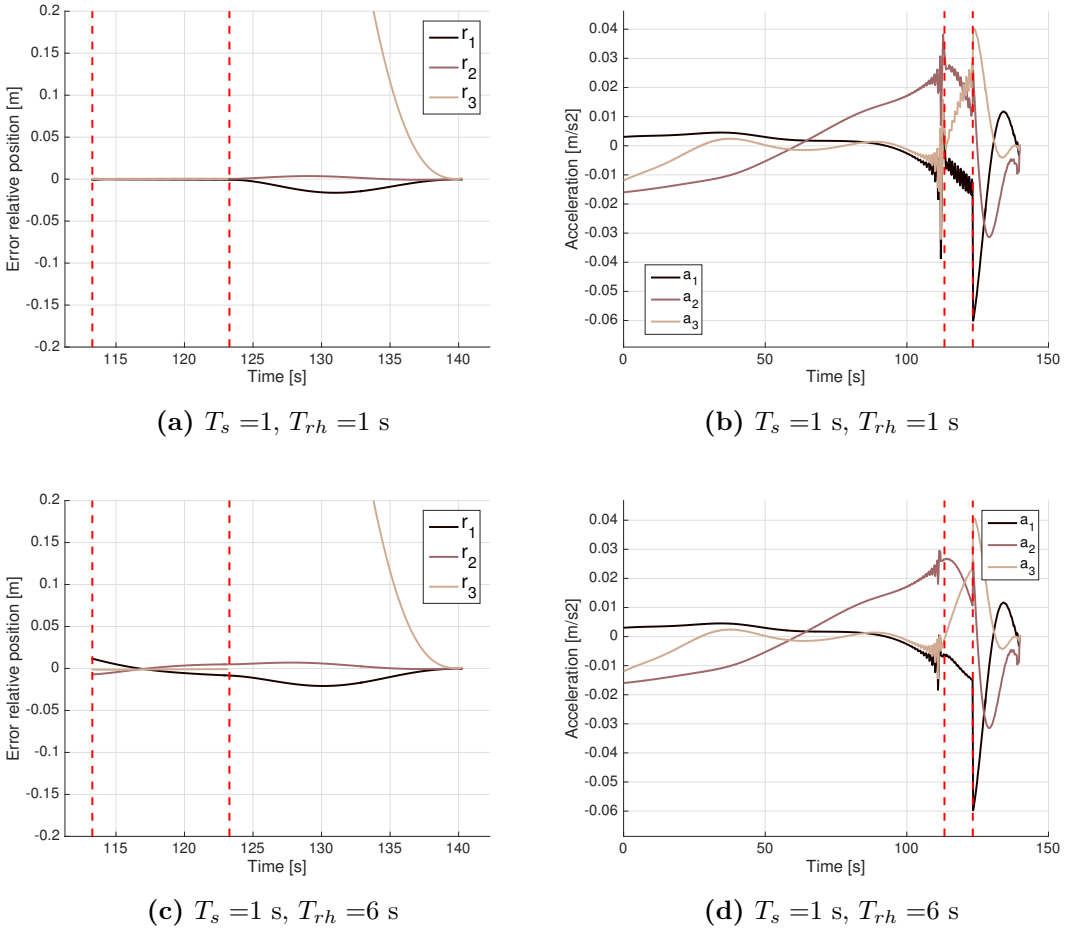

(a) T_s =1, T_{rh} =1 s

(b) T_s =1 s, T_{rh} =1 s

(c) T_s =1 s, T_{rh} =6 s

(d) T_s =1 s, T_{rh} =6 s

Figure 4.51: Relative position error of the hovering and final segments, comparing different receding horizon times (with same T_s =1 s).

complex cylinder with elliptical base. Given some boundary conditions, the only variable required to define a trajectory is the manoeuvre duration, making this approach computationally efficient. Other variables such as the initial time and free coefficients of higher-order polynomials can be considered in order to further optimise the trajectory. Via inverse dynamics, fuel and thrust can be evaluated, leading to the minimisation of fuel consumption (amongst this class of polynomial trajectories) while ensuring the feasibility of the motion. Obstacle avoidance is also taken into account, with a prescribed keep-out surface enclosing the target with its appendages. The trajectory planning method depends on the prediction of the target's attitude and motion a certain time of arrival. In order to keep computational cost low, an axisymmetric approximation has been considered, for which closed-form solutions of the target's attitude motion exist. Due to the

discrepancy between the internal and actual model of the target's inertia matrix, the trajectory planner is implemented in a closed-loop fashion whose frequency is limited by the pose estimation sensors.

In conclusion, a feasible and quasi-optimal trajectory is quickly obtained before the manoeuvre is executed, which is followed by re-computing the polynomials' coefficients with the updated boundary conditions. Results show that this guidance scheme is able to successfully reject the model inaccuracy disturbance, a relatively low sampling rate, and the fictitious acceleration due to the orbital relative motion.

There are many possible variants to the approach strategy, such as matching accelerations between segments to ensure thrust smoothness, which results in different fuel consumptions. Since the goal of this work is to show the functionality of the polynomial planning method, not all the possible alternatives have been presented. In a real ADR mission, an extended analysis would be undertaken tailored to the specific requirements and constraints, where the theoretical tools and some recommendations are provided in this chapter.

This work focuses on guidance and control, however a good navigation system is fundamental to accurately predict the current state of the target. It has been shown that a long sample time is not an insurmountable challenge, thus, more time can be invested in obtaining precise sensor data. In the simulations, the orbital dynamics and a non-diagonal inertia matrix have been modelled. Given the short duration of the manoeuvre compared with the orbital period of the system, the "formation flying" dynamics were negligible (equal results are obtained if the chaser-target pair is modelled in a deep space environment). A perfect RCS and navigation systems have been considered. However, given the deliberately large error of the internal model, the robustness of the guidance method presented has been put to test all the same.

Regarding the use of higher-order polynomials (in the optimisation of the first segment), with no free coefficients considered, it is possible to satisfy all the constraints with small variations of the initial time and duration only. The performance index (fuel) can be further optimised if more degrees of freedom are considered in the form of the coefficients of the polynomials' additional terms. However, in the cases studied, the difference in the fuel consumption optimal value between a minimum-order polynomial and one with two additional coeffi-

cients is not very high (a 35% improvement, Table 4.1), showing that good results can be obtained using low computational resources.

Chapter 5

The Attitude Stabilisation Electromagnetic Module concept for detumbling debris

In this chapter, the ASEM system is designed and the feasibility of the concept is assessed.

The Envisat case is considered again as the baseline scenario. In this work, a trade-off discussion of various architectures is realised. The control problem of detumbling a spacecraft by magnetic means is addressed, firstly using a 2D simplified model in order to obtain some quick estimations during the system optimisation. A preliminary sizing of the system elements is realised, where the polynomial motion planning method is used to size the propulsion system (and demonstrate the feasibility of autonomous docking). Finally, simulations are performed, using an orbital model, where different cases are tested and compared.

5.1 Baseline architecture selection

The fundamental concept consists in an external module, piggyback-carried by the chaser or servicing spacecraft, whose purpose is to stabilise the tumbling motion of the target in order to facilitate the docking of the chaser. The concept requires the module to be moved from the chaser spacecraft to the target and to be be physically attached to the surface of the target. The module as a system includes an actuator and a power source or fuel in order to detumble the target

when attached to it. In this section, a variety of possible architectures for this concept module are outlined.

5.1.1 Actuator systems

Different alternatives regarding the actuators can be considered:

5.1.1.1 Thrusters

The module may carry a cluster of thrusters to stabilise the target acting as an externally attached RCS. This module would be attached as far as possible from the centre of mass (CM) of the target (to maximise the lever arm length), and also away from its principal axes of inertia (to be able to actuate on the three of them). Envisat features a set of 15 N monopropellant hydrazine thrusters, generating torque in pairs. Thus, for a back-of-the-envelope sizing, 30 N thrusters are considered with an I_{sp} of 230 s, weighting an estimated 800 g each. An ideal case is considered where the target is spinning at 1 rpm about one axis (with a moment of inertia of 127000 kgm^2), and the module with the thruster(s) is placed with a 5 m lever arm (Fig. 5.1).

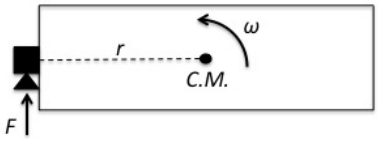

Figure 5.1: 2D representation of the spinning target, with the module attached on one end.

If the torque is

$$T = Fr = \dot{\omega} I \tag{5.1}$$

where F is the thrust, r the lever arm length, I the moment of inertia about the spin axis, and $\dot{\omega} = \frac{\Delta\omega}{\Delta t}$. The thrust can be related with the mass flow rate $\dot{m}$, specific impulse I_{sp}, and $g_E = 9.81$, as

$$F = \dot{m} g_E I_{sp} \tag{5.2}$$

where $\dot{m} = \frac{\Delta m}{\Delta t}$ for a constant thrust. By combining Eqs. 5.1 and 5.2, it is possible to evaluate the fuel consumption and detumbling time with the parameters previously outlined. In this case, the thruster would use 1.2 kg of propellant to nullify the spin rate in 90 s.

However, in a real scenario, the target would be tumbling about all axes. Ideally, the module should be placed on one end of the target, so that maximum torque along the major axes is achieved. It should be aligned with the minor axis of inertia, and the thrust directions should be parallel to the other axes, so that there is no torque coupling. However, torque coupling will exist since the exact moments of inertia and centre of mass position would be an estimation. In order to control the rotation about the minor axes, trusses would be needed in order to provide a lever arm to thrusters placed on their tips (Fig. 5.2). These thrusters could also compensate for torque coupling.

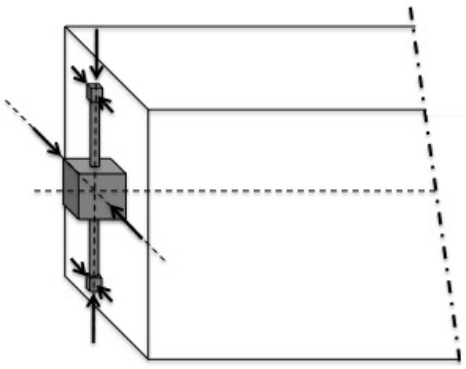

Figure 5.2: 3D representation of the module with two trusses, placed on one end of the target along its minor axis. Arrows depict the direction of thrust.

In the particular case of Envisat, however, one end of the body is cluttered with instruments and the other one (where the launcher adaptor ring is) is shadowed by the solar panel. Thus, it is no easy task to attach the module on either end of the satellite. Alternatively the module could be placed at any other point on the target, such as on one side, if there were trusses that provided controllability in 3 DOF. However, the system would be heavier and more complex, the presence of torque coupling would cause more fuel expenditure, and it would be a challenging control problem. Finally, a simpler cold gas propulsion system could also be considered, instead of a hydrazine monopropellant system. However, for the impulse required (275 kgs), the mass estimate of the cold gas system would be slightly higher [2].

5.1.1.2 Reaction wheels

Using the same simplified spinning model, reaction wheels can be sized in order to dampen the rotation of the target. The angular momentum of the target spinning at 1 rpm is 13300 Nms. In order to stop the rotation of the target, the reaction wheel must be able to absorb this amount of momentum. For comparison, a 270 kg control momentum gyroscope (CMG) has a maximum angular momentum of less than 4800 Nms (data based on the CMG of the International Space Station [82]).

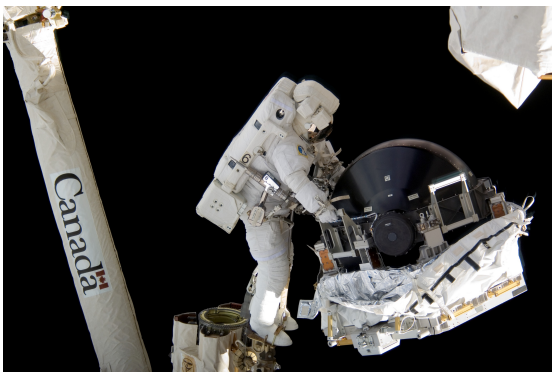

Figure 5.3: CMG mounted on the International Space Station—astronaut for scale (NASA)

While a ballpark sizing of the momentum storage actuators needed to equip the module has not been realised, the fact that the largest existing CMG would not be able to detumble the baseline target makes it reasonable to believe that this option leads to a dead end.

5.1.1.3 Magnetorquers

Magnetic torquers, also known as magnetorquers or torque rods, are used in spacecraft for post-launch detumbling operations (amongst other uses such as reaction wheel desaturation or coarse attitude control), making them a natural choice to consider. Moreover, magnetorquers are compact, simple, and reliable devices. For a rough sizing the system, a simplified 2D model of a spacecraft rotating in a constant magnetic field is considered, where a control law actuating the magnetorquers stabilises it. Again, the model is inspired in Envisat, which rotates at 1 rpm about the axis of largest inertia. The magnetic flux density (or simply the magnetic field) $\mathbf{B}$ corresponds to an orbit 1000 km high. In Fig.

5.4, the reference frame is fixed on the body while the magnetic field vector **B** rotates, and 2 magnetorquers (depicted in black) are placed perpendicular to one another.

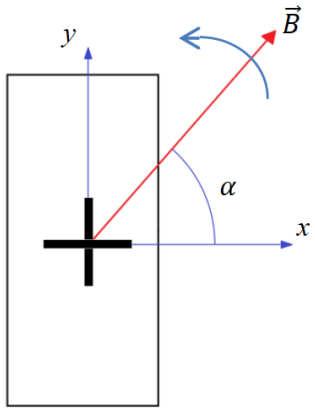

Figure 5.4: Simplified model of a body spinning in a magnetic field

The magnetorquers generate a dipole moment **m** along their axis, which interacts with the environmental magnetic field resulting in a torque orthogonal to both vectors:

$$\mathbf{T} = \mathbf{m} \times \mathbf{B}_s \tag{5.3}$$

where **T** is the torque, **m** is the magnetorquers' moment and $\mathbf{B}_s$ is the Earth magnetic field relative to the body frame.

The conventional control law for detumbling is the so-called B-dot, where the magnetic moment generated by the actuators is proportional to the time derivative of $\mathbf{B}_s$.

$$\mathbf{m} = -C\dot{\mathbf{B}}_s = \begin{bmatrix} -CB_E \sin\alpha\dot{\alpha} \\ CB_E \cos\alpha\dot{\alpha} \\ 0 \end{bmatrix} \tag{5.4}$$

where C is a control parameter, B_E is the magnetic field magnitude and α is the angle of the magnetic field vector with respect to the X-axis of the body frame. Using the law of 5.4 on the simplified 2D model, two magnetorquers with a maximum magnetic moment of 400 Am^2 stabilise the rotation in 90 days. (In comparison, Envisat's magnetorquers output a magnetic moment of 315 Am^2.) This is a long stabilisation time, which could be reduced to more reasonable values by increasing the size and mass of the magnetorquers. However, note that

the torque of the B-dot law is proportional to the angular rate of the body, hence the angular rate decreases asymptotically with time. To avoid this dynamical behaviour, an alternative on-off control law (also known as commutation) can be applied, where the magnetorquers generate a constant maximum magnetic moment in either direction according to the relative direction of $\mathbf{B}$ [16]. The downside is that there is a loss of efficiency, since the magnetorquers always operate at full power but $\mathbf{m}$ is not always orthogonal to $\mathbf{B}$ (only the orthogonal projection $\mathbf{m}$ with respect to $\mathbf{B}$ generates useful torque). A compromise between the two is a modified B-dot law where the magnetic moment is constant in magnitude and always orthogonal to $\mathbf{B}_s$, therefore the torque is constant and the angular rate decreases linearly instead of asymptotically. This is achieved by eliminating the speed factor $\dot{\alpha}$ from Eq. (5.4). Using this modified B-dot control law, the target is stabilised in 20 days, using 6000 Wh.

Taking advantage of the chaser being in close proximity of the target (with the module attached to it), the chaser could generate a magnetic field to help decrease the stabilisation time. If the chaser stands 15 m from the target, in order to double the Earth magnetic field magnitude at this distance, an electromagnet in the chaser would have to generate a magnetic moment of $3.5{\cdot}10^5$ Am^2, three orders of magnitude greater than Envisat's own magnetorquers. Hence, the mass would be of the order of metric tons for the electromagnet alone.

5.1.1.4 Power source

In the case of magnetorquers, a power source is required. Alternatives include batteries, solar panels, and fuel cells. Exotic systems such as wireless energy transfer (to be transmitted from the chaser to the module) have a too low TRL, and radioisotope thermal generators (RTG) are too costly, hence they are not considered. A priori, solar panels are a less-than-optimal solution since the target is tumbling, likely causing an eclipse at every revolution and having an average sun incidence angle. If the solar panels are on eclipse as much as they are on daylight (accounting for the target spinning and the Earth eclipses), and considering a sun incidence (average) of 55 deg, 3 magnetorquers consuming 10 W each would require a 70×70 cm array. The battery would weigh under 1 kg. Fuel cells have relatively high specific power (275 W/kg [83]) and specific energy (500 Wh/kg [84]). However, they require the handling and storage of hydrogen and oxygen, which adds complexity. Batteries, on the other hand, are much simpler energy

storing devices. Rechargeable or secondary batteries have specific energies of 60-80 Wh/kg, which is rather low for this mission (although new developments could bring it up to 200 Wh/kg [83]). However, primary batteries have energy densities over 500 Wh/kg (higher than fuel cells) but they are not rechargeable, and must be isolated enough to survive several days in an space environment.

5.1.2 Docking methods

Two alternative methods are proposed to approach and attach the module to the target: a harpoon-tether system and an autonomous propulsion system.

5.1.2.1 Harpoon-tether

In the harpoon-tether strategy (Fig. 5.5), first, the chaser spacecraft hovers in close proximity to the target satellite. Then it fires a harpoon towards a specified spot on the target (taking care of not piercing a fuel tank). As soon as the harpoon is firmly attached, the module moves along the tether using a pulley towards the target. During this phase the attitude of the module could be controlled to some extent by pivoting the point in the pulley where tension from the tether is applied. Finally, after contact with the target satellite, the module is locked in place by applying tension to the tether, pressing it against the surface. This operation is performed with a tumbling target, thus it has to be carried out quickly to avoid the tether from tangling with the satellite and its appendages. (As a rough approximation, in Fig. 5.5 the target appears static.)

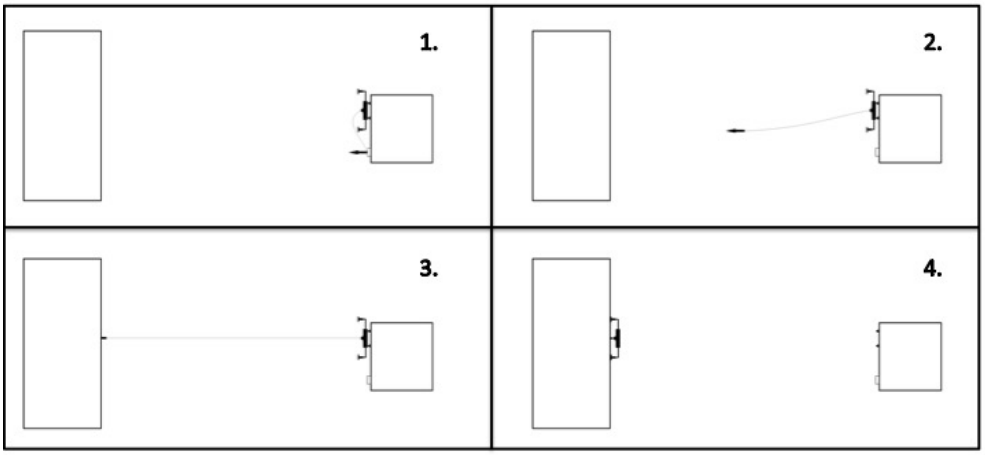

Figure 5.5: Schematics of the harpoon-tether docking strategy.

Consequently, the contact speed would be relatively high, requiring a suspension system capable of absorbing the kinetic energy softly. For instance, a requirement could be set so that the module shall reach the target in 5 seconds. In the worst case scenario, where the module docks along an axis perpendicular to the spinning axis, at 1 rpm this time span would allow for a 30 deg. rotation during the approach. If the target stands 15 m away from the centre of the target (barely outside of a 25 m wide obstacle-free area) the contact speed would be 6 m/s. This value could be halved if the module was spring-released at 3 m/s.

5.1.2.2 Autonomous propulsion

An alternative docking method for the device would be the use of an autonomous propulsion system, so that it can manoeuvre from the chaser to the target. This method requires the implementation of complex on-board GNC capabilities, due to the challenge of docking with an uncooperative tumbling target. However, it allows the chaser to stand farther away from the target, and there is the possibility for the module to abort the manoeuvre and repeat. Cold gas or monopropellant hydrazine systems are scalable enough to fit into a small module. Given the results obtained in Chapter 4, the module may use propellant in the order of hundredths of grams. The set of thrusters configuring the reaction control system (RCS) should provide 6 DOF motion, so that pointing is independent from translation.

5.1.2.3 Attachment to the target

One of the challenges of the concept proposed is how the module is attached to the target. The use of robotic arms in the module are discarded to keep the complexity as low as possible. The first assumption is that the module docks on the honeycomb sandwich panels usually found in satellites (the "skin" of the satellite, see Fig. 5.6) or a similarly soft material.

Once the module has made contact with the target at the prescribed docking point, the module must anchor to the panel firmly enough so that the torque exerted by the actuators do not detach it. In this sense, the attachment strength required if detumbling with thrusters will be higher than in the magnetorquer case. An existing similar case is that of Philae, the lander of the Rosetta mission, which was required to attach itself to the cometary surface to prevent it from

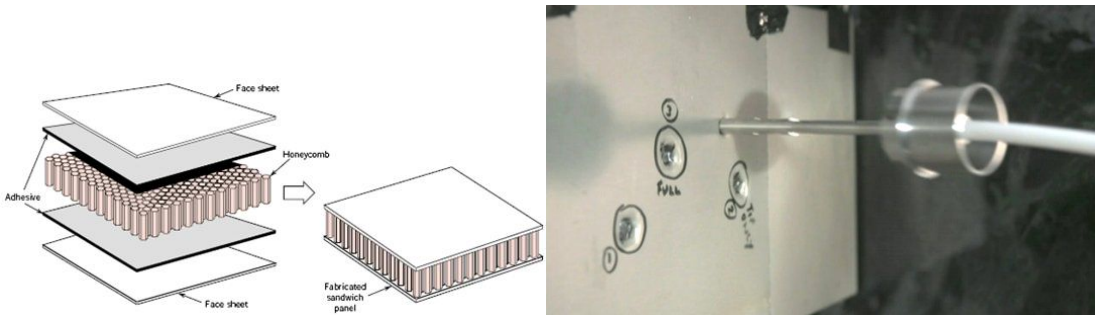

(a) Honeycomb sandwich **(b)** Harpoon piercing a panel (Airbus DS)

Figure 5.6: Honeycomb panels are used to recover spacecraft. Harpoons are being tested to penetrate on them and capture debris.

floating away, given the weak gravity field. The system is composed by a nadir-pointing harpoon that is fired upon contact, and subsequently drills on the landing gear anchor to the surface. The same method can be used in the scenario at hand, only adapting the harpoon and drills to the properties of the target's structure. (Some lessons should be learned from the Philae experience, e.g. why did the harpoon fail.) A more exotic yet promising method involves using a space-rated adhesive being developed at the JPL [85], which mimics the glue-free adhesion of gecko paws. The module could get attached upon contact and applying some pressure with thrusters or the harpoon.

5.1.3 Decision

A variety of alternatives have been considered for the module system. On the actuators side, the thruster option has strong constraints regarding the attachment point and orientation (to avoid torque coupling), and the system is not compact due to the trusses required (they could be deployable, at the cost of increased complexity). However, the detumbling time is fast, and the same RCS system can be used to dock autonomously. Also, a thruster along the direction of the minor axis could be used for de-orbiting, provided that enough propellant is carried on and the axis misalignment is small. Magnetorquers take much longer to stabilise the target, but they are simple, reliable, and compact.

Regarding its power source, solar panels are low weight and preliminary calculations show a manageable area is required, but given the fact that they would be body-mounted (on one side only) and that the orientation cannot be controlled,

they are not a robust solution. Fuel cells have a relatively high energy density, but it is difficult to manage and store hydrogen. In this sense, primary batteries have similar energy density, while being much simpler and robust devices. Rechargeable batteries, however, have low energy density. Thus, a battery of a reasonable size would need to un-dock, fly back to the chaser, recharge, and dock again to achieve full stabilisation. If reusability is required, A fuel cell system could store all the energy needed for a single detumbling operation, and it could be refuelled to service other targets. However, the Envisat mission (as is the case study in this work) would most likely be a single-target mission, given the large size of the satellite.

Given these considerations, a module equipped with magnetorquers powered by a primary battery is selected as baseline architecture in this work. The drawbacks of this system is that magnetorquers can only operate at LEO, and in orbits parallel to the magnetic equatorial plane, a residual spin about the magnetic field direction will remain.

Regarding the docking strategy, the harpoon method is simple, however, it is a one-shot scenario (not robust) and the technologies associated with harpoons fired at satellites have not been space-proven yet. Besides, this method forces the chaser to stand close to the target. The autonomous approach requires an RCS system and state-of-the-art GNC components. However, it allows the chaser to stand farther away from the target, and provides the possibility of aborting the approach and having a second chance—thus, this option is selected over the harpoon-tether. To anchor the module to the target, the thrusters apply downward pressure while drills penetrate the surface. If the space-rated adhesive technology were ready for implementation, it would likely be a more reliable alternative.

5.2 Control law for magnetic detumbling

Before presenting the preliminary design of the system, this section discusses the control laws governing magnetic detumbling with magnetorquers. A simplified 2D model is analysed, where analytical expressions can be obtained to be used in the preliminary system optimisation. Then, the modified B-dot used in the simulations is presented.

5.2.1 2D model analysis

In the simplified 2D scenario, as previously presented in Sec. 5.1.1.3, a large satellite is spinning about one of its axis at 1 rpm, immersed in a constant magnetic field. For a given magnetorquer design that provides a magnetic moment of 400 Am^2 and consumes 8 W of power, the performances of three control laws are compared. Those are the B-dot law (Eq. 5.4), the on-off or commutation law [16] (where the magnetorquers apply full magnetic moment in either direction according to the relative direction of $\mathbf{B}$), and the modified B-dot that is proposed in this work.

Figure 5.7 shows the time evolution of the angular rate during the stabilisation process. On one hand, the B-dot law is the least effective regarding the stabilization time, and although the mean power used in the overall process is small, the large final time implies larger energy expenditure, as shown in Fig. 5.8. On the other hand, the on-off law provides the minimum final time, but the fact that full power is constantly applied to the actuator, even if no effective torque is produced, makes it inefficient in terms of energy. The modified B-dot law is a fair compromise, achieving a relatively good stabilisation time (Fig. 5.7) with minimum energy expenditure (Fig. 5.8). Therefore, the system will be sized taking this control law into account.

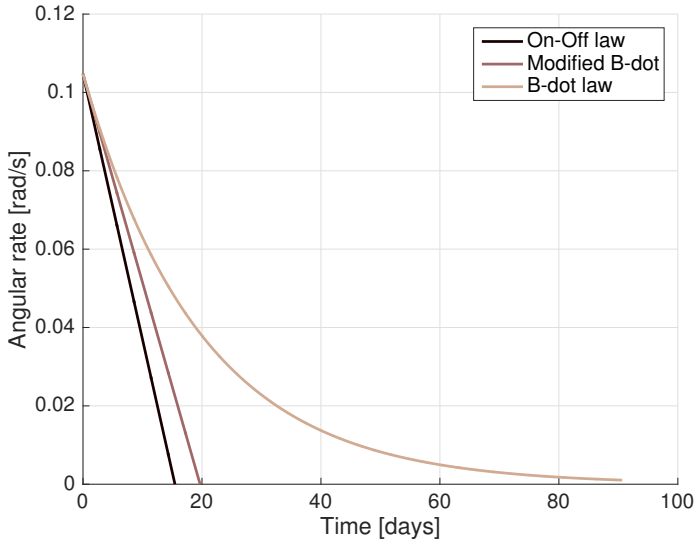

Figure 5.7: Stabilisation time for different control laws

The control for the magnetic moment for the modified B-dot is:

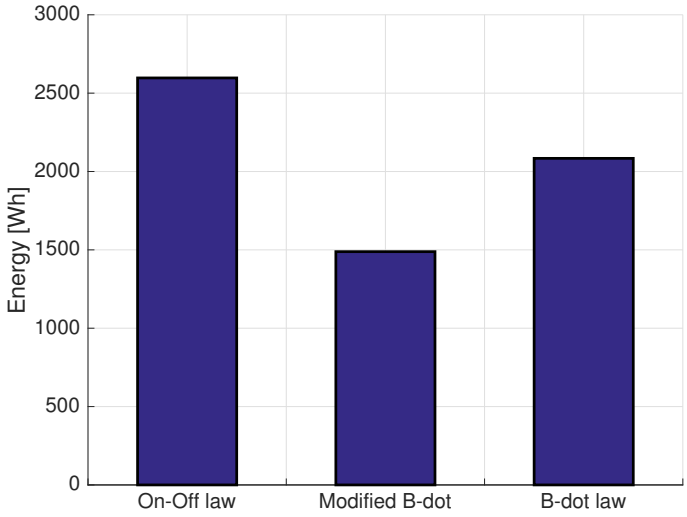

Figure 5.8: Energy spent using different control laws

$$\mathbf{m} = \begin{bmatrix} -CB_E \sin\alpha \\ CB_E \cos\alpha \\ 0 \end{bmatrix} \tag{5.5}$$

Where C is a control parameter and α is the angle of the magnetic field vector with respect to the X-axis of the body frame, obtained using magnetometers. The $\mathbf{B}$ field relative to the body frame is:

$$\mathbf{B}_s = \begin{bmatrix} B_E \cos\alpha \\ B_E \sin\alpha \\ 0 \end{bmatrix} \tag{5.6}$$

Applying Eq. 5.3 we have the torque (normal to the plane):

$$\mathbf{T} = -CB_E^2\hat{\mathbf{k}} = \ddot{\alpha} I_3 \hat{\mathbf{k}} \tag{5.7}$$

Where I_3 is the model's inertia about the rotation axis. If $\ddot{\alpha} = \dot{\omega}$ and we integrate Eq. 5.7 with respect to time, the equation for the angular rate is:

$$\omega_3 = \omega_{3i} - \frac{CB_E^2}{I_3} t \tag{5.8}$$

Where ω_{3i} is the initial angular rate. By finding

$$C = \frac{\omega_{3i} I_3}{B_E^2 t_s} \tag{5.9}$$

and using Eq.(5.5) we can obtain the maximum magnetic moment needed by the magnetorquers in order to stabilise the target spinning at ω_{3i} in t_s:

$$m_{MT} = \frac{\omega_{3i} I_3}{B_E t_s} \tag{5.10}$$

5.2.2 Modified B-dot

In this subsection, the modified B-dot for the full 3D scenario is developed, considering sets of 2 and 3 orthogonal magnetorquers.

The B-dot is a classic and most popular control law for detumbling or stabilising the rotation of spacecraft. Since the orbital angular rate is small compared to the tumbling of the spacecraft, the $\dot{\mathbf{B}}$ term can be approximated, and the B-dot law becomes

$$\mathbf{m} = -C(\mathbf{B} \times \boldsymbol{\omega}) \tag{5.11}$$

As mentioned before, the B-dot dissipates the spacecraft angular rate asymptotically—since as the angular rate decreases, the control effort also decreases. Additionally, the control effort is also proportional to the angular distance $\angle \mathbf{B}\boldsymbol{\omega}$ (peaking at $\pi/2$). Thus, in order to derive a control law that dissipates rotational energy rapidly, it is required to apply the maximum control effort available during the whole detumbling process. The total moment $\mathbf{m}$ applied by the magnetorquers should always lie on the plane defined by B in order to maximise the efficiency of the torque generated as

$$\mathbf{T} = \mathbf{m} \times \mathbf{B} \tag{5.12}$$

Additionally, in order to effectively dissipate rotational energy, the torque $\mathbf{T}$ should be parallel and opposed to the orthogonal component of $\boldsymbol{\omega}$ with respect to $\mathbf{B}$, or $\boldsymbol{\omega}_\perp$. Hence, assuming that $\mathbf{m}$ is orthogonal to $\mathbf{B}$, the desired torque is

$$\mathbf{T} = \|m\|\|B\|\hat{\boldsymbol{\omega}}_\perp \tag{5.13}$$

where

$$\boldsymbol{\omega}_\perp = (\mathrm{I}_3 - \hat{\mathbf{B}}\hat{\mathbf{B}}^T)\boldsymbol{\omega} \tag{5.14}$$

with I_3 being the identity matrix. (The vectors can be visualised in Fig. 5.9.)

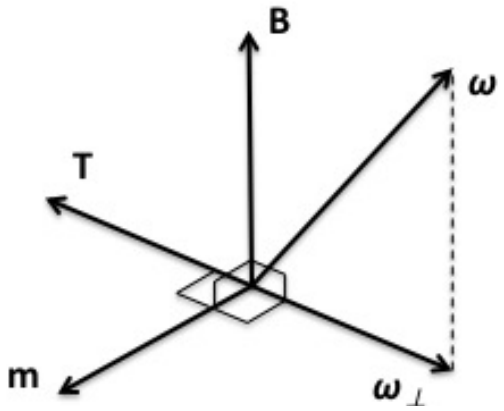

Figure 5.9: Vector representation of magnetic control

The necessary magnetic moment vector, orthogonal to $\mathbf{B}$, $\boldsymbol{\omega}$, and $\mathbf{T}$, is thus

$$\mathbf{m} = m_{max} \frac{\boldsymbol{\omega} \times \mathbf{B}}{\|\boldsymbol{\omega} \times \mathbf{B}\|} \tag{5.15}$$

where m_{max} is the maximum magnetic moment that can be achieved in this direction. A simple solution would be to set $m_{max} = m_{MT}$ (a single magnetorquer maximum moment). In this case, $\mathbf{m}$ would be constrained in a sphere of radius m_{MT}, but the capability of the three magnetorquers combined would be underused. The domain of actual maximum values is the surface of a cube defined by the three orthogonal magnetorquers, of $2m_{MT}$ edge length. In Eq.5.15 (equivalent to $\mathbf{m} = m_{max}\hat{\mathbf{m}}$), the factor m_{max} is limited by the maximum moment of the individual magnetorquers. Assuming that the magnetorquers are aligned with the body basis vectors, the possible magnitude of the $\mathbf{m}$ vector is calculated for each component, as

$$k_i = \frac{m_{MT}}{\hat{m}_i} \tag{5.16}$$

for $i = 1, 2, 3$, and $\hat{m}_i$ being the components of $\hat{\mathbf{m}}$. The smallest k_i is chosen as the vector magnitude, or $m_{max} = \min_i k_i$.

The latter control law assumes that there are three magnetorquers that can build an $\mathbf{m}$ vector in any direction of the Euclidean space. However, in this study the possibility of having only two magnetorquers (even in the 3D case) is considered. In this case, the magnetic moment vector lies in the plane defined by the basis vector $\hat{\mathbf{e}}_3$, if the magnetorquers are aligned with $\hat{\mathbf{e}}_1$ and $\hat{\mathbf{e}}_2$. Thus, either (a) the torque is parallel to $\boldsymbol{\omega}_\perp$ but $\mathbf{m}$ is not perpendicular to $\mathbf{B}$ (Fig. 5.10a), or (b) $\mathbf{m}$ is orthogonal to $\mathbf{B}$, but$\mathbf{T}$ is not parallel to $\boldsymbol{\omega}_\perp$ (Fig. 5.10b).

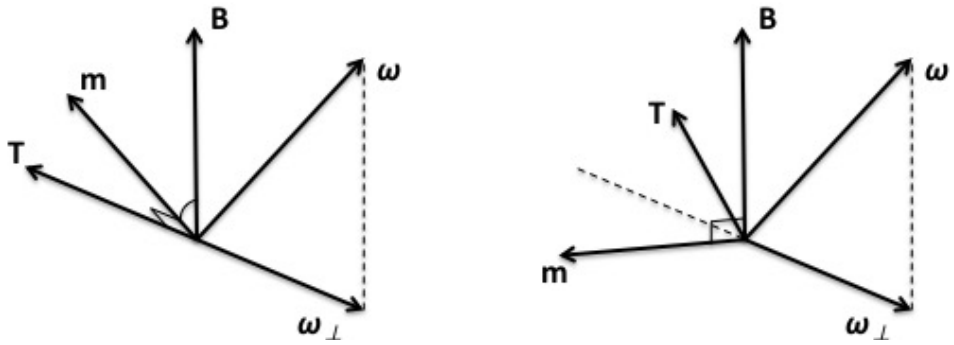

(a) **T** parallel to $\boldsymbol{\omega}_\perp$ **(b)** **m** orthogonal to **B**

Figure 5.10: Vector representation of magnetic control with two magnetorquers. The **m** vector lies in the arbitrary $\hat{\mathbf{e}}_3$ plane (not shown).

In the first case, the magnetic moment vector lies in the intersection between the $\hat{\mathbf{e}}_3$ plane and the $\boldsymbol{\omega}_\perp$ plane:

$$\hat{\mathbf{m}} = \frac{\boldsymbol{\omega}_\perp \times \hat{\mathbf{e}}_3}{\|\boldsymbol{\omega}_\perp \times \hat{\mathbf{e}}_3\|} \tag{5.17}$$

which is not necessarily perpendicular to **B** (implying an efficiency loss). The magnitude of the magnetic moment vector is calculated as in Eq. 5.16 (the third component is null).

In the second case, **m** is perpendicular to **B**, thus it lies in the intersection between the $\hat{\mathbf{e}}_3$ plane and the **B** plane:

$$\hat{\mathbf{m}} = \frac{\mathbf{B} \times \hat{\mathbf{e}}_3}{\|\mathbf{B} \times \hat{\mathbf{e}}_3\|} \tag{5.18}$$

The torque **T** generated by $\mathbf{m}_i$ should oppose the angular velocity vector at least in part, thus the angle between $\mathbf{T}_i$ and $\boldsymbol{\omega}_\perp$ should be larger than $\pi/2$ in order to dissipate energy. Thus, a sign factor is used in $\mathbf{m} = s_i m_{max} \hat{\mathbf{m}}$, where s_i is

$$s_i = -\text{sgn}(\mathbf{T} \cdot \boldsymbol{\omega}_\perp) \tag{5.19}$$

As a final remark, this control law tends to dissipate the component of the angular velocity vector $\boldsymbol{\omega}$ orthogonal to the magnetic field vector **B**. Hence, at some point the magnetorquers could drive the system to a state where $\boldsymbol{\omega}$ is parallel to **B**. At this point, the magnetorquers tend to align themselves to **B**, generating an orthogonal component of velocity, while at the same time they try to dissipate that velocity component. In the case of an inertially fixed magnetic field, this

state is locked. In the real world, as the spacecraft moves along the orbit, the direction of $\mathbf{B}$ changes, separating it from $\boldsymbol{\omega}$, a situation where the magnetorquers can work. However, if the magnetorquers are very powerful relative to the spacecraft's inertia, they will quasi-instantaneously dissipate the newly generated orthogonal component, driving $\boldsymbol{\omega}$ again to a parallel state with $\mathbf{B}$, without having been able to dissipate a significant amount of energy. The result in this case is the magnetorquers locking the spacecraft in this state, and rotating it with $\mathbf{B}$. Avanzini [86] proposed a variant of the B-dot law that avoid this situation by selecting an appropriate gain, however, the control effort also depends on the angular rate.

However, in the scenario considered here, the spacecraft has a large mass relative to the magnetorquers torque, hence the stabilisation process spans tenths of orbits. This allows the vector $\mathbf{B}$ to separate enough from $\boldsymbol{\omega}$, so the magnetorquers can dissipate energy using the control law described in Eq. 5.15 without risk of locking the spacecraft rotation.

5.3 Preliminary design

In this section, the different subsystems of the module are outlined, and a preliminary system optimisation is undertaken. The system elements discussed are the propulsion system (which allows the module to move from the chaser to the target), the navigation and attitude determination system, the magnetorquers, the battery to power them, and the control law to detumble the target by magnetic means.

In Fig. 5.11 the module features a propulsion system, including drills on the legs. The magnetorquers are placed perpendicular to one another. In order to have a compact device, each rod is divided in two parts and placed in parallel, forming a square. In the model of Fig. 5.11, only two pairs of orthogonal magnetorquers are shown. However, a third magnetorquer perpendicular to the other two could be included, either deployable or fixed. Also, the number of fuel tanks shown are twice what would be needed in the case under study. The battery and other subsystems of the module (power distribution, on-board computer (OBC), and communications) are placed at the centre of the module.

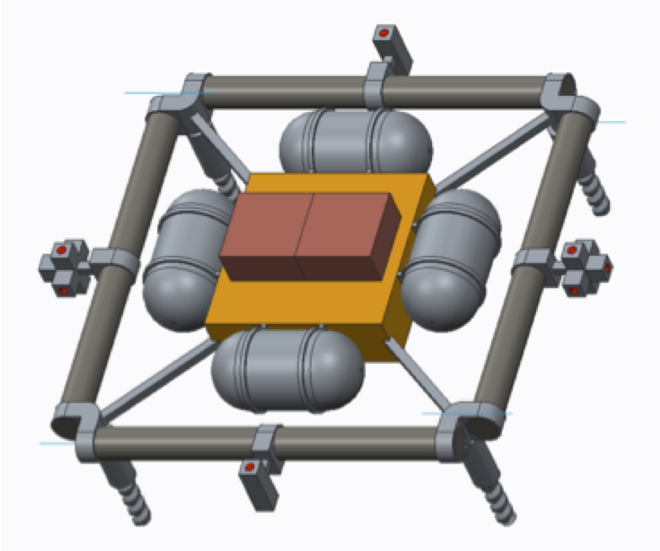

Figure 5.11: ASEM module with a propulsion system, two pairs of magnetorquers (the two full magnetorquers are cut in half), and drills

5.3.1 System elements

Here the expressions and assumptions for the preliminary design of several elements of the system are outlined.

5.3.1.1 Propulsion system

A propulsion system allows the module to fly autonomously from the chaser to the target satellite, in order to softly dock onto it. In this scenario, the module incorporates a set of thrusters (providing 6-DOF control) and propellant tanks, along with the necessary plumbing. Also, it shall be accompanied by a robust and performing GNC system, to manoeuvre safely to the specified spot on the surface of the tumbling target. Finally, once it makes contact with the surface, drills on the legs anchor the module in place.

The two considered options for the propulsion system are cold gas and mono-propellant hydrazine [83]. The first is simple and reliable, but has low specific impulse (50-80 s). Thrust is provided by pressurised gas, which requires relatively bulky tanks but low-weight and simple thrusters. The second option uses an exothermic decomposition of the propellant (usually hydrazine, N_2H_4), which provides a higher specific impulse (200-230 s). The high toxicity of hydrazine is an issue when handling and storing the propellant. Considering the thrust require-

ments specified above, the mass of a 3 N hydrazine thruster is about 500 g, while a typical 3 N cold gas thruster weighs up to 20 g (and is much smaller). Thus, just the added mass of the set of hydrazine thrusters is higher than a cold gas system with the same requirements, including tanks. A comparison between both systems can be visualised in Fig. 5.12, where cold gas systems are more appropriate for low-impulse scenarios (such as the one under study). Therefore, a cold gas system is selected for its mass and reliability, with nitrogen as the propellant for its storage density, performance and lack of contamination concerns.

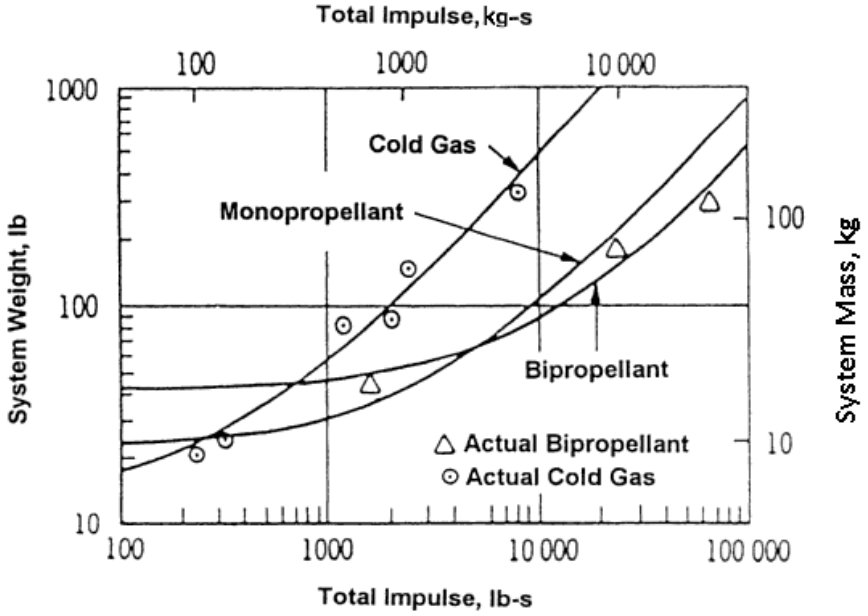

Figure 5.12: Comparison of propulsion systems relating mass and total impulse [2]

A docking manoeuvre is simulated with the motion planning method for uncooperative docking described in Chapter 4. The module's initial position is 50 m away, and the target is rotating at 1 rpm. The trajectory has three distinct segments: initial approach to a point above the docking location, hovering for 10 s, and final approach along the docking axis. The obstacle keep-out area is defined by a cylinder enclosing the target. An estimated wet mass of 30 kg has been considered. Note that the end boundary conditions are selected so that the thrusters plume is not directed towards the target's surface. Figure 5.13 shows the simulated path of the module in body frame.

Figure 5.14 shows the total thrust profile of the docking trajectory. In the first segment, the fuel is minimised, resulting in relatively low maximum thrust. At

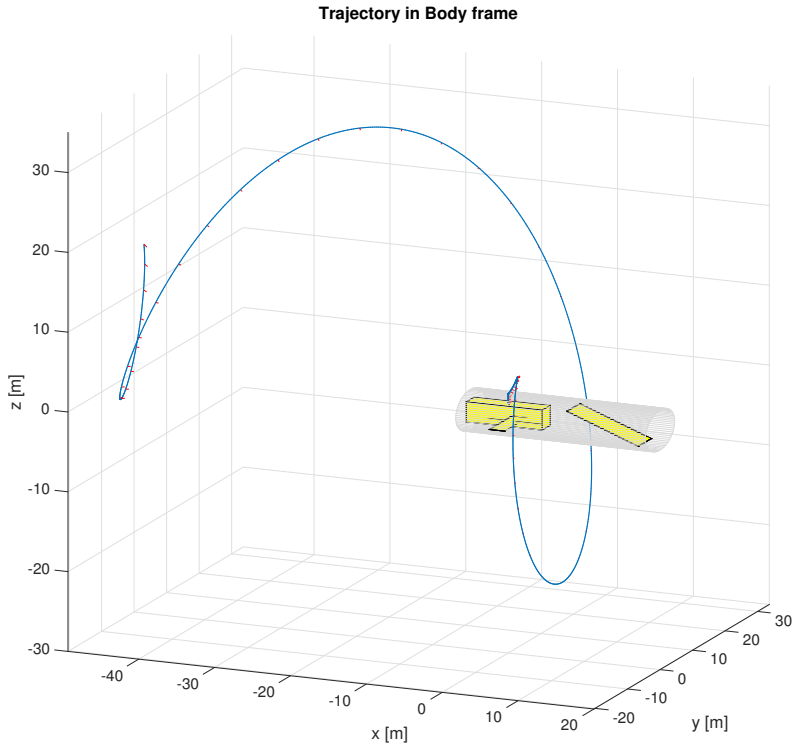

Figure 5.13: Path of the module resolved in the target's rotating body frame (the cylindrical keep-out area is shown).

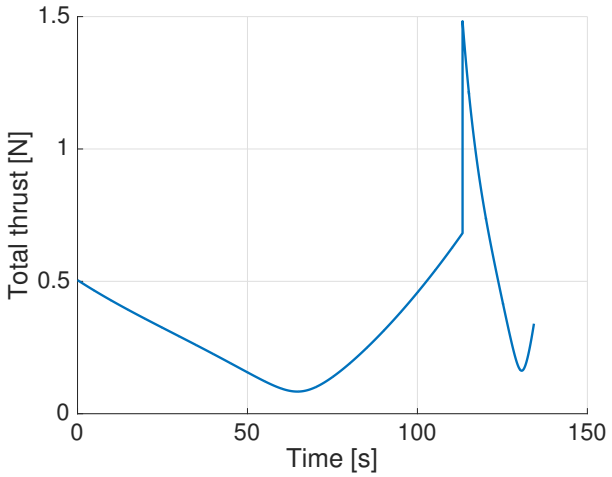

Figure 5.14: Thrust profile for a 25-kg module docking to the target (including 10 s of hovering)

the beginning of the final segment there is a thrust peak. The selected duration of the final segment influences the magnitude of the initial torque peak and the fuel consumed. The minimum-fuel duration causes a peak of 2 N, thus it has been allowed to last a few more seconds in order to reduce it to 1.5 N. The parameters

considered for this sizing (target rotation rate, module mass, etc) are an over-estimation, which adds some margin to the system. For instance, if the tumbling rate was reduced to 0.5 rpm, the thrust peak would be of 1 N. However, in the hypothetical case that the target was tumbling at 2 rpm, the thrust peak would be 4 N and the fuel consumption would double (Fig. 5.15).

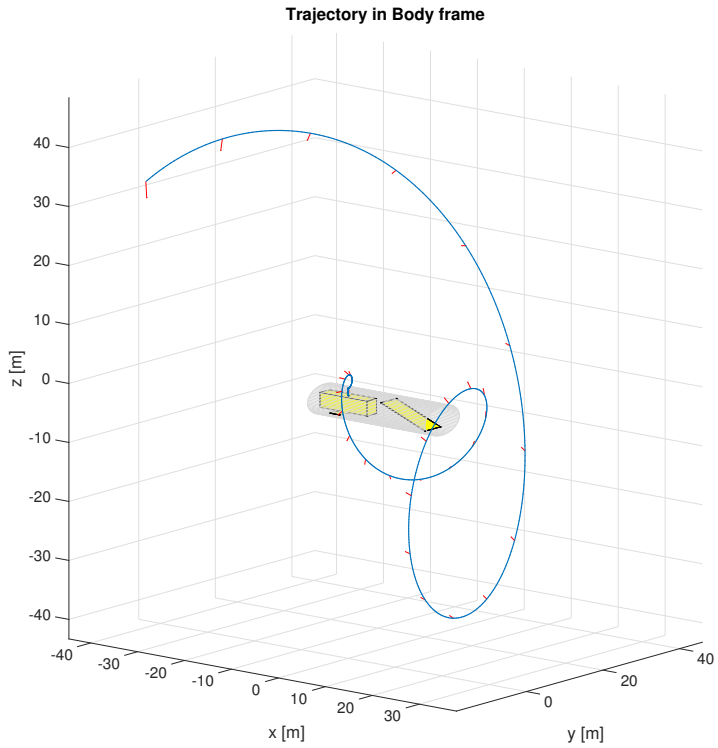

Figure 5.15: Path of the module resolved in the target's rotating body frame, tumbling at 2 rpm.

A set of 14 thrusters distributed across the module structure can provide full control (see Fig. 5.11). Where four thrusters are aligned with the main motion direction, each thruster shall provide at least 0.4 N. Directions with only one thruster shall ensure a minimum of 1.5 N, whereas directions with two thrusters must provide 0.75 N. An average mass of 15 g is considerd for all thrusters, with a total set weight of 210 g.

In this baseline manoeuvre 77 g of propellant are consumed, considering a specific impulse of 70 s for the nitrogen cold gas system. Since the order of magnitude of the propellant mass is small compared to the module mass, a safety factor of 3 has been applied, totalling 231 g. This would allow for several docking attempts, or provide more flexibility to the operators in face of unforeseen events. The

corresponding volume at a typical operating pressure of 135 bars is, according to the ideal gas law, 1.5 litres. The mass of the spherical tanks is calculated using

$$\sigma = \frac{Pr}{2t} \tag{5.20}$$

which relates the tensile stress of the material (σ), the pressure (P), radius (r) and thickness (t).

Given the estimated volume, if we divide it in two tanks, each one will have a radius of 5.8 cm. Selecting aluminium as the tank material we have the value for its allowable stress, and thickness can be evaluated, resulting in an estimated tank mass of 0.1 kg. If we add a 20% of the overall tankage mass for mounting hardware and propellant management devices [83], the total tank and pipe system weighs 0.24 kg. A pressure regulator must be included, with an estimated mass of 300 g (as made by Moog). Summing up the mass of propellant, tanks and thrusters, the overall cold gas propulsion system has an approximated mass of 1 kg.

5.3.1.2 Navigation and attitude determination

The concept proposed, where the module docks autonomously with the tumbling target, needs a state-of-the-art GNC system. Since the target is uncooperative—no state data comes from it—the module needs to determine its own state and that of the target. To determine the state (attitude and angular velocity) of the target, an observer requires computer vision systems and LIDARs [87], which can be implemented together for redundancy and increased accuracy. However, it the scenario considered in this chapter, an external observer can monitor both the target and the module approaching it. The chaser spacecraft, having more resources, could take the greater share of image processing, while easily determining the module's position relative to the target (given the vantage point of view). Alternatively, and depending on the bandwidth available for ground communication, the module could be remotely piloted. It would soften the GNC requirements, but it is unclear whether this approach would be more reliable or simpler than an autonomous one. In any case, the trajectory would be sub-optimal.

Once the target is attached to the target, the controller requires information on the local Earth magnetic field vector. Magnetometers are simple devices that directly sense the direction of the magnetic field, but if magnetorquers are switched

on, they will disturb the measurements. This implies that during the magnetometers operation the current through the magnetorquers should be turned off so that the B-field can be measured. This process is inefficient and may lead to instabilities. However, it is possible again to use the chaser as an external observer, so that it determines the target's attitude (knowing the orientation of the magnetorquers attached to it). Using its own magnetometers and inertial reference sensors, the chaser spacecraft can obtain the direction of the local B-field. Then the orientation of the B-field relative to the target will be calculated and sent to the module.

5.3.1.3 Battery

Primary batteries are not rechargeable, but have a much larger specific energy (SE, in Wh/kg) than rechargeable secondary batteries. The battery should be sized to store enough energy to detumble the target satellite using magnetorquers. With the mean power required by the magnetorquers and the stabilization time, the mass of the battery of a certain type can be approximated simply using its SE value. Similarly, the energy density can be described as the energy per unit volume (ED, in Wh/l), thus the approximate volume of the battery can also be obtained. It is desired to select a battery with high SE and ED, as well as a good temperature range. Lithium-carbon monofluoride (CFx) primary batteries are very efficient, low weight and compact. According to a NASA manual [88], they have a specific energy up to 625 Wh/kg and an energy density up to 1070 Wh/l (specifications of more modern models of this type of battery, e.g. the ones manufactured by Quallion, are similar).

The battery mass and volume are calculated using the mean value of the total power. In our model, the power applied to each magnetorquer is a sinusoidal wave, phased 90 degrees according to the control law (Eq. 5.5). Since the magnetic moment is proportional to the power, and if P is the maximum power applied to a single magnetorquer, then the total power as a function of the angle α with the magnetic field vector $\mathbf{B}_s$ is:

$$P_{total} = P(-\sin\alpha + \cos\alpha) \tag{5.21}$$

The mean value is calculated as follows:

$$\langle P_{total} \rangle = P\frac{1}{\pi}\int_{-\frac{\pi}{4}}^{\frac{5\pi}{4}}(-\sin\alpha + \cos\alpha)\mathrm{d}\alpha = P\frac{2\sqrt{2}}{\pi} \tag{5.22}$$

5.3.1.4 Magnetorquer design

The simplest magnetorquer is a solenoid or wire coil. Most of them, also known as torque rods, have a ferromagnetic core inside the coil greatly amplifies the magnetic moment generated when a current is applied, when the magnetic field generated orients the molecular dipoles in the material. Once all the molecular dipoles are oriented, the core saturates and no longer amplifies the magnetic field regardless of further increases in current. It is important for cores to have a high relative magnetic permeability (μ_r), so that magnetisation is easily achieved, and high saturation points. However, for attitude control magentorquers, it is also important for the magnetic field to exhibit low hysteresis and linearity. Typical core materials are ferrite alloys, with a minimum relative permeability of $\mu_r = 2000$.

The equations governing the electromagnetism of a solid core solenoid can be found in [89]. The design approach is based on the saturation point (as in Black [90]), which corresponds to the maximum magnetic moment the magnetorquer can deliver. The magnetic dipole moment $\mathbf{m}$ for a solenoid with air core is simply a function of its cross-section area A, the current I, and the number of loops of the wire coil N, as expressed in Eq. 5.23. The direction of the magnetic moment is given by the normal of the cross-section area, $\hat{\mathbf{n}}$.

$$\mathbf{m} = NIA\hat{\mathbf{n}} \tag{5.23}$$

The total magnetic field in the core is:

$$\mathbf{B} = \mu_0(\mathbf{H} + \mathbf{M}) \tag{5.24}$$

where μ_0 is the magnetic permeability of free air, $\mathbf{H}$ is the magnetic field intensity in the core, and $\mathbf{M}$ is the magnetization vector field (or magnetic dipole moment per unit volume). For a solenoid with solid core, we can obtain the magnetisation vector with this expression relating it to the magnetising field :

$$\mathbf{H} = \frac{NI}{l} - N_d\mathbf{M} \tag{5.25}$$

where l is the length of the magnetorquer and N_d is the demagnetising factor, evaluated with the following expression:

$$N_d = \frac{4(\ln\left(\frac{l}{r}\right) - 1)}{\left(\frac{l}{r}\right)^2 - 4\ln\left(\frac{l}{r}\right)} \tag{5.26}$$

Notice that this factor is a function only of the core geometry, where r is the radius. For long thin rods, as considered in this work, $N_d \ll 1$. Assuming linearity between the dipole moment and current, $\mathbf{B}$ and $\mathbf{H}$ can be related as:

$$\mathbf{H} = \frac{\mathbf{B}}{\mu_0 \mu_r} \tag{5.27}$$

where μ_r is the relative magnetic permeability of the core material and $\mu_0 = 4\pi 10^{-7}$ is the permeability of free space—a constant. The magnetic moment due to the magnetisation of the ferromagnetic core is (vector norms are used)

$$m_C = V_C M = V_C(\frac{B}{\mu_0} - H) \tag{5.28}$$

where V_C is the volume of the core, and M has been replaced using Eq. (5.24). The term H can be neglected in Eq. (5.28), using (5.27) and knowing that $\mu_r \gg 1$. Then, B_s being the saturation magnetic field in the core, and assuming that the contribution to the magnetic moment due to the core magnetisation is much larger than that of the solenoid alone, the maximum magnetic moment is

$$m_{MT} = V_C(\frac{B_s}{\mu_0}) \tag{5.29}$$

Finally, combining Eqs. (5.24) and (5.25):

$$\frac{NI}{l} = H_s + N_d \frac{B_s}{\mu_0} \tag{5.30}$$

where $H_s = B_s/(\mu_0 \mu_r)$.

In order to size the magnetorquer, it is important to know the properties of the wire for the solenoid.

$$l_w = \frac{RA_w}{\rho_w} = \frac{R}{R_w} \tag{5.31}$$

Eq. 5.31 relates the resistance with the geometry of the wire (l_w and A_w are the length and cross-section area of the wire) and its specific resistance, either in terms of copper resistivity ρ_w [Ωm] or resistance per metre R_w [Ω/m]. The number of turns of the wire can be related to resistance:

$$N = \frac{l_w}{2\pi r} = \frac{R}{R_w 2\pi r} \tag{5.32}$$

where the resistance R can be expressed in terms of power, voltage and/or current using Ohm's law $V = RI$. Also, it is possible to relate the term NI/l, obtained in Eq. (5.30) from the magnetic saturation or the maximum magnetic moment, with the rod geometry and wire resistance:

$$\frac{NI}{l} = \frac{V}{R_w 2\pi r l} \tag{5.33}$$

Which, in terms of the maximum magnetic moment is:

$$m_{MT} = \frac{VA}{R_w 2\pi r k_1} \tag{5.34}$$

where

$$k_1 = \frac{1}{\mu_r} + N_d \tag{5.35}$$

5.3.2 System optimisation

Using the expressions described in the previous section, the characteristics of a magnetorquer (mass, power, etc) can be obtained, with the goal of minimising the mass of the system and the stabilisation time. However, since the battery needs to store the energy required for the detumbling operation, the power drawn by the magnetorquers and the stabilisation time affect the battery mass. However, the stabilisation time and the maximum magnetic moment are related by Eq. (5.10). In other words, using the 2D model, the interdependency between the battery and magnetorquer designs is approached analytically, which simplifies the optimisation process. Nonetheless, a detailed simulation is required in order to validate or refine the preliminary design. Note that two magnetorquers are considered.

The angular rate for this case study has been set to 1 rpm, or 6 deg/s. While there is no exhaustive study on the tumbling rates of inoperative satellite in LEO, Nishida and Kawamoto [7] consider that 1 rpm falls into the medium range of angular rate, requiring some slow-down before capture. Castronuovo [6] highlights that a robotic arm could capture a Soyuz (7 tons) spinning at 4 deg/s, with a peak torque of 80 Nm.

First, the properties of the core, wire, and battery are selected. A ferrite core is used, which has a minimum μ_r =2000, a maximum density of $\rho = 5240$ kg/m^3, and a saturation magnetic field of B_s =0.5 T. Suitable wires for the solenoid are 24, 28 or 32 AWG (American Wire Gauge). The low-resistivity 24 AWG is selected since it provides, for the same mass as its counterparts, more reasonable values of current, voltage, and coil turns. Finally, the battery is a CFx type, described in Section 5.3.1.3. The design variables left to size the system are: the magnetic moment of the magnetorquer, the power, and the geometry of the ferromagnetic rod. The design process is summarised:

Problem parameters

- Orbit altitude $h = 1000$ km (determines geomagnetic field strength)
- Initial angular rate $\omega_{3i} = 6$ deg/s (flat spin)
- Target moment of inertia $I = 129112$ kgm^3

System parameters

- Frozen
  - Wire 24 AWG $R_w = 0.084$ Ω/m, $\rho_w = 8940$ kg/m^3
  - Battery CFx $SE = 625$ Wh/kg, $ED = 1070$ Wh/l
  - Ferromagnetic core $\mu_r = 2000$, $\rho_c = 5240$ kg/m^3
- Optimisation variables
  - Magnetic moment m_{MT} or stabilisation time t_s
  - Power P
  - Magnetorquer slenderness λ

Design process

1. Calculate stabilisation time t_s for the given m_{MT} (Eq. 5.10)
2. Magnetorquer volume and geometry (Eqs. 5.29 and 5.37)

3. Required voltage (given the m_{MT}, geometry, and wire resistivity, Eq. 5.34)
4. Number of wire turns (given geometry and power, Eq. 5.32)
5. Magnetorquer mass (wire mass and core mass, from geometry and materials' density)
6. Battery mass (given t_s, $\langle P_{total} \rangle$, and SE)
7. Total mass (battery and magnetorquers)

In (5.29), the maximum magnetic moment of the magnetorquer and the saturation magnetic field (a property of the ferromagnetic material) give the volume of the core, thus its mass is constant for a prescribed magnetic moment. However, the mass of the wire depends on the length of the rod, or more accurately (since the volume is constant), the slenderness ratio

$$\lambda = l/d \tag{5.36}$$

where $d = 2r$ is the diameter of the core. Given the core volume V_C, the diameter is

$$d = \left(\frac{4V_C}{\pi \lambda} \right)^{1/3} \tag{5.37}$$

For a given magnetic moment and power, Fig. 5.16 shows the wire mass as a function of λ.

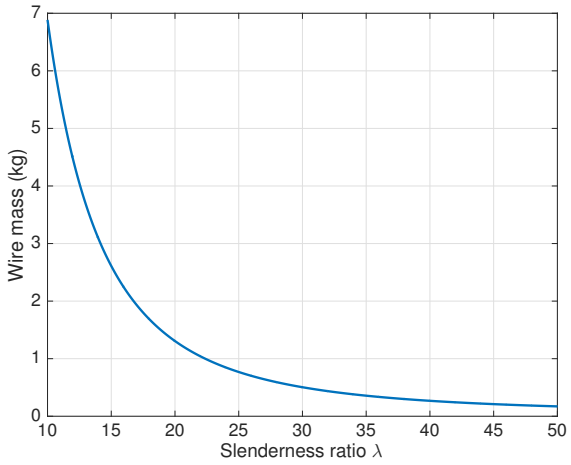

Figure 5.16: Wire mass as a function of the slenderness ratio of the core (for m =400 Am^2 and P =10 W)

In terms of mass, the more slender the better, since less turns are required in the coil. For the same applied power higher current will go through, which could limit the slenderness. However, the requirement for the magnetorquer to be compact is more restrictive than the currents involved. In a full optimisation of all the variables, the slenderness of the minimum-mass system would be the maximum allowed. In this work, a slenderness ratio of λ =25 is selected.

Having fixed the geometry variable (λ), the optimisation variables are the magnetic moment (related to the stabilisation time) and the power. In Fig. 5.17, the mass of the system as a function of power is shown, for a given magnetic moment.

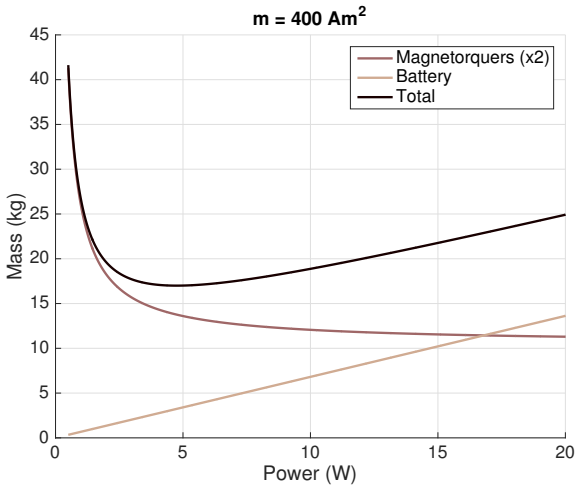

Figure 5.17: Mass of magnetorquers and battery as a function of power (for m =400 Am^2 and λ =25)

Figure 5.17 shows that for every magnetic moment, there is a certain power that minimises the total mass, which is the sum of the magnetorquers' mass (decreases logarithmically) and the battery's mass (increases linearly).

Figure 5.18 shows that the minimum total as a function of the stabilisation time (this is, for every time the optimal power is selected), thus there is a trade-off decision between those two parameters. The breakdown of the different elements of the system shows that the bulk of the mass is due to the magnetorquers, not the battery, which remains between 5.5 and 3.5 kg for the span shown. Figure 5.19 shows the magnetic moment of the magnetorquers required to stabilise the target in the specified times.

Selecting the stabilisation time is now the main design decision. It is desirable to minimise the time, while keeping the mass of the system low. On one hand,

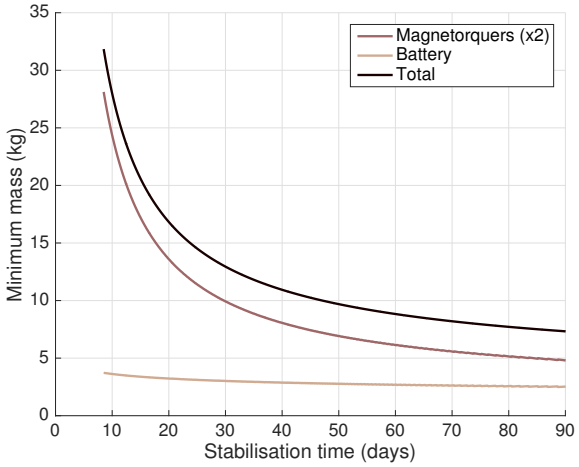

Figure 5.18: Mass of the system (magnetorquers and battery) as a function of the stabilisation time

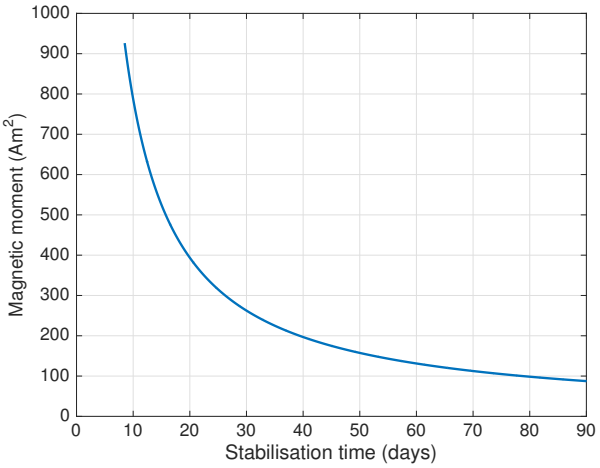

Figure 5.19: Mass of the system (magnetorquers and battery) as a function of the magnetic moment

mass minimisation is relevant not only for launch costs, but also for the fact that a lighter module will be more agile when reaching the target satellite from the chaser spacecraft. On the other hand, high stabilisation times increase the operational cost, the amount of time that the spacecraft flies in close proximity to the target (thus spending more fuel), and the risk of failure associated to long operation times.

If, according to the simplified 2D model, the target is to be stabilised in 19.5 days, 400 Am^2 magnetorquers are required. With these specifications, the optimal power is 4.8 W, with a voltage of 18.7 V and a current of 0.25 A. Each

magnetorquer is 0.9 m long and 37 mm thick, the wire makes 7500 turns forming 4 layers, and its overall weight is 6.9 kg. To rend the module more compact, the magnetorquers can be cut in half. The battery weighs 3.2 kg and its volume is 2 litres. The combined mass of two magnetorquers and the battery (the two elements of the module which depend on the stabilisation time) is 17 kg. Adding 1 kg for the propulsion system, and an estimate of 15% in terms of structure and avionics, the total mass is 20.7 kg.

5.4 Detumbling simulations

In order to outline a preliminary design, a 2D model and simplified dynamics has been used. In this section, simulations of a realistic scenario have been realised, including the orbital dynamics and a model of the Earth magnetic field [16]. The effects of atmospheric drag, solar radiation pressure, and gravity gradient are neglected, their torques being three orders of magnitude below that of the magnetorquers. Consequently, their effects are imperceptible in compared simulations but they slow down considerably the simulation speed.

In the baseline scenario, an orbit similar to that of Envisat is considered, with an inclination of 98 degrees and an altitude of 1000 km. The principal moments of inertia of the target satellite are $\mathbf{I} = [17023\,124825\,129112]^T$ kgm^2. The module, attached to a side of the target, can be equipped with two or three orthogonal magnetorquers, assumed to be aligned with the principal axes of the target. The initial angular velocity of the satellite is $\boldsymbol{\omega}_0 = [0.07\,0.04\,0.07]^T$ rad/s, whose norm equals approximately 6 deg/s or 1 rpm. The satellite is tumbling, thus its angular velocity vector is not aligned with any axis and it changes according to the free motion of an asymmetric rigid body. The magnetorquers in the simulation provide a maximum magnetic moment of 400 Am^2 each. The actuators progressively stabilise the tumbling of the target until a threshold of 0.01 rpm is achieved, then they are turned off.

Three orthogonal magnetorquers can generate a magnetic moment in any direction. The third magnetorquer could be deployed once the module is attached to the target, so that the system is compact while stored and during the manoeuvre. Figure 5.20 shows that the target is stabilised in 12.2 days, achieving a pure spin in 6 days. From this point onwards, the angular rate decreases linearly. However,

the mass of the additional magnetorquer (7 kg) must be taken into account, along with a required 4.1 kg power source.

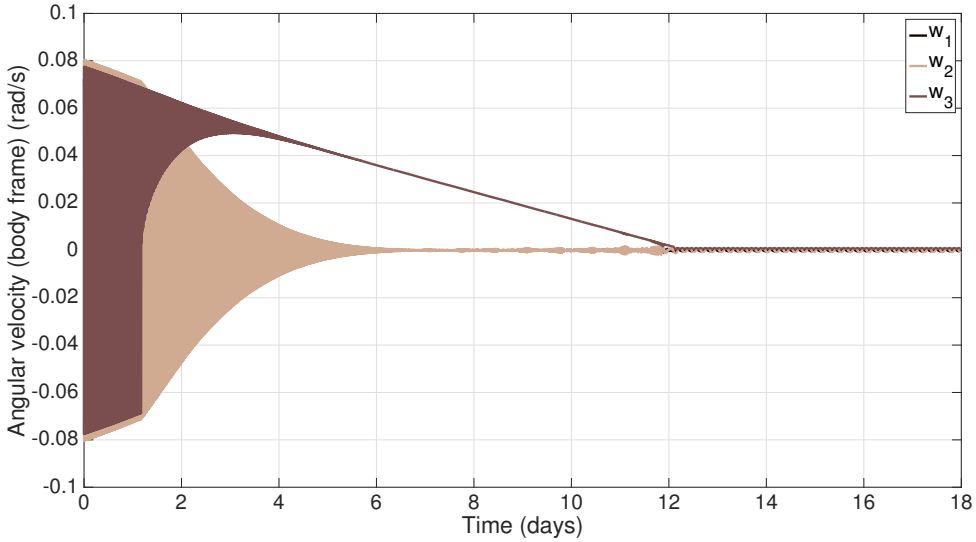

Figure 5.20: With 3 magnetorquers, evolution of the angular velocity components in the body frame

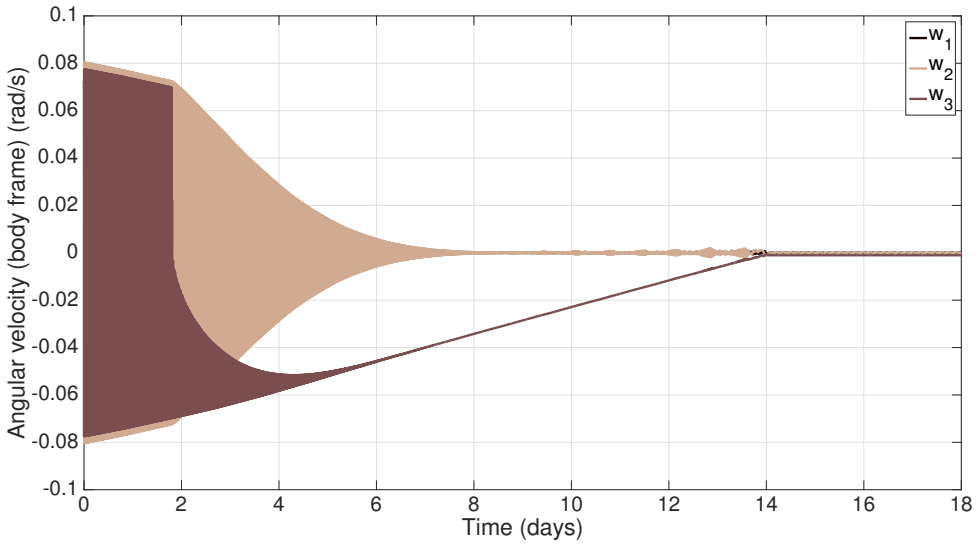

Figure 5.21: With 2 magnetorquers, first variant of the control law where $\mathbf{T}$ is parallel to $\boldsymbol{\omega}_{\perp}$

Since the Earth magnetic field relative to the satellite varies with the target's position along the orbit, two magnetorquers suffice for stabilisation purposes, although the control law has limitations, as discussed in Sec. 5.2.2. The two

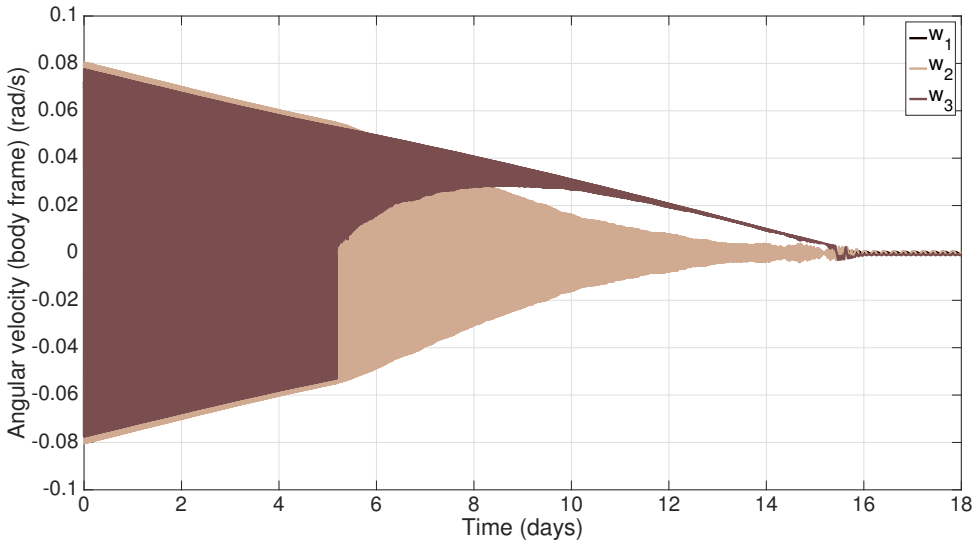

Figure 5.22: With 2 magnetorquers, second variant of the control law where **m** is orthogonal to **B**

variants of the control law for two magnetorquers have been simulated. In the first case, where **T** is parallel to $\boldsymbol{\omega}_{\perp}$, the satellite is stabilised in 14 days and a 4.6 kg battery (Fig. 5.21); in the second case, where **m** is orthogonal to **B**, the stabilisation takes 15.9 days and a 4.8 kg battery (Fig. **??**). Furthermore, in the first case a pure spin is achived much earlier.

Other scenarios can be considered for an Envisat-like satellite, and three magnetorquers in the detumbling module. A 1 rpm figure has been used for the baseline scenario in this work, but the latest data on Envisat's rotational state [39] shows that it is tumbling at about 0.5 rpm. In this case, three magnetorquers can stabilise it in 6.1 days. If the target was found to rotate at 2 rpm (mainaining the rest of the parameters of the baseline scenario) it would be stabilised in 22.5 days, using a battery of 7.2 kg.

Alternatively, at 1 rpm, if the target was in a 500 km high orbit (where the magnetic field is stronger) it would be stabilised in 9.4 days, 3 days less than at 1000 km. If the target was placed in a 2000 km orbit (the conventional limit of the LEO region) the stabilisation would take 20.5 days (however, the large majority of debris objects in the LEO region are located between 400 and 1100 km [1]).

At low inclination orbits, the external magnetic field vector does not change as much with respect to the orbit position. In those cases, control by magnetic means

Scenario	**Time (days)**	**Battery (kg)**	**Module (kg)**
Baseline, 3 MT*	12.2	4.1	30.0
Baseline, 2 MT, ctrl. (a)	14.0	4.6	22.5
Baseline, 2 MT, ctrl. (b)	15.9	4.8	22.8
ω =0.5 rpm, 3 MT	6.1	1.9	27.5
ω =2.0 rpm, 3 MT	22.5	7.2	33.6
h =500 km, 3 MT	9.4	3.2	29.0
h =2000 km, 3 MT	20.5	6.4	32.7
i =30 deg, 3 MT	21.5	7.1	33.5
m_{MT} =600 Am^2, 2 MT	10	4.6	28.8
m_{MT} =600 Am^2, 3 MT	7.6	3.9	39.1

Table 5.1: Simulation results for different scenarios. *MT = magnetorquers.

is not as effective—in the ideal case of an equatorial orbit on the geomagnetic reference frame, one axis would remain uncontrolled. For instance, in an orbit with an inclination of 30 degrees, three magnetorquers would take 21.5 days to stabilize the satellite.

The baseline scenario considers 400 Am^2 magnetorquers. If 600 Am^2 were used (weighting an estimate of 9.7 kg each), with three and two magnetorquers the target would be stabilised in 7.6 and 10 days respectively, and the energy consumption would be lower.

Table 5.1 summarises the results for different scenarios (the module mass includes the propulsion system and the structure (15% of total system mass)). With three magnetorquers, the module mass is around 30 kg. Using two magnetorquers, the mass is less than 23 kg and the module is more compact, but the stabilisation time is somewhat longer (2.2 days). If a total mass of 30 kg is acceptable, then using two 600 Am^2 magnetorquers might be a good compromise between mass and stabilisation time. However, a set of three magnetorquers, which provide greater control capability, may be an option more robust to unforeseen situations.

Comparing these results to the estimation made using the 2D model, the stabilisation time using two 400 Am^2 magnetorquers with a constant torque is about 20 days. However, this result is obtained if the same conditions are set in the simulation. In the simulation the stabilisation times obtained are lower, but the energy spent is higher and heavier batteries are required (as opposed to the 3.2 kg one of the simplified model). Generally speaking, the battery shall be oversized

by a certain safety factor to allow for uncertainties and for longer stabilisation times than expected.

5.5 Chapter summary

A concept that tackles the problem of detumbling an uncooperative target has been presented. The concept is based on a 20-30 kg compact module carried by the chaser spacecraft, which is attached to the target using drills or a space adhesive. The transfer from the chaser to the target is realised with its own cold gas propulsion system, using the guidance method presented in Chapter 4. Once attached, a set of two or three magnetorquers proceed to stabilise the tumbling motion of the target, powered by primary batteries. The concept has been dubbed Attitude Stabilisation Electromagnetic Module (ASEM). A reusable version could use fuel cells as the power source, and thrusters can be considered in a future work with a focus on underactuated attitude systems. The feasibility of this concept has been studied using the Envisat satellite as the baseline scenario.

A simplified model has been used to obtain analytical expressions (relating magnetic moment, stabilisation time, and energy) which help providing an order of magnitude of the sizing parameters. On the one hand, the 2D model can be considered a worst-case scenario since the angular velocity is aligned with the largest axis of inertia (while in the 3D case it is pointed in an arbitrary direction), and the magnetic moment is constant and limited to the maximum capacity of a single magnetorquer. On the other hand, the simplified model has a constant magnetic field vector orthogonal to the angular velocity, whereas in the simulations the magnetic field vector changes with time. Thus, the preliminary results need to be refined after analysing simulations of every special case, but results indicate that a priori the initial guess can be considered an over-estimation.

Additionally, a modified B-dot control law has been proposed. It can stabilise a spacecraft faster than the popular B-dot control and is more efficient than the on-off method. However, it is not applicable to cases where the magnetorquers' capability is so large (relative to the spacecraft mass) that the angular velocity becomes locked with the magnetic field. (The baseline scenario is far from this case.) Additionally, the modified B-dot been adapted to function with two magnetorquers. Two variants of the law have been devised, but results show that the first variant ($\mathbf{T}$ parallel to $\boldsymbol{\omega}_\perp$) is overall better than the second. Generally,

three magnetorquers 400 Am^2 stabilise the target faster (13.5 days), but the total module mass is larger (around 30 kg). In constrast, a module with two magnetorquers weights 22 kg and can stabilise the target in 16.6 days. A compromise solution can be a two-magnetorquer module with 600 Am^2 capacity.

Simulation results show that the time required for stabilisation varies with the inclination and altitude of the orbit (the Envisat orbit inclination is favourable for magnetic actuation). Nevertheless, the majority of the satellites in LEO are not placed in low inclination orbits, the most problematic for the use of this system. A figure of 1 rpm for the angular velocity has been used, but the current tumbling rate of Envisat (as of 2014) is 0.5 rpm, which can be stabilised in 6.1 days.

Chapter 6

Conclusions

6.1 On the polynomial motion planning method

6.1.1 Conclusions and discussion

A polynomial motion planning method has been presented, and applied in different ways to a variety of problems. The broad applications under study have been attitude manoeuvres and docking manoeuvres to an uncooperative tumbling target. In the first, quaternion attitude coordinates (lying in a 4D hypersphere space) are shaped with polynomials; in the second, three independent Cartesian coordinates are used—which are more intuitive and are not normalised.

Although the scenarios are very different, there are aspects of polynomial planning method applicable to both. For instance, an appropriate selection of boundary conditions, to match the rotation of the target in the docking case, but used to minimise vibrations in attitude manoeuvres.

In the docking problem, feedback was introduced by re-computing the trajectory during the manoeuvre, in order to update it to the current state of the target and to reject external perturbations. In the attitude problem, the trajectory was planned once and it was tracked using a simple PD controller. (An open-loop approach could still be feasible if the internal model is accurate and the spacecraft is very rigid, with a linear controller nullifying any residual error a the end of the manoeuvre. Trajectory tracking was not used in the docking scenario since the sample frequency of the controller would not be high enough to deliver good performance. Besides, the internal model in the attitude scenario would be more

accurate than the docking scenario, where the target is a little-known piece of debris or an old satellite. In contrast, only minor adjustments are required in the attitude trajectory to achieve the final state.

In the special case of hovering, a receding horizon approach is used (in a similar way as in Model Predictive Control). Higher order polynomials are a way of introducing more degrees of freedom in the trajectory, and the potential numerical issues can be solved with scaling (not a problem for the orders used in this work). Regarding optimisation strategies, efficient unconstrained methods can be applied, and the root-finding approach can be used in the attitude case. In obstacle avoidance, simple attitude manoeuvres crossing a keep-out cone can be solved efficiently with a waypoint, although in the more complex case of docking, where the keep-out volume is still convex but it rotates, the trajectory has to be re-shaped by iterating its variables (initial and final times and free coefficients). Generally, however, in the optimisation with or without path constraints, relatively good solutions can be obtained by adjusting time only, using a minimum-order polynomial that just matches the boundary conditions, making it an efficient suboptimal method.

Overall, an effort for computational efficiency has been made, through a variety of strategies. At the same time, the polynomial family of functions seems to naturally provide good trajectories in the applications studied, since low-order polynomials perform relatively well. Also, while higher-order polynomials improved the trajectory (in terms of the performance index), feasible solutions can be also found with low-order polynomials. Also, just one free coefficient (per coordinate) can yield a measurable improvement.

Inherently, trajectory planning is a robust approach, since the constraints are taken into account and a feasible motion is ensured before the manoeuvre even starts. It is, of course, subject to the accuracy of the internal model (which cannot be too complex, if time-consuming numerical integration is to be avoided), and the convergence rate of the optimisation algorithms. Unconstrained optimisation with penalty functions is suggested in this thesis as a more efficient approach than constrained optimisation algorithms. The problem with unconstrained optimisation is that, despite penalty functions modifying the performance function accounting for the constraints, technically speaking it could converge into an infeasible solution. However, if the constraints are not satisfied, the optimisation could be run again with different initial guesses or adjusted weights—in any case,

the manoeuvre would not executed until a feasible motion is found. Constrained optimisation methods will not output an infeasible solution, but if the problem is too constrained, it might not converge at all.

In terms of the applications of this method, apart from the general benefits of attitude trajectory optimisation (e.g. agile satellites, nano-spacecraft), flexible spacecraft is a promising one. On the one hand, this method enables the use of reaction wheels (delivering precise and smooth torque), even if they do not have high power or momentum storage, since those constraints are taken into account and prevent the wheels from saturating mid-manoeuvre. On the other hand, the continuous and smooth polynomial trajectories, with emphasis in the endpoints, is shown to effectively reduce vibrations. Interestingly, Singh [91] devleops an input-shaped control which uses to minimize the tip deflection of appendages and spillover vibrations. The torque profile obtained with the input-shaped method is made of discrete jumps (although not bang-bang), but if the discretisation was infinitesimally small, or an interpolation of the discrete torque profile was realised, the result would be a smooth, sinusoidal-like shape. This type of shape is the same as the one obtained with inverse dynamics in this polynomial trajectory planning.

While the planning method has been applied to the attitude case in a variety of forms, it has also been applied with the very specific purpose of uncooperative docking. Unlike attitude manoeuvres, where using on-board trajectory planning is an optional feature in most missions, docking to a tumbling target is a scenario that has never occurred and where trajectory planning might be the only way to comply with the mission requirements. Additionally, the three-segment docking strategy is designed to enhance robustness and focus on specific guidance problems in each of them (first, moving around the obstacle up to its surface; second, perform hovering to lock in the docking point and axis and allow a safe abort before entering the keep-out area; third, follow an obstacle-free linear path down to the docking point). Hence, in this thesis it has been shown how polynomial motion planning for guidance and control, combined with a segmented trajectory approach and an appropriate keep-out surface, is a feasible method to be considered.

6.1.2 Future work

During the research there have been, however, dead ends. In the rotational motion case, the dynamic equations of motion the torques depend on quaternions, angular velocity, and angular acceleration. The components of angular velocity and acceleration are themselves a function of quaternions and their derivatives, through the kinematic equation. Quaternions are time polynomials, whose coefficients are in turn a function of the final time (a variable) and endpoint quaternions (boundary conditions). In this thesis, the time domain was discretised and the torques calculated at every node with the dynamic equations (i.e. inverse dynamics), reconstructing the torque profile. Since the torque peaks (the maxima and minima of the torque profile) depend on the final time, then they could be evaluated analytically with the roots of the derivatives of the dynamic equations. Similarly, a derivative-based approach could be undertaken to obtain the final time that makes the highest torque peak be equal to the torque limit—which corresponds to the time-optimal solution (of polynomial trajectories). Although the approach is analytical it is also rather complex, the main reason being that the polynomials are in fact rational—since the quaternions are normalised. (Attempting to generate code with symbolic mathematics software either crashed or resulted in thousands of code lines.) However, using Taylor differential algebra (TDA) [92, 93] could be a potential start point, since it can be used to manipulate polynomials as a whole.

In the case of attitude manoeuvres, work was done to apply the motion planning method to rotation matrices, which is the only global and unique way of representing attitude. The approach was shaping individually several elements of the matrix, but the orthogonality and normalisation conditions could not be met satisfactorily and without the presence of singularities.

In the docking scenario, a new guidance strategy could be developed. First, an optimal trajectory is planned in the ground (using powerful computational resources) and sent it over to the chaser. The chaser would then track it *in the body frame*, so that the endpoint of the trajectory is the docking port, regardless of any inaccuracy in predicting the attitude of the target at the end of the manoeuvre. In order to track this path, the polynomial planning method can be used with a receding horizon. The trajectory segment between sample times could be approximated with a polynomial (i.e. a sort of Taylor approximation,

not necessarily linear), and the thrust profile computed via inverse dynamics. Alternatively, an existing robust control method could be used to track the optimal trajectory.

A natural follow-up of this thesis is a study on the implementation of the algorithms proposed (and others) in the embedded systems of a spacecraft on-board computer, since emphasis has been made on the computational efficiency. A physical testbench should be built for the purpose, if an existing one is not available. Various aspects should be investigated such as the best way to organise the computer's architecture (e.g. separate processors for different layers of the algorithm, FPGA or CPU implementation), the computational resources utilised, the optimisation of the algorithms, and the code's language. Ultimately, a flight test would rend this motion planning method flight-proven—ESA's cubesat OPS-SAT, designed as a flight testbed for space software and to be launched in 2016, is an opportunity in this regard.

6.2 On the ASEM system

6.2.1 Conclusions and discussion

A concept for stabilising a tumbling target is presented and developed. A small external module carried by the chaser kg, separates when the chaser is in close proximity flight and performs a docking to the tumbling target. At this point, the module has the mission of detumbling the debris so that the chaser, a larger and less sturdy spacecraft, can approach it slowly. In this thesis, magnetorquers are proposed as the detumbling actuators, powered with a non-rechargeable battery, and the system is dubbed ASEM for Attitude Stabilisation Electromagnetic Module. This configuration yields a 20-40 kg module that can stabilise an Envisat-based target rotating at 1 rpm in 12-8 days.

In conclusion, the module is compact and lightweight enough to be carried by the chaser spacecraft. Potentially, more than one module could be carried on the chaser to use on several targets, or a reusable version could be devised. An ASEM system may allow the designer of the chaser spacecraft to relax the requirements on agility and size, since it does not have to manoeuvre to approach and capture a tumbling target. Instead, this task is performed by the module, which can use the polynomial planning method for guidance and control. Since the module

is small compared to the target, it can be considered a point-mass in terms of obstacle avoidance.

When the angular momentum of the target is high (e.g. in large tumbling satellites), the ASEM would save the extra mass associated with a strong robotic arm requiring to withstand high torque loads. Also, the collision risk for the chaser would be greatly reduced. Regarding the navigation aspect, the fact that an external observer is available (the chaser), it might facilitate the state estimation of both the module and the target. This might also help during detumbling, when the magnetic field measurement can be performed by the chaser, relieving the module from having to turn-off the magnetorquers during the measurement.

Overall, the concept proposed intends to provide a new alternative to the existing pool of detumbling systems and methods.

6.2.2 Future work

Other configurations are possible, such as using fuel cells, solar panels, or a rechargeable battery as power source, or thrusters as detumbling actuators. Among those alternatives, the most feasible options could be fuel cells, which are rechargeable, and thrusters, although the control system might present serious challenges due to the limited choice in the thrusters location on the target.

This system could be considered as an element within the wider scope of an ADR mission, for instance a parametric study of a campaign to remove various targets. It could be assessed its impact at system level on other ADR elements such as robotic arms or deorbiting devices.

In this thesis, a fast detumbling magnetic control law has been presented—fast in relative terms, when the MOI of the body is large with respect to the torque of the magnetorquers. If this condition does not hold (for instance in cases when a spacecraft can be detumbled in one or two orbits) it has been mentioned that this control law brings the system to a locked situation, where the angular velocity vector is parallel to the magnetic field vector (even if the latter is moving along the orbit). A study was undertaken with the goal of developing a fast detumbling control law (i.e. achieving a linear decrease of angular rate by means of constant torque, instead of asymptotic) for the case of high-power magnetorquers. A number of methods were tried, including an attempt (unsuccessful) of using an

optimal control solver, and many simulations were performed. The modified B-dot method proposed by Avanzini [86] aimes to solve this problem (and even becomes a main reference of the Markley and Crassidis book [13]). Although it is an asymptotic law, it can detumble a spacecraft pretty fast, but it was found in some simulations that it could also lock the spacecraft angular velocity. In any case, a lot of insight was acquired in the magnetic detumbling problem, and future efforts to develop a time-optimal, constant-torque detumbling control law could be fruitful. The key might be to not let the angular velocity vector come close (in angular terms) to the magnetic field vector. A lead to this problem could be to not only take advantage of the time-varying nature of the magnetic field along the orbit, but also the precession and nutation motions of asymmetric bodies.

There are other possible future work suggestions, regarding ASEM and uncooperative docking, that could be deemed more outlandish. For instance, it would be interesting to consider manned docking, via remote control. The performance of a trained operator could be compared to that of the polynomial motion planning or any other method. Yet another guidance approach, besides autonomous trajectory planning or remote control, is using machine learning to train a neural network, in the same way that is applied to self-driving cars. In fact, this approach has already been studied by Furfaro [94] in the case of asteroid and planetary landing.

Finally, the idea of an external module to act on a target spacecraft could be used to help the Kepler space telescope (an exoplanet finder). Due to a mechanical failure it was left with only two reaction wheels, but the engineers of the mission managed to make the most of those in the extended $K2$ mission [95]. Nonetheless, its performance was compromised. However, a study could be realised to assess the feasibility of a service mission, where an external module equipped with a reaction wheel is attached to the Kepler spacecraft.

Bibliography

[1] Liou, J.-C. [2011]. An active debris removal parametric study for leo environment remediation, *Advances in Space Research* **47**: 1865–1876.

[2] Brown, C. D. [1996]. *Spacecraft Propulsion*, American Institute of Aeronautics and Astronautics, Washington.

[3] LaValle, S. M. [2006]. *Planning Algorithms*, Cambridge University Press, Cambridge, U.K.

[4] Fahroo, F. and Ross, I. [2008]. Advances in Pseudospectral Methods for Optimal Control, *AIAA Guidance, Navigation and Control Conference and Exhibit*, number August, pp. 1–23.
URL: *http://arc.aiaa.org/doi/pdf/10.2514/6.2008-7309\nhttp://arc.aiaa.org/doi/abs/10.2514/6.2008-7309*

[5] Betts, J. T. [1998]. Survey of Numerical Methods for Trajectory Optimization, *Journal of Guidance, Control, and Dynamics* **21**(2): 193–207.

[6] Bollino, K. P. and Ross, I. M. [2007]. A pseudospectral feedback method for real-time optimal guidance of reentry vehicles, *Proceedings of the American Control Conference* pp. 3861–3867.

[7] Biagiotti, L. and Melchiorri, C. [2008]. *Trajectory Planning for Automatic Machines and Robots*, Springer.

[8] Kim, M.-J., Kim, M.-S. and Shin, S. Y. [1995]. A general construction scheme for unit quaternion curves with simple high order derivatives, *Proceedings of the 22nd annual conference on Computer graphics and interactive techniques* pp. 369–376.
URL: *http://portal.acm.org/citation.cfm?doid=218380.218486*

[9] Guan, Y., Yokoi, K. and Stasse, O. [2005]. On Robotic Trajectory Planning Using Polynomial Interpolations, *IEEE International Conference on Robotics and Biomimetics*, pp. 111–116.

[10] Richter, C., Bry, A. and Roy, N. [2013]. Polynomial Trajectory Planning for Aggressive Quadrotor Flight in Dense Indoor Environments, *International Symposium of Robotics Research (ISRR)*.
URL: *http://groups.csail.mit.edu/rrg/papers/ISRR13_Richter.pdf*

[11] Williams, R. [2013]. Simplified Robotics Joint-Space Trajectory Generation with a via Point Using a Single Polynomial, *Journal of Robotics* **2013**.
URL: *http://www.hindawi.com/journals/jr/2013/735958/abs/*

[12] *Autonomy in space exploration: Current capabilities and future challenges* [2007]. *AI Magazine* **28**(4): 27–42.

[13] Markley, F. L. and Crassidis, J. L. [2014]. *Fundamentals of spacecraft attitude determination and control*, Springer.

[14] Sidi, M. J. [1997]. *Spacecraft Dynamics and Control: A practical engineering approach*, Cambridge University Press, 32 Avenue of the Americas, New York.

[15] Wie, B. [2008]. *Space Vehicle Dynamics and Control, Second Edition*, AIAA, Reston, Virginia.

[16] Wertz, J. R. [1990]. *Spacecraft Attitude Determination and Control*, Kluwer Academic Publishers.

[17] Shuster, M. D. [1993]. A Survey of Attitude Representations, *The Journal of the Astronautical Sciences* **41**(4): 439–517.

[18] Globus, A., Crawford, J., Lohn, J. D. and Pryor, A. [2004]. A Comparison of Techniques for Scheduling Earth Observing Satellites, *Sixteenth Conference on Innovative Applications of Artificial Intelligence*, pp. 836–843.

[19] McInnes, C. R. [1998]. Satellite attitude slew manoeuvres using inverse control, *The Aeronautical Journal* pp. 259–265.

[20] Biggs, J. D. and Horri, N. [2012]. Optimal geometric motion planning for a spin-stabilized spacecraft, *Systems and Control Letters* **61**(4): 609–616.

[21] Zhang, Y. and Zhang, J.-R. [2013]. Combined control of fast attitude maneuver and stabilization for large complex spacecraft, *Acta Mechanica Sinica* **29**(6): 875–882.
URL: *http://link.springer.com/10.1007/s10409-013-0080-8*

[22] Tanygin, S. [2006]. Parametric optimization of closed-loop slew control using interpolation polynomials, *AAS/AIAA Space Flight Mechanics Meeting*, pp. 1–21.

[23] Boyarko, G., Romano, M. and Yakimenko, O. [2011]. Time-Optimal Reorientation of a Spacecraft Using an Inverse Dynamics Optimization Method, *Journal of Guidance, Control, and Dynamics* **34**(4): 1197–1208.

[24] Ventura, J., Romano, M. and Walter, U. [2015]. Performance evaluation of the inverse dynamics method for optimal spacecraft reorientation, *Acta Astronautica* **110**: 266–278.
URL: *http://linkinghub.elsevier.com/retrieve/pii/S0094576514004950*

[25] Bilimoria, K. D. and Wie, B. [1993]. Time-optimal three-axis reorientation of a rigid spacecraft, *Journal of Guidance, Control, and Dynamics* **16**(3): 446–452.

[26] Junkins, J. L. and Turner, J. D. [1985]. *Optimal spacecraft rotational maneuvers*, Elsevier Scientific, New York.

[27] Kim, Y., Mesbahi, M., Singh, G. and Hadaegh, F. Y. [2004]. On the constrained attitude control problem, *AIAA Guidance, Navigation, and Control Conference and Exhibit*.

[28] Cheng, X., Cui, H., Cui, P. and Xu, R. [2010]. Large angular autonomous attitude maneuver of deep spacecraft using pseudospectral method, *ISSCAA2010 - 3rd International Symposium on Systems and Control in Aeronautics and Astronautics* pp. 1510–1514.

[29] Kjellberg, H. C. and Lightsey, E. G. [2014]. A Constrained Attitude Control Module for Small Satellites, *Proceedings of the AIAA/USU Conference on Small Satellites*, SSC12-XII-1.

[30] Frazzoli, E., Dahleh, M. A., Feron, E. and Kornfeld, R. [2001]. A randomized attitude slew planning algorithm for autonomous spacecraft, *AIAA Guidance, Navigation, and Control Conference*.

[31] Tanygin, S. [2015]. Fast Three-Axis Constrained Attitude Pathfinding and Visualization Using Minimum Distortion Parameterizations, *Journal of Guidance, Control, and Dynamics* pp. 1–13.
URL: *http://arc.aiaa.org/doi/10.2514/1.G000974*

[32] Singh, G., Kabamba, P. T. and Mcclamrochj, N. H. [1989]. Bang-bang control of flexible spacecraft slewing maneuvers: Guaranteed terminal pointing accuracy, *Journal of Guidance, Control, and Dynamics* **13**(2): 376–379.

[33] Skaar, S. B. and Tang, L. [1986]. On-Off attitude control of flexible satellites, *Journal of Guidance, Control, and Dynamics* **9**(4): 507–510.

[34] Singh, T. [2004]. Jerk limited input shapers, *Proceedings of the American Control Conference* **5**(March): 4825–4830.

[35] Kim, J.-J. and Agrawal, B. N. [2006]. Experiments on Jerk-Limited Slew Maneuvers of a Flexible Spacecraft, *AIAA Guidance, Navigation, and Control Conference and Exhibit*, pp. 1–20.

[36] Byers, R. M., Vadali, S. R. and Junkins, J. L. [1990]. Near-minimum time, closed-loop slewing of flexible spacecraft, *Journal of Guidance, Control, and Dynamics* **13**(1): 57–65.

[37] Liou, J.-C. and Johnson, N. L. [2008]. Instability of the present leo satellite populations, *Advances in Space Research* **41**(7): 1046–1053.

[38] Liou, J.-C. and Johnson, N. L. [2010]. Controlling the growth of future leo debris populations with active debris removal, *Acta Astronautica* **66**: 648–653.

[39] Bastida Virgili, B., Lemmens, S. and Krag, H. [2014]. Investigation on envisat attitude motion, *e.Deorbit Workshop*.

[40] Bastida, B. and Krag, H. [2009]. Strategies for active removal in leo, *Proceedings of the 5th European Conference on Space Debris ESA SP-672*.

[41] Castronuovo, M. [2011]. Active space debris removal a preliminary mission analysis and design, *Acta Astronautica* **69**: 848–859.

[42] Nishida, S. and Kawamoto, S. [2011]. Strategy for capturing of a tumbling space debris, *Acta Astronautica* **68**: 113–120.

[43] Reed, J., Busquets, J. and White, C. [2012]. Grappling system for capturing heavy space debris, *2nd European Workshop on Active Debris Removal*.

[44] Ahedo, E., Merino, M., Bombardelli, C., Urrutxua, H., Pelaez, J. and Summerer, J. [2011]. Space debris removal with an ion beam shepherd satellite: target-plasma interaction, *47th IAA/ASME/SAE/ASEE Joint Propulsion Conference and Exhibit*.

[45] Hughes, P. [1986]. *Spacecraft Attitude Dynamics*, Dover Publication Inc.

[46] Lampariello, R. [2013]. On Grasping a Tumbling Debris Object with a Free-Flying Robot, *IFAC Symposium on Automatic Control in Aerospace* **19**(1): 161–166.
URL: *http://www.ifac-papersonline.net/Detailed/63171.html*

[47] Fehse, W. [2003]. *Automated rendezvous and docking of spacecraft*, Cambridge Aerospace Series, Cambridge, U.K.

[48] Fenton, R. C. [2008]. A ladar-based pose estimation algorithm for determining relative motion of a spacecraft for autonomous rendezvous and dock, *PhD dissertation,Utah State University* .

[49] Cropp, A., Palmer, P. and Underwood, C. I. [2000]. Pose Estimation of Target Satellite for Proximity Operations, *14th Annual AIAA/USU Conference on Small satellites.*

[50] Rusinkiewicz, S. M. [2001]. *Real-Time Acquistion and Rendering of Large 3D Models*, PhD thesis, Stanford University.

[51] English, C., Okouneva, G., Saint-Cyr, P., Choudhuri, A. and Luu, T. [2011]. Real-Time Dynamic Pose Estimation Systems in Space: Lessons Learned for System Design and Performance Evaluation, *The International Journal of Intelligent Control and Systems* **16**(2): 79–96.

[52] Post, M. A., Li, J. and Clark, C. [2015]. Visual pose estimation system for autonomous rendezvous of spacecraft, *13th Symposium on Advanced Space Technologies in Robotics and Automation.*

[53] Harland, D. M. [2005]. *The Story of Space Station Mir*, Praxis Publishing/Springer.

[54] Oda, M. [2000]. Summary of NASDA?s ETS-VII robot satellite mission, *Journal of Robotics and Mechatronics* **12**(4): 417–424.

[55] Shoemaker, J. and Wright, M. [2003]. Orbital Express Space Operations Architecture Program, *17th Annual AIAA/USU Conference on Small satellites.*

[56] Ogilvie, A. and Allport, J. [2008]. Autonomous satellite servicing using the orbital express demonstration manipulator system, *9th International Symposium on Artificial Intelligence.*
URL: *http://robotics.estec.esa.int/i-SAIRAS/isairas2008/Proceedings/SESSION 14/m113-Ogilvie.pdf*

[57] Pinson, R., Howard, R. and Heaton, A. [2008]. Orbital Express Advanced Video Guidance Sensor: Ground Testing, Flight Results and Comparisons, *AIAA Guidance, Navigation and Control Conference and Exhibit.*

[58] Rank, P., Mhlbauer, Q., Naumann, W. and Landzettel, K. [2011]. The DEOS Automation and Robotics Payload, *Advanced Space Technologies in Robotics and Automation (ASTRA).*
URL: *http://robotics.estec.esa.int/ASTRA/Astra2011/Papers/04B/FCXNL-11A06-2139219-1-2139219rank.pdf*

[59] McInnes, C. R. [2000]. Autonomous path planning for on-orbit servicing vehicles, *Journal of the British Interplanetary Society* **53**: 26–38.

[60] Park, H., Cairano, S. D. and Kolmanovsky, I. [2011]. Model Predictive Control for Spacecraft Rendezvous and Docking with a Rotating / Tumbling Platform and for Debris Avoidance, *American Control Conference*, pp. 1922–1927.

[61] Lu, W., Geng, Y., Chen, X. and Zhang, F. [2011]. Relative position and attitude coupled control for autonomous docking with a tumbling target, *International Journal of Control and Automation* **4**(4): 1–22.

[62] Di Mauro, G., Di Lizia, P., Armellin, R. and Lavagna, M. [2012]. A Novel Nonlinear Control Approach for Rendezvous and Docking Manoeuvring, *63rd International Astronautical Congress*.

[63] Nolet, S., Kong, E. and Miller, D. W. [2009]. Ground and Flight Testing of Multiple Spacecraft Control on SPHERES During Close Proximity Operations, *Journal of Spacecraft and Rockets* **46**(6): 1–19.

[64] Fejzic, A. [2008]. *Development of Control and Autonomy Algorithms for Docking to Complex Tumbling Satellites*, PhD thesis, University of Washington.

[65] Michael, J., Chudej, K. and Pannek, J. [2012]. Modelling and Optimal Control of a Docking Maneuver with an Uncontrolled Satellite, *ArXiv* .
URL: *http://arxiv.org/abs/1203.6782*

[66] Ciarcia, M. and Romano, M. [2012]. Suboptimal guidance for orbital proximity maneuver with path constraints capability, *AIAA Guidance, Navigation, and Control Conference*.

[67] *Autonomous capture of a tumbling satellite* [2007]. *Journal of Field Robotics* **24**(4): 275–296.

[68] Aghili, F. [2009]. Optimal control of a space manipulator for detumbling of a target satellite, *Proceedings - IEEE International Conference on Robotics and Automation* pp. 3019–3024.

[69] Nishida, S. and Kawamoto, S. [2011]. Dynamical simulations for space debris capture, *SICE Annual Conference*, pp. 2283–2286.

[70] Araromi, O. A., Gavrilovich, I., Shintake, J., Rosset, S., Richard, M., Gass, V. and Shea, H. R. [2015]. Rollable multisegment dielectric elastomer minimum energy structures for a deployable microsatellite gripper, *IEEE/ASME Transactions on Mechatronics* **20**(1): 438–446.

[71] Yoshida, K. and Nakanishi, H. [2001]. The tako (target collaborativize) flyer: a new concept for future satellite servicing, *Proceeding of the 6th International Symposium on Artificial Intelligence and Robotics & Automation in Space* pp. 2–5. **URL:** *http://robotics.estec.esa.int/i-SAIRAS/isairas2001/papers/Paper_AS028.pdf*

[72] Bombelli, A., Benvenuto, R., Carta, R., Lavagna, M. and Armellin, R. [2012]. Optimal design of a net-shaped space debris removal system, *Proc. of 5th ICATT*.

[73] Peters, T., Escorial, D., Pellacani, A. and Aviles, M. [2014]. The COBRA IRIDES experiment, *65th International Astronautical Congress*.

[74] Bennett, T. and Schaub, H. [2014]. Touchless Electrostatic Three-Dimensional De-tumbling Of Large Geo Debris, *AAS/AIAA Spaceflight Mechanics Meeting*.

[75] Ortiz, N. and Walker, S. [2014]. Eddy currents applied to detumbling of space debris: analysis and validation of approximate proposed methods, *65th International Astronautical Congress*.

[76] Chaturvedi, N., Sanyal, A. and McClamroch, N. [2011]. Rigid-Body Attitude Control, *IEEE Control Systems* **31**(3): 30–51.

[77] Shahriari, S., Azadi, S. and Moghaddam, M. M. [2010]. An accurate and simple model for flexible satellites for three-dimensional studies, *Journal of Mechanical Science and Technology* **24**(6): 1319–1327.

[78] Storch, J. and Gates, S. [1989]. Motivating Kane's method for obtaining equations of motion for dynamic systems, *Journal of Guidance, Control, and Dynamics* **12**(4): 593–595.

[79] Bedrossian, N., Bhatt, S., Lammers, M. and Nguyen, L. [2007]. Zero Propellant Maneuver Flight Results for 180 deg ISS Rotation, *Proceedings of the International Symposium on Space Flight Dynamics*.

[80] Maclean, C., Pagnozzi, D. and Biggs, J. [2014]. Planning natural repointing manoeuvres for nano-spacecraft, *IEEE Transactions on aerospace and electronic systems* **50**(3): 2129–2145.

[81] Rusinkiewicz, S. M. [2001]. Real-time acquisition and rendering of large 3d models, *PhD dissertation, Stanford University* .

[82] Gurrisi, C., Seidel, R., Dickerson, S., Didziulis, S., Frantz, P. and Ferguson, K. [2010]. Space Station Control Moment Gyroscope Lessons Learned, *40th Aerospace Mechanisms Symposium*.

[83] Wertz, J. R. and Larson, W. J. [1999]. *Space Mission Analysis and Design, 3rd ed.*, Microcosm Press/Kulwer Academic Publishers.

[84] Griffin, M. D. [2004]. *Space Vehicle Design, 2nd ed.*, AIAA Education series.

[85] Parness, A., Hilgendorf, T., Daniel, P., Frost, M., White, V. and Kennedy, B. [2013]. Controllable on-off adhesion for earth orbit grappling applications, *IEEE Aerospace Conference*, pp. 1–11.

[86] Avanzini, G. and Giulietti, F. [2012]. Magnetic detumbling of a rigid spacecraft, *Journal of Guidance, Control, and Dynamics* **35(4)**: 1326–1334.

[87] Jasiobedzki, P., Se, S., Pan, T., Umasuthan, M. and Greenspan, M. [2010]. Autonomous satellite rendezvous and docking using lidar and model based vision, *SPIE Proceedings: Spaceborn Sensors II*, Vol. 5798.

[88] Bragg, B. J., E, C. J. and B, T. J. [1994]. NASA Reference Publication 1353, *Primary Battery Design and Safety Guidelines Handbook*.

[89] Wolf, D. A. [2001]. *Essentials of Electromagnetism*, Cambridge University Press.

[90] Black, W. L. [1965]. Technical Note 1965-45, Lincoln Laboratory, *Design of Electromagnetic Torque Rods*.

[91] Singh, T. and Vadali, S. R. [1993]. Input-shaped control of three-dimensional maneuvers of flexible spacecraft, *Journal of Guidance, Control, and Dynamics* **16**(6): 1061–1068.

[92] Makino, K. and Berz, M. [1996]. Remainder Differential Algebras and their Applications, *Chapter of "Computational Differentiation: Techniques, Applications, and Tools"* pp. 63–74.

[93] Bignon, E., Mercier, P., Azzopardi, V. and Pinede, R. [2015]. Accurate numerical orbit propagation using Polynomial Algebra Computational Engine PACE, *ISSFD Congress*.

[94] Furfaro, R., Simo, J., Gaudet, B. and Wibben, D. R. [2014]. Neural-based trajectory shaping approach for terminal planetary pinpoint guidance, *Advances in the Astronautical Sciences* **150**: 2557–2574.

[95] Vanderburg, A. and Johnson, J. A. [2014]. A Technique for Extracting Highly Precise Photometry for the Two-Wheeled Kepler Mission, *Publications of the Astronomical Society of the Pacific* **126**(944): 11.
URL: *http://arxiv.org/abs/1408.3853*